Best
Available
Copy

AD-A013 121

APPLICATION OF ADVANCED METHODS FOR IDENTIFICATION AND DETECTION OF NUCLEAR EXPLOSIONS FROM THE ASIAN CONTINENT

T. C. Bache, et al

Systems, Science and Software

Prepared for:

Air Force Office of Scientific Research
Advanced Research Projects Agency

May 1975

DISTRIBUTED BY:

NTIS
National Technical Information Service
U. S. DEPARTMENT OF COMMERCE

224154

AFOSR - TR - 75 - 0962

AD A013121

SYSTEMS, SCIENCE AND SOFTWARE

SSS-R-75-2646

APPLICATION OF ADVANCED METHODS FOR IDENTIFICATION AND DETECTION OF NUCLEAR EXPLOSIONS FROM THE ASIAN CONTINENT

T. C. Bache
J. T. Cherry
K. G. Hamilton
J. F. Masso
J. M. Savino

AIR FORCE OFFICE OF SCIENTIFIC RESEARCH (AFSC)
NOTICE OF TRANSMITTAL TO DDC
This technical report has been reviewed and is approved for public release IAW AFR 190-12 (7b).
Distribution is unlimited.
D. W. TAYLOR
Technical Information Officer

Semi-Annual Technical Report

Sponsored by:
Advanced Research Projects Agency
ARPA Order No. 1827
Program Code 4F10

DDC
RECEIVED
JUL 29 1975
A

Contract No. F44620-74-C-0063
Effective Date of Contract: 4/1/74
Contract Expiration Date: 3/31/76
Amount of Contract: $567,312

S^3 Project 261

May 1975

Approved for public release;
distribution unlimited.

P.O BOX 1620, LA JOLLA, CALIFORNIA 92037, TELEPHONE (714) 453-0060

Reproduced by
NATIONAL TECHNICAL
INFORMATION SERVICE
US Department of Commerce
Springfield, VA. 22151

UNCLASSIFIED

SECURITY CLASSIFICATION OF THIS PAGE *(When Data Entered)*

REPORT DOCUMENTATION PAGE		READ INSTRUCTIONS BEFORE COMPLETING FORM
1. REPORT NUMBER AFOSR - TR - 75 - 0962	2. GOVT ACCESSION NO.	3. RECIPIENT'S CATALOG NUMBER
4. TITLE *(and Subtitle)* APPLICATION OF ADVANCED METHODS FOR IDENTIFICATION AND DETECTION OF NUCLEAR EXPLOSIONS FROM THE ASIAN CONTINENT		5. TYPE OF REPORT & PERIOD COVERED Semi-Annual Technical
		6. PERFORMING ORG. REPORT NUMBER SSS-R-75-2646
7. AUTHOR(s) T. C. Bache, J. T. Cherry, K. G. Hamilton, J. F. Masso and J. M. Savino		8. CONTRACT OR GRANT NUMBER(s) F44620-74-C-0063
9. PERFORMING ORGANIZATION NAME AND ADDRESS Systems, Science and Software P.O. Box 1620 La Jolla, California 92038		10. PROGRAM ELEMENT PROJECT, TASK AREA & WORK UNIT NUMBERS 62701E AO 1827-17
11. CONTROLLING OFFICE NAME AND ADDRESS Advanced Research Projects Agency/NMR 1400 Wilson Boulevard Arlington, Virginia 22209		12. REPORT DATE May 1975
		13. NUMBER OF PAGES 233
14. MONITORING AGENCY NAME & ADDRESS *(if different from Controlling Office)* Air Force Office of Scientific Research 1400 Wilson Boulevard Arlington, Virginia 22209		15. SECURITY CLASS. *(of this report)* Unclassified
		15a. DECLASSIFICATION/DOWNGRADING SCHEDULE

16. DISTRIBUTION STATEMENT *(of this Report)*

Approved for public release; distribution unlimited.

17. DISTRIBUTION STATEMENT *(of the abstract entered in Block 20, if different from Report)*

18. SUPPLEMENTARY NOTES

19. KEY WORDS *(Continue on reverse side if necessary and identify by block number)*

Seismology
Nuclear Explosions
Teleseismic Ground Motion
Seismic Discrimination
Time Series Analysis

20. ABSTRACT *(Continue on reverse side if necessary and identify by block number)*

The underlying theme of our approach to the seismic discrimination problem is the development of deterministic computational models which predict the teleseismic ground motion from earthquakes and nuclear explosions. This theoretical data base is then used to evaluate existing discriminants and to design new discriminants based on expected differences between earthquakes and nuclear explosions in the teleseismic field.

(over)

DD FORM 1 JAN 73 1473 EDITION OF 1 NOV 65 IS OBSOLETE

UNCLASSIFIED

SECURITY CLASSIFICATION OF THIS PAGE *(When Data Entered)*

For the most part, the computer models required to generate this data base are completed. Equivalent elastic sources from both earthquakes and nuclear explosions are being generated and these sources are then propagated to teleseismic distances. Furthermore, a new discriminant is being evaluated which promises to obviate the requirement for surface wave recording and reduce the magnitude at which discrimination is possible to $m_b \approx 4.0$.

TABLE OF CONTENTS

			Page
FOREWORD			6
I.	INTRODUCTION		7
II.	THE EQUIVALENT ELASTIC SOURCE FROM A NUCLEAR EXPLOSION		11
	2.1	INTRODUCTION	11
	2.2	THE REDUCED DISPLACEMENT POTENTIAL	11
	2.3	CALCULATION OF THE RDP	14
	2.4	DESCRIPTION OF THE MATERIAL MODEL	18
		2.4.1 Introduction	18
		2.4.2 The Pressure Component	19
		2.4.3 Material Strength	25
	2.5	RESULTS OF THE PARAMETER STUDY	27
		2.5.1 Introduction	27
		2.5.2 The Sensitivity of $\Psi(\infty)$ to Air-Filled Porosity, Material Strength and Overburden Pressure	30
	2.6	SUMMARY AND COMMENTS	36
III.	A THEORETICAL INVESTIGATION OF THE TELESEISMIC P WAVE FROM UNDERGROUND EXPLOSIONS		38
	3.1	INTRODUCTION	38
	3.2	THE DEPENDENCE OF THE TELESEISMIC P WAVE TRAIN ON THE SOURCE SPECTRUM FOR EXPLOSIONS IN NTS TUFF	38
	3.3	THE DISPERSION ASSOCIATED WITH A CONSTANT Q, LINEAR ABSORPTION OPERATOR	63
	3.4	THE EFFECT OF NEAR SOURCE CRUSTAL STRUCTURE ON THE TELESEISMIC P WAVE	70

Page

3.5 THE INFLUENCE OF HIGHER ORDER PERTURBATIONS ON THE SPHERICALLY SYMMETRIC EXPLOSION GENERATED P WAVE 35

IV. VARIABLE FREQUENCY MAGNITUDE DISCRIMINANT . 85

4.1 INTRODUCTION 85

4.2 TECHNIQUE. 85

4.3 SHALLOW EVENTS RECORDED AT LASA . . 88

4.4 DEEP EVENTS RECORDED AT LASA 95

4.5 SHALLOW EVENTS RECORDED AT NORWAY . 97

4.6 DEEP EVENTS RECORDED AT NORWAY . . . 101

4.7 MULTIPLE EXPLOSION SCENARIO 104

4.8 SUMMARY 106

V. MULTIPLE DISCRIMINANT TEST 109

5.1 INTRODUCTION 109

5.2 COMPLEXITY 109

5.3 SPECTRAL RATIO 112

5.4 HIGHER MOMENTS OF FREQUENCY 113

5.5 $M_s - m_b$ 121

5.6 MULTIPLE EXPLOSION SCENARIO 121

5.7 SUMMARY 124

VI. DATA ACQUISITION AND EDITING 125

VII. REFERENCES 127

APPENDIX A 132

APPENDIX B 140

APPENDIX C 161

APPENDIX D 171

Page

APPENDIX E 188

APPENDIX F 204

APPENDIX G 209

FOREWORD

This semiannual technical report entitled, "Application of Advanced Methods for Identification and Detection of Nuclear Explosions from the Asian Continent," is submitted by Systems, Science and Software (S^3) to the Advanced Research Projects Agency and to the Air Force Office of Scientific Research (AFOSR). This report presents the results of a continuing effort to obtain an optimum multi-discriminant/detection procedure for earthquakes and explosions occurring within the Asian Continent. The work is being performed under Contract Number F44620-74-C-0063. Mr. William J. Best is the AFOSR technical contracting officer.

Dr. J. Theodore Cherry is the S^3 project manager. Drs. Thomas C. Bache and Joseph F. Masso are responsible for the development and application of the seismic ground motion prediction work. Dr. John M. Savino and Mr. Kenneth G. Hamilton are responsible for the analysis of the seismic data against which all theoretical developments must eventually be tested. Acting as consultants on the project are Professors Charles B. Archambeau of the University of Colorado, David G. Harkrider of the California Institute of Technology and Donald V. Helmberger of the California Institute of Technology.

The authors wish to extend their sincere appreciation to Ms. Bernadine Ludwig and Ms. Darlene Roddy for the many hours spent on the preparation of this report.

I. INTRODUCTION

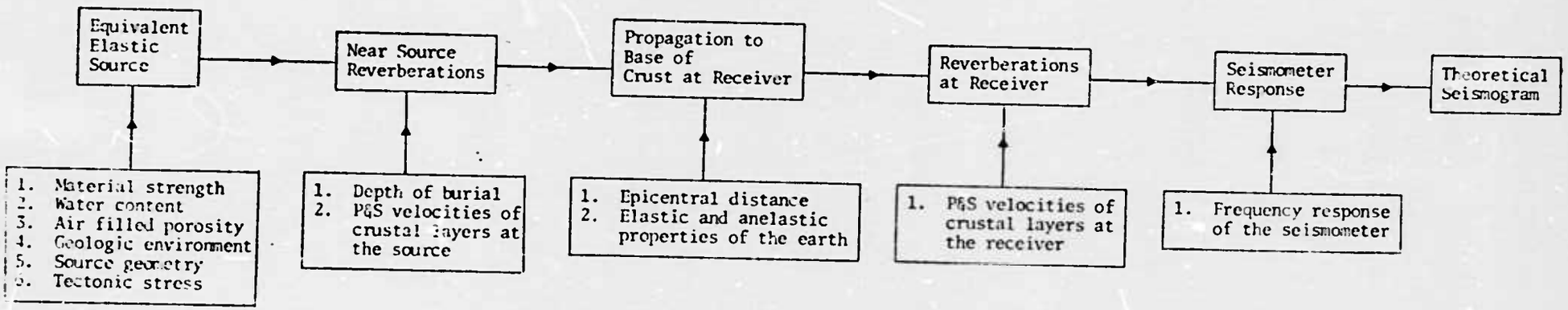
The fundamental problem toward which our research has been directed is seismic discrimination. That is, from the background of an earthquake and microseismic signals, one wishes to identify those teleseismic events which are caused by nuclear explosions.

Our approach to the problem's solution has been the development of a deterministic methodology for predicting teleseismic ground motion from both earthquakes and nuclear explosions. This predictive capability provides a theoretical basis against which existing discriminants may be tested and new discriminants designed.

Figure 1.1 is a schematic of the technique used to predict the body wave seismogram generated by a nuclear explosion. This model has been separated into five parts, which are treated independently. These are:

1. Calculation of the equivalent elastic source generated by the explosion.
2. Modification of the equivalent source by reverberations in the near source crustal structure.
3. Propagation of the rays, emerging from the base of the crust, through the upper mantle to the base of the crust in the vicinity of the receiver.
4. Pulse modifications by crustal reverberations at the receiver.
5. Modification of the computed ground motion by the characteristics of the seismometer.

In a similar fashion, given the equivalent elastic source from the explosion, teleseismic ground motion from



R-2646

Figure 1.1. Schematic representation for the deterministic prediction of the teleseismic ground motion from a nuclear explosion.

Rayleigh and Love surface waves are computed using a computational technique based on the Thomson-Haskell matrix method (Harkrider (1964)).

Both body wave and surface wave teleseismic ground motion from earthquakes may be predicted if the earthquake equivalent source replaces the explosion equivalent source.

Therefore, our research may be subdivided into the following four categories:

1. The prediction of the equivalent elastic source from nuclear explosions.
2. The prediction of the equivalent elastic source from earthquakes.
3. Propagation of these sources to teleseismic distances including both body waves and surface waves.
4. Evaluation of existing discriminants and identification of improved discriminants based on these predictions.

For the most part the predictive capability required for the analysis (Items 1, 2 and 3) is now available. These theoretical models are being used to predict the equivalent elastic sources from earthquakes and explosions and to propagate these sources to teleseismic distances. Furthermore, based on expected differences between earthquake and explosion sources, a new discriminant is being evaluated.

Section II of this report presents our current understanding of the equivalent elastic source generated by a nuclear explosion. These source functions represent the coupling of the explosion into the elastic regime, i.e., seismic coupling. The effects of elastic and inelastic near source material properties and changes in explosion yield are

identified and interpreted in terms of changes in teleseismic magnitude.

In Section III, theoretical body wave seismograms are computed at teleseismic distances using specific source functions from Section II. The effect on these seismograms and on m_b is presented as a function of depth of burial, explosion yield, the inelastic properties of the upper mantle, tectonic stress release and near source reverberations in the crust.

Section IV presents the results of a variable frequency magnitude (VFM) discriminant operating on body wave seismograms which exploits theoretically predicted spectral differences in the equivalent source between earthquakes and explosions. Complete separation of earthquake and explosion populations is achieved down to body wave magnitudes, m_b, of the order 4.0 to 4.5.

In Section V a comparison is made between the effectiveness of the VFM discriminant and other proposed discriminants (complexity, spectral ratio, higher moments of frequency and $m_b - M_s$). All discriminants are applied to the same data base: the large Eurasian population recorded at LASA. It appears that a combined application of the VFM and modified moment of frequency (MMF) discriminants may provide a very effective technique for event identification.

The appendices (A through G) present theoretical justification for a number of key issues presented in the various sections of the report. Sections IV and V should be read in sequence. All other sections and the appendices are essentially self-contained and may read independently.

II. THE EQUIVALENT ELASTIC SOURCE FROM A NUCLEAR EXPLOSION

2.1 INTRODUCTION

The common element required for predicting both body wave and surface wave teleseismic ground motion from a nuclear explosion is the equivalent elastic source of the explosion.

By and large, seismologists have been forced to use experimentally determined explosion source functions for teleseismic ground motion predictions. These source functions are limited in number, quality and the rock environment they represent. These limitations are due mainly to the expense and technical difficulty involved in fielding an experiment designed to obtain free field, time history data in the elastic regime for a nuclear source.

Computational techniques and material models have been developed at S^3 which permit a prediction of the equivalent elastic source given the yield of the explosive and the material properties of the near source geologic environment.

Since laboratory tests on rock samples provide the essential data base for a preshot estimate of material properties, it is important to determine the sensitivity of the equivalent source to those material properties which are subject to routine laboratory measurement. In this chapter we present the results of a computational parameter study which identifies the dependence of teleseismic magnitude on near source material properties.

2.2 THE REDUCED DISPLACEMENT POTENTIAL

If $u(r,t)$ is the radial displacement from a spherically symmetric explosion (see Appendix G for the general equivalent source representation) where $u(r,t)$ is measured in the linear elastic region, then

$$u(r,t) = -\frac{\partial}{\partial r}\left(\frac{\Psi(\tau)}{r}\right) = \frac{\Psi(\tau)}{r^2} + \frac{\dot{\Psi}}{r\alpha} \qquad (2.1)$$

where

$\frac{\Psi(\tau)}{r}$ = the equivalent source potential

$\Psi(\tau)$ = the reduced displacement potential (RDP)

$\tau = t - r/\alpha$

α = P wave velocity in the source region

For body waves we save only the r^{-1} components in the equivalent source expansion. Therefore

$$u(r,t) \simeq \frac{\dot{\Psi}(\tau)}{r\alpha} \qquad (2.2)$$

For surface waves (see Appendix D for a detailed analysis of Rayleigh wave amplitude scaling) the forcing function is an equivalent radial stress σ_{rr} applied to the interior of a spherical cavity where

$$\sigma_{rr} = -\rho\left[\frac{\ddot{\Psi}(\tau)}{r} + 4\beta^2\left(\frac{\Psi(\tau)}{r^3} \quad \frac{\dot{\Psi}(\tau)}{r^2\alpha}\right)\right] \qquad (2.3)$$

where ρ is the density

$\beta = \sqrt{\mu/\rho}$ is the shear wave velocity

μ is the shear modulus.

For those frequencies of interest for teleseismic surface waves, Eq. (2.3) reduces to

$$\sigma_{rr} \simeq -4\mu\frac{\Psi(\tau)}{r^3} \qquad (2.4)$$

Equations (2.2) and (2.4) isolate the elastic properties of the source region responsible for body wave and surface wave amplitude. Body wave amplitude is inversely proportional to compressional wave velocity α, while surface wave amplitude is directly proportional to the shear modulus μ.

If we assume that over a limited frequency band

$$\hat{\dot{\psi}} = \frac{A}{f^n} \tag{2.5}$$

where $\hat{\dot{\psi}}$ is the amplitude spectrum of $\dot{\psi}$ and f is frequency, then at a given yield, W_1, body wave amplitude is proportional to

$$\hat{\dot{\psi}}_1 = \frac{A}{\alpha f_0^n} \tag{2.6}$$

where f_0 is the dominant frequency of the pulse. If the combination of the earth's Q and the seismometer band pass is very narrow with center frequency f_0 then at a new yield W_2

$$\dot{\psi}_2 = \frac{A}{\alpha f_1^n} \frac{W_2}{W_1}$$

where f_1 cube root scales into f_0, i.e.,

$$f_0 = f_1 \left(\frac{W_1}{W_2} \right)^{1/3}$$

Therefore

$$\hat{\dot{\psi}}_2 = \frac{A}{\alpha f_0^n} \frac{W_2}{W_1}^{(1-n/3)} = \dot{\psi}_1 \left(\frac{W_2}{W_1} \right)^{(1-n/3)} \tag{2.7}$$

For surface waves, Eqs. (2.4) and (2.6) give

$$\hat{\Psi}_1 = \mu \frac{A}{f_0^{(n+1)}}$$

Changing the yield to W_2 and assuming a narrow band filter gives

$$\hat{\Psi}_2 = \hat{\Psi}_1 \left(\frac{W_2}{W_1}\right)^{1-n/3} \tag{2.8}$$

This scaling law is identical to that obtained for body waves (Eq. (2.7)). Both surface waves and body waves scale with yield according to the $1-n/3$ power where n corresponds to the slope of $\hat{\Psi}$ in the frequency band of interest.

If the source spectrum is flat, then $n = 0$ and teleseismic amplitudes scale with the first power of the yield.

2.3 CALCULATION OF THE RDP

If we assume that the displacement is linear within a given time interval defined by

$$\tau_1 < \tau < \tau_2$$

then Eq. (2.1) gives

$$\Psi(\tau_2) = ar^2 \left[\tau_2 - \tau_1 e^x\right] + r^2\left(b - \frac{ar}{\alpha}\right)\left[1-e^x\right] + e^x \Psi(\tau_1) \tag{2.9}$$

where

$$a = \frac{u(\tau_1,r) - u(\tau_2,r)}{\tau_1 - \tau_2}$$

$$b = \frac{-u(\tau_1,r)\tau_2 + u(\tau_2,r)\tau_1}{\tau_1 - \tau_2}$$

$$x = \frac{c(\tau_1 - \tau_2)}{r}$$

At late times when the displacement becomes constant, τ_2 can be much larger than τ_1 so that

$$e^x \to 0$$

$$a \to 0$$

$$b = u(\infty, r)$$

The steady-state value of the RDP becomes

$$\Psi(\infty) = r^2 \, u(\infty, r) \tag{2.10}$$

This result also follows directly from Eq. (2.1) since

$$\dot{\Psi}(\infty) = 0 \tag{2.11}$$

In an entirely analogous manner, the reduced velocity potential (RVP) may be computed from the velocity-time history of a particle. If $u(t,r)$ is radial particle velocity, then

$$\dot{u}(t,r) = -\frac{\partial}{\partial r}\frac{\dot{\Psi}(\tau)}{r} = \frac{\dot{\Psi}(\tau)}{r^2} + \frac{\ddot{\Psi}(\tau)}{\alpha r} \tag{2.12}$$

where $\dot{\Psi}(\tau)$ is the RVP.

If $\dot{\Psi}(\tau)$ replaces $\Psi(\tau)$ and $\dot{u}(\tau,r)$ replaces $u(\tau,r)$ in Eq. (2.9), then the algorithm for calculating the RVP follows directly.

It is highly desirable to transform the equivalent source into the frequency domain in order to identify the

frequency dependence of the spectrum required for yield scaling (Eqs. (2.5), (2.7) and (2.8)). Since $\dot{\Psi}(\infty) = 0$, then $\hat{\dot{\Psi}}$ is bounded at zero frequency and the Fourier transform of $\dot{\Psi}(\tau)$ may be done numerically.

An important relation is that the zero-frequency limit of the RVP is equal to the steady state value of the RDP. Since

$$\hat{\dot{\Psi}}(f=0) = \int_0^\infty \dot{\Psi}(\tau)\, d\tau = \int_0^\infty \frac{d\Psi(\tau)}{d\tau}\, d\tau$$

Therefore, since $\Psi(0) = 0$,

$$\hat{\dot{\Psi}}(0) = \Psi(\infty) \tag{2.13}$$

Reduced velocity potentials have been computed for a variety of near source geologic environments. These calculations were performed on a Lagrangian finite difference code, SKIPPER, that simulates a propagating stress wave in one space dimension. The difference equations in the code are identical to those given by Cherry and Petersen (1970). The code is capable of carrying the propagating stress wave into the small displacement, elastic regime and yet flexible enough to permit appropriate material response formulations in the large displacement, nonlinear regime.

Figure 2.1 shows $\hat{\dot{\Psi}}$ versus frequency for a nuclear explosion of 20 kT. Each source function in the figure is identified by an integer and corresponds to the 20 kT explosion detonated in a geologic environment with a specific set of material properties. For all practical purposes the spectra are flat (n=0) within the teleseismic frequency band ($f < 3$ Hz) for yields up to at least 200 kT. This implies that teleseismic body wave and surface wave amplitudes should be directly

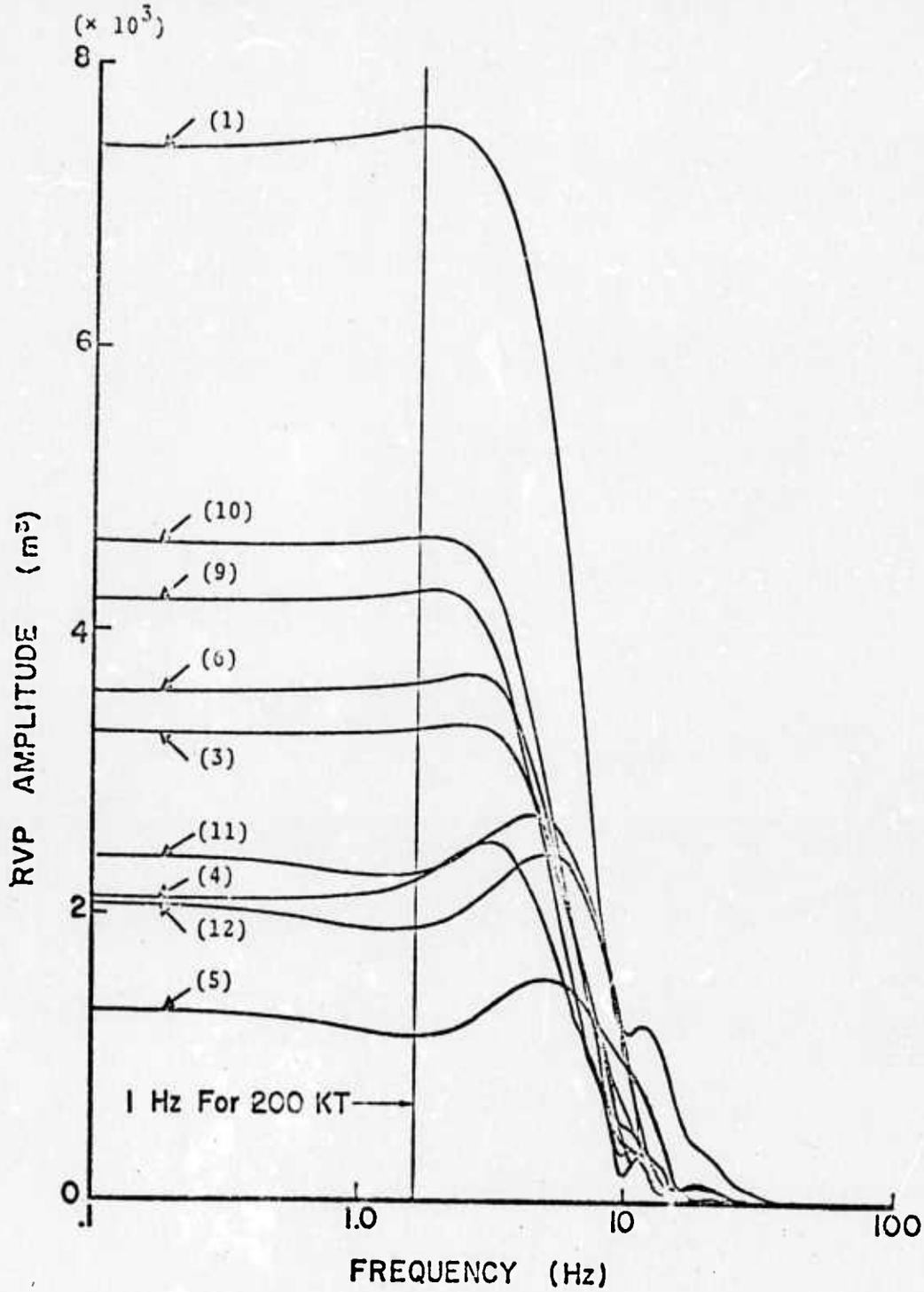


Figure 2.1. Source functions scaled to 20 kT.

proportional to the yield of the explosion. Deviation from this linear scaling should occur within the yield interval 200 kT < W < 1,000 kT, depending on the source function used to represent the rock material near the source.

2.4 DESCRIPTION OF THE MATERIAL MODEL

2.4.1 Introduction

Our goal was to establish both the shape and amplitude of the RVP spectrum as a function of near source material properties. The properties chosen were

f = mass fraction of water in the rock.

ϕ_0 = the initial air-filled volume fraction.

P_e = the elastic pressure.

P_c = the crush pressure.

k_0 = the zero pressure bulk modulus.

P_0 = the overburden pressure.

μ = the shear modulus.

Y_m = the maximum value of material strength.

P_m = the pressure at which Y_m is attained.

e_m = the internal energy required to melt the rock-water mixture.

In order to uncover the dependence of the RVP spectrum on these parameters it is important that the pressure component, P, of the equation-of-state and the material strength, Y, be

uniquely determined when these parameters are specified. We have chosen the rock constituent to be NTS tuff. The following sections, 2.4.1 and 2.4.2, present the pressure and material strength formulation used in the parameter study.

2.4.2 The Pressure Component

Given the pressure component of the equation of state for both water and grain density tuff, then the pressure component for a fully saturated mix is obtained by specifying

$$f = \frac{M_w}{M_r + M_w} = \text{mass fraction of water} \qquad (2.14)$$

For water we used the EOS formulation of Bjork and Gittings (1972) while for tuff we used the formulation given by Riney, et al. (1972) with a grain density of 2.4 g/cc. Figures 2.2 and 2.3 show the Hugoniot and release isentropes for these two constituents.

At a given pressure $\overline{P}$ a pressure equilibrium mix is obtained if

$$\overline{v} = \frac{v_r + f' v_w}{1 + f'} \qquad (2.15)$$

$$e = \frac{e_r + f' e_w}{1 + f'} \qquad (2.16)$$

where

$$f' = \frac{f}{1-f} = \frac{M_w}{M_r} \qquad (2.17)$$

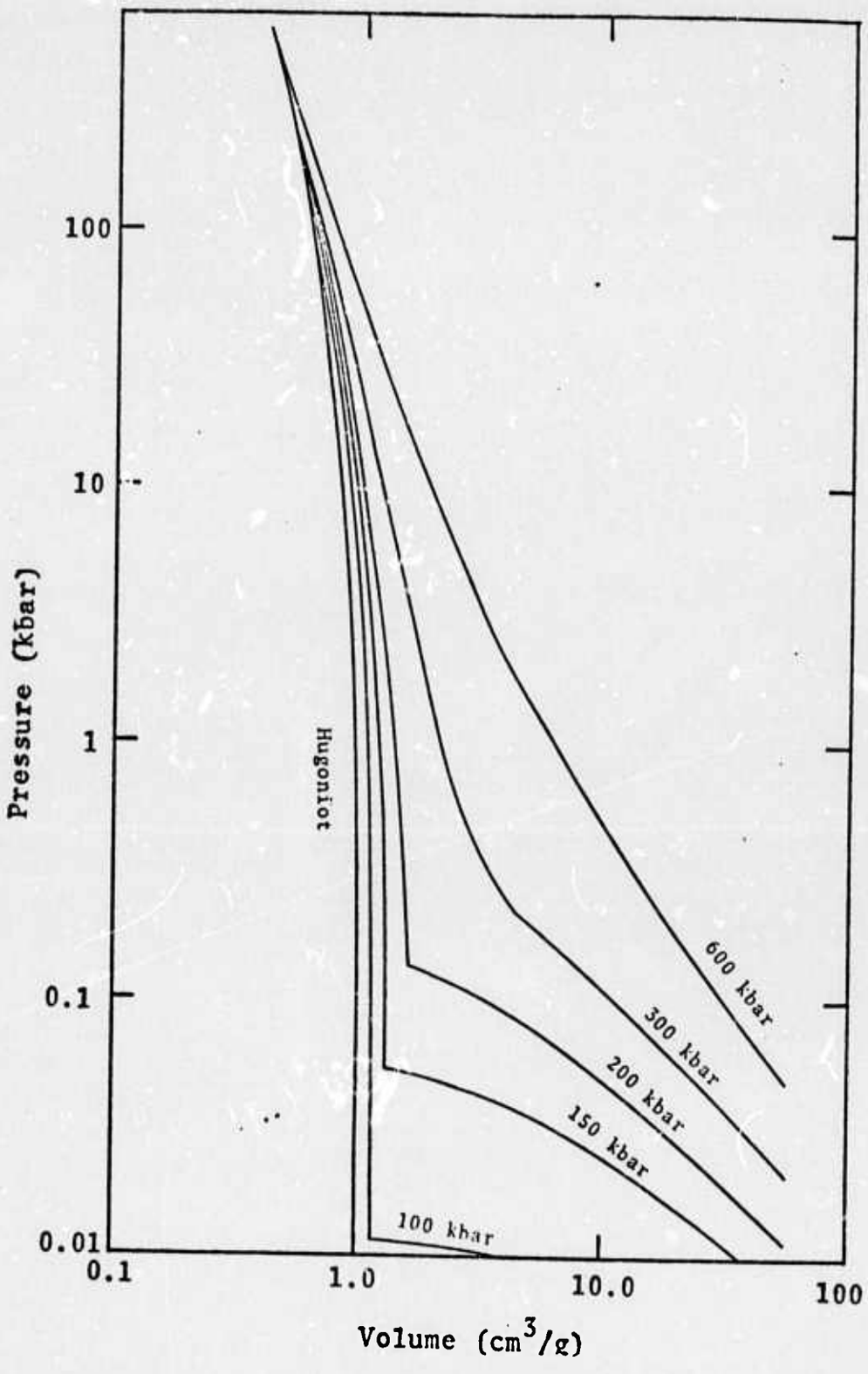


Figure 2.2. Hugoniot and release isentropes for water.

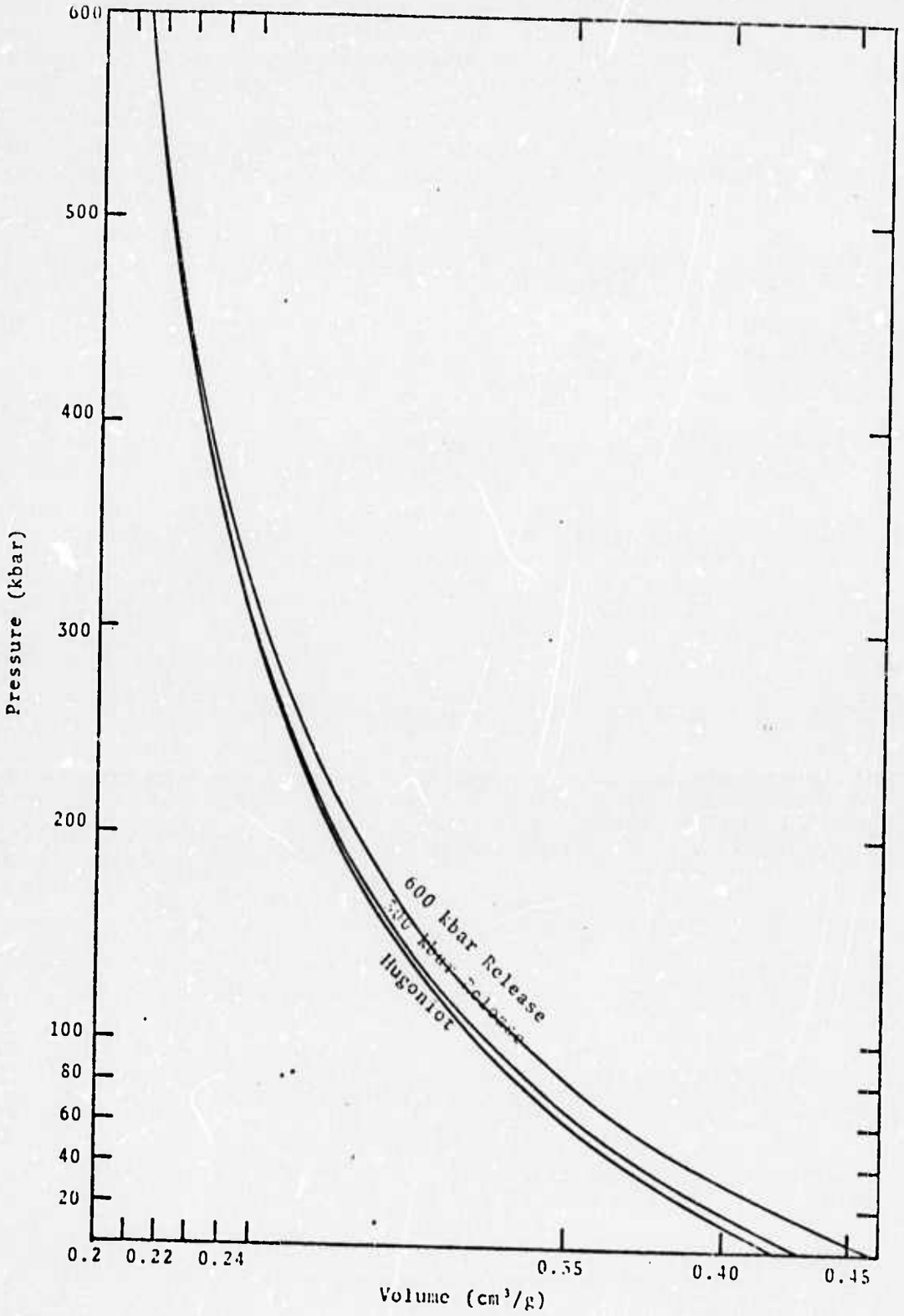


Figure 2.3. Hugoniot and release isentropes for tuff, ρ_0 = 2.4 g/cc.

v_r, v_w, e_r and e_w are specific volumes and energies of the rock and water components at the pressure $\bar{P}$. It is now possible to generate a table that gives $\bar{P}$ as a function of $\bar{v}$ and e. This table (Riney, et al. (1972)) suitably chooses values of $\bar{v}$ and e so that no time consuming search is needed when performing an interpolation at a given thermodynamic state. Figure 2.4 shows the result of mixing the rock and water constituents shown in Figs. 2.2 and 2.3 using a 0.17 value for f.

Air-filled porosity is included in the model by defining a parameter α, given by

$$\alpha = \frac{V_r + V_w + V_p}{V_r + V_w} = \frac{v}{\bar{v}} \tag{2.18}$$

where v is the specific volume of the partially saturated mix. Then

$$P = \frac{1}{\alpha} \bar{P}(v/\alpha, e) \tag{2.19}$$

where $\bar{P}$ is found from the table using v, α, e. Equation (2.19) is equivalent to the porosity model proposed by Herrmann (1969) except $\bar{P}$ is weighted with $1/\alpha$. Both v and e are zone variables and are obtained from SKIPPER at any given time cycle.

The parameter α is assumed to vary in the following way during loading (pore collapse) (Cherry, et al., 1972)

$$\alpha = 1 \quad P > P_c \tag{2.20a}$$

$$\alpha = 1 + (\alpha_e - 1)\left(1 - \frac{P-P_e}{P_c-P_e}\right)^2 \quad P_e \leq P \leq P_c \tag{2.20b}$$

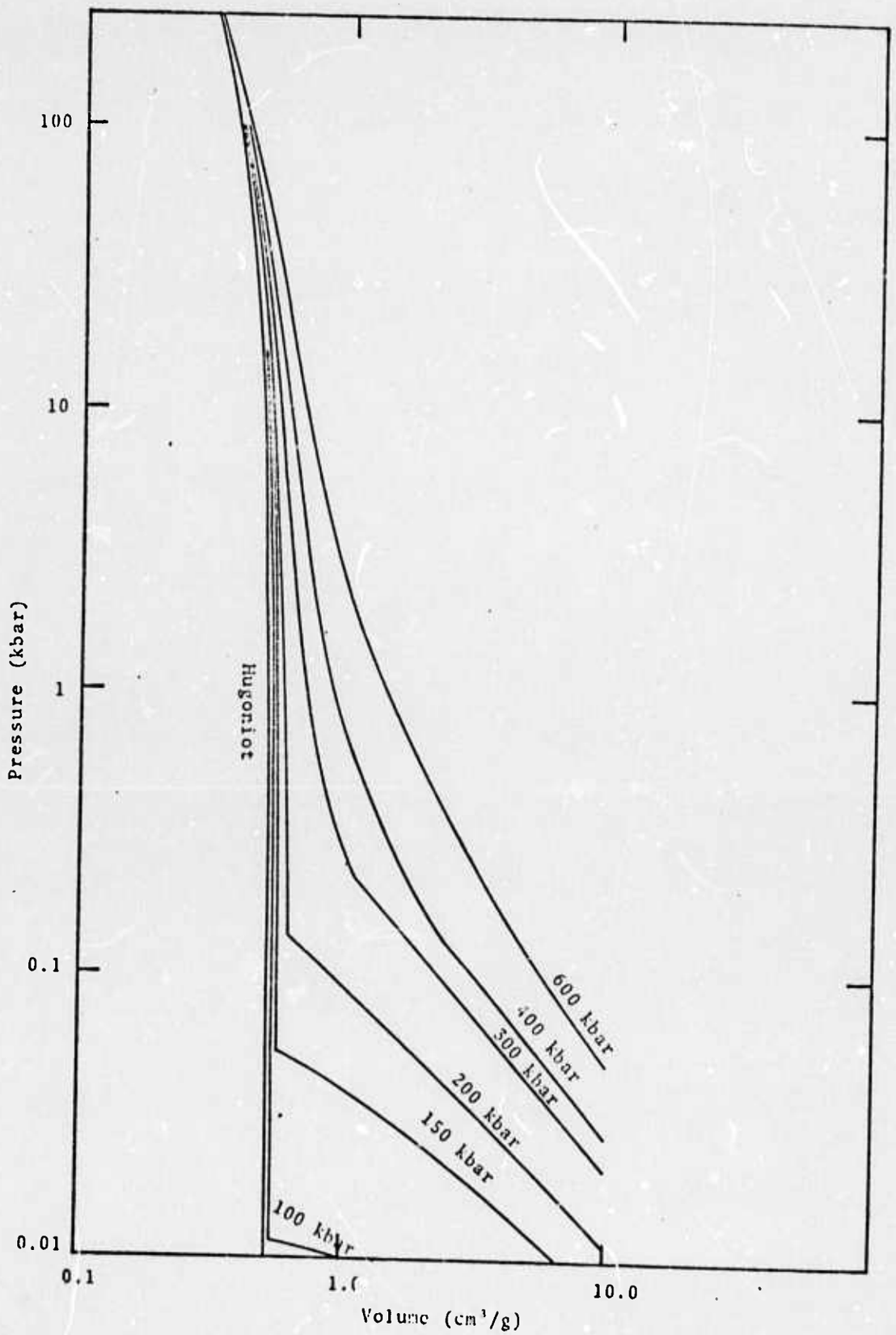


Figure 2.4. Hugoniot and release isentrope for saturated tuff (f = 0.17).

$$\alpha = \alpha_0 + \beta \left(1 - e^{n\, P/P_e}\right) \quad 0 \leq P \leq P_e \tag{2.20c}$$

$$\alpha = P\alpha'_{P=0} + \alpha_0 \quad P < 0 \quad (\alpha' = d\alpha/dp) \tag{2.20d}$$

where P_e and P_c are the elastic and crush pressure. β and η are determined by specifying the zero pressure bulk modulus (k_0) of the porous mix and requiring that α' be continuous at $P = P_e$. The initial air-filled volume fraction (ϕ_0) and α_0 are related by

$$\phi_0 = \frac{\alpha_0 - 1}{\alpha_0} = \frac{V_p}{V_w + V_r + V_p} \tag{2.21}$$

while the volume fractions of rock and water (ϕ_r and ϕ_w) are given by

$$\phi_r = \frac{1 - \phi_0}{1 + A} \tag{2.22}$$

$$\phi_w = \left(\frac{1 - \phi_0}{1 + A}\right) A \tag{2.23}$$

where

$$A = \frac{\rho_r}{\rho_w} \frac{f}{1-f} \qquad \rho_r = 2.4 \text{ g/cc} \qquad \rho_w = 1.0 \text{ g/cc}$$

We have found (Cherry, et al. (1972)) that a pore recovery formulation needed to be included in the model in order to insure a smooth transition between loading states near P_e. If α^* is the minimum α seen by a zone then

$$\alpha = t\alpha^* + (1 - t)\, \alpha\,(P) \tag{2.24}$$

where $\alpha(P)$ is given by Eqs. (2.21) and

$$t = 0,\ \alpha^* \geq \alpha_e = \frac{\alpha^* - \alpha_e}{1 - \alpha_e},\ 1 \leq \alpha^* \leq \alpha_e \qquad (2.25)$$

This assures full recovery when $\alpha^* = \alpha_e$ and zero recovery when $\alpha^* = 1$.

Figure 2.5 shows the loading and release P-v curves that result from adding 5 percent air-filled porosity to the mix of Fig. 2.4. We assume $P_e = 0.15$ kbar and $P_c = 1.25$ kbar. Also shown for comparison in the figure are the hydrostatic unloading data for unit 3 tuff at the Diamond Dust site (Stephens, et al. (1970)).

In summary, the pressure component of the equation of state is uniquely determined by assuming a pressure equilibrium mix and specifying f (Eq. (2.14)), ϕ_0 (Eq. (2.21)), P_e, P_c, k_0 (Eq. (2.20b) and (2.20c)) and the grain density of the rock component.

2.4.3 Material Strength

A strength relation of the form

$$S_{ij}S_{ij} \leq \frac{2}{3} Y^2 (P_T, e) \qquad (2.26)$$

where S_{ij} is the stress deviator, $P_T = P + P_0$, P_0 equals the overburden pressure, and

$$Y(P,e) = \frac{Y_m}{P_m} P \left[2 - \frac{P_T}{P_m}\right]\left[1 - \frac{e}{e_m}\right] \qquad P < P_m$$

$$= Y_m \left[1 - \frac{e}{e_m}\right] \qquad P \geq P_m \qquad (2.27)$$

$$= 0 \qquad e \geq e_m$$

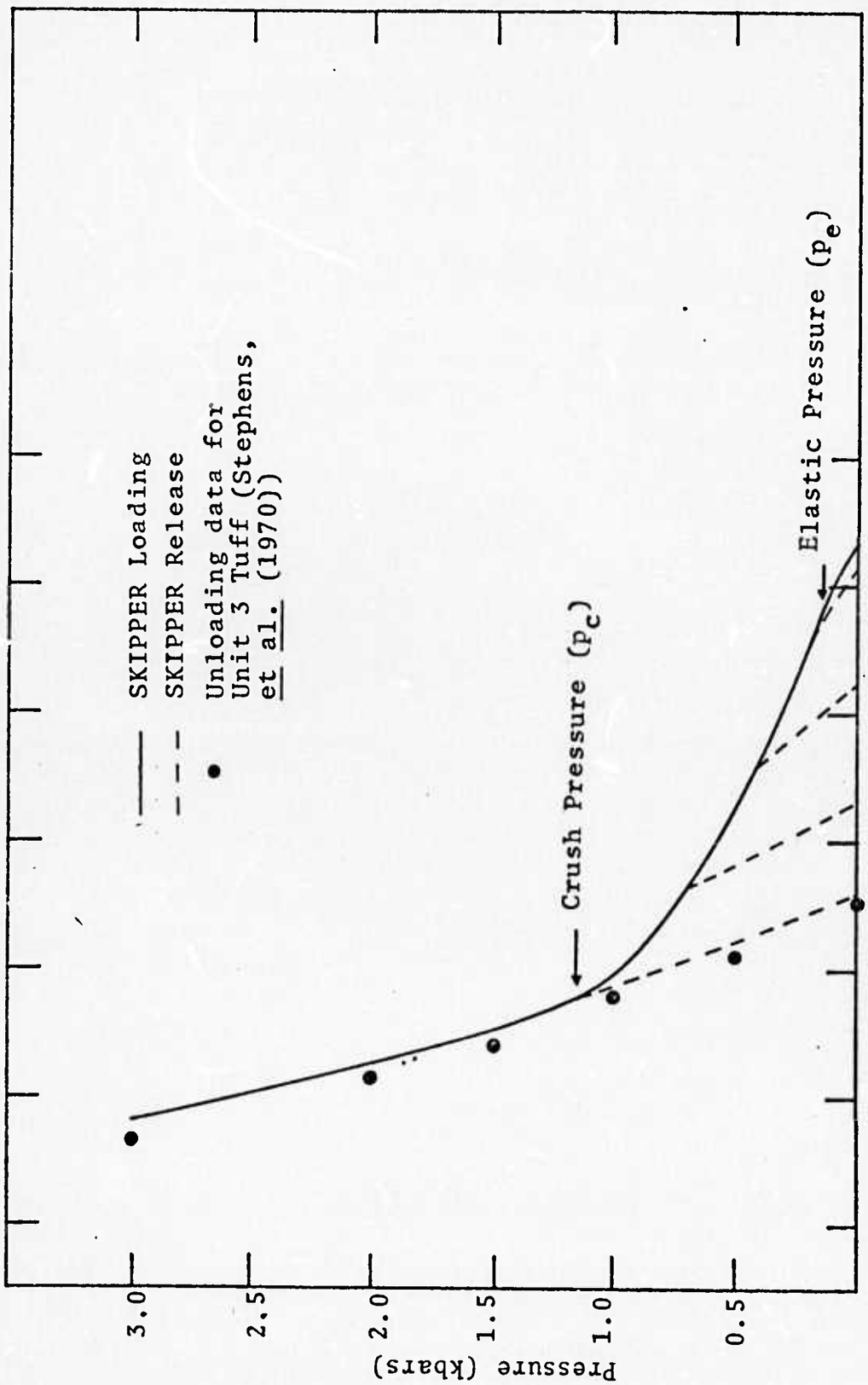


Figure 2.5. Loading and release p-V curves for partially saturated tuff (f = 0.17, ϕ_0 = 0.05).

For spherical symmetry Eq. (4.26) becomes

$$|S_1| \leq \frac{2}{3} Y \ (P_T, e) \tag{2.28}$$

For all the calculations discussed here, a generalized associated flow rule was used for the material in which the volumetric plastic strain rate was assumed to be zero. This assumption implies (Cameron and Scorgie (1968)) that if $|\hat{S}_1|$, calculated from Eq. (2.20), exceeds $\frac{2}{3} Y$, then

$$S_1 = \left(\frac{2}{3} Y\right) \text{ sign } (S_1) \tag{2.29}$$

The material strength dependence on P_0, Y_m and P_m is summarized in Fig. 2.6. The shock loading path is also shown in the figure to have a slope of μ/k, where k is the effective bulk modulus of the shock wave. This loading path is only valid for regions where the radial strain is much greater than the tangential strain, i.e., at the shock front.

2.5 RESULTS OF THE PARAMETER STUDY

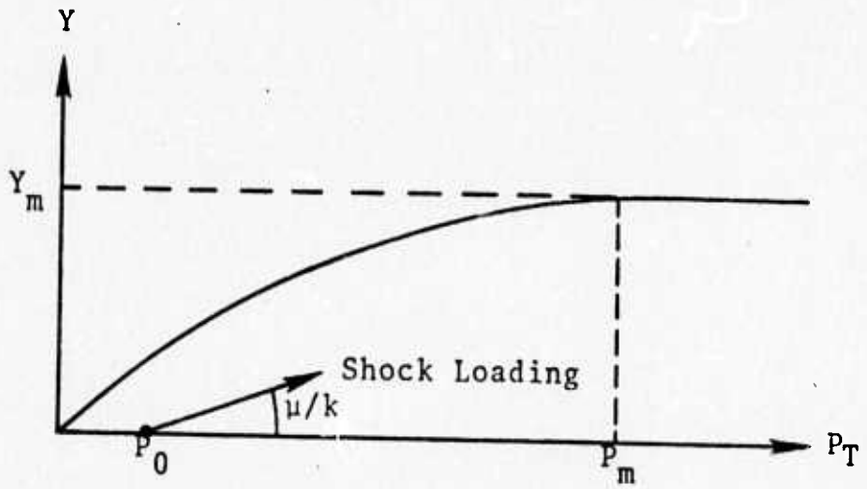
2.5.1 Introduction

The results presented in Fig. 2.1 show the calculated RVP spectra using the material model presented in Section 2.4. As noted earlier, the spectra are essentially flat in the teleseismic frequency band for device yields at least as large as 200 kT. This result along with Eq. (2.4), (2.4), and (2.13) imply that surface wave magnitude, m_b, has the proportionality

$$m_b \sim \log \left[\frac{\Psi(\infty)}{\alpha}\right] \tag{2.30}$$

while surface wave magnitude, M_s, obeys

$$M_s \sim \log [\mu \ \Psi(\infty)] \tag{2.31}$$



$$Y = \frac{Y_m}{P_m} P_T \left[2 - \frac{P_T}{P_m} \right] \qquad P < P_m$$

$$= Y_m \qquad P_T > P_m$$

Y = Maximum allowable stress difference

P_T = Hydrodynamic component of the stress tensor including overburden pressure

P_0 = Overburden pressure

Figure 2.6. Assumed relationship between the material strength (Y) and the hydrodynamic component of stress (P_T).

If $\Psi_i(\infty)$ and $\Psi_k(\infty)$ are two values of $\Psi(\infty)$ corresponding to materials i and k then the change in teleseismic magnitude is given by

$$\Delta m = m^i - m^k = \log \left[a \frac{\Psi_i(\infty)}{\Psi_k(\infty)} \right] \tag{2.32}$$

where

$$a = \frac{\alpha_k}{\alpha_i} \quad \text{for } m_b$$

$$a = \frac{\mu_i}{\mu_k} \quad \text{for } M_s.$$

If material properties remain constant and the only change in device yield then according to Eqs. (2.7) and (2.8)

$$\Delta m = m^i - m^k = \log \frac{W_i}{W_k}$$

Equation (2.32) gives the "scaling" law for teleseismic magnitudes in terms of $\Psi(\infty)$. This equation is always valid as long as the spectrum of the equivalent source is flat within the teleseismic frequency band and path effects associated with earth structure are invariant between events.

As an example, assume that the values of $\Psi(\infty)$ for a yield of 0.02 kT in tuff and granite are 8 m^3 and 12.5 m^3 with corresponding values of α being 2.6 km/sec and 5.6 km/sec, and μ of 40 kbar and 275 kbar respectively, then

$$m_b^T - m_b^G = \log \frac{8}{2.6} - \log \frac{12.5}{5.6} = 0.14$$

while

$$M_S^T - M_S^G = \log (40)(8) - \log (275)(12.5) = -1.03$$

While both m_b and M_s are measures of $\Psi(\infty)$ they also are severely affected by α and μ. The above example serves to illustrate the importance of these near source elastic parameters on seismic coupling.

2.5.2 The Sensitivity of $\Psi(\infty)$ to Air-Filled Porosity, Material Strength and Overburden Pressure

Table 2.1 lists the material properties (ϕ_0, P_e, P_c, Y_m, P_0, ρ_0) along with the calculated values of $\Psi(\infty)$ for an explosion yield of 0.02 kT. Also included in the table is Δm, computed from Eq. (2.32) where calculation 5 has been chosen for the reference magnitude. The value of "a" in Eq. (2.32) is unity (α = 2.4 km/sec, μ = 40 kbar for all calculations) and f = 0.17.

The following expansion summarizes the results of the parameter study

$$\Delta m = (-20.2 + 355\ \phi_0)\ \Delta\phi_0 - 0.38\ Y_m\ (\text{kbar})$$
$$- 0.34\ P_0^{-1}\ \Delta P_0 + 2.0\ \Delta P_e\ (\text{kbar}) + 0.057\ \Delta P_c\ (\text{kbar})$$
$$+ 0.41\ \Delta P_m\ (\text{kbar}) \qquad (2.33)$$

Increasing ϕ_0, Y_m and P_0 decreases teleseismic magnitude while increasing P_e, P_c and P_m increases teleseismic magnitude.

Figure 2.7 shows Δm versus ϕ_0 for calculations 1, 6 and 4. Δm is highly sensitive to change in ϕ_0. Over the internal $0 < \phi_0 < 0.02$, Δm decreases by 0.313 units and the seismic coupling is reduced by a factor of two.

TABLE 2.1

SUMMARY OF SOURCE COMPUTATIONS

ϕ_0	P_e (kbar)	P_c (kbar)	P_m (kbar)	Y_m (kbar)	P_0 (kbar)	ρ_0 (g/cc)	$\psi(\infty)$ (m^3)	ΔM	Calculation No.
0	--	--	0.6	0.5	0.116	1.94	7.4	0.739	(1)
0.02	0.075	0.5	0.6	0.5	0.116	1.90	3.6	0.426	(6)
0.05	0.075	0.5	0.6	0.5	0.116	1.84	2.1	0.192	(4)
0.02	0.075	0.5	0.6	0.5	0.075	1.90	4.2	0.493	(9)
0.02	0.075	0.5	0.6	0.5	0.348	1.90	2.41	0.252	(11)
0.02	0.075	0.5	0.6	0.5	0.619	1.90	2.08	0.188	(12)
0.02	0.075	1.25	0.6	0.5	0.075	1.90	4.6	0.532	(10)
0.05	0.15	1.25	0.6	0.5	0.116	1.84	3.3	0.388	(3)
0.05	0.075	0.5	0.6	1.0	0.116	1.84	1.35	0	(5)
0.02	0.075	0.5	1.25	0.5	0.075	1.90	7.7	0.756	(7)

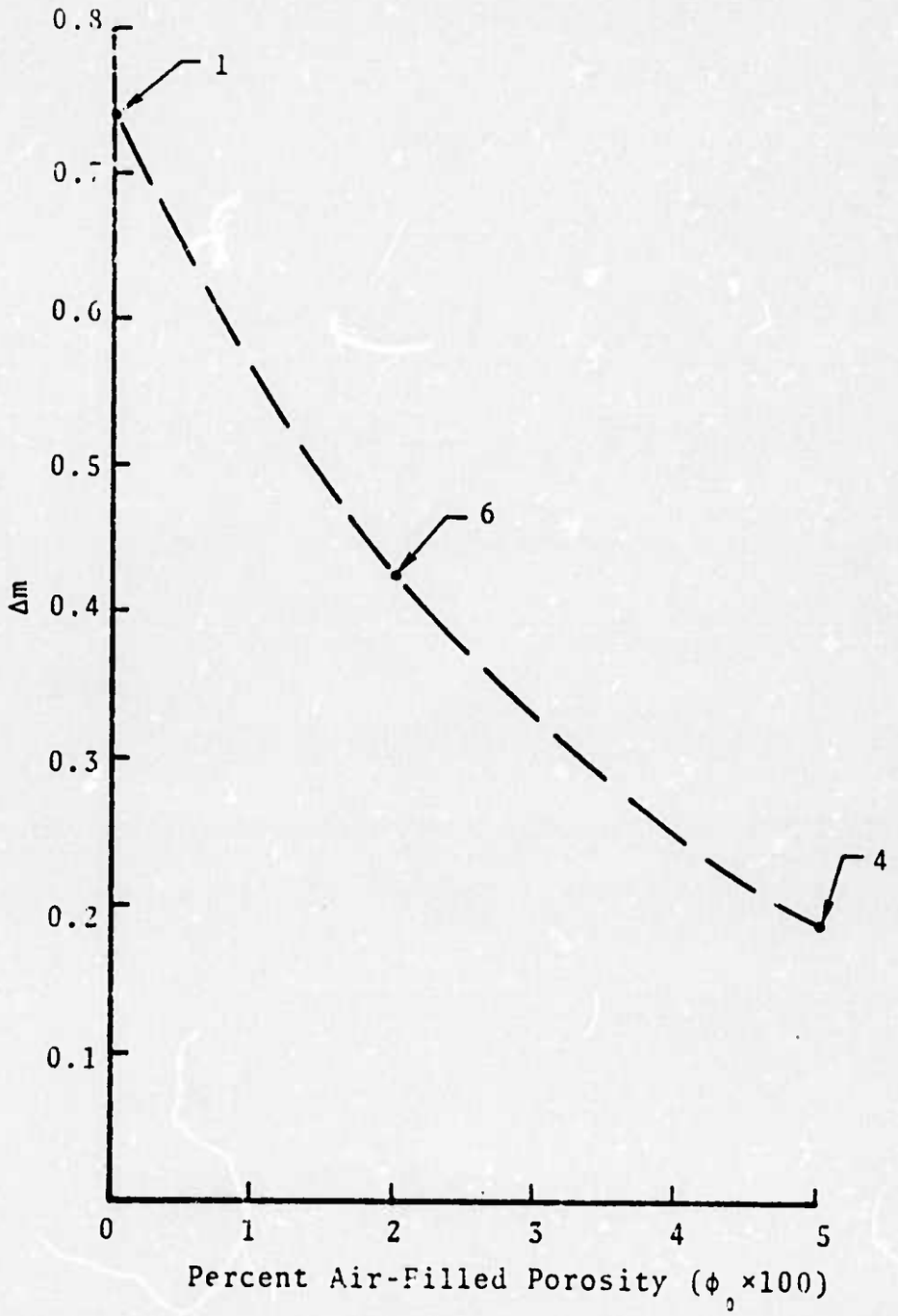


Figure 2.7. Effect of air-filled porosity on magnitude.

Figure 2.8 shows the influence that the maximum allowable material strength, Y_m, has on magnitude. Increasing Y_m by a factor of two causes magnitude to decrease by 0.192 magnitude units. Therefore, the device yield could be increased by a factor of 1.55 in the strong material.

These calculations show that a porous, high strength material optimizes teleseismic decoupling. Increasing both the porosity and material strength may obscure the device yield by at least a factor of three when teleseismic magnitube is used to infer yield. We should note that both high air-filled porosity and high material strength imply that the material characterizing the near source environment is above the water table.

For a given value of Y_m, the shape of the material strength surface is controlled by P_m, the pressure at which Y_m is attained. From calculations 9 and 7 we see that increasing P_m by a factor of 2.08 causes magnitude to increase by 0.26 units. The coupling efficiency increases as P_m is increased, which is opposite to the effect of increasing ϕ_0 or Y_m. This simply indicates that the shape of the failure surface plays an important role in determining coupling efficiency. The material has less strength at low pressures when P_m is increased and we should expect a corresponding increase in magnitude.

The effect of overburden pressure, P_0, on magnitude is shown in Fig. 2.9. Coupling efficiency decreases with increasing overburden pressure, when all other material properties remain constant. An increase in the depth of burial (DOB) by a factor of six causes magnitude to decrease by 0.3 units, which in turn permits a yield increase by a factor of two. The decrease in magnitude is not uniform with depth. An increase in DOB at shallow depths causes magnitude to decrease more then that caused by an equivalent increase

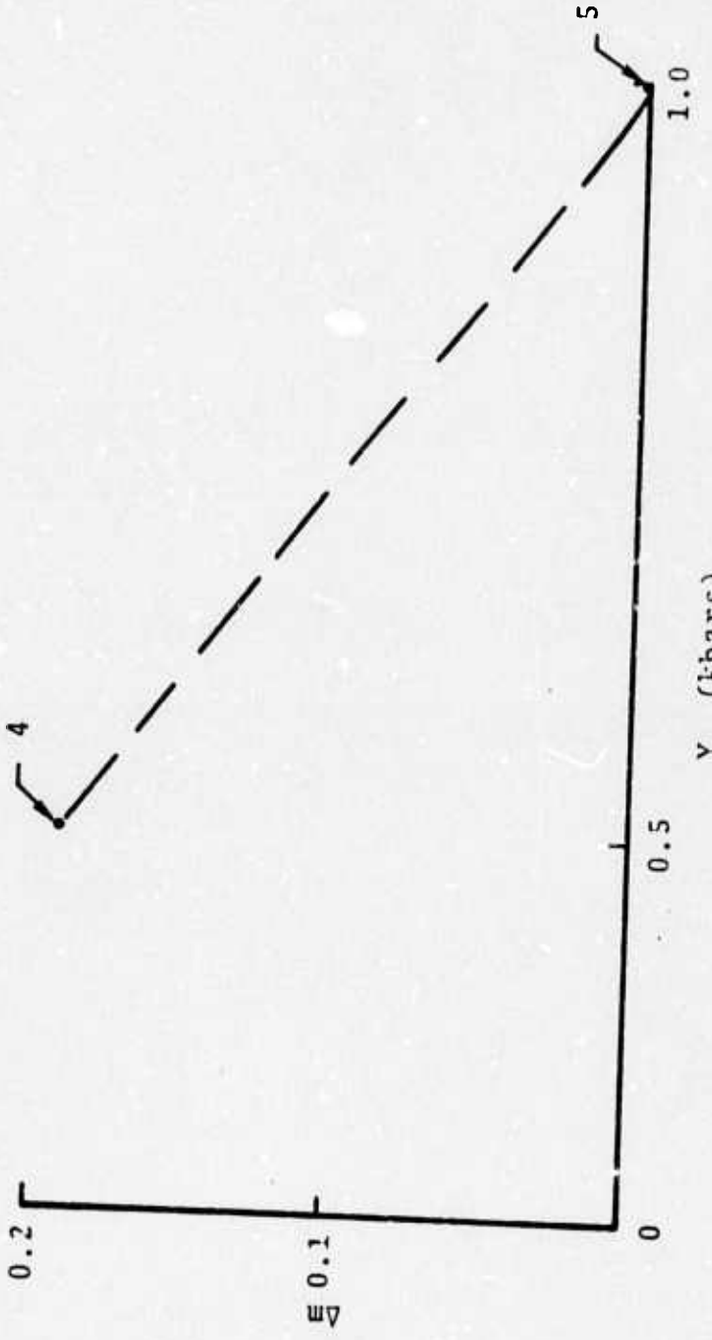


Figure 2.8. Effect of maximum allowable material strength on magnitude.

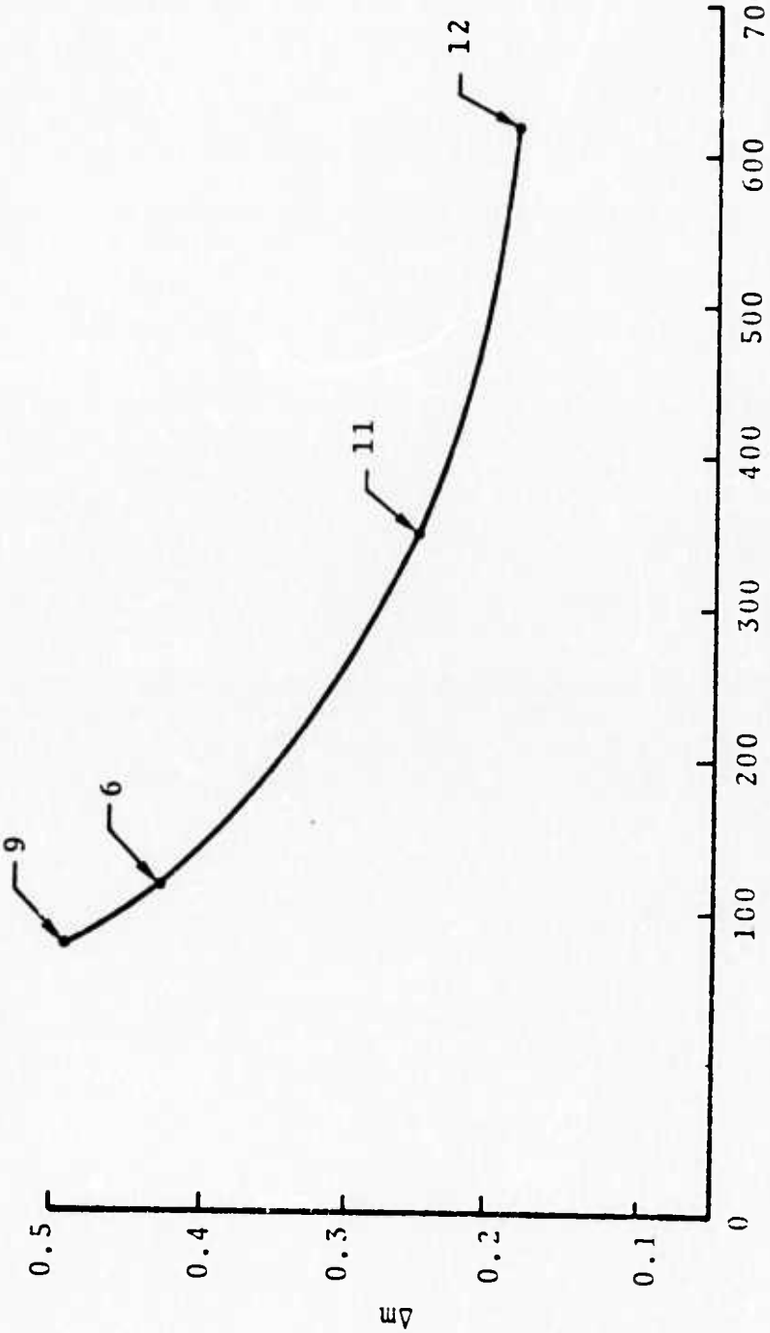


Figure 2.9. Δm versus overburden pressure (P_o).

in DOB at greater depths. This effect results from the rapid increase in material strength at low pressures.

We should note that it is unlikely that material properties would remain invariant as overburden pressure is increased from 100 bars to 600 bars. An increased DOB usually corresponds to an increase in water content, resulting in decreased air-filled porosity and material strength. These changes would more than compensate for the overburden pressure decoupling effect.

Calculations 9 and 10 show that magnitude is not very sensitive to large changes in P_c, the pressure at which all ambient porosity is irreversibly removed. An increase in P_c by a factor of 2.5 produces an increase in magnitude of 0.03 units.

Finally, calculations 4 and 3 show the sensitivity of magnitude to P_e, the pressure limit at which irreversible pore collapse begins. An increase in P_e produces an increase in coupling efficiency. A preshot estimate of P_e that is incorrect by a factor of two will result in an error in predicted magnitude by 0.2 units.

2.6 SUMMARY AND COMMENTS

1. All RVP spectra calculated to date have been flat in the teleseismic frequency bend for device yields at least as large as 200 kT. For this yield interval, both body wave and surface wave amplitudes should scale linearly with device yield.

2. The near source elastic constants which influence teleseismic amplitudes are the P wave velocity, α, and the shear modulus, μ. Body wave amplitude is inversely proportional to α. Surface wave amplitude is directly proportional to μ.

3. Increases in air-filled porosity (ϕ_0), maximum material strength (Y_m) and overburden pressure (P_0) causes a reduction in seismic coupling. Equation (2.33) shows that increasing ϕ_0 from 0 to 0.01 causes magnitude to decrease by 0.2 units. Increasing Y_m by 0.5 kbar also causes magnitude to decrease by 0.2 units. Magnitude dependence on overburden pressure is given by $(-0.34\ \Delta P_0/P_0)$. At shallow burial depths magnitude is very sensitive to small changes in overburden pressure. For example, if $P_0 = 0.075$ kbar and $\Delta P_0 = 0.044$ kbar then magnitude decreases by 0.2 units. This change in overburden pressure corresponds to a change in DOB of approximately 650 feet.

4. Increases in the elastic pressure (P_e), the crush pressure (P_c) and the pressure at which the material reaches its maximum strength (P_m) cause an increase in seismic coupling. Equation (2.33) shows that increasing P_e by 0.1 kbar causes a magnitude increase of 0.2 units. Increasing P_m by 0.5 kbar also causes a magnitude increase of 0.2 units. Magnitude is not very sensitive to changes in P_c.

5. The results summarized by Eq. (2.33) are dependent on the material model assumed for the rock-water mixture. Neither strain rate effects on brittle fracture of the material as the failure surface is exceeded have been included. The latter is certain to be important at shallow depths of burial. The former may play a major role in broadening the pulse shape and reducing the yield range over which the spectrum is flat.

III. A THEORETICAL INVESTIGATION OF THE TELESEISMIC P WAVE FROM UNDERGROUND EXPLOSIONS

3.1 INTRODUCTION

Using our deterministic computational techniques, we have been attempting to identify and understand the important features controlling the teleseismic signature of underground explosions. For short period P waves, some interesting results obtained during the last year are summarized below.

In Section 3.2 the influence of the source spectrum on the shape (frequency content) of the teleseismic P wave signature of explosions is discussed. We also discuss the dependence of amplitude-yield scaling on various source, propagation path and measurement techniques.

Some interesting, and perhaps paradoxical consequences of the standard formulation of the anelastic attenuation of teleseismic waves are discussed in Section 3.3.

In Appendix B is given a theory whereby an arbitrary explosion or earthquake source may be embedded in a plane layered model of the earth's crust. This theory is applied in Section 3.4 to investigate the influence of near source crustal structure on the teleseismic P wave. Finally, in Section 3.5 we study the influence of tectonic release superposed on the spherically symmetric explosion source.

3.2 THE DEPENDENCE OF THE TELESEISMIC P WAVE TRAIN ON THE SOURCE SPECTRUM FOR EXPLOSIONS IN NTS TUFF

We know that the teleseismic P wave signatures of underground explosions are affected by the characteristics of the source and its immediate vicinity, the travel path through the upper mantle, the geology of the receiver vicinity, etc. When possible, one tries to isolate the various important parameters for separate study. In this section the intention is to study the effect of the source and its immediate vicinity.

A set of observed seismograms for five explosions located within a few kilometers of each other in the same region at NTS is shown in Fig. 3.1. The yields of these five explosions vary by at most a factor of two while the burial depths are the same to within 10 percent. All five recordings are from an array of short-period sensors located more than 30 degrees from NTS. While the recordings are similar, they have distinct differences. Due to the similarities of the events, these differences can only be accounted for by the source itself and its immediate vicinity -- to a depth of one or two kilometers. We first examine the possible influence of the source spectrum on the observed signals.

The results of a series of one-dimensional explosion source calculations for material parameters typical of NTS tuff have been described in previous S^3 reports (e.g., Cherry, et al., (1974b), Bache, et al., (1974)). As was pointed out in those reports, the far field component of the source generated P wave is

$$\bar{u}_S(R,\omega) = \frac{\bar{\dot{\Psi}}(\omega)}{R\alpha} e^{-i\omega R/\alpha} \qquad (3.2)$$

where α is P wave velocity and R is the radial coordinate. The source spectrum is then given by $\dot{\Psi}(\omega)$, the reduced velocity potential transform. This quantity is plotted for a range of material properties typical of NTS tuff in Fig. 3.2. The calculations portrayed in the figure are those of the parameter study described in the above named references.

Most apparent in Fig. 3.2a is the essential similarity of the amplitude spectrum for a wide range of coupling efficiencies. That is, while the zero frequency limit, Ψ_∞, varies by as much as a factor of 5.5, the basic shape of the spectra are relatively unchanged.

In Fig. 3.2b a detailed look at one of these spectra, #10 of 3.2a, is given on a log-log plot, along with an

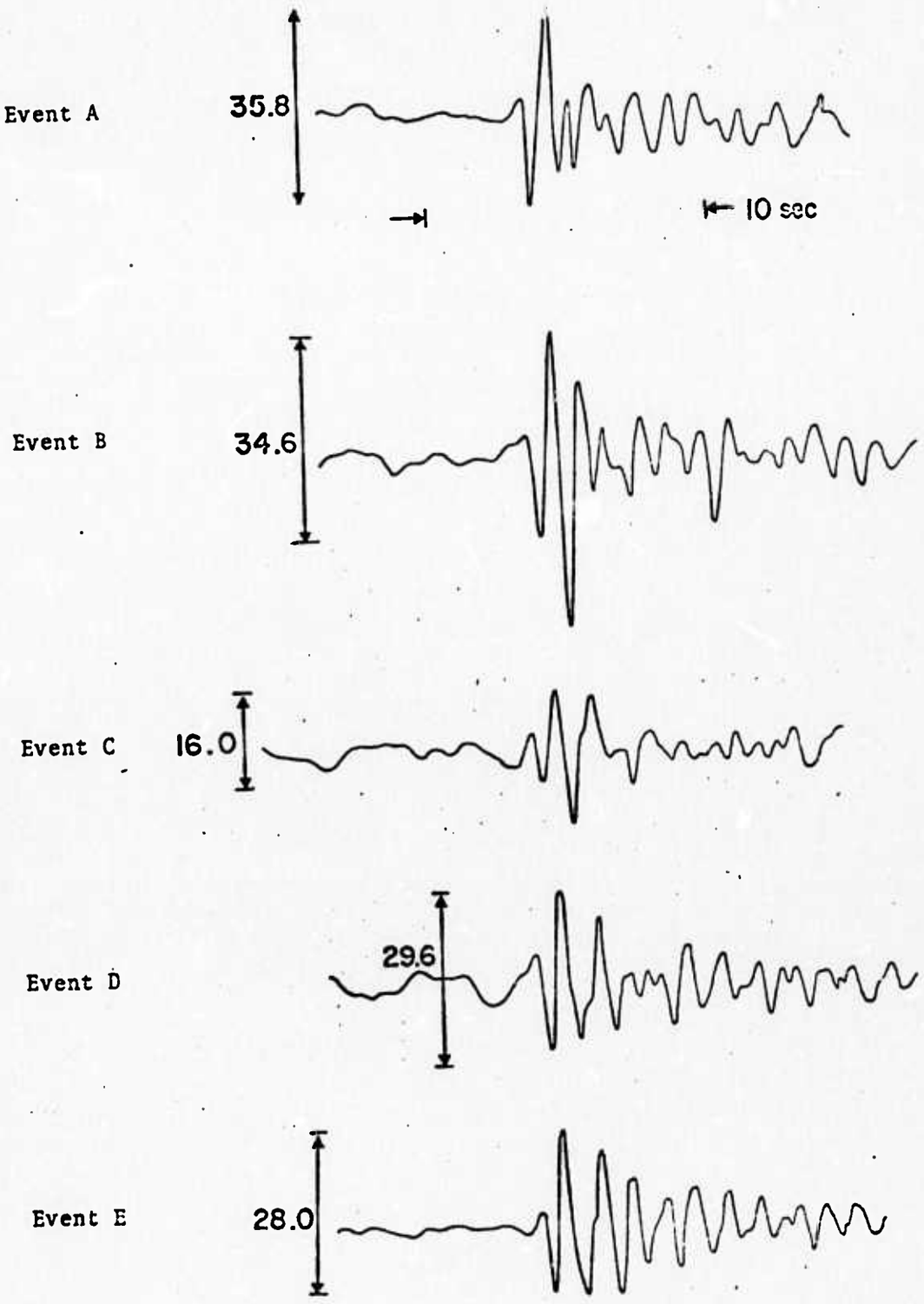
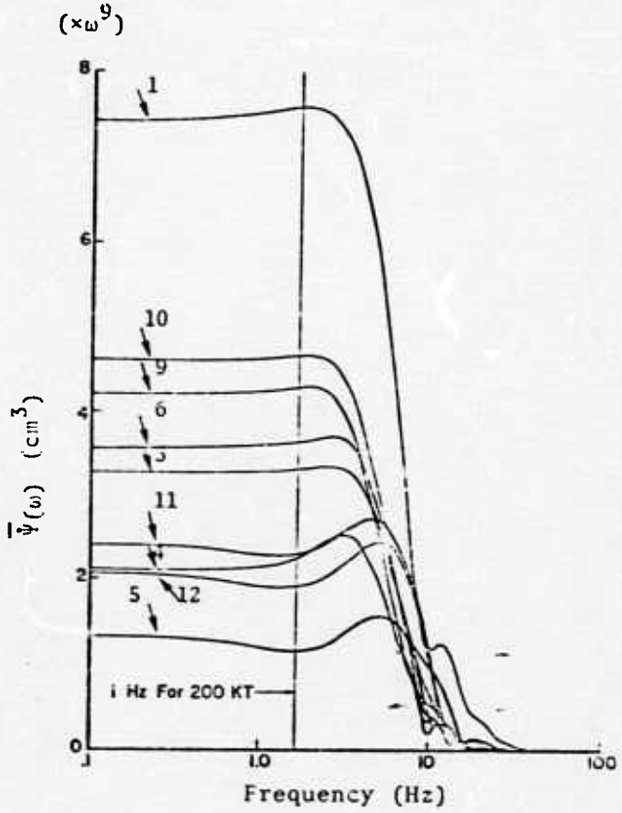
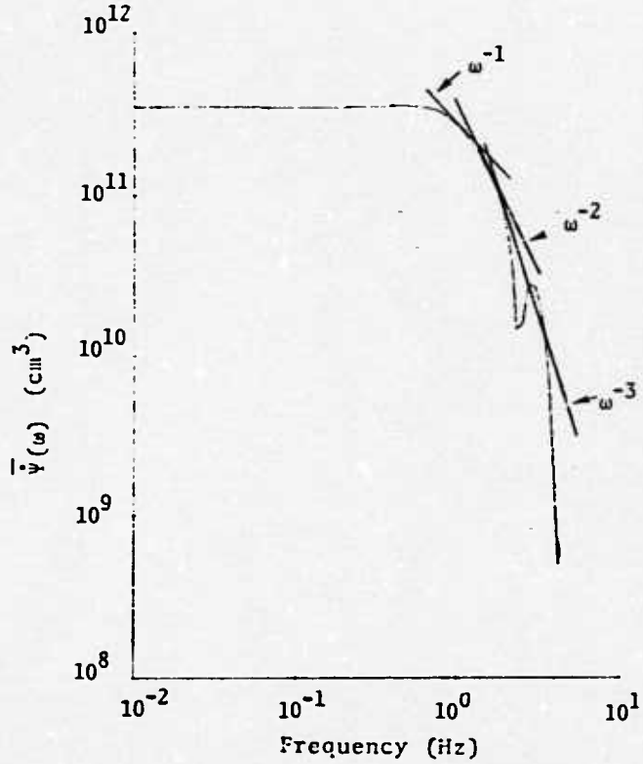


Figure 3.1. Recorded short period P wave seismograms from a single well maintained station for five similar NTS explosions. The explosions were at nearly the same yield and depth of burial and were located a few kilometers apart and more than 30° from the receiver. The numbers to the left of the arrows indicate peak-peak amplitudes in millimicrons.



(a) The far field displacement spectra scaled to 20 kT.



(b) Explosion #10 scaled to 1500 kT.

Figure 3.2. The reduced velocity potential (RVP) spectra for a series of explosion calculations in which the material properties were varied over a range typical of NTS tuff (Cherry, et al. (1974b)).

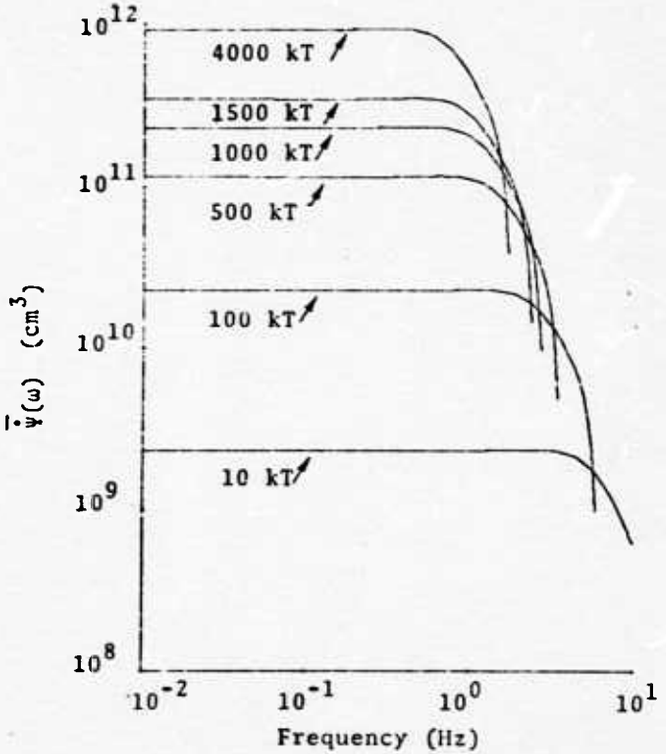
indication of the rate of falloff beyond the corner. All the source calculations were carried out at the same yield. Cube root scaling is applied to obtain source spectra at differing yields.

The source #10 of Fig. 3.2 is scaled to a wide range of yields from 10 to 4,000 kT in Fig. 3.3a. It is seen that, for the lower yields, the source spectrum is flat over the entire band of frequencies (0.5 - 2.0 Hz) of interest for short period P waves. For high yields the corner does appear in the teleseismic frequency band. However, attenuation by Q tends to obscure this effect.

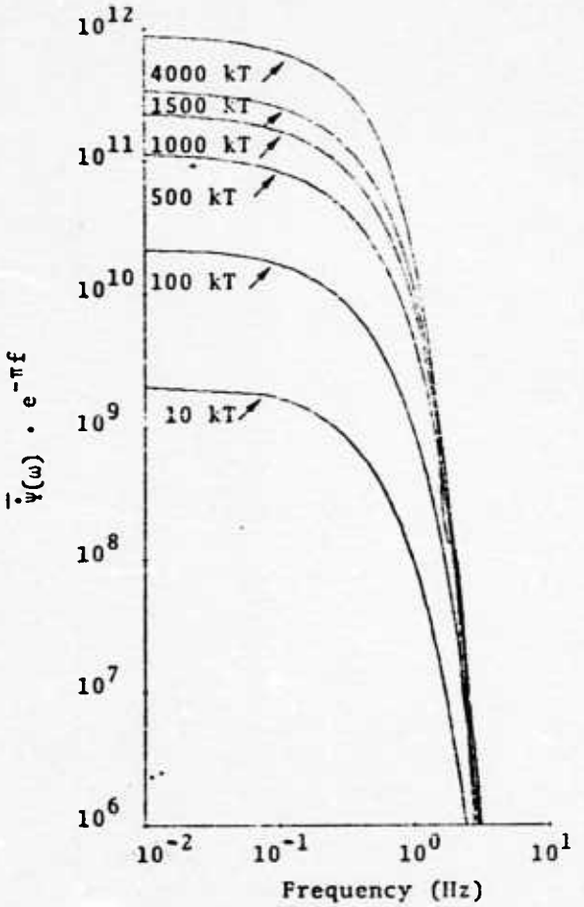
In Fig. 3.3b the source spectra of 3.3a are multiplied by exp $[-\pi f]$. That is, T/Q is taken to be unity. This value of T/Q has been found by our studies and by others (e.g., Helmberger (1973), Carpenter (1966)) to be reasonable for most teleseismic P wave phases.

The direct P waves represented by the spectra of Fig. 3.3 are, of course, seen by an instrument which further masks details of the source spectra. In Fig. 3.4a the spectra of 3.3b are multiplied by the instrument transfer function for an LRSM short period seismograph. As seen through the filter of the instrument and the anelastic earth, the source amplitude spectra are almost identical in shape over this broad yield range. To provide an upper bound on the kinds of source amplitude spectral differences expected from yield scaling alone, the same information is plotted in Fig. 3.4b, this time for T/Q = 0.5. Values of Q this high are not expected to be encountered for teleseismic P waves from NTS explosions.

It should be emphasized that the spectra shown thus far are for the direct P wave only. That is, modification by reflection from the free surface and other near source velocity discontinuities is not included. The effect of the

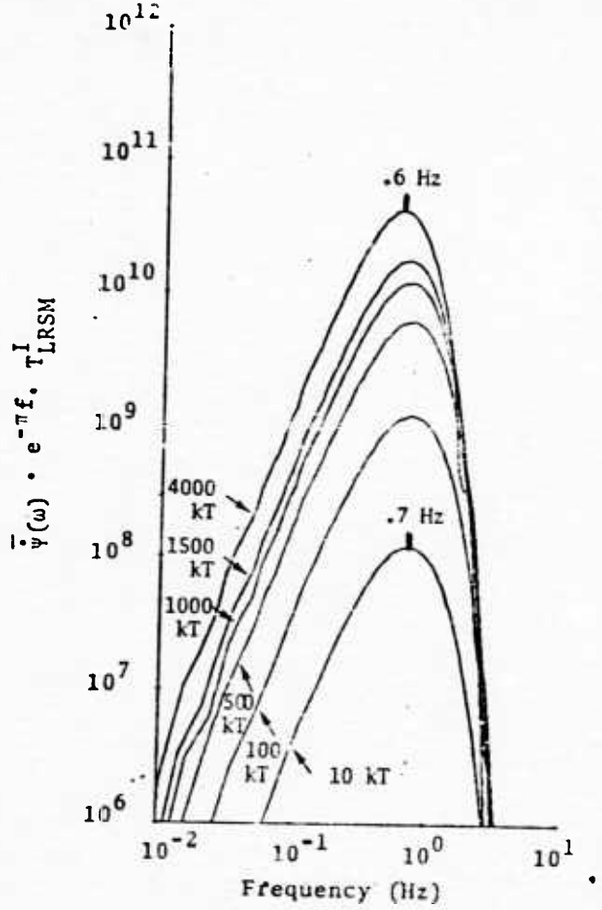


(a) Explosion #10 scaled to a range of yields. High frequency details are omitted for clarity.

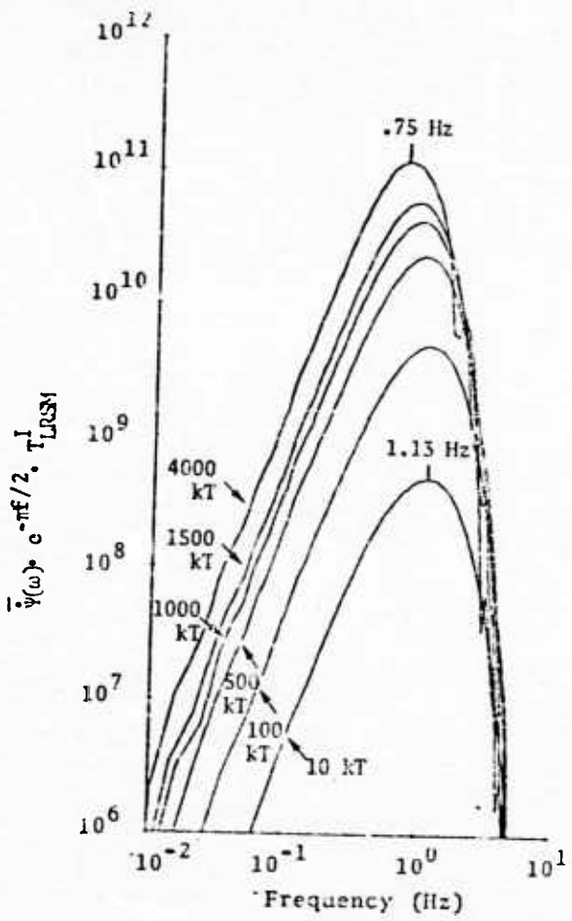


(b) The spectra of (a) multiplied by exp[-πf].

Figure 3.3 The RVP spectra for explosion #10 cube root scaled to a wide range of yields, then multiplied by the attenuation operator exp[-ωT/2Q] with T/Q = 1.0.



(a) T/Q = 1.0



(b) T/Q = 0.5

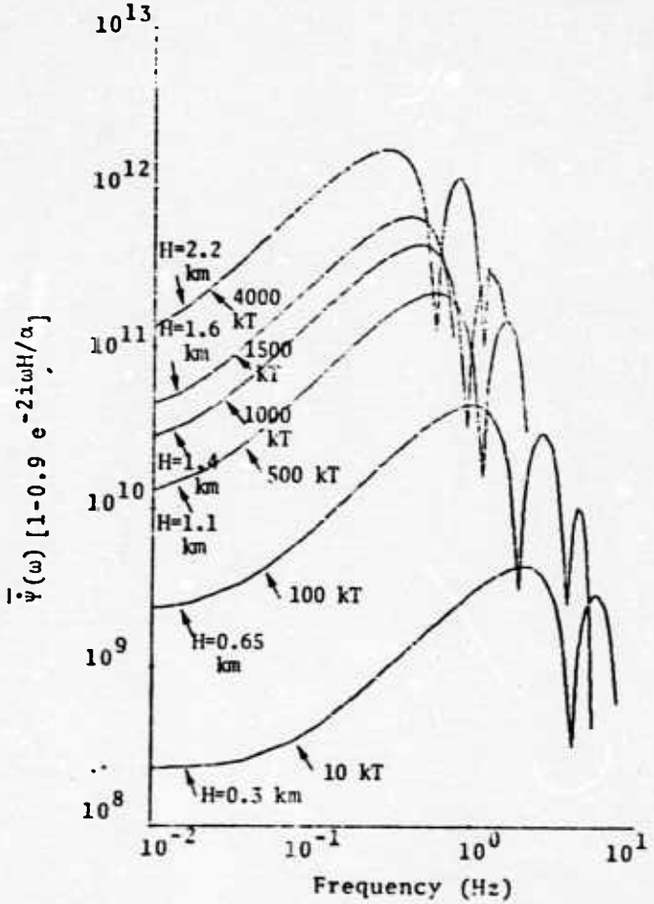
Figure 3.4 The RVP spectra of Fig. 3.3 modified by an LRSM short period instrument transfer function. Spectra with T/Q = 1.0 and T/Q = 0.5 in the attenuation are shown.

most elementary modification by reflected phases is shown in Fig. 3.5. First, the source spectra for the six yields of Fig. 3.3a at scaled depths of burial are shown including the direct and free surface reflected (pP) phases. The reflection coefficient was taken to be 0.9 which is typical for takeoff angles for teleseismic P waves. The burial depths were cube root scaled to an assumed depth of 300 m for the 10 kT explosion. The modification of these source spectra by the LRSM instrument and Q (T/Q = 1.0) is indicated in Fig. 3.5b.

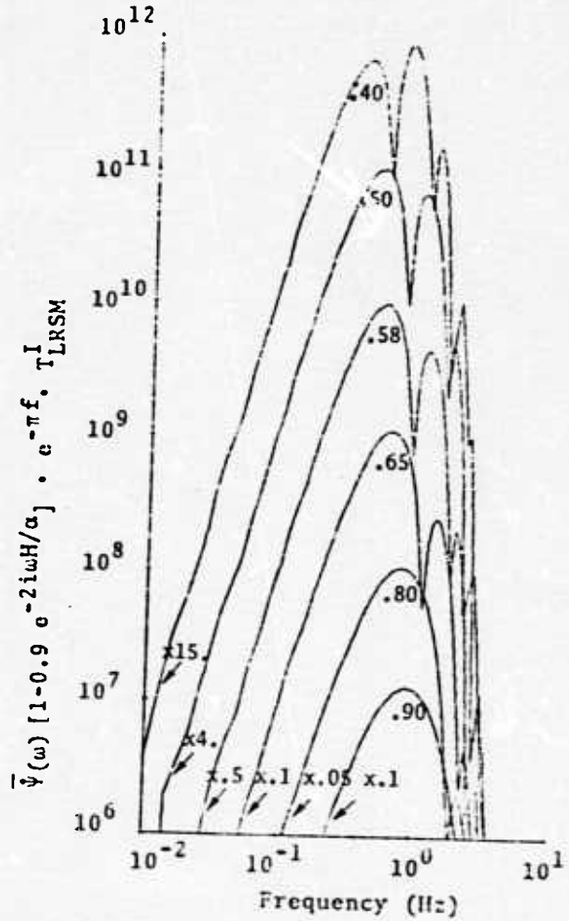
These amplitude spectral density plots clearly indicate how source spectrum details, such as corner frequency or rate of amplitude decay beyond the corner for teleseismic P wave spectra, are almost totally obscured by the filter of the earth and instrument (in principle, both can be removed) and, more importantly, by the presence of later arriving phases such as pP.

Source spectra having a pronounced hump near the corner (#4 of Fig. 3.2 exhibits this behavior to a small degree) have been suggested by some investigators (e.g., Werth and Herbst (1963)). Presence of such an overshoot of moderate size would have negligible effect on the results presented above. Aki, et al. (1974) have inferred the presence of an overshoot of as much as five times the low frequency value and tentatively attributed this to spallation, an effect not included in our calculations. A huge overshoot of this kind, should it cube-root scale with yield, would have a noticeable effect on the teleseismic spectrum.

Examination of amplitude spectral density plots are useful, but can be misleading since the phase component of the spectrum is ignored. Therefore, we move on to an examination of results in the time domain; that is, synthetic seismograms.



(a) The source spectra as modified by the free surface reflected phase with reflection coefficient 0.9 and a P wave velocity α = 2.4 km/sec. High frequency details are omitted for clarity.



(b) The source spectra of (a) multiplied by $e^{-\pi f}$ and the LRSM instrument transfer function. Note the indicated multiplying factors added to improve the plot clarity.

Figure 3.5. The source spectra of the previous figures as modified by the free surface reflected phase.

Illustrative synthetic seismograms are given in Figs. 3.6 through 3.9. For each seismogram the source, #10 of Fig. 3.2, was embedded at the indicated depth of burial in a crustal structure typical of NTS. The theory of Appendix B was used with the crustal structure of Table 3.1.

TABLE 3.1

NTS CRUSTAL STRUCTURE FOR THE SYNTHETIC SEISMOGRAMS OF FIGURES 3.6 THROUGH 3.9

Depth	P Velocity	S Velocity	Density
2.5 km	2.4 km/sec	1.47 km/sec	1.9 g/cm^3
18.0	6.0	3.5	2.8
31.0	6.7	3.85	3.0
∞	7.9	4.6	3.3

The seismograms are for the first mantle arrival at a distance of 4,000 km. A geometric spreading factor of 0.63×10^{-4} for the travel path between the base of the crust at the source and the earth's surface at the receiver was computed by ray theory and applied. The Q operator including dispersion as formulated by Strick (1970) and discussed in Section 3.3 was applied.

In Figs. 3.6 and 3.7 the effect of yield scaling of the source spectrum is shown by seismograms at a wide yield range but at a single depth of burial. For these seismograms we have taken $T/Q = 1.1$. The seismograms of Fig. 3.7 are repeated in Fig. 3.8 for the case of a Q which is twice as high ($T/Q = 0.55$). Finally, in Fig. 3.9 the seismograms at scaled depth of burial are shown. Except for the somewhat lower Q, the latter set correspond directly to the spectra of Fig. 3.5.

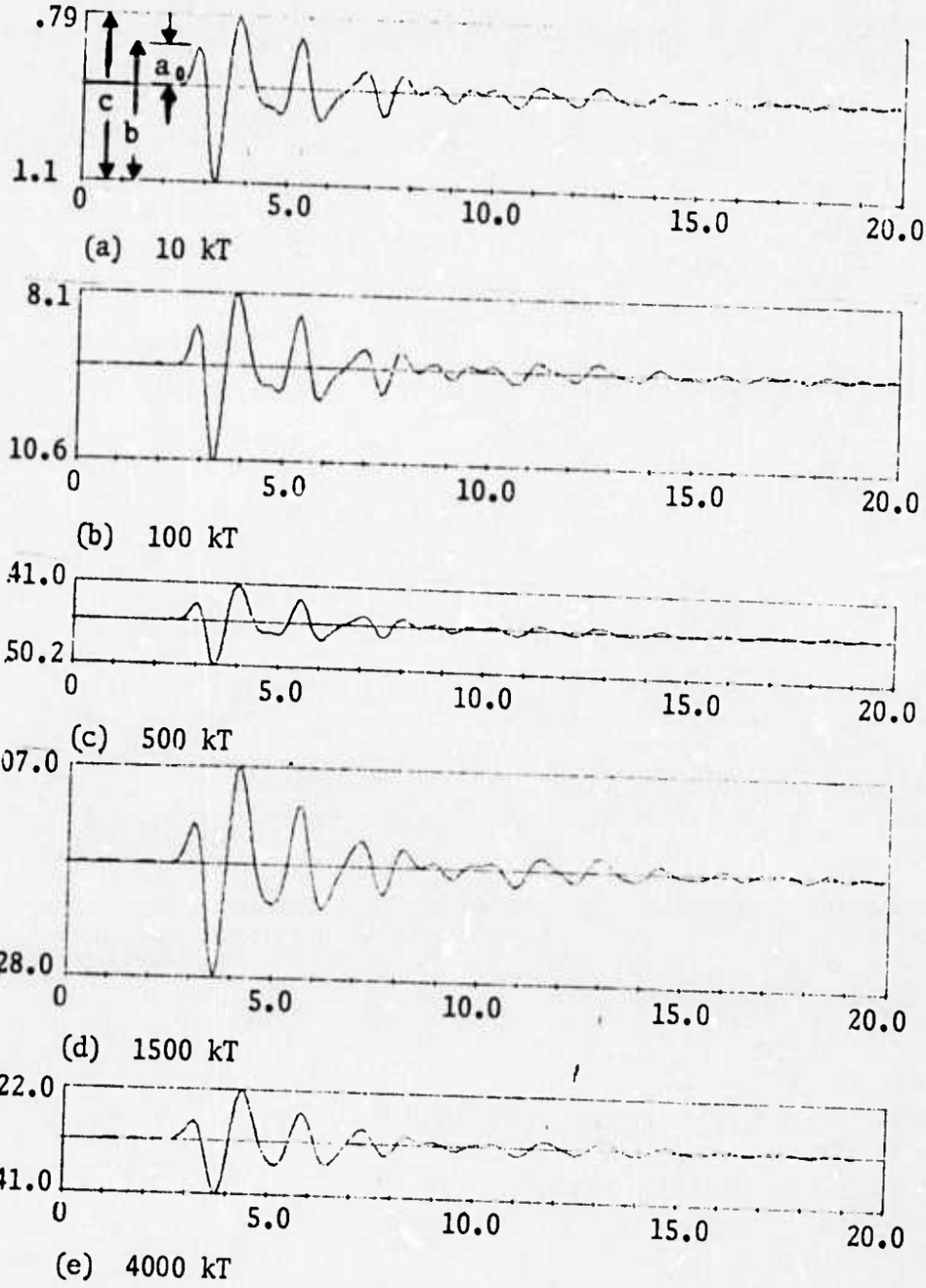


Figure 3.6. Synthetic seismograms at 4000 km due to explosion source #10 at a depth of 0.5 km in the crustal structure of Table 3.1. Attenuation with T/Q = 1.1 and an LRSM instrument were applied. The maximum amplitudes are indicated in millimicrons.

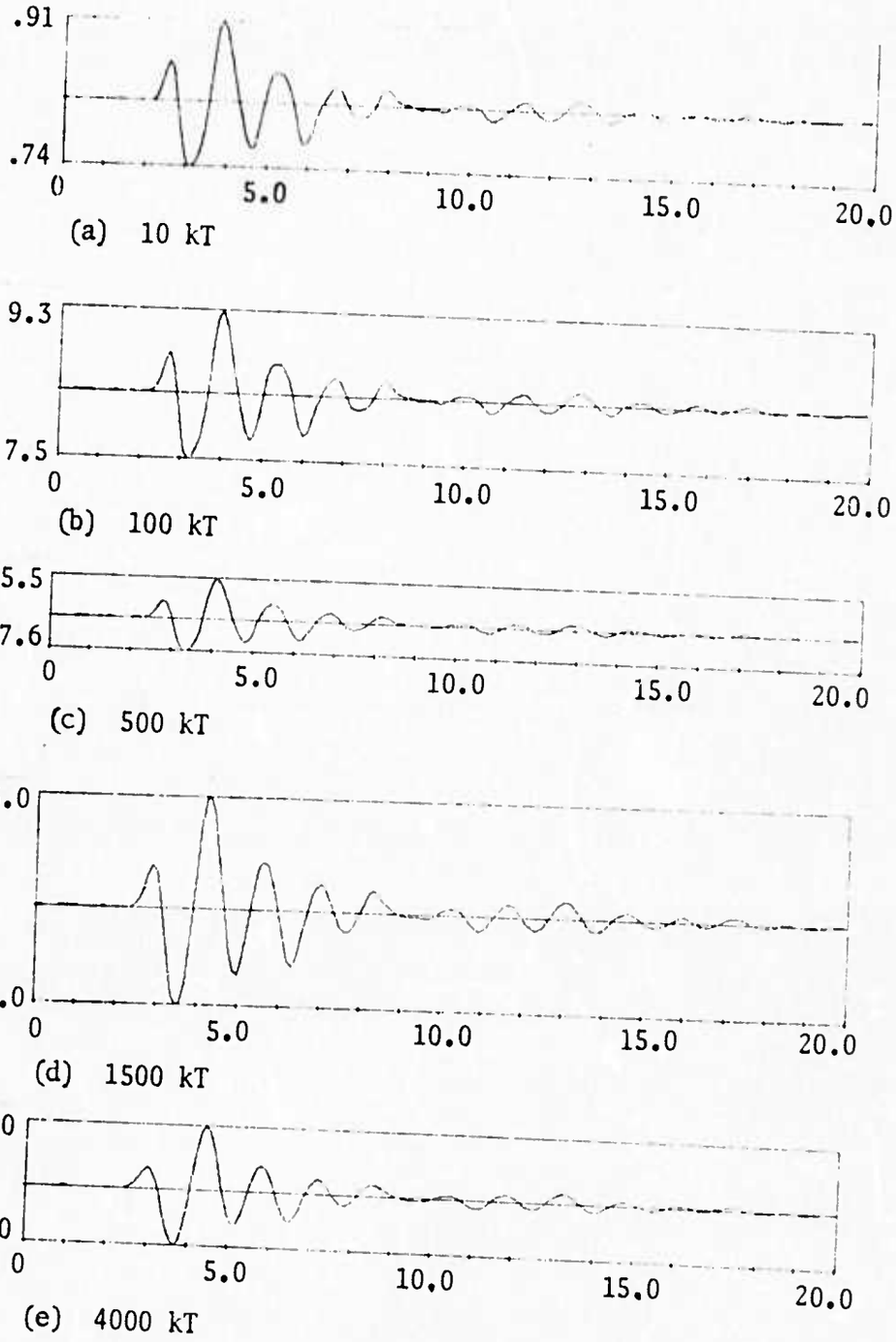


Figure 3.7. Repeating the synthetic seismograms of Fig. 3.6 with the burial depth changed to 1.0 km.

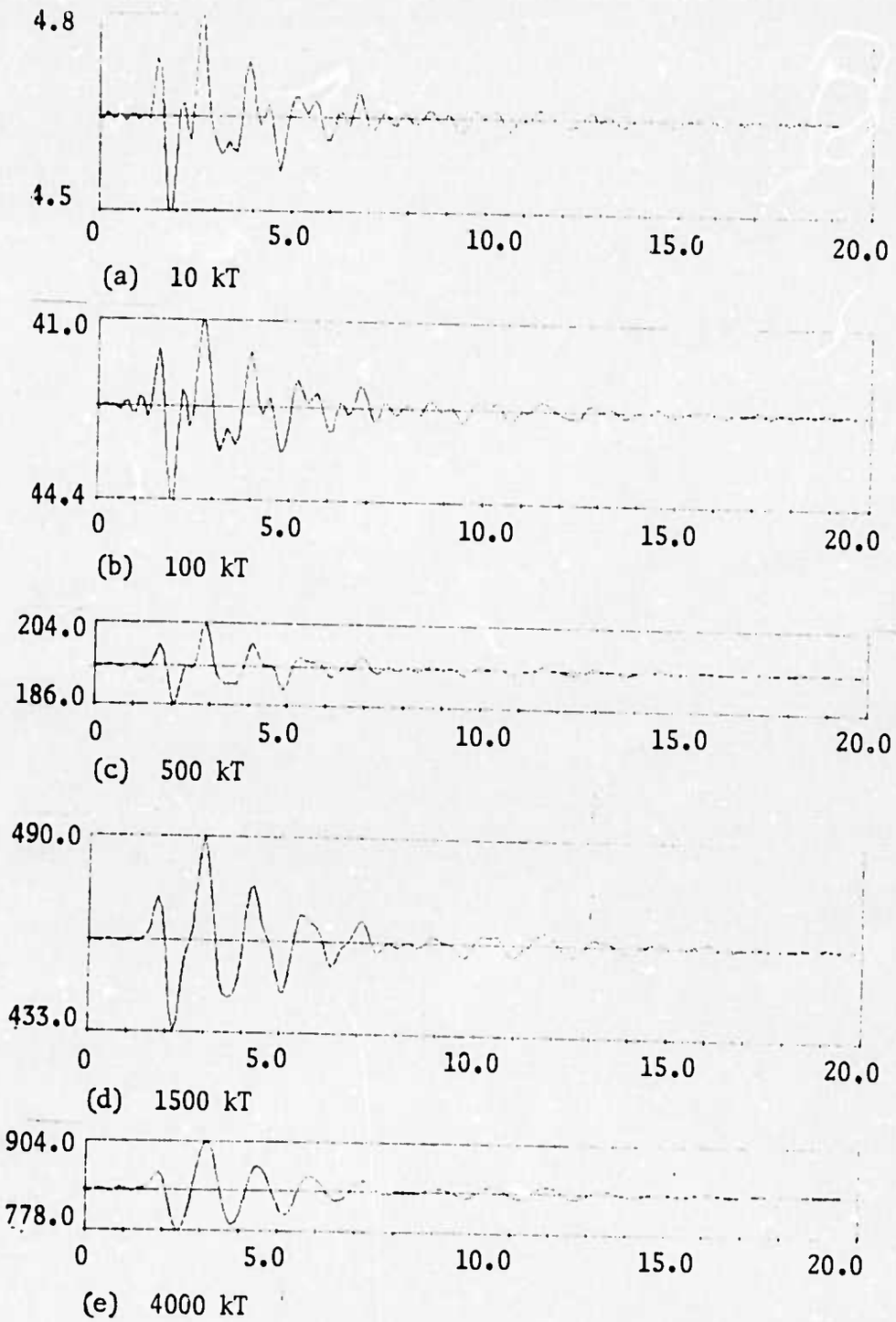
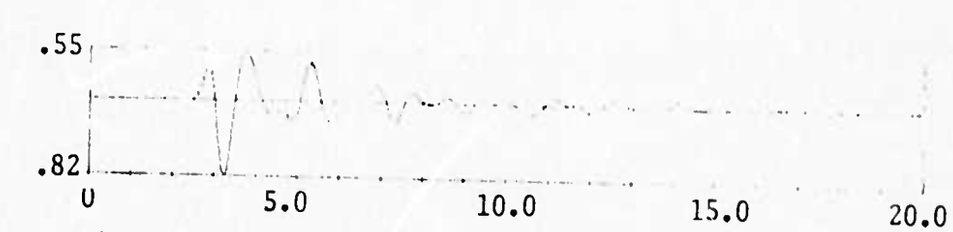
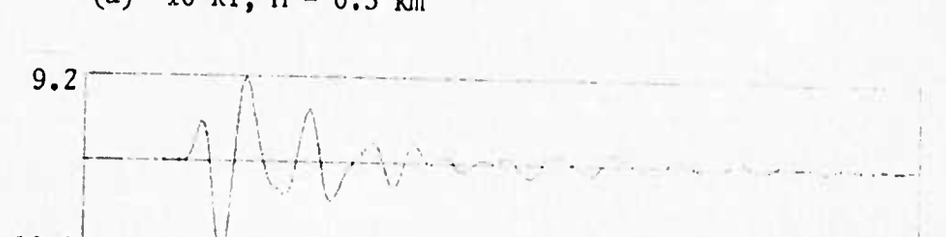


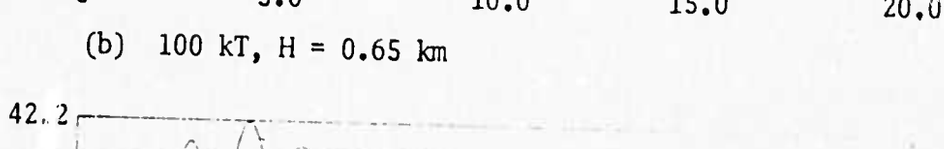
Figure 3.8. Repeating the seismograms of Fig. 3.7 with Q twice as large; that is, T/Q = 0.55. The burial depth is 1.0 km.



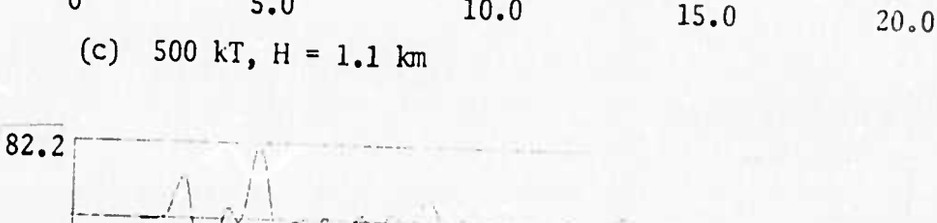
(a) 10 kT, H = 0.3 km



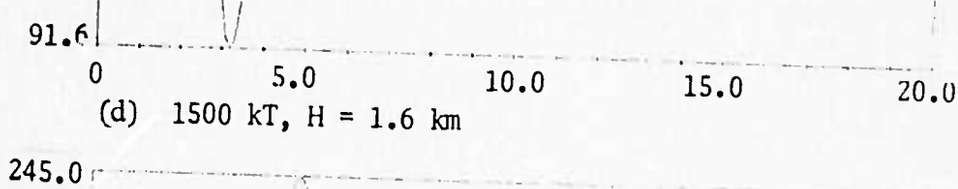
(b) 100 kT, H = 0.65 km



(c) 500 kT, H = 1.1 km



(d) 1500 kT, H = 1.6 km



(e) 4000 kT, H = 2.2 km

Figure 3.9. Repeating the seismograms of Figs. 3.5 – 3.6 with the depth of burial cube-root scaled to the yield.

The synthetic seismograms shown in Figs. 3.6 through 3.9 were used to generate amplitude-yield scaling relationships. These seismograms, which correspond to four different physical situations previously described, allow us to examine the dependence of amplitude-yield scaling on factors such as depth-of-burial, anelastic attenuation (Q) and the details of the manner in which the actual amplitude/period measurements are made.

Amplitude and half-period measurements were made for three different wavelets (a_0, b and c) for each of the P wave trains in Figs. 3.6 through 3.9. All measurements were taken from computer printouts of the seismograms, rather than the plots in Figs. 3.6 to 3.9, for increased precision. The definitions of a_0, b and c (Fig. 3.6a) are the same as those given by Springer and Hannon (1973). In addition to these measurements the rise-times of the a_0 wavelet were also determined.

In Figs. 3.10, 3.11 and 3.12 we have plotted the amplitudes of a_0, b and c versus yield, respectively. For any given figure there are three different types of symbols plotted (■, ▲ , and ●). The convention adopted for these symbols is the following: ■ represents amplitude measurements uncorrected for instrument response; ▲ represents amplitudes divided by the instrument response factor appropriate to twice the half-period of the particular wavelet under consideration; the ● represents amplitudes divided by the product of the instrument response factor and twice the half-period of the wavelet. Each figure in the sequence 3.10, 3.11, 3.12 for a_0, consists of four parts (a-d) corresponding to the four different situations of depth-of-burial and T/Q described in Figs. 3.6 - 3.9.

Considering the a_0 wavelet of Figs. 3.10a-d, there are several points to be made. First, for the seismograms of Figs. 3-7 - 3.8 corresponding to 3.10b-c, the maximum duration

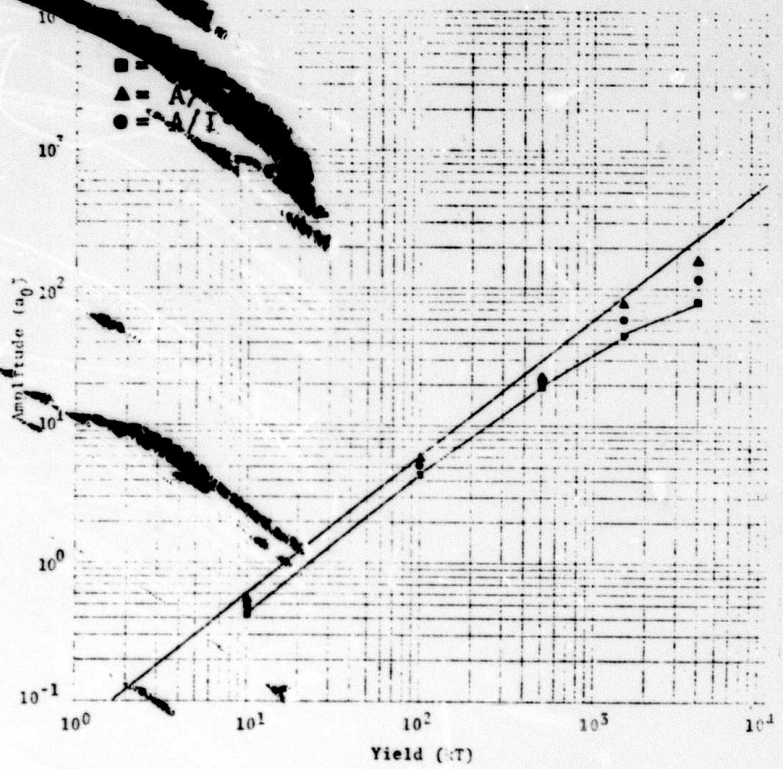


Figure 3.10a. Predicted amplitudes of the a_0 wavelet versus yield. T/Q = 1.1, DOB = 0.5 km. Lines of slope one are drawn on this and subsequent figures in this series to facilitate comparison. When markedly different, the trend of the data points corresponding to uncorrected amplitudes (■) is also indicated.

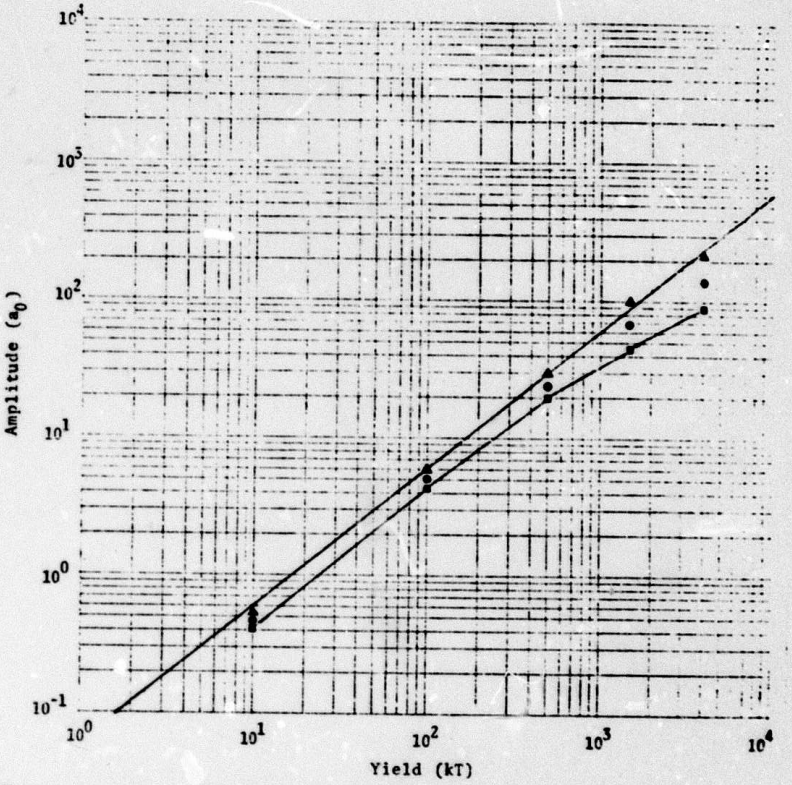


Figure 3.10b. Predicted amplitudes of the a_0 wavelet versus yield. T/Q = 1.1, DOB = 1 km.

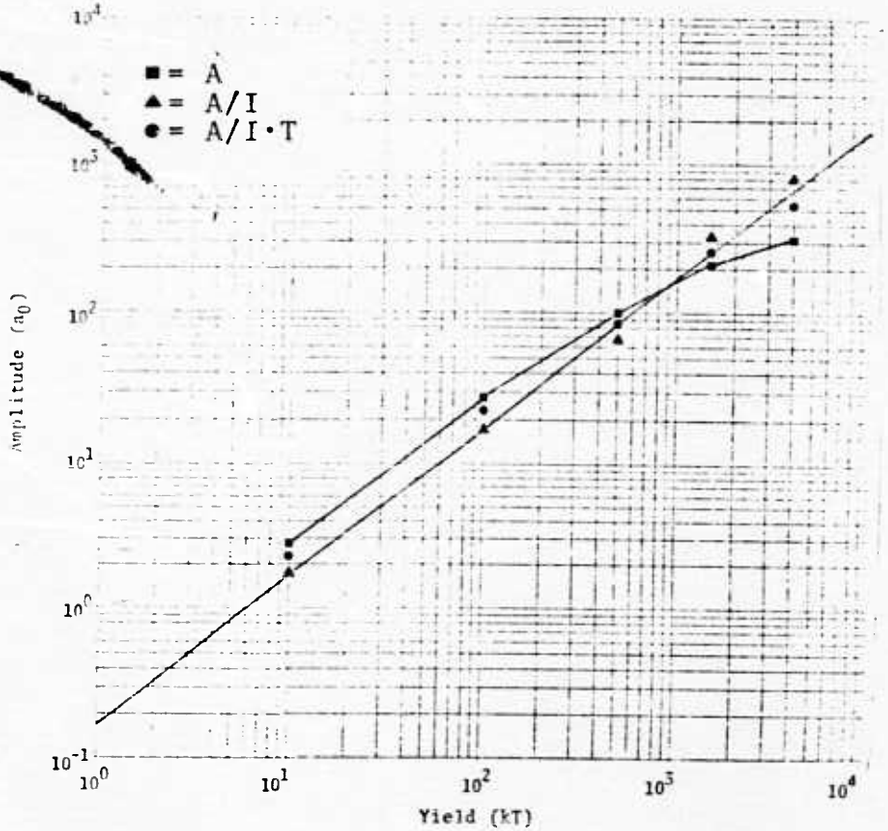


Figure 3.10c. Predicted amplitudes of the a_0 wavelet versus yield. T/Q = 0.55, DOB = 1 km.

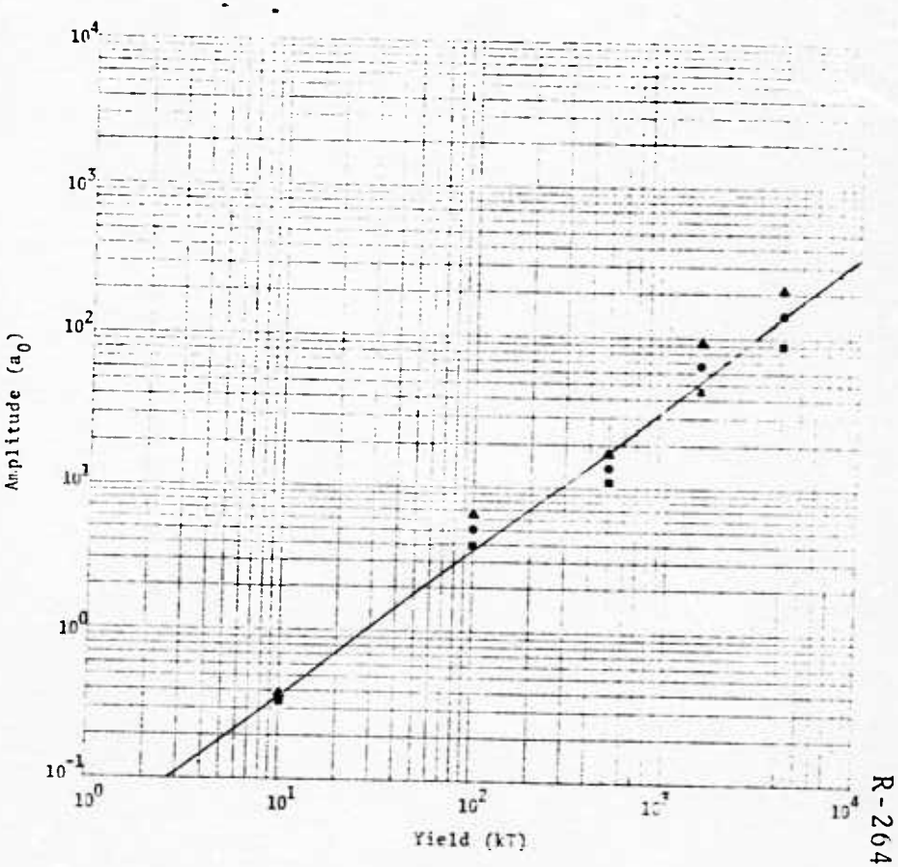


Figure 3.10d. Predicted amplitudes of the a_0 wavelet versus yield. T/Q = 1.1, scaled DOB.

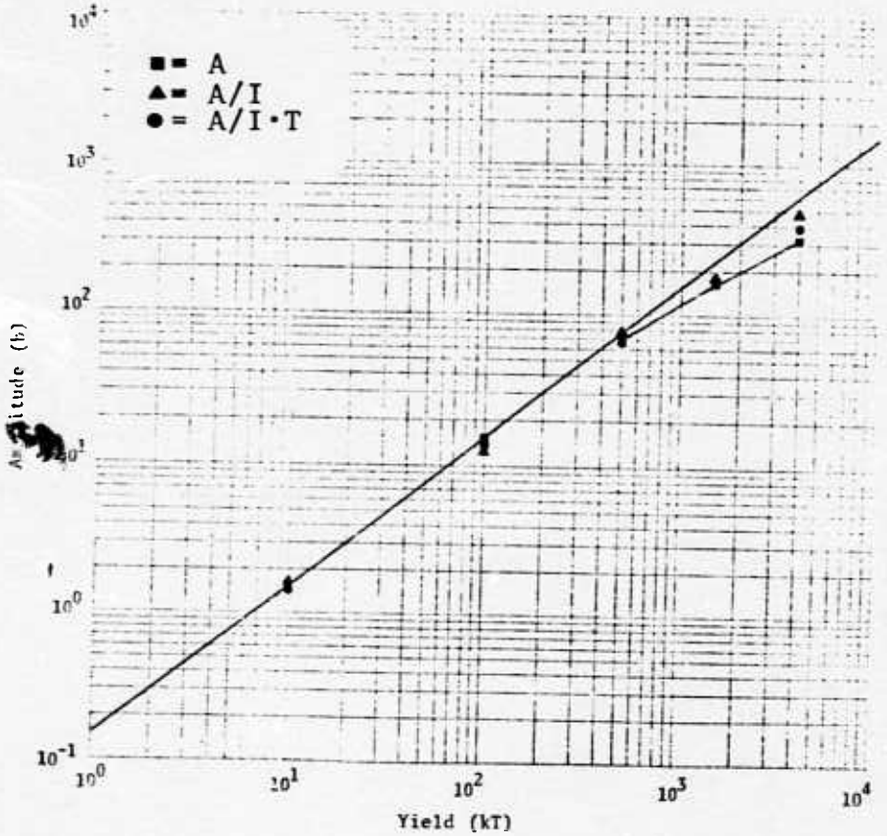


Figure 3.11a. Predicted amplitudes of the b wavelet versus yield. T/Q = 1.1, DOB = 0.5 km.

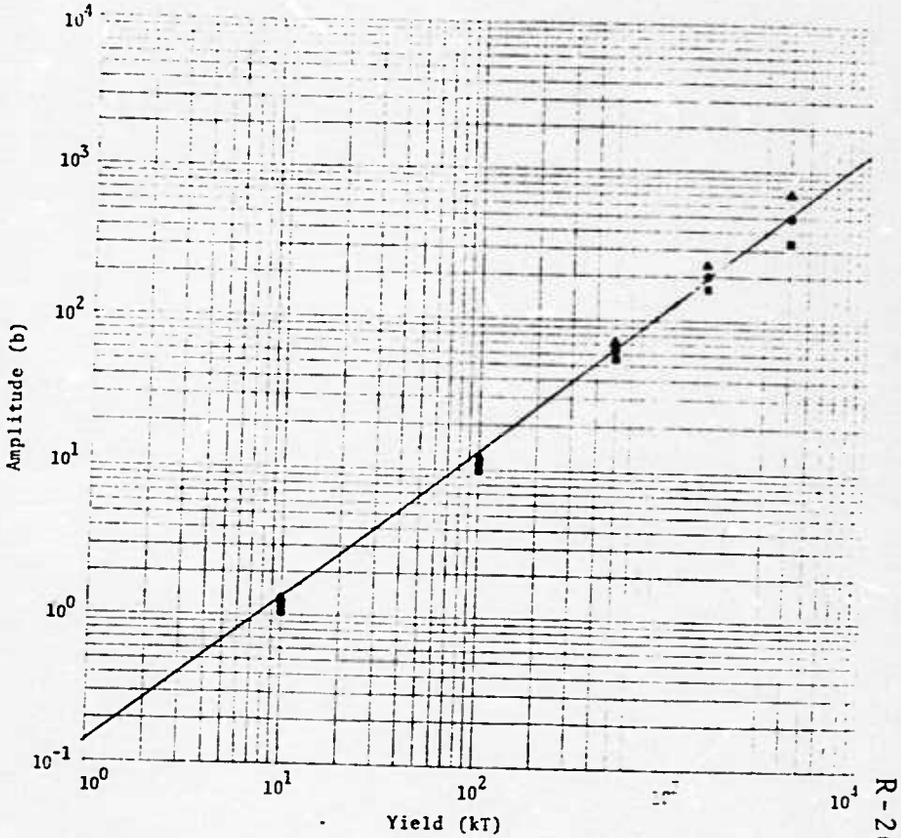


Figure 3.11b. Predicted amplitudes of the [illegible] wavelet versus yield. T/Q = 1.1, DOB = 1 km.

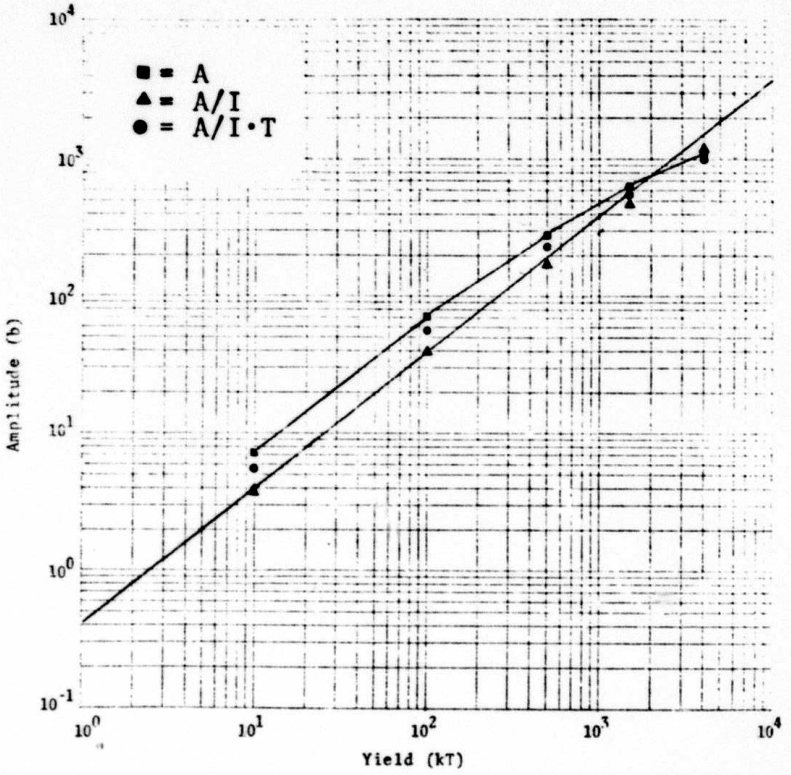


Figure 3.11c. Predicted amplitudes of the b wavelet versus yield. T/Q = 0.55, DOB = 1 km.

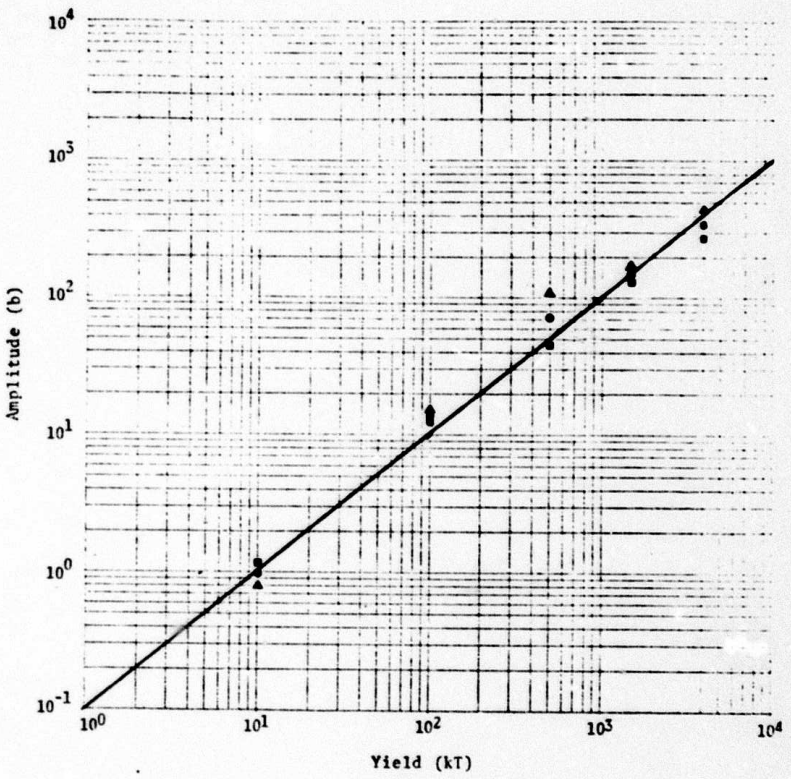


Figure 3.11d. Predicted amplitudes of the b wavelet versus yield. T/Q = 1.1, scaled DOB.

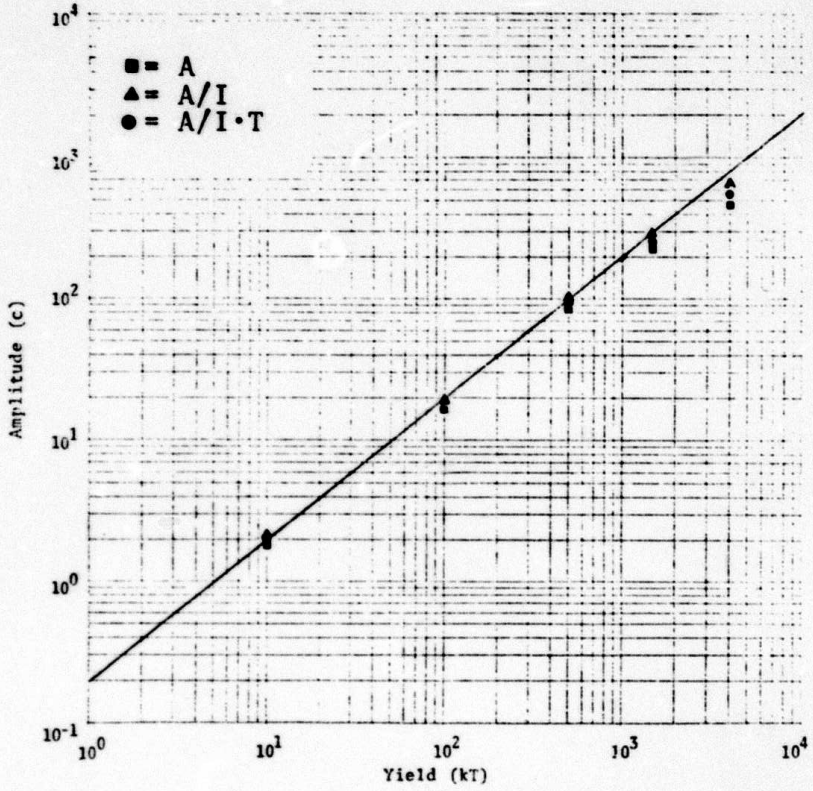


Figure 3.12a. Predicted amplitudes of the c wavelet versus yield. T/Q = 1.1, DOB = 0.5 km.

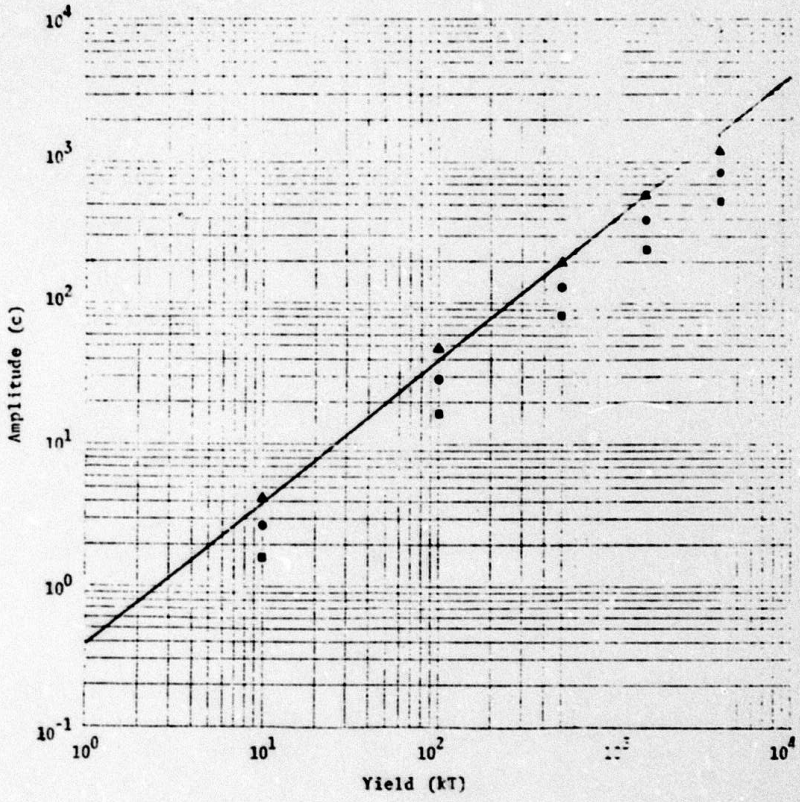


Figure 3.12b. Predicted amplitudes of the c wavelet versus yield. T/Q = 1.1, DOB = 1 km.

Reproduced from best available copy.

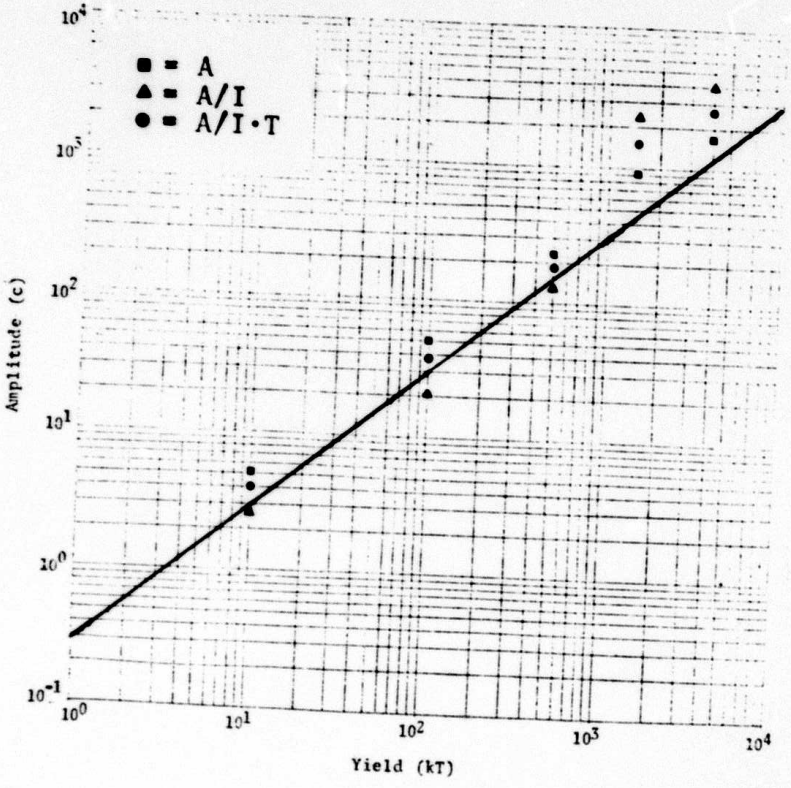


Figure 3.12c. Predicted amplitudes of the c wavelet versus yield. T/Q = 0.55, DOB = 1 km.

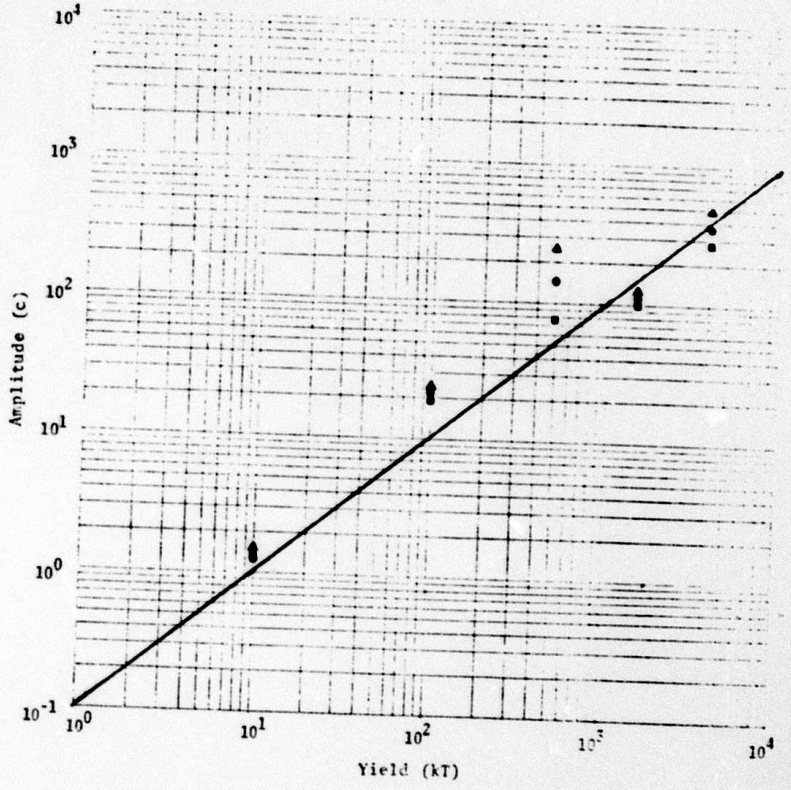


Figure 3.12d. Predicted amplitudes of the c wavelet versus yield. T/Q = 1.1, scaled DOB.

(0.775 sec) of this wavelet is less than the pP-P delay time (0.83 sec). Thus, these two cases demonstrate the dependence of amplitude-yield scaling on details of the measurements alone. The situation in Fig. 3.6 or 3.10a is just the opposite; that is, the pP-P delay time (0.42 sec) is less than the minimum duration (0.525 sec) of the a_0 wavelet which implies that a_0 is a mixed (pP+P) phase. In the case of Fig. 3.9 or 3.10d (scaled depth-of-burial), a_0 is a mixed phase for yields of 10 and 100 kT but not for the higher yields.

The amplitudes (■), uncorrected for instrument response and dominant period, of the a_0 wavelet in Figs. 3.10a-c show a marked departure from a linear dependence on yield at yields > 100 kT. This behavior, particularly for the situations of Figs. 3.10b and c where depth-of-burial is not influencing the results, is ascribed to the explosion corner frequencies shifting to lower frequencies with increasing yield and sliding into the passband of the instrument (LRSM in this case). This explanation has been invoked by others (Haskell, (1967), Evernden and Filson, (1971)) for similar behavior of later portions of the P-wave trains from explosions. Simple correction of these amplitudes for instrument response at the dominant period (equal to twice the duration of a_0) results in approximately linear amplitude-yield relationships (note the trends of the ▲'s in Figs. 3.10a-c). Further manipulation of the amplitudes, namely division by the dominant period, reintroduces a flattening in the data at higher yields. This last result is quite significant since amplitude/period is the quantity employed in conventional m_b estimates and the data in Figs. 3.10a-c indicate that even in the absence of such effects as depth-of-burial, m_b will not exhibit a linear dependence on explosion yield. The quantity that should be compared with explosion yield is amplitude corrected for instrument response; that is, apparent ground motion.

The scaling relationships shown for a_0 (Fig. 3.10) and the b and c wavelets in Figs. 3.11 and 3.12, respectively, are complicated by depth-of-burial effects, particularly in Figs. 3.10d, 3.11d and 3.12d corresponding to the situation where the explosions are detonated at scaled depths. The c wavelet in Figs. 3.10a and b corresponds to the maximum amplitude in the P-wave trains considered here (see Figs. 3.6 and 3.7) and would be used for conventional m_b estimates. The data in Figs. 3.12a and b suggest that the amplitude of ground motion rather than amplitude/period once again results in a more nearly linear dependence on yield.

The synthetic seismograms shown in Figs. 3.8 (T/Q = 0.55, DOB = 1 km) and Fig. 3.9 (scaled depth-of-burial) demonstrate one of the major problems in magnitude estimates for explosions. The maximum amplitudes of the first few cycles in these figures are sometimes associated with the b wavelet and other times with the c wavelet. As expected, this variation contaminates the amplitude-yield relationships as can be clearly seen in Fig. 3.11d and Figs. 3.12c and d. While the amplitude of the a_0 wavelet is the preferred measurement for yield estimates, signal-to-noise problems might be too severe in the case of low yield explosions recorded at teleseismic distances. This being the case, then the data shown here support a preference for the b wavelet rather than the c or maximum cycle in the P-wave train.

As previously remarked, the duration of the a_0 wavelet is relatively (with few exceptions) uncontaminated by such effects as the free surface reflection (pP) and receiver crustal structure. As a result, this wavelet was chosen for a special investigation of the behavior of dominant period with explosion yield as modified by attenuation (Q) and instrument response.

The duration of a_0 was determined for a series of explosions detonated at Pahute Mesa. The seismograms used were recorded at one of the short-period stations of the Palmer network in Alaska. Because of classification considerations a fit (solid line) to the observed data, rather than the data set itself, is given in Fig. 3.13. The vertical bars with arrows enclosed give a measure of the precision of these data. The one-sided arrow with Δt_0 above is an estimate of the maximum amount by which the duration of the a_0 wavelet may be underestimated for the lower yield explosions studied. This underestimate arises because of the tendency to pick a late arrival-time for the onset of the a_0 wavelet in a background of seismic noise. While the error is on the order of 0.1 sec for explosions of 100 kT yield, it is considerably less (< 0.05 sec) for higher yield (> 1 MT) explosions. The dashed line indicates a "fit" to the data with Δt_0 added to estimates of the duration of a_0, thus illustrating the bound on the possible range of the duration underestimates. The remaining points on Fig. 3.13 (see legend) are from theoretical seismograms and correspond to the four different combinations of depth of burial and attenuation (T/Q) described previously.

While not conclusive, there are a few points that we can make about the results of Fig. 3.13. First, the predicted behavior for the case of T/Q = 0.55, DOB = 1 km (◇) is definitely at variance with the observations. However, for the same DOB (1 km) but T/Q = 1.1 the predicted points (○) actually follow the observed trend within the uncertainty of the observations. In the case of scaled depth of burial (□) the point at 100 kT plots outside the range of observations. While the actual Pahute Mesa explosions were approximately buried at scaled depths for containment purposes, it has been reported (Frasier (1972); Springer (1974)) that the pP-P delay times for Pahute Mesa events

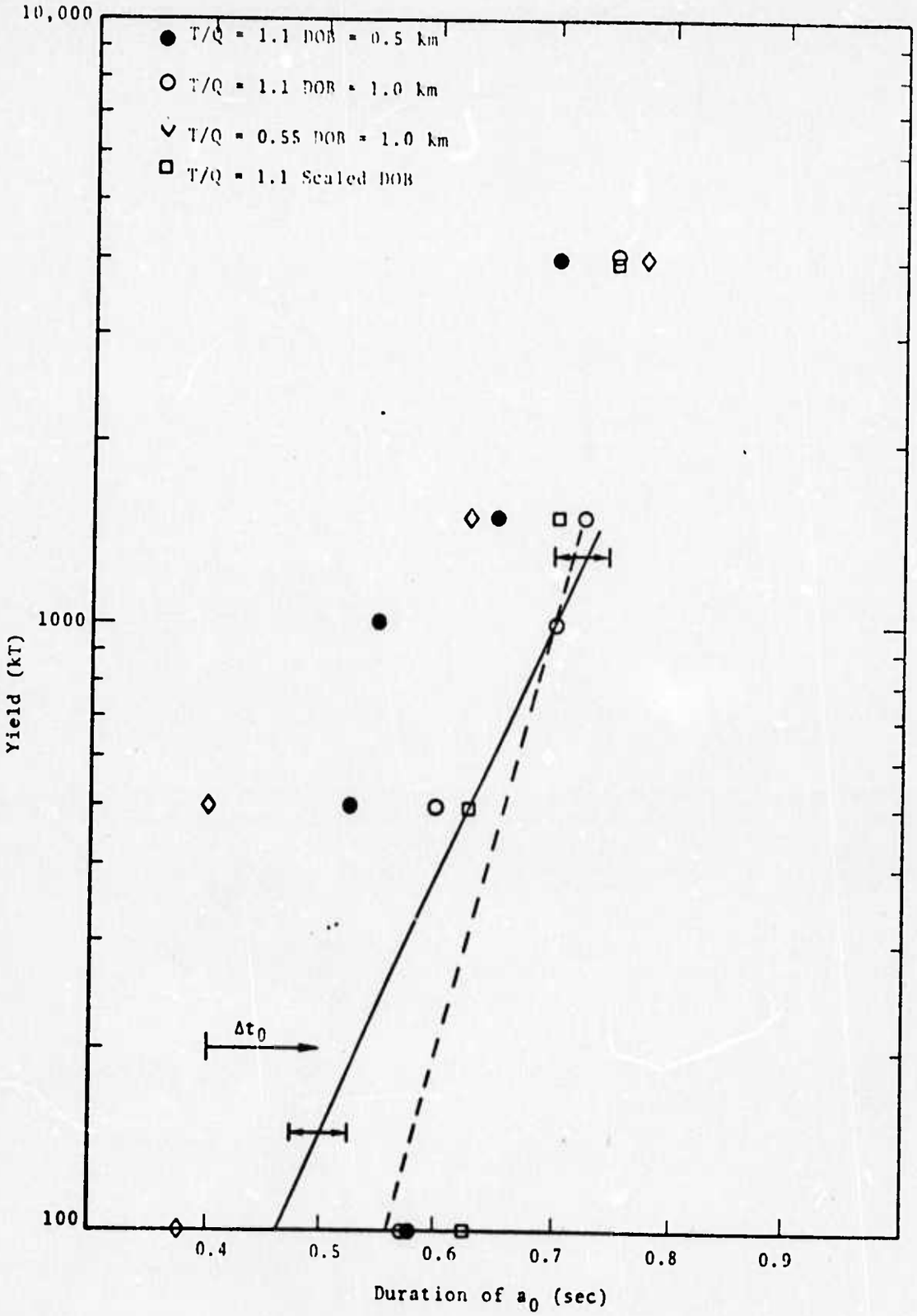


Figure 3.13. Yield versus duration of a_0 wavelet for predicted and observed seismograms. Measurements for ◊ and □ not available at 1000 kT.

are considerably greater than those used in the computations. If this is correct, then the open circle turns out to be more appropriate, since for that case the pP-P delay is greater than the duration of a_0, whereas in the case of the 100 kT explosion at a scaled depth of burial the a_0 wavelet was contaminated by pP.

An investigation such as the one described in this section is quite instructive for pointing out optimum procedures for yield estimation of underground explosions. It allows one to isolate those factors that most strongly affect the frequency content and amplitude of observed explosion signatures and thereby correct amplitude-yield scaling relationships accordingly.

3.3 THE DISPERSION ASSOCIATED WITH A CONSTANT Q, LINEAR ABSORPTION OPERATOR

It is universally accepted that seismic waves are attenuated anelastically during their passage through the earth. The mechanism of this attenuation, and even its form over the measurable frequency band is, however, far from being fully understood. For those interested in the construction of synthetic seismograms, the common practice is to assume that the attenuation is satisfactorily represented by a frequency independent Q and apply the operator $\exp[-\omega T/2Q]$ where T is the source-receiver travel path and Q is the effective attenuation factor characteristic of the travel path. Determination of appropriate values for Q, either in the form of a Q-depth profile or a characteristic T/Q for a given source-receiver pair is an important and active research area.

A necessary consequence of an absorption operator of the kind discussed here is the presence of dispersion. Theories to account for this dispersion have been given by

Lomnitz (1957), Futterman (1962) and Strick (1970). The formulations of Lomnitz and Futterman have recently been compared by Savage and O'Neill (1975). The difficulty with all these theories is that an arbitrary cutoff frequency is required beyond which the constant Q assumption no longer obtains. Choices of this cutoff frequency at the high or low ends, along with assumptions about the physical bases for the cutoff, account for the differences between the theories.

The three absorption operators, including attenuation and dispersion, are as follows:

Lomnitz (1957);

$$\exp\left\{-i\omega T\left[1 - \frac{2}{\pi Q}\ln\left(\frac{\gamma\omega}{a}\right)\right]^{1/2}\right\} \cdot \exp - \frac{\omega T}{2Q} \qquad (3.2)$$

$\ln \gamma = 0.577216 \ldots,$

a = high frequency cutoff,

Futterman (1962);

$$\exp\left\{-i\omega T\left[1 - \frac{i}{2Q}\frac{1}{\pi Q}\ln\left(\frac{\omega}{\omega_0}\right)\right]\right\}, \qquad (3.3)$$

ω_0 = low frequency cutoff,

Strick (1970);

$$\exp\left\{-i\omega T\left[1 - \frac{i}{2Q} + \frac{1}{\pi Q}\ln\left(\frac{\omega_h}{\omega}\right)\right]\right\} \qquad (3.4)$$

ω_h = high frequency cutoff.

Let us compare a synthetic seismogram computed with no dispersion to those in which dispersion is included using the three formulations above. The cutoff frequencies chosen are:

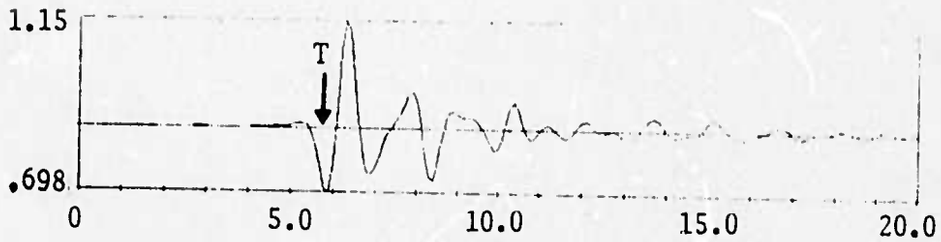
$$a = 10^{10},$$
$$\omega_0 = 10^{-5}/\gamma, \qquad (3.5)$$
$$\omega_h = 2000\ \pi$$

The first two are the values suggested by Savage and O'Neill while the last was selected by numerical experiments at S^3. In any event, the pulse shapes are quite insensitive to these cutoff values.

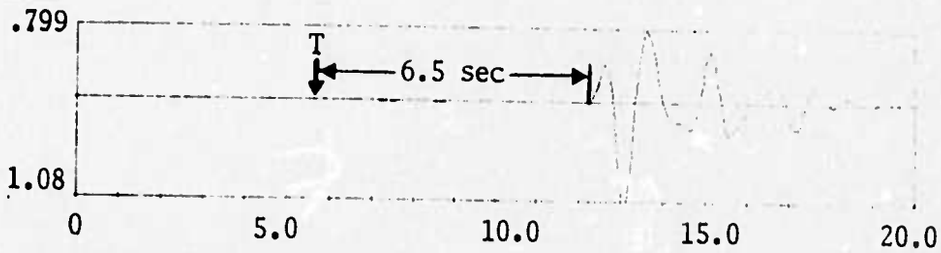
The seismograms of Fig. 3.6 - 3.9 were computed using the Strick formulation. We shall use that of 3.6a, a 10 kT explosion at a depth of 0.5 km in the crustal structure of Table 3.1. The epicentral distance is 4,000 km and T/Q = 1.1 was used. An LRSM instrument transfer function was applied. In Fig. 3.14, the same seismogram is shown with the Q operator of Futterman and Lomnitz being applied and also with no dispersion applied.

Comparing Figs. 3.14a-d, we first note that the three formulations of dispersion all have identical effects on the pulse shape. In fact, when the three pulses are overlain, they are indistinguishable. Failure to include this dispersion has a rather dramatic effect on the seismogram, however.

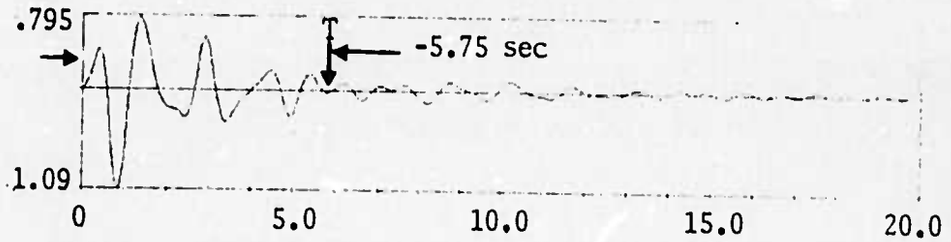
A peculiar feature of the dispersion for these linear Q operations is its effect on the travel time. The ray theoretic travel time is indicated on each record by T. The non-causality of the non-dispersed pulse is clearly evident in 3.14a where the pulse begins before the arrival time and a sharp pulse onset is not evident. Adding dispersion, a sharp onset appears but the pulse is moved several seconds from the arrival time - later in the high cutoff frequency cases and earlier in the low cutoff frequency formulation of Futterman. Though Futterman's work is often cited by those computing synthetic seismograms, the bothersome



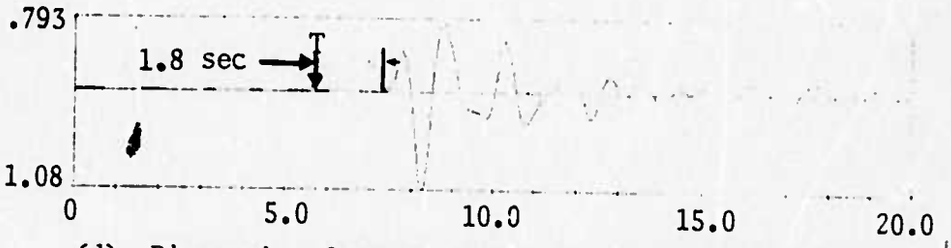
(a) Attenuation with no dispersion included



(b) Dispersion formulation according to Lomnitz (1957)



(c) Dispersion formulation according to Futterman (1962)



(d) Dispersion formulation according to Strick (1970)

Figure 3.14. Comparison of synthetic seismograms at 4000 km for attenuation without dispersion and three different formulations of the required dispersion. The event is the same as that in Fig. 3.6a and T/Q = 1.1. The ray theoretic travel time is indicated by T.

forward time shift introduced by his formulation has not been mentioned to our knowledge. However, this shift is quite apparent in the examples given in his 1962 paper. The shifts to later time in the Lomnitz and Strick formulations are, of course, hardly more satisfying.

The form of the travel time shift introduced by the dispersive operators (3.2 - 3.4) can be deduced by some elementary manipulations. Let the elastic or ray theoretic travel time be denoted T. Then the actual travel time for the three formulations is:

Lomnitz

$$T_L \simeq T - \frac{T}{\pi Q} \ln \left(\frac{\gamma\omega}{a}\right) , \tag{3.6}$$

Futterman

$$T_F = T - \frac{T}{\pi Q} \ln \left(\frac{\omega}{\omega_0}\right) , \tag{3.7}$$

Strick

$$T_S = T - \frac{T}{\pi Q} \ln \left(\frac{\omega}{\omega_h}\right) . \tag{3.8}$$

For fixed values of the cutoff frequencies the travel time shift, ΔT, is therefore linearly proportional to T/Q. A series of synthetic seismograms are constructed at T/Q = 0.55, 1.1, 2.2, for each of the dispersion formulations to illustrate this proportionality. The set at T/Q = 1.1 is shown in Fig. 3.14. For these cases the travel time shift ΔT is plotted versus T/Q in Fig. 3.15. It should also be mentioned that the near identity of the pulse shapes for all three formulations which was apparent in Fig. 3.14 continues to hold for these widely different T/Q values.

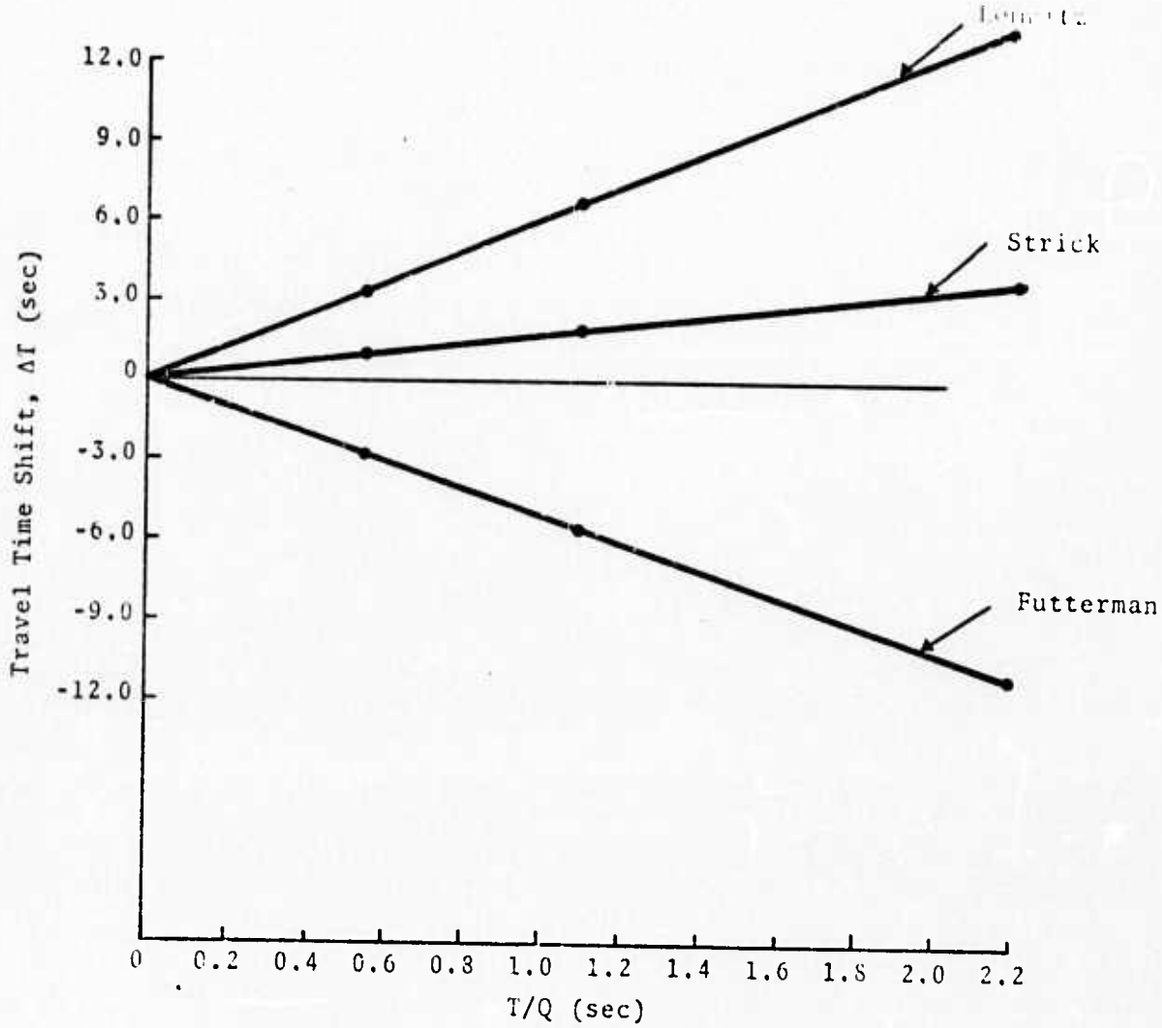


Figure 3.15. The travel time shift as a function of T/Q for the three dispersion formulations with fixed values of the cutoff frequencies given in Eq. (3.5). The data points were determined from synthetic seismograms.

Not only is the travel time shift proportional to T/Q, which is at least associated with the properties of the earth, it is also dependent on the value of the cutoff frequency, a rather arbitrary quantity. Multiplying the cutoff frequency by M, the travel time shift changes by approximately $T \ln M/\pi Q$. This is apparent by comparing the Strick and Lomnitz formulations in Eq. (3.6) and (3.8) and Fig. 3.15. The selected values of the cutoff frequencies are such that $a/\gamma \simeq 10^7\ \omega_h$. This accounts for the considerably larger shift for the Lomnitz formulation, yet the pulse shapes are identical. The same kind of comparison can be made using the Futterman operator. In any case, the variation in pulse shape among seismograms computed with cutoff frequencies varying over several orders of magnitude about the values of Eq. (3.5) is like the trivial variation apparent in Fig. 3.14 where the three formulations were compared.

The time shift introduced by these forms for including dispersion is troublesome because of the ambiguity it introduces in the travel time and, therefore, in interpretations of travel time data. We have three different formulations, none of which can be discarded on theoretical grounds. They have essentially identical effects on the pulse shape. Yet the resulting travel time differs by as much as tens of seconds depending on T/Q and the cutoff frequency chosen. That is, for the same earth structure the travel time varies widely depending on the way dispersion is introduced.

We have posed an unresolved question which certainly needs greater attention. For the time we have chosen to use the Strick formulation for routine applications, if only because the time shift is minimal for this case.

3.4 THE EFFECT OF NEAR SOURCE CRUSTAL STRUCTURE ON THE TELESEISMIC P WAVE

It is well known that the first few cycles of the teleseismic short period P wave record of explosions, and hence m_b, are strongly influenced by the free surface reflected phase pP. This effect has been studied in previous S^3 reports (e.g., Cherry, et al. (1974b)). It has also been pointed out by a number of investigators that details of the near source crustal structure can affect the shape of the teleseismic P wave record. A discussion of this effect was given in our last contract report (Bache, et al., (1974)). A simple example will suffice to illustrate the kinds of effects that may occur.

Using the theory of Appendix B, a spherically symmetric explosion source may be buried in a layered model of the crust. A series of illustrative synthetic seismograms are shown in Fig. 3.16. These are appropriate to an epicentral distance of 4,000 km (one mantle arrival is computed) with T/Q = 0.84. The source is a spherically symmetric 20 kT explosion in NTS tuff which is characterized by a source spectrum much like #1 of Fig. 3.2. The explosion is buried at five different burial depths in the indicated crustal structure which is typical of NTS. Therefore, the important contributing phases may include arrivals from the tuff-hard rock interface at 2.5 km as well as P and pP. With each seismogram is indicated the probable measurement for conventional m_b. The results indicate that burial depth alone can contribute to m_b changes up to 0.3 units. The coupling into elastic waves of an explosion of constant yield will, of course, be dependent on depth of burial in a complex way as the rock properties are depth dependent.

At the beginning of this section in Fig. 3.1 a set of seismograms for five similar NTS events were shown. As

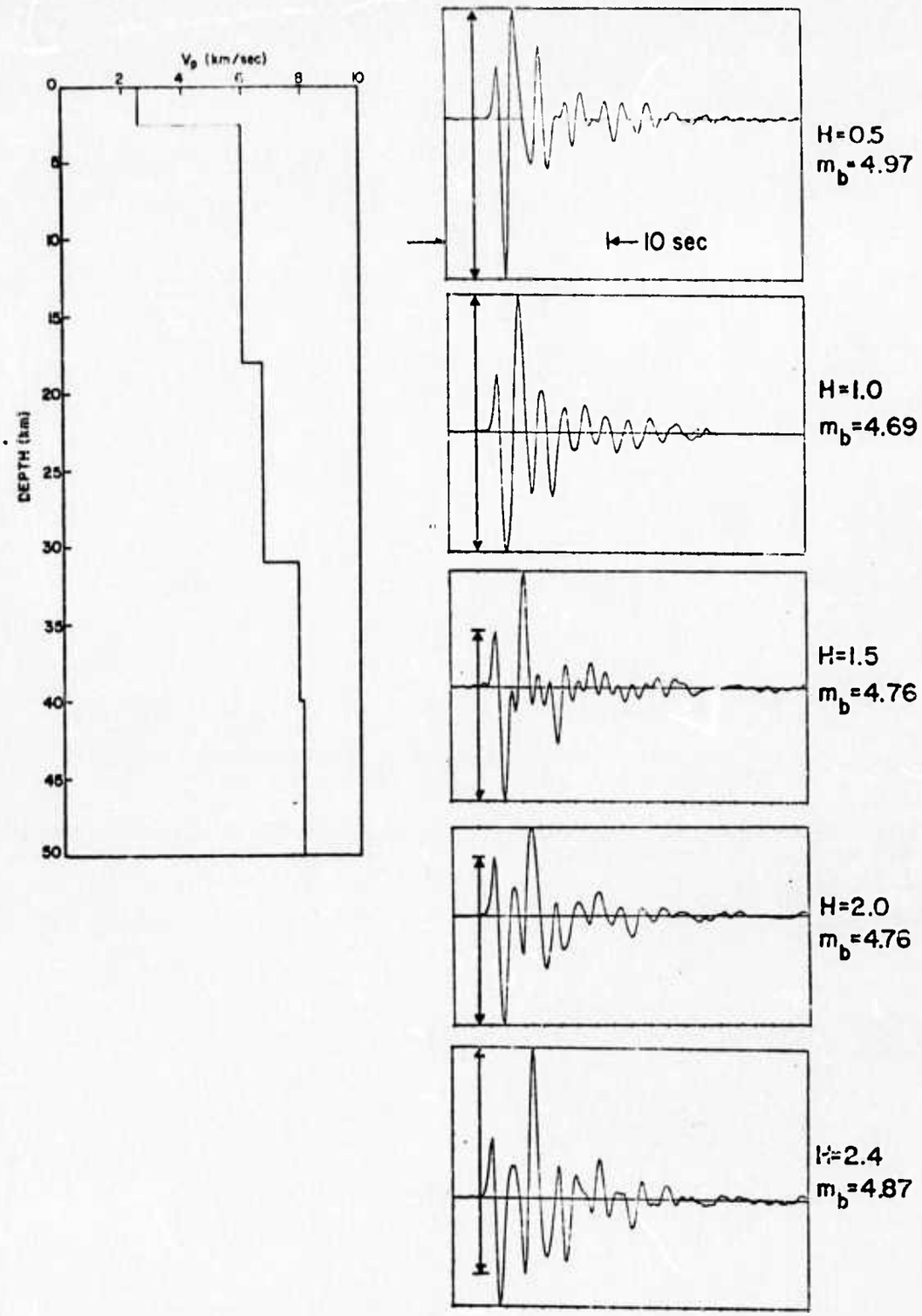


Figure 3.16. Synthetic seismograms for the first mantle arrival at 4000 km from a 20 kT explosion in tuff at a series of burial depths in a crustal structure typical of NTS. Travel through the upper mantle was characterized by T/Q = 0.84. The conventional m_b as determined from the indicated phase is given with each seismogram.

discussed in connection with that figure, differences between these seismograms can only be attributed to the explosion source itself and the crustal structure in the immediate source vicinity. A subsequent discussion of the character of the one-dimensional source characteristics for NTS tuff explosions made clear that, even over a broad yield range, one must look for higher order perturbations on the center of dilatation to explain source generated teleseismic wave form differences from event to event. Near source crustal structure may, of course, always play a part.

In order to gain some insight into the extent to which fine details of the crustal structure may be responsible for the differences apparent in Fig. 3.1, an attempt to match these seismograms using elementary models was used. The results of this exercise will be presented here. Details of the event and receiver characteristics are omitted for security reasons, but these should be inessential for our purposes.

In computing synthetic seismograms to match the data of Fig. 3.1, the following information was used:

1. Reasonable estimates of the material properties at the shot point were available allowing a finite difference (SKIPPER) calculation of the reduced displacement potential (RDP). Analysis of the data indicated that one RDP scaled to the proper yield would suffice.

2. Along with the event yield, the depth of burial, average source-surface travel times and approximate depth to the underlying Paleozoic rock interface were known for the five events. Also, a detailed average velocity-density profile for the event region to a depth of 1 km was compiled.

3. Average crustal structures for NTS (Hill and Pakiser (1967)) and the receiver region were used. Since the receiver was located on a transparent region of the crust, the receiver crustal structure had little effect.

4. The response characteristics, both amplitude and phase, of the sensing instrument were known.

5. For the travel in the upper mantle, T/Q = 1.1 was used. The geometric spreading was computed with geometric ray theory (Julian and Anderson (1968)) and the upper mantle model CIT 109 of Archambeau, et al. (1969). Since geometric ray theory leads to inaccuracies in amplitude calculations, the geometric spreading factor is only approximate. Therefore, the maximum amplitudes of the observed and synthetic records for event A were scaled by multiplying all synthetics by a factor of 2.1.

The results are shown in Fig. 3.17. The agreement of the shape of the wave form for the first few cycles of motion is quite good.

The extended train of higher amplitude motion appearing on the observed seismogram may be due to later arriving mantle phases. While only one mantle arrival was treated in our calculations of four of the five cases, an indication of the improved match which is possible by including later mantle phases is shown in event D where a second arrival appears on the synthetic record.

Also indicated on each seismogram is a consistently measured m_b using the phase indicated on the event A on each record.

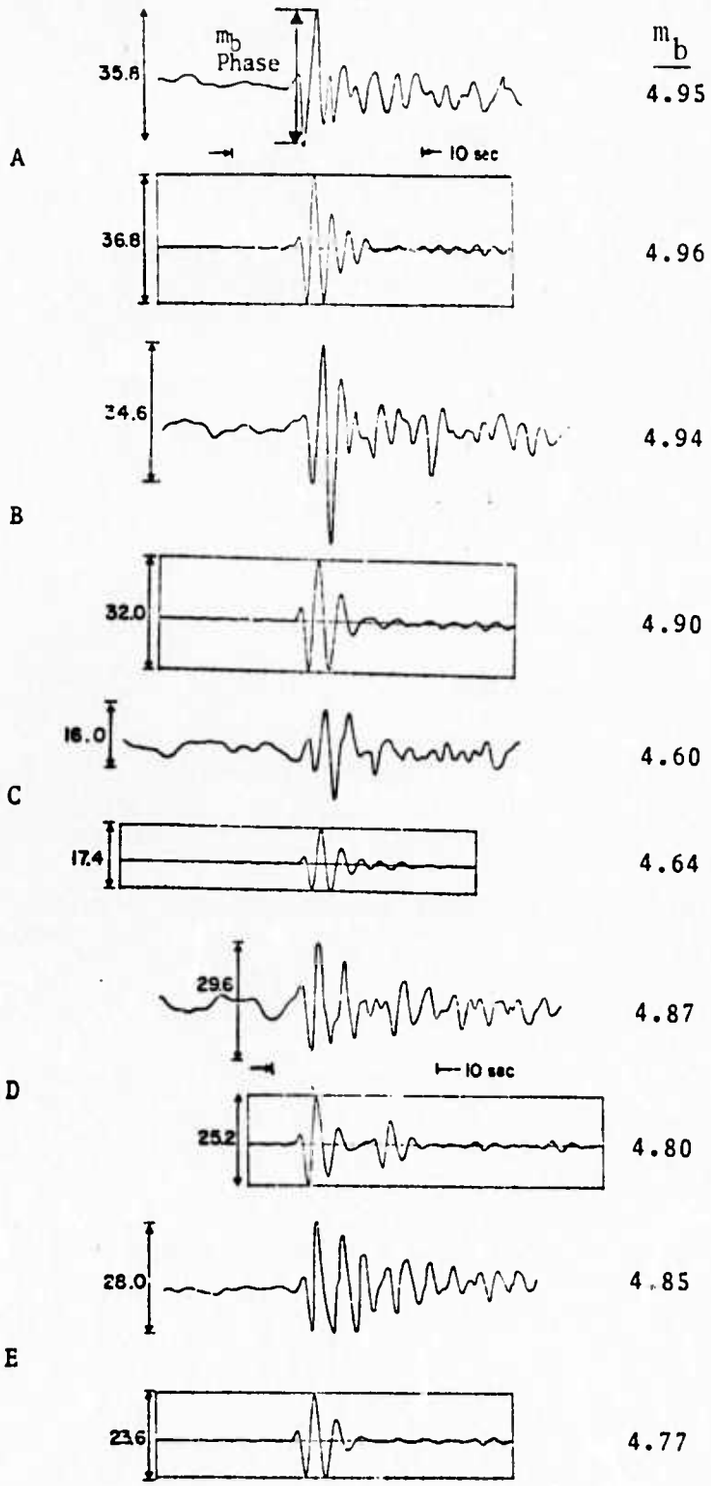


Figure 3.17. A comparison of observed and synthetic seismograms for five similar NTS events. A consistent m_b, measured as indicated, is given for each record.

3.5 THE INFLUENCE OF HIGHER ORDER PERTURBATIONS ON THE SPHERICALLY SYMMETRIC EXPLOSION GENERATED P WAVE

The existence of SH and Love waves as well as the azimuthal dependence in observed Rayleigh wave amplitudes are strong indicators that a simple center of dilatation model of an underground explosion is insufficient. Higher order perturbations on the spherically symmetric monopole source are apparently present. A number of mechanisms accounting for these effects have been postulated including tectonic release, earthquake triggering, jointing, spallation, etc.

The theory of Appendix B was developed in order to provide an interface between seismic wave propagation methods and the nonlinear finite difference codes through which many of the complicated phenomena leading to a departure from spherical symmetry may best be studied. A few simple examples which provide a qualitative estimate of the possible effect on the teleseismic short period record will now be given for one important cause of higher order source perturbations, tectonic release.

Archambeau (1972) has given a theory for the dynamic stress relaxation due to the creation of a cavity and surrounding zone of fractured material in a prestressed geologic formation (tectonic release). We now consider an explosion plus tectonic release and examine the teleseismic P wave seismogram.

The spherically symmetric explosion source will be taken to be that denoted as #4 in Fig. 3.2, scaled to 65 kT. That is, we take a rather weak coupling explosion in NTS tuff. For the tectonic release calculation the prestress was taken to be 120 bars. The radius to which shock induced fracture begins is R_C = 30 meters. This fracture then propagates to a final radius of R_0 = 300 meters. These values for the tectonic release model compare to the SKIPPER computed cavity

radius of 54 meters and an elastic radius of 266 meters. The physical parameters for the explosion and tectonic release calculations are therefore not entirely compatible, but this is not of much importance here.

A source consisting of an explosion plus tectonic release will be composed of a center of dilatation plus a double couple. In the notation of Appendix B, the nonzero multipole coefficients will be $A_{00}^{(4)}(\omega)$ for the explosion and the double couple or quadrupole terms $A_{2m}^{(j)}$, $B_{2m}^{(j)}$; $m = 0,1,2$; $j = 1,2,3,4$; excited by tectonic release. The nonzero quadrupole terms are determined by the orientation of the prestress field.

Let us first consider a horizontally oriented prestress that is, the prestress is $\sigma_{12} = 120$ bars, where the 3-axis is vertical. The geometry is depicted in Fig. 3.18. In this case the nonzero multipole coefficients are $B_{21}^{(4)}(\omega)$ for the P wave excited by tectonic release and $B_{21}^{(2)}(\omega) = A_{22}^{(3)}(\omega) = -A_{21}^{(1)}(\omega)$ for the S wave.

In order to visualize the elastic waves excited by this source, several radiation pattern plots are given in Fig. 3.19. In the figure are several two-dimensional sections showing the 1 second spectral component of the P and SV wave displacement 1.0 km from the source. This source is, of course, a strong radiator of SH waves, but these are not shown. Three of the plots show the vertically emitted radiation at selected azimuths. We shall subsequently present synthetic seismograms computed at 4,000 km. At this distance the earth model used gives a takeoff angle of 14.7° for the direct P wave and 7.8° for the free surface reflected sP phase. The takeoff angles for the three main phases, P, pP, sP, are indicated on the azimuthal plots. For any reasonable earth model and over the entire teleseismic distance range,

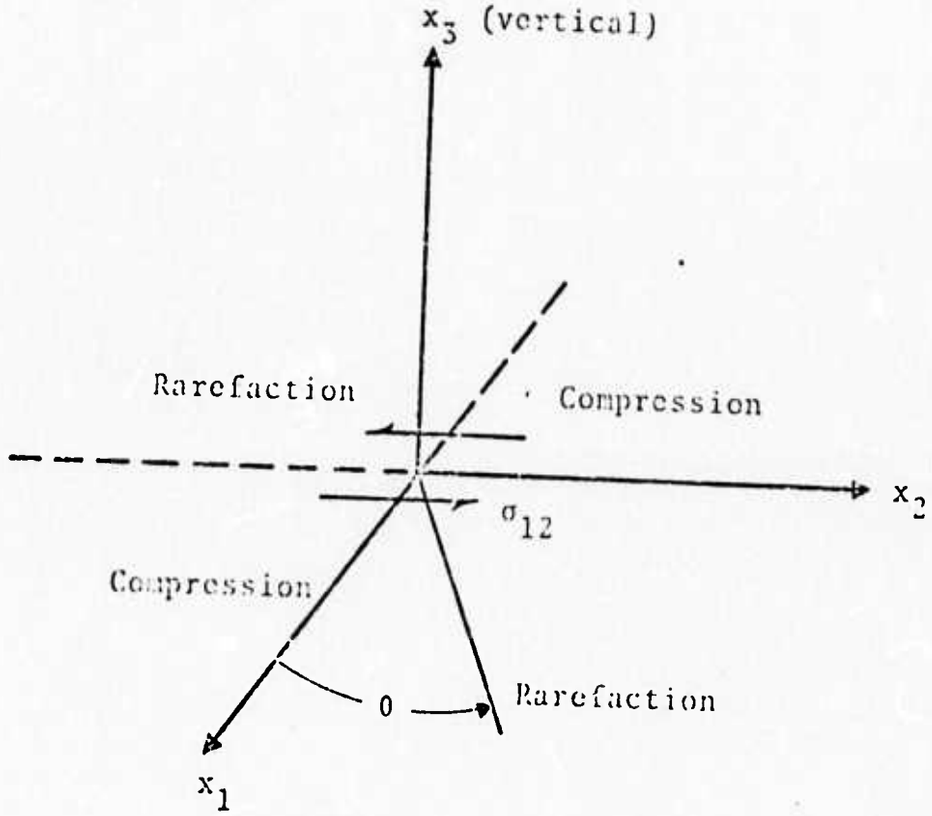
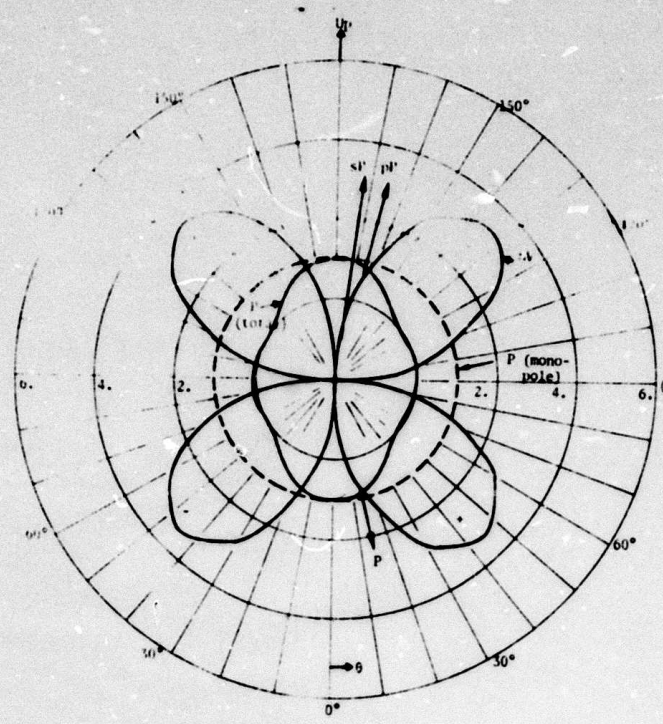
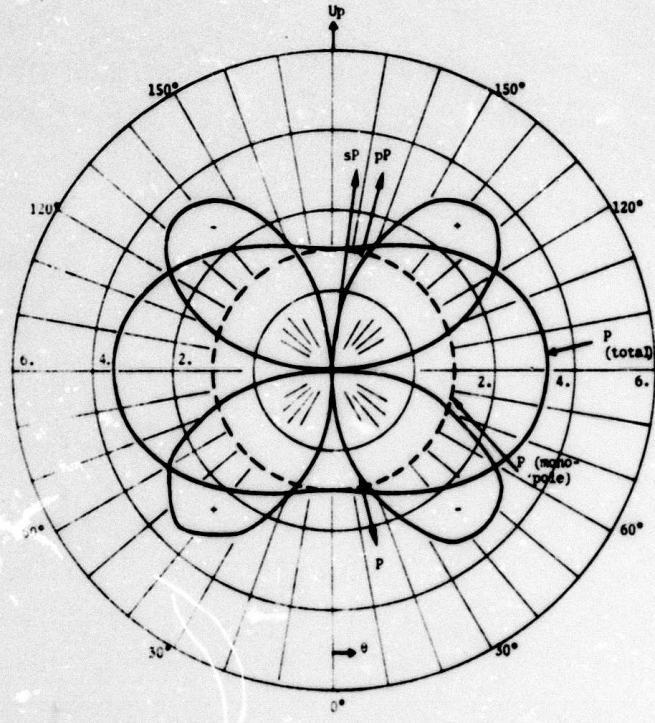


Figure 3.18. Coordinate system for defining the prestress (arrows) and source-to-receiver azimuth (θ). The first motion in the four quadrants due to an explosion in a medium with prestress $\sigma_{12} > 0$ is also indicated. Definitions of σ_{13} and σ_{23} are consistent with that of σ_{12}.

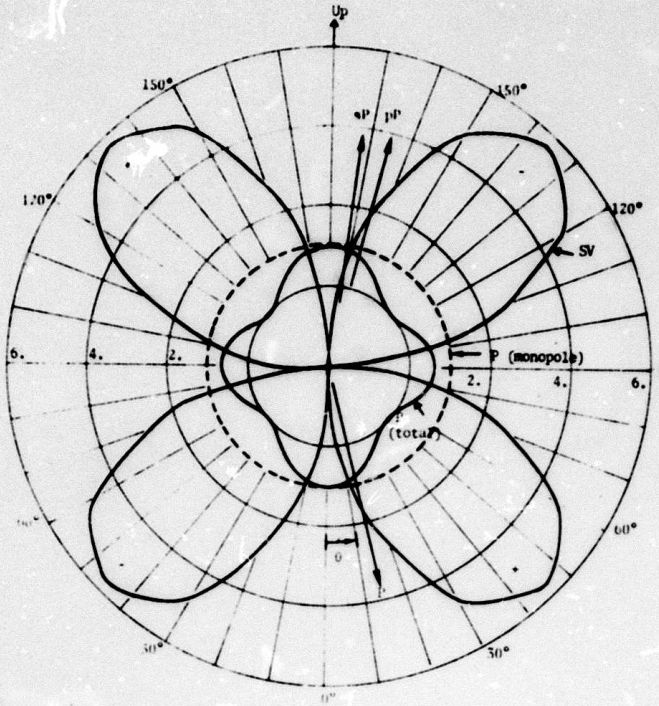


(a) Azimuth ϕ = 22.5°

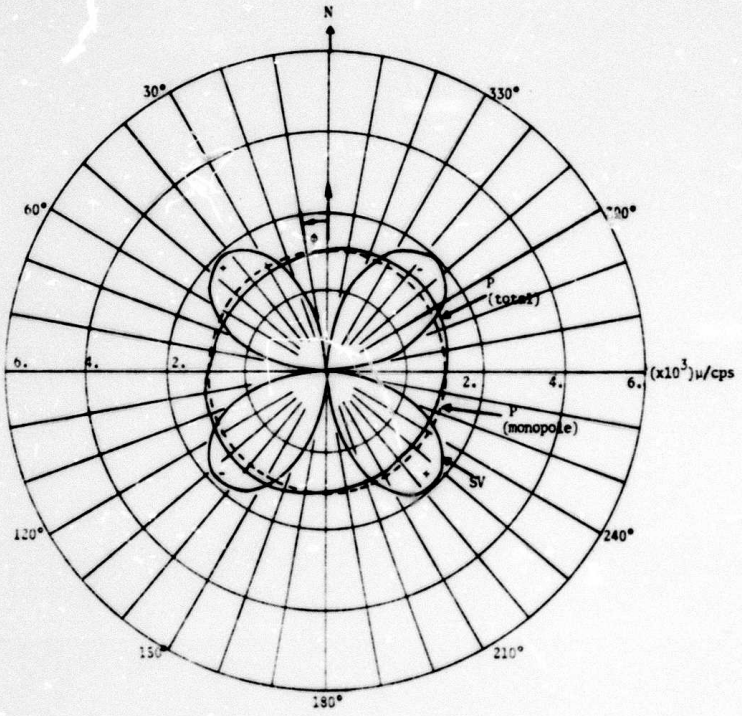


(b) Azimuth ϕ = 337.5°

Figure 3.19. Elastic wave radiation patterns for an explosion plus tectonic release. Depicted are the 1 Hz spectral components of the P and SV wave displacement 1.0 km from the source. The contribution of the spherically symmetric explosion to the P wave is indicated separately by the dashed curve.



(c) Azimuth ϕ = 45°



(d) Takeoff Angle
θ = 15°

Figure 3.19 (Continued)

the takeoff angles of interest are not far different from these. Some idea of the azimuthal pattern is given by the fourth plot in which is depicted the P and SV waves omitted at the typical teleseismic takeoff angle, $\theta = 15°$.

It is clear that the orientation of the prestress will strongly influence the ratio of the P and S waves directed into the teleseismic field. It is useful to look at the orientation at which the greatest enhancement of S waves will occur; that is, the orientation at which the S wave lobe is directed vertically. Such an orientation is given by rotating the prestress field of Fig. 3.18 by 45° about the x_2 axis, then by 45° about the x_1 axis. The result is a prestress field that, in earthquake parlance, has strike, dip and plunge of 90°, 45°, 45°. Using the theory worked out by Minster (1974) for rotating the multipole coefficients, we find the new nonzero quadrupole coefficients are $A^{(4)}_{\quad}(\omega) = 0.2\ A^{(4)}_{\quad}(\omega) = -1.5\ A^{(4)}_{\quad}(\omega)$ for the P wave and $A^{(2)}_{\quad}(\omega) = 3B^{(1)}_{21}(\omega) = -B^{(3)}_{21}(\omega) = -6A^{(2)}_{22}(\omega) = -2B^{(1)}_{22}(\omega) = 6B^{(3)}_{22}(\omega)$ for the S wave. For this orientation the one second spectral component of the S wave displacement is about 4.0 times as large as the corresponding P wave displacement along the teleseismic takeoff angles.

We have now constructed two sources consisting of an explosion in tuff plus tectonic release. The tectonic release component is rather large, perhaps providing an upper bound to what may be encountered. In one case, the prestress field is horizontal, while in the second it is rotated to maximize the sP phase on the teleseismic record. Let us characterize the two sources by the ratio of the displacement along the direction marked P to the direction marked sP in the takeoff angle radiation patterns of Fig. 3.14. This ratio will be denoted P/SV.

Having constructed these sources, let us now study the resulting teleseismic short period P wave record. Let the explosion be buried at a depth of 400 meters in a typical NTS crustal structure. A series of seismograms at an epicentral distance of 4,000 km are shown in Figs. 3.19 - 3.20 where T/Q = 1.1 was used.

In Fig. 3.20 two crustal structures are used, one with the tuff-hard rock interface at 2.5 km and one with it at 0.7 km. Seismograms for both sources, that with the prestress horizontal (P/SV = 2.0) and that for which the prestress field was rotated to optimize the sP phase (P/SV = 0.25), were computed. The top seismogram shows the effect of ignoring reverberations in the crust; that is, only the P, pP and sP phases are included. For the P/SV = 2 source the sP phase is too small to have any appreciable effect on the record. In the second synthetic seismogram crustal reverberations are included, having a major effect on the pulse shape and m_b.

The second and third records of Fig. 3.20 give a direct comparison of the two sources. Only the orientation of the prestress field differs between the two but the change in m_b of nearly 0.2 units is significant. Finally, the last record indicates the possible importance of the tuff-hard rock interface. Note the deep second trough, a peculiar characteristic of several of the observed records shown in Fig. 3.1.

In Fig. 3.21 we compare the pure explosion to the explosion plus tectonic release. The tectonic release component is expected to represent an upper bound for the contribution to the teleseismic short period P wave record. Three slightly different crustal models are compared; model B of the previous figure, the same model with the tuff-hard rock interface at 1 km, and a model in which the velocity transition is less abrupt. The difference between the three

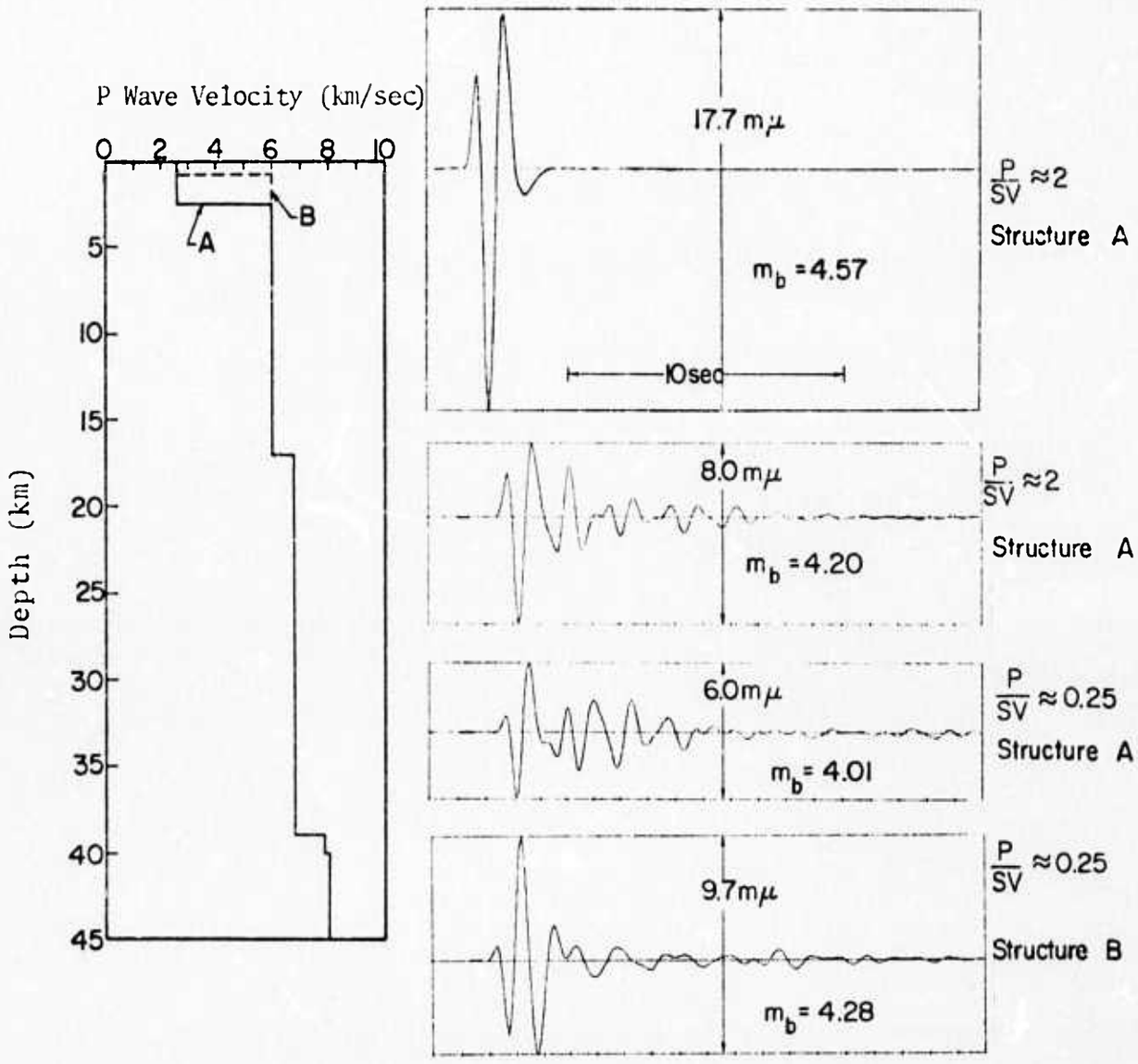


Figure 3.20. Synthetic seismograms at an epicential distance of 4,000 km for an explosion plus tectonic release in NTS tuff. Attenuation was characterized by T/Q = 1.1 and the explosion depth of burial was 0.4 km. The indicated m_b values were computed in the conventional way from the maximum phase.

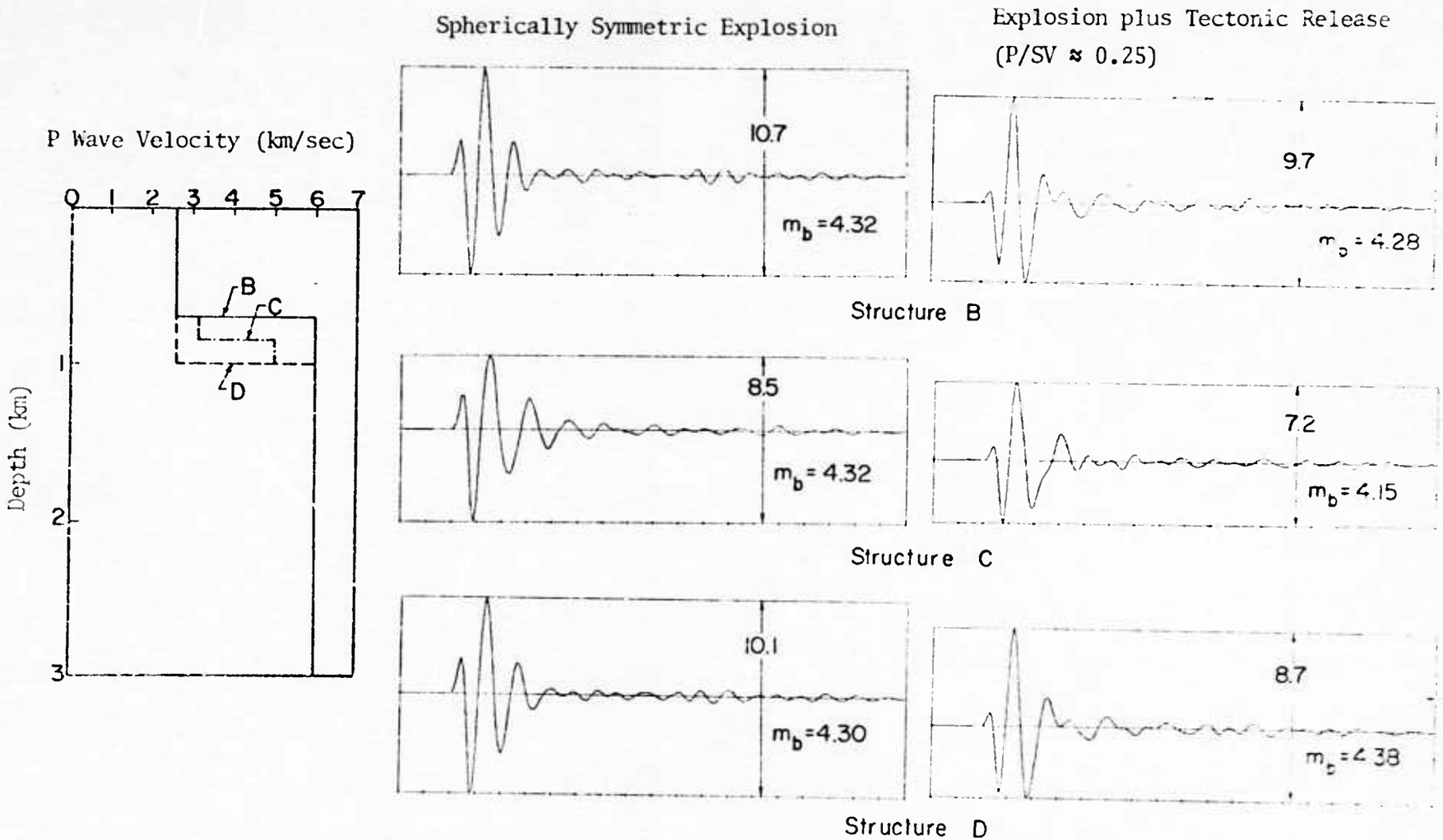


Figure 3.21. A comparison of a pure explosion to the same explosion plus a large tectonic release component for three similar near source crustal structures. The indicated m_b values were computed in the conventional way.

cases is not dramatic, but indicates that the presence of a sharp velocity discontinuity is more important than its exact location.

Finally, these few examples seem sufficient to conclude that only under optimal circumstances can tectonic release have a noticeable effect on m_b and the teleseismic P wave record.

IV. VARIABLE FREQUENCY MAGNITUDE DISCRIMINANT

4.1 INTRODUCTION

During the past several months we have been actively engaged in the development and testing of techniques for improved discrimination between earthquakes and both single and multiple underground explosions. As reported previously (Savino and Archambeau, 1974; Bache, et al., 1974), this program has resulted in the formulation of an extremely promising and very effective variable frequency magnitude (VFM) discriminant which exploits spectral differences between earthquakes and explosions. To date our attention has focussed on the application of the VFM technique to short period body waves from events at teleseismic distances from recording sites. As will be shown, obviating the requirement for recording small explosions results in an extended magnitude range over which the VFM discriminant can be applied. Complete separation of earthquake and explosion populations is achieved down to event magnitudes, m_b, in the range 4.0 to 4.5.

Following a brief description of the VFM technique, the results of its application to a large population of shallow and deep focus events recorded at LASA and the original Oyer subarray in Norway will be described. Finally, the VFM technique will be tested for its effectiveness as a discriminant on a simulated multiple explosion similar to the scenario proposed by Kolar and Pruvost (1975).

4.2 TECHNIQUE

The variable frequency magnitude discriminant, originally proposed by Archambeau, et al. (1974), is designed to exploit spectral differences between earthquakes and underground explosions. Essentially, the VFM technique consists

of a comparison of a magnitude measurement $m_b(f_1)$ at a relatively low frequency (e.g., f_1 = 0.45 Hz) to a magnitude measurement $\bar{m}_b(f_2)$ at a higher frequency (e.g., f_2 = 2.25 Hz). The body wave magnitude $\bar{m}_b$ is defined as the log of the amplitude of the output from a narrow-band (high Q) phaseless filter, centered at frequency f_c, plus a distance correction factor $\bar{B}$. That is

$$\bar{m}_b = \log_{10}\left[\frac{A_M}{T_c}\right] + \bar{B} \quad , \tag{4.1}$$

where the center period $T_c = 1/f_c$ and A_M is the maximum amplitude of the envelope of the filter output. The filters employed are digitally constructed in either the time domain (recursive) and/or frequency domain. The recursive filter is made phaseless by filtering an original time series in both the forward and backward time sense and summing the two results.

Examples of narrow-band recursive filter outputs for a presumed Eurasian explosion and a shallow earthquake recorded by the Oyer subarray in Norway are shown in Fig. 4.1. The top traces on the right- and left-hand sides of this figure correspond to the unfiltered best beam recordings of the P-wave trains, preceded by about 30 seconds of background noise, from the earthquake and presumed explosion, respectively. Note the enhancement of the high frequency (f_c = 6.0 Hz) filter output versus the low frequency (f_c = 0.3 Hz) filter output for the presumed explosion signal as compared to the filter outputs for the earthquake signal. The $\bar{m}_b(f_c)$ estimates for these events would be based on the maximum amplitudes of the envelopes of the filter outputs at the corredponding f_c's. As an example, the $\bar{m}_b$ (6.0 Hz) estimate for the presumed explosion would be based on the amplitude

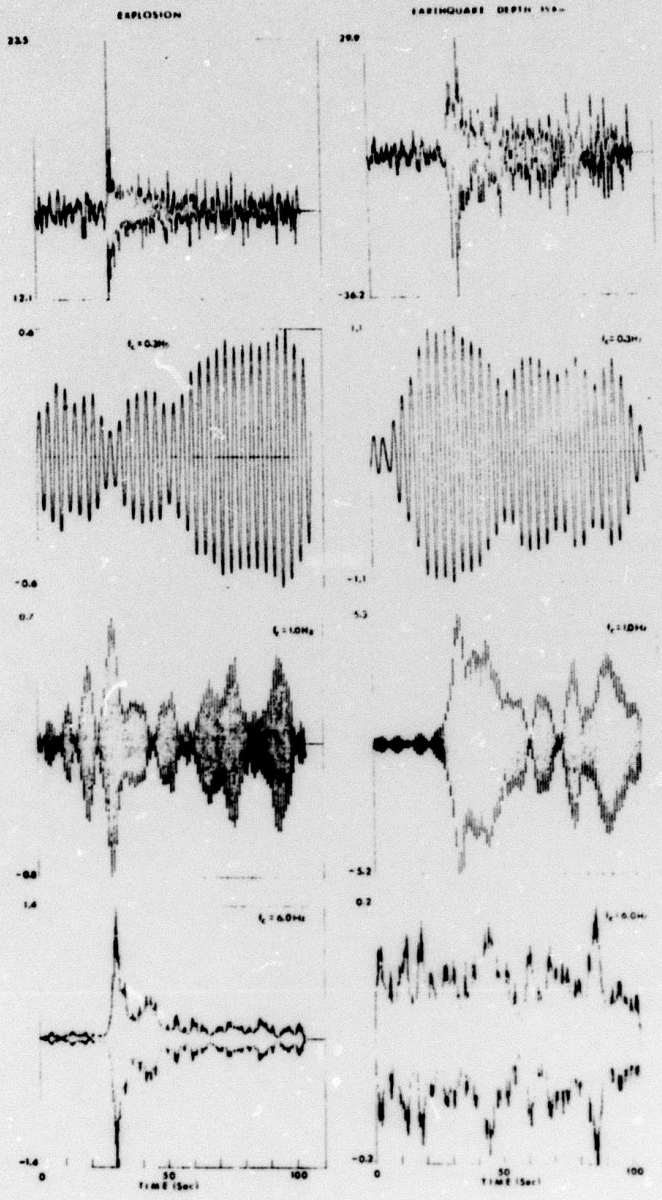


Figure 4.1. Examples of narrow band filter outputs at three center frequencies (0.3 Hz, 1.0 Hz and 6.0 Hz) for an explosion (left-hand side) and a shallow earthquake (right-hand side).

of the envelope of the f_c = 6.0 Hz filter output at about 30 seconds.

4.3 SHALLOW EVENTS RECORDED AT LASA

The data base employed in the first test of the VFM discriminant consists of LASA short-period recordings of P-wave trains from 34 presumed explosions and 156 earthquakes (Lacoss, 1969). Thirty of the presumed explosions originated within the mainland USSR, two in Novaya Zemlya, one (Longshot) in the Aleutians and one in the Sahara Desert. The earthquakes are distributed along the Alpide seismic belt, the Kuril-Kamchatka arc and the Arctic Ocean. The epicentral distances of these events range from 45° to about 100° with more than half of the events between 65° and 85° from LASA.

Figure 4.2 is a plot of spectral magnitude estimates, $\bar{m}_b(f_c)$, at a low frequency (f_c = 0.45 Hz) versus a high frequency (f_c = 2.25 Hz) for all 34 presumed explosions and those earthquakes in the data base that were reported in the Monthly Listings of Events, published by the USGS (formerly NOAA), as having shallow focal depths, h < 70 km. This figure clearly demonstrates the enriched high frequency content of the explosion body wave spectra as compared to the earthquake spectra. For instance, for a given value of $\bar{m}_b$ (0.45 Hz) the explosions exhibit $\bar{m}_b$ (2.25 Hz) values that are typically 0.6 to 1.0 unit larger than the $\bar{m}_b$ (2.25 Hz) values for earthquakes.

The high degree of discrimiantion of earthquakes from explosions evident in Fig. 4.2 is especially significant in view of the non-regionalization of the event population. The variety of tectonic settings of this event population ranges from relatively stable shield regions to seismically active oceanic arc systems. An indication that discrimination could be further enhanced by regionalizing the event population comes from the fact that for $\bar{m}_b$ (2.25 Hz) > 4.0 the two

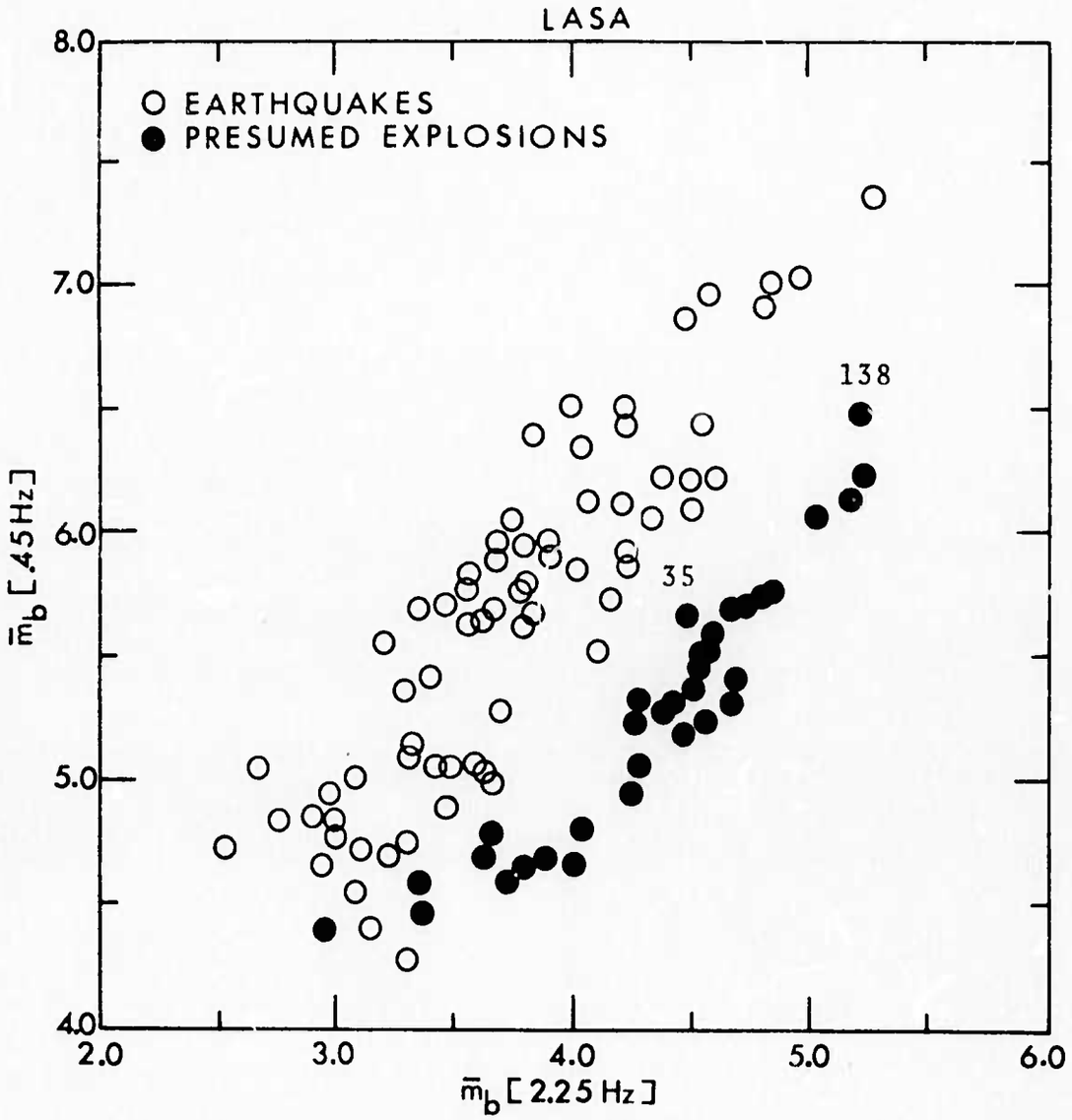


Figure 4.2. Spectral magnitudes, $\bar{m}_b$, computed at 0.45 Hz and 2.25 Hz. The presumed explosions numbered 35 and 138 occurred at Novaya Zemlya.

presumed explosions (#35 and #138) plotting closest to the earthquake population occurred at Novaya Zemlya. Several of the earthquakes that plot closest to the explosion population occurred along the Kurile-Kamchatka arc or at locations far removed from the explosion epicenters.

The apparent bending of the explosion population into the earthquake population at $\bar{m}_b$ (2.25 Hz) < 3.5 in Fig. 4.2 is mainly a result of microseismic noise inflating the low frequency (f_c = 0.45 Hz) magnitude estimates for the relatively small (signal-to-noise wise) explosions. In order to see the effects of noise contamination more clearly, magnitude estimates based on a series of low-frequency (0.3 to 0.6 Hz) narrow band filters versus the f_c = 2.25 Hz high frequency filter for a subset of the event population in Fig. 4.2 are shown in Fig. 4.3a-d. Note how the trends of the explosion population (x's) in the case of the low frequency (f_c = 0.3 and 0.4 Hz) filters, which are closest to the main concentration of noise power at LASA between about 0.1 to 0.3 Hz (Lacoss and Toksöz. 1967), exhibit rather abrupt bends near $\bar{m}_b$ (2.25 Hz) = 5.0 and flatten out at $\bar{m}_b$ (2.25 Hz) < 5.0. Examination of Fig. 4.3a-d indicates that the prevailing level and spectral distribution of microseismic noise at LASA sets gradually decreasing lower limits on the low-frequency magnitude estimates as the narrow band filter frequency increases from 0.3 Hz to 0.6 Hz, thereby moving away from the main noise band. In the case of Fig. 4.3d, for $\bar{m}_b$ (0.6 Hz) versus $\bar{m}_b$ (2.25 Hz), the trend of the explosion population is more nearly linear and parallel to the earthquake population over the entire magnitude range of the data. Noise contamination of the earthquake magnitude estimates in Fig. 4.3a-d is obviously not as serious a problem since the earthquake signals for a given value of $\bar{m}_b$ (2.25 Hz) are richer in low frequencies and show only a slight tendency to decrease in value as the filter frequency increases from 0.3 Hz to 0.6 Hz.

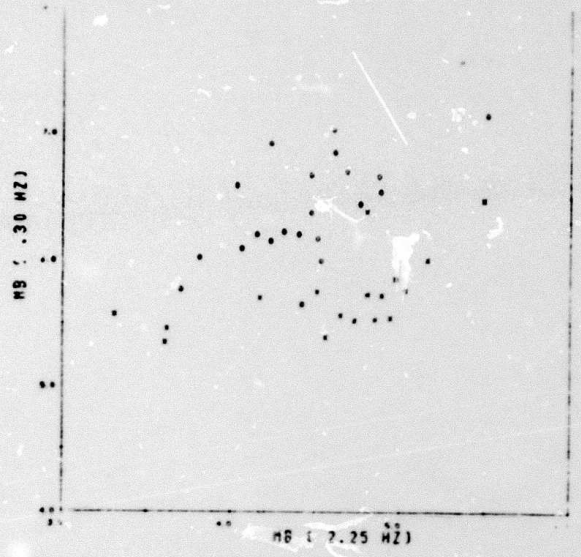


Fig. 4.3a

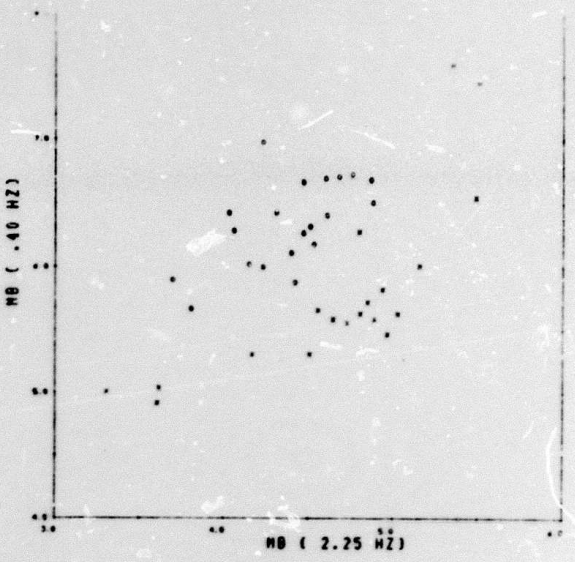


Fig. 4.3b

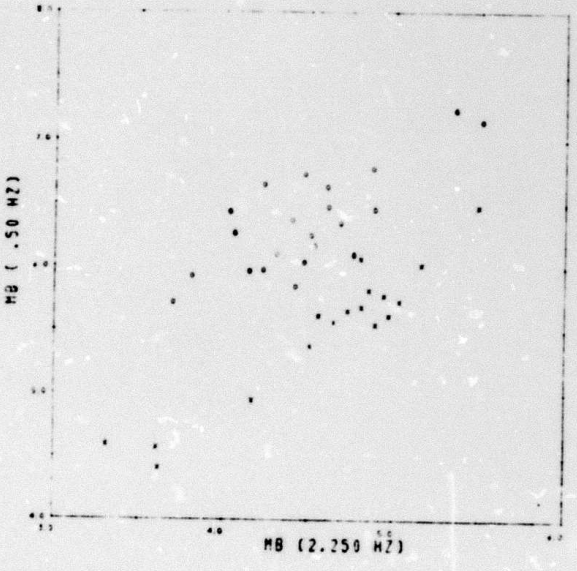


Fig. 4.3c

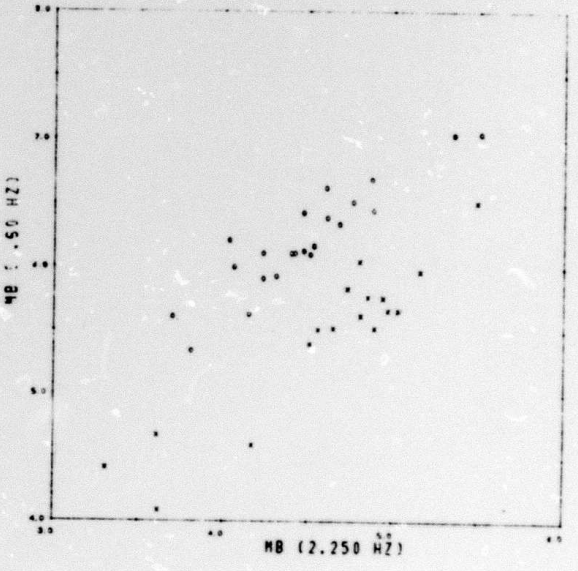


Fig. 4.3d

Figure 4.3. Spectral magnitude estimates for a subset of the LASA event population showing the effect of varying the f_c of the low frequency magnitude estimates.

On the high frequency end of the seismic bandpass it is the interplay of mainly three factors that limit the applicability of the VFM discriminant, as well as other short-period discriminants, to small magnitude teleseismic events recorded at LASA. These three factors are source spectrum, anelastic attenuation and high-frequency background noise at LASA. Definitive information on the source parameters of the earthquakes included in this data base are not available. However, the NOAA magnitudes of all the reported events are greater than $m_b = 4.7$. Thus, we will assume that the source spectra corner frequencies are less than 2.0 Hz and further that the source spectra are into the high frequency roll-off (ω^{-2} to ω^{-3}) for the high frequency range of interest here.

As is well known, for a fixed source-receiver distance, anelastic attenuation gives rise to an exponential decay with increasing frequency of the amplitudes of seismic waves. Thus the amplitudes of P-waves of frequency higher than 2.5 to 3 Hz from many of the events in the particular magnitude and distance range of interest here will be suppressed below the high frequency noise level at LASA.

The combined effect of these different factors on the magnitude estimates, $\bar{m}_b$, can be seen in Fig. 4.4a-f. In each of these figures the low frequency magnitude estimates are computed at the same frequency, $f_c = 1.75$ Hz to 3.25 Hz. Starting with the $f_c = 1.75$ Hz estimates in Fig. 4.4a, we see that the explosion and earthquake populations are not separated as much as in Fig. 4.2. This is undoubtedly due to the relatively close spacing of the high and low center frequencies, 0.5 Hz and 1.75 Hz. As the center frequency of the high frequency magnitude estimates increases (Figs. 4.4b-d), the separation of the event population increases. Finally, as the center frequency is further increased (Figs. 4.4e and f) the event populations begin to merge. The majority of

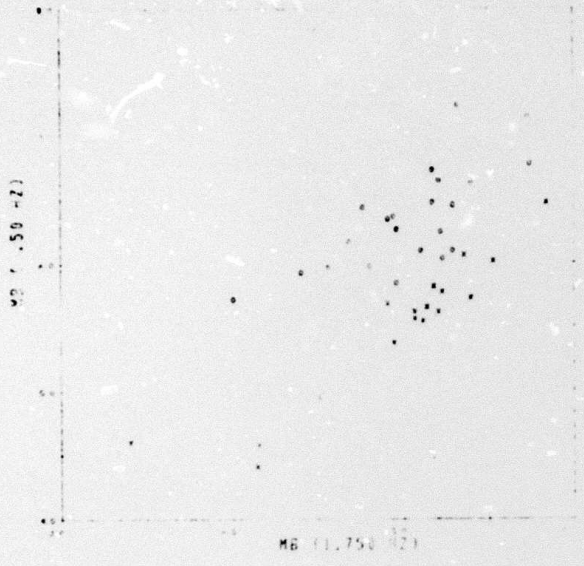


Fig. 4.4a

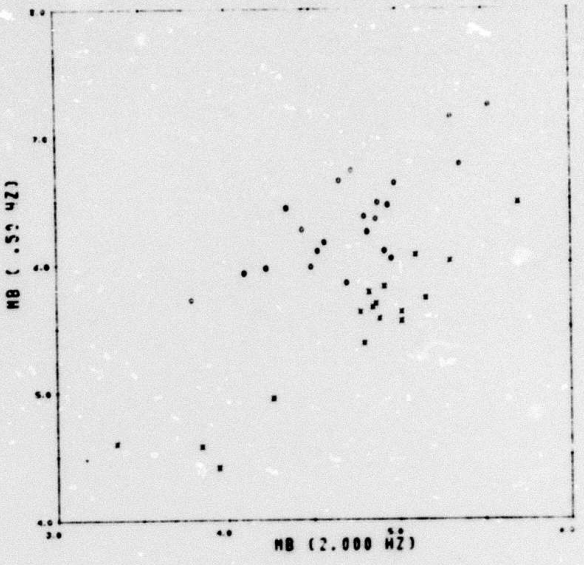


Fig. 4.4b

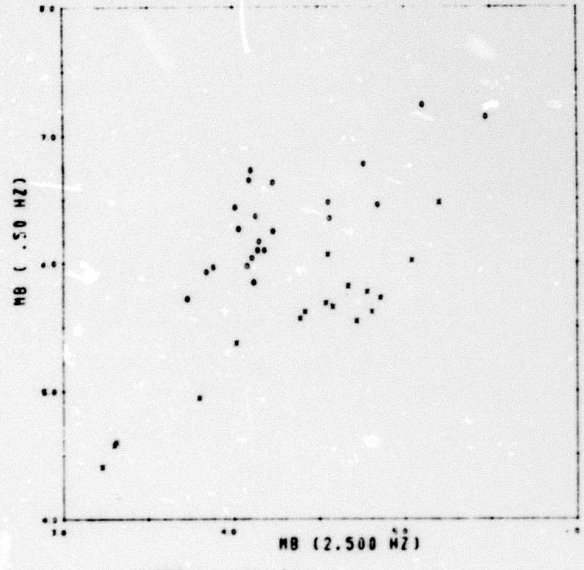


Fig. 4.4c

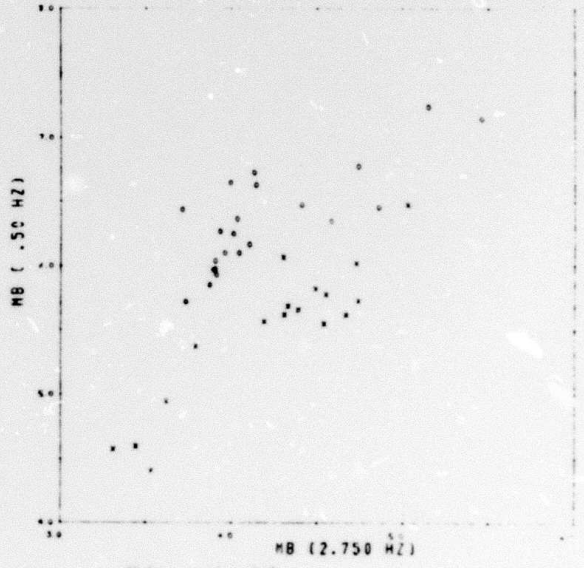


Fig. 4.4d

Figure 4.4. Spectral magnitude estimates for a subset of the LASA event population showing the effect of varying the f_c's of the high frequency magnitude estimates.

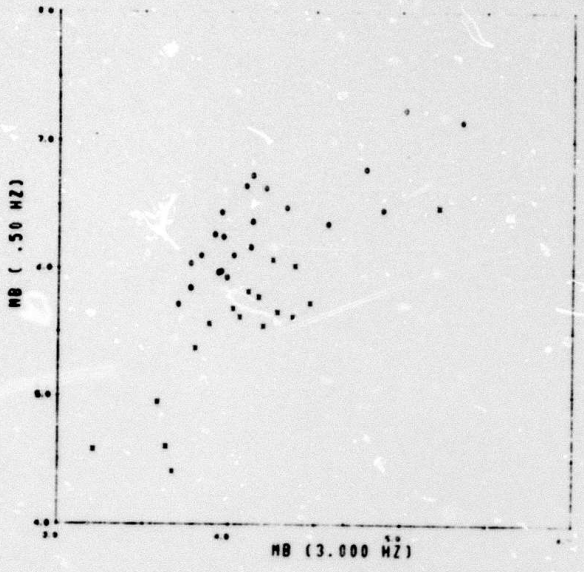


Fig. 4.4e

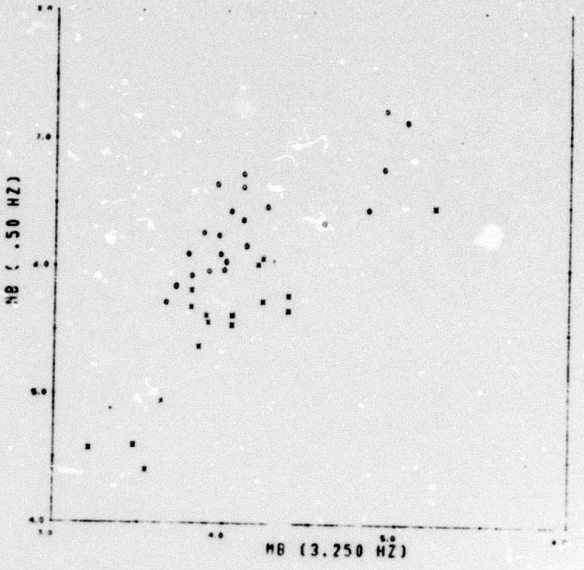


Fig. 4.4f

Figure 4.4 (Concluded)

earthquakes reach a high frequency lower noise limit of about $\bar{m}_b(f_c) = 4.0$ at $f_c = 2.5$ Hz while a comparable noise limit for the explosions is not reached until $f_c = 3.0$ Hz. Thus, while optimum discrimination would result for spectral magnitudes computed at frequencies (f_c) separated by a decade or more, noise and anelastic attenuation of the earth combine to constrain the useable bandwidth of frequencies in the case of the LASA data set to approximately one-half a decade.

4.4 DEEP EVENTS RECORDED AT LASA

Twenty events in the depth range 80 km to 580 km are included in the LASA data base. Magnitude estimates for these events based on narrow band filter outputs at the same center frequencies as in Fig. 4.2 are plotted in Fig. 4.5 and compared with the shallow earthquake and explosion populations which are contoured by the dashed and solid lines, respectively. All of the events with focal depths h > 300 km occurred beneath the Japan and/or the Kurile-Kamchatka arcs. The epicentral locations of the intermediate depth events range from the Aegean Sea, Rumania, Hindu Kush regions to the Japan and Kurile-Kamchatka arcs.

Deep earthquakes often fail to separate from explosion populations when examined with any of the discriminants, short-and/or long-period, proposed to date. As can be seen in Fig. 4.5, such is the case for several of the deep events examined with the VFM technique. Suggestions as to the reason for the lack of discrimination of many deep events range from impulsive source-time functions, small source-dimensions, and high-Q propagation path to the receiver. While the behavior of the deep events in Fig. 4.5 cannot be explained at this time, it should be noted that the majority of intermediate depth events lie within the bounds of the shallow earthquake population.

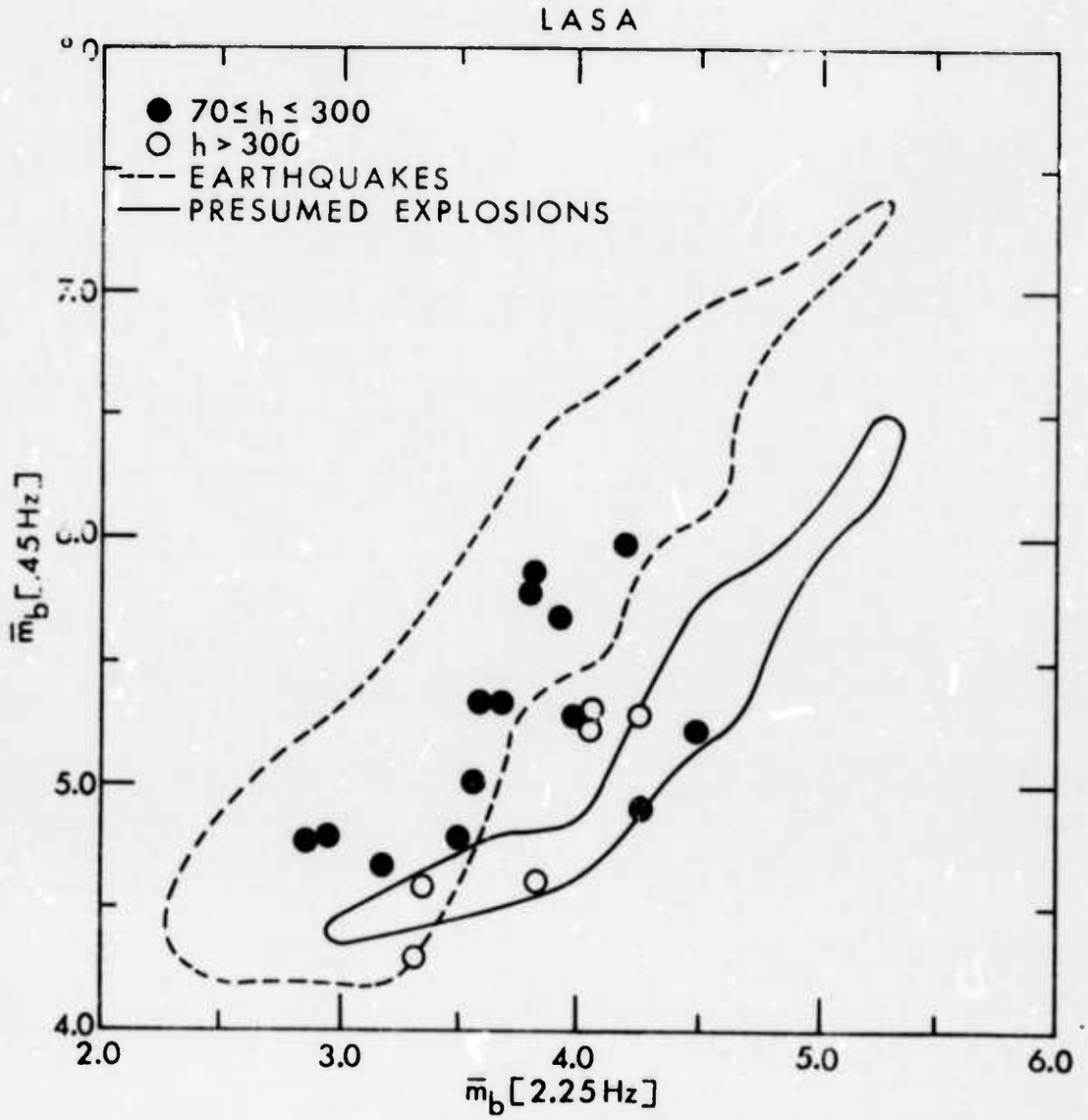


Figure 4.5. Spectral magnitude estimates of deep earthquakes recorded at LASA. The shallow earthquake and explosion populations plotted in Fig. 4.2 are contoured in this figure.

4.5 SHALLOW EVENTS RECORDED AT NORWAY

A subset of the event population recorded at LASA was also recorded by the limited Oyer array in Norway. The spectral magnitude discriminant was applied to this smaller population of events and the results are presented in Figs. 4.6 and 4.7. In Fig. 4.6, spectral magnitudes, $\bar{m}_b$, at 0.6 Hz and 5.0 Hz are given for shallow earthquakes (open circles) and presumed explosions (closed circles). Analogous to the results at LASA in Fig. 4.7, there is discrimination of events over most of the magnitude range of the events except for the smallest magnitude explosion.

The arrows attached to the explosion points indicate that the low frequency magnitude, $\bar{m}_b$ (0.6 Hz), is contaminated by noise. In Fig. 4.7 the output amplitudes from the narrow-band filters are corrected for noise and replotted. Comparing Figs. 4.6 and 4.7 it becomes clear that the cause of the bend in the explosion population toward the earthquake population at small magnitudes is the inflation of the low frequency explosion magnitudes by noise. Correction for this noise results in complete separation of the earthquake and explosion populations.

The effects of noise in different frequency bands can be seen in Fig. 4.8. In this figure the unfiltered time series corresponding to the smallest explosion recorded at Norway is plotted in the top-left frame. The remaining frames show the effect on the time series of the application of five narrow band filters of increasing center frequency (0.3 Hz to 6.0 Hz). The gradual emergence of the signal at $f_c > 1.0$ Hz is quite striking. The persistance of a high signal-to-noise ratio for this very small event probably results from the high-Q nature of the propagation path.

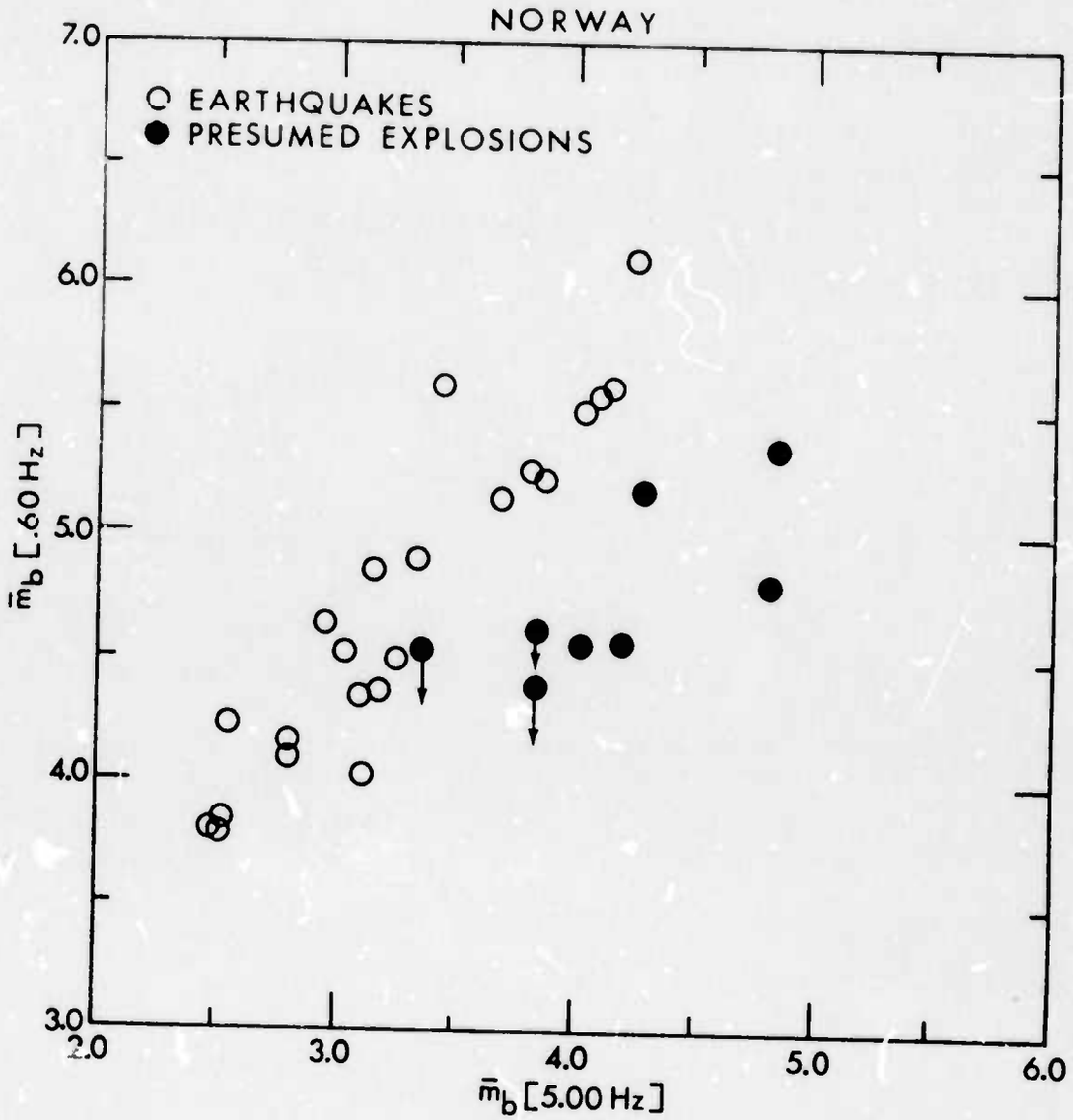


Figure 4.6. Spectral magnitude estimates at f_c = 0.6 Hz and f_c = 5.0 Hz for an event population recorded at the Oyer array in Norway.

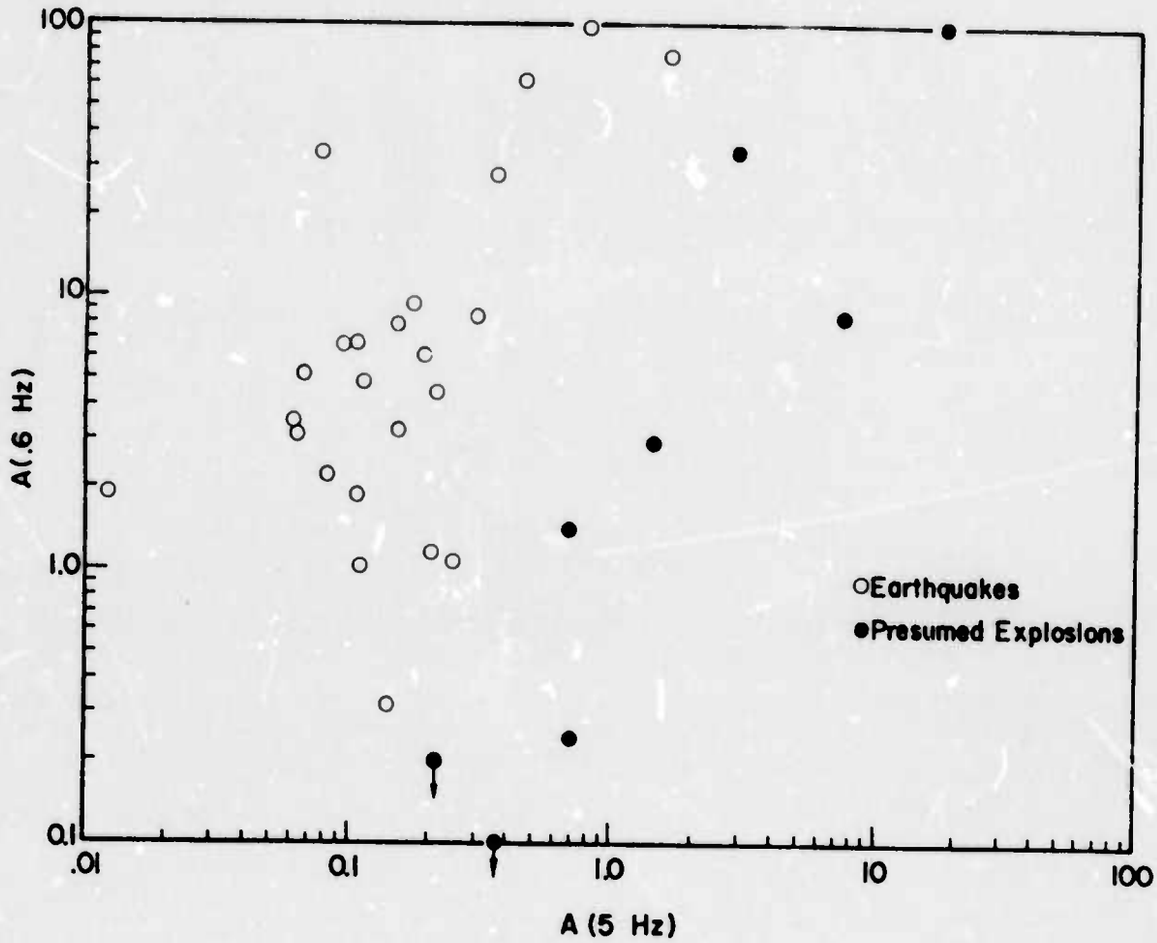


Figure 4.7. Filter amplitudes (maximum) with noise corrections for the same event population plotted in Fig. 4.6. Note the enhanced separation of the earthquake and explosion populations.

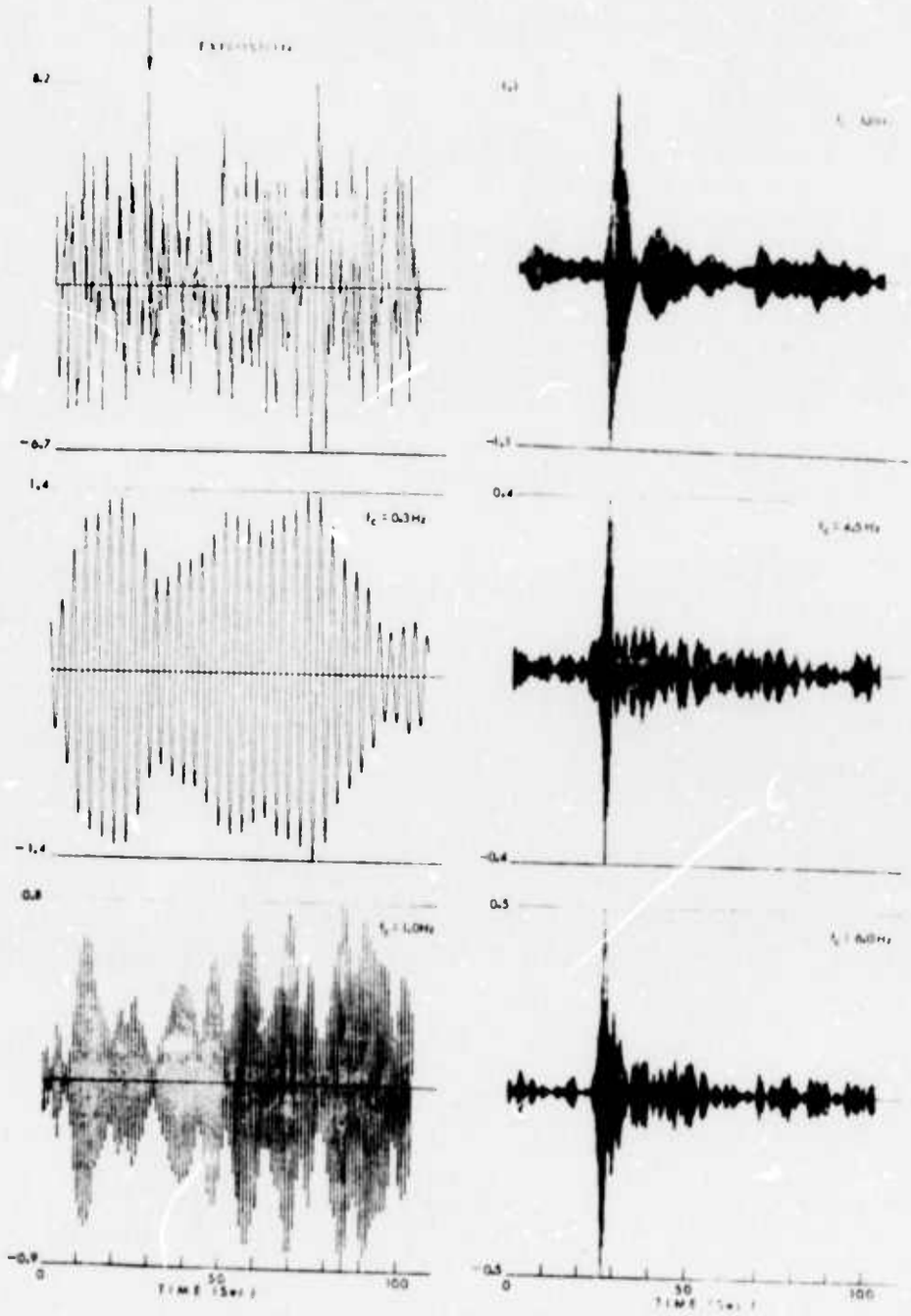


Figure 4.8. Examples of increasing signal-to-noise ratio for a presumed explosion (top-left frame) recorded at Norway with successive application of high frequency narrow band filters. Arrow at top denotes approximate arrival of the explosion P-wave on the unfiltered trace.

4.6 DEEP EVENTS RECORDED AT NORWAY

Eleven events in the Norway data base were assigned focal depths > 70 km. Amplitudes of narrow-band filter outputs with the same f_c's used in Figs. 4.7 and 4.8 were computed for these eleven events and are plotted in Fig. 4.9. The frequency dependent amplitudes were corrected for noise based on measurements taken before the onset of each event P-wave signal. The bounds of the shallow earthquake and explosion populations plotted in Figs. 4.7 and 4.8 are indicated in Fig. 4.9 by the broken and dashed curves, respectively.

As was the case with the deep events in the LASA data set shown previously in Fig. 4.5, the deep events recorded at Norway (Fig. 4.9) exhibit considerable scatter without any obvious pattern of behavior. While several of these deep earthquakes fail to discriminate in this figure they are really not as troublesome as they might seem since these events can often be identified as naturally occurring earthquakes on the basis of other information (e.g., hypocentral location using P, pP and/or sP travel times).

A rather dramatic example of the short-period spectral similarities between an explosion and a deep earthquake is shown in Fig. 4.10. Approximately 80 seconds of an unfiltered explosion time series and the output amplitudes of three narrow band filters (f_c = 0.3 Hz, 1.0 Hz and 6.0 Hz) applied to the time series are shown on the left-hand side of this figure. A similar sequence of pictures is shown on the right-hand side for a deep (h = 115 km) earthquake. Note how the signal-to-noise ratio of the narrow band filter outputs for both events increases as the center frequencies of the filters increase from 03. Hz to 6 Hz. Comparison of the spectral behavior of the deep earthquake in this figure with the shallow earthquake (h = 35 km) shown in Fig. 4.1 clearly

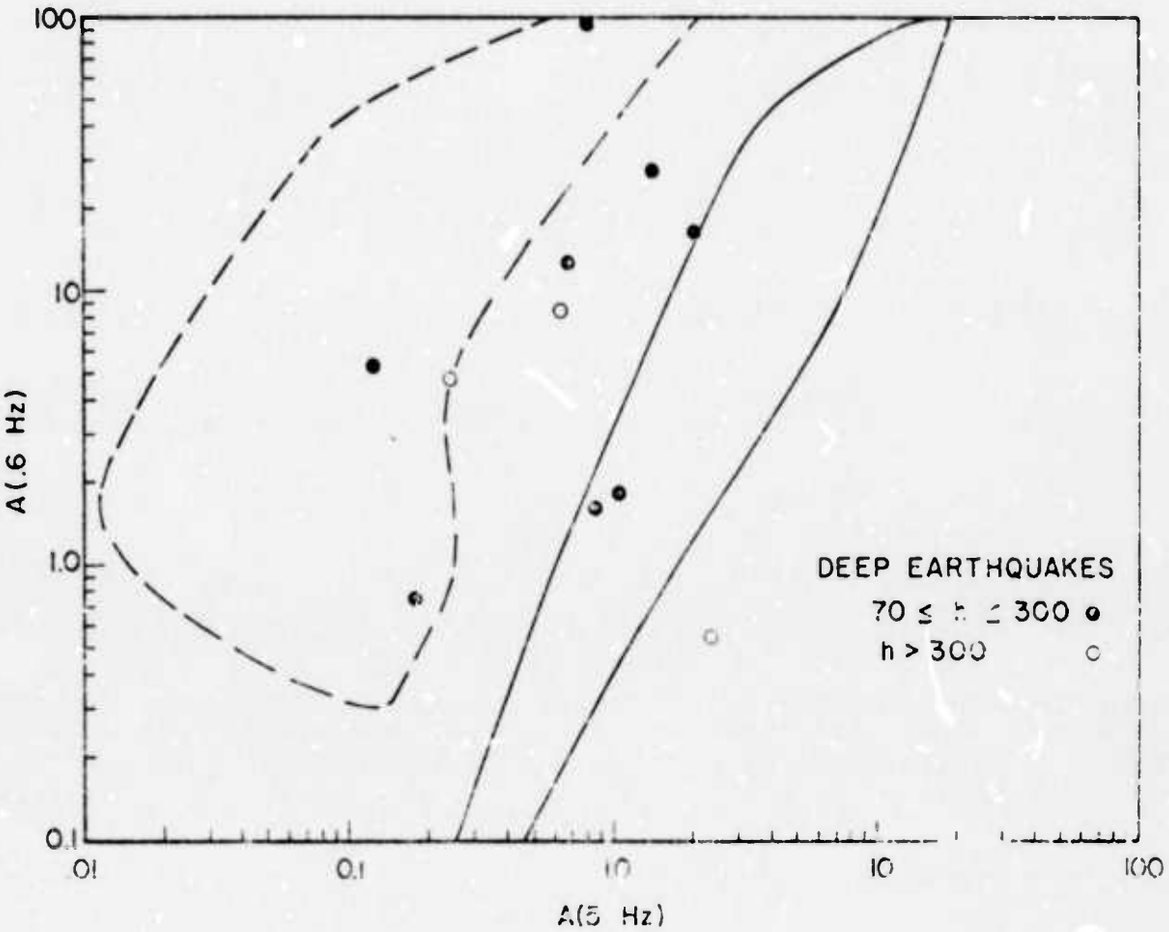


Figure 4.9. Amplitudes of narrow band filter outputs at two different frequencies for deep earthquakes recorded at Norway.

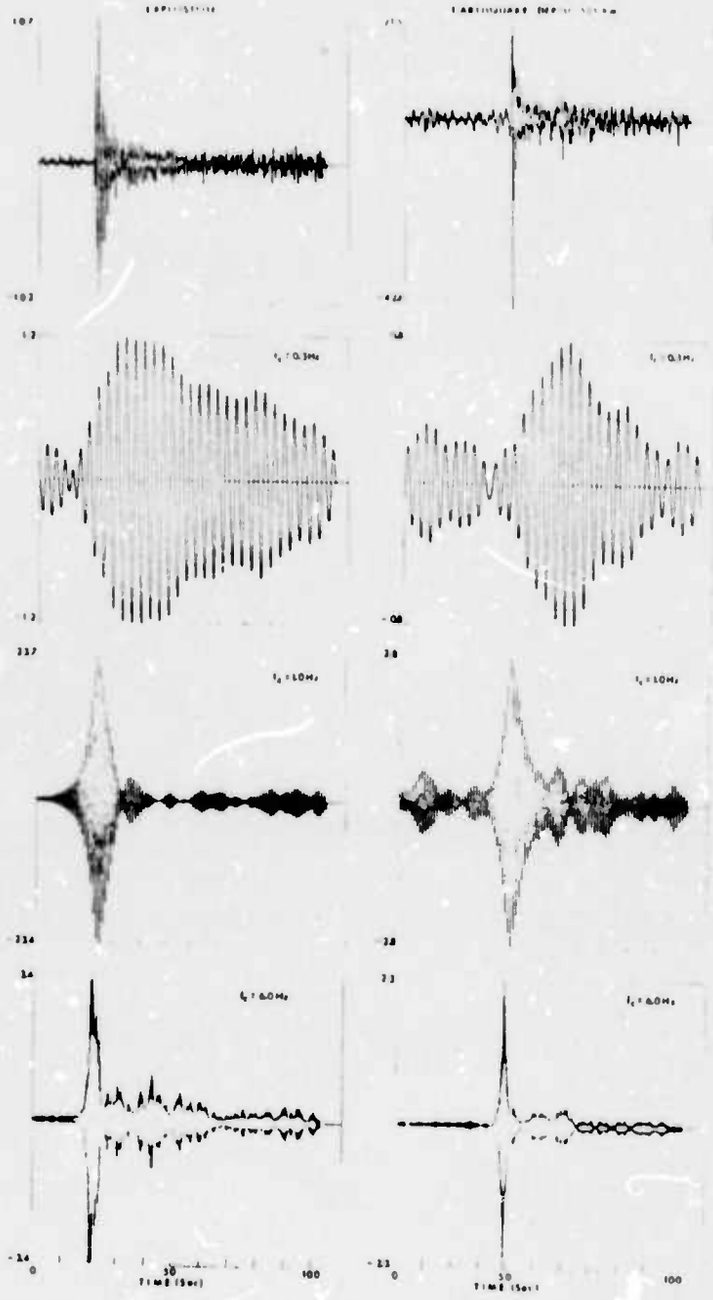


Figure 4.10. Narrow band filter outputs at three different center frequencies (f_c = 0.3 Hz, 1.0 Hz and 6.0 Hz) for an explosion (left-hand side) and a deep earthquake (right-hand side).

points out the far field spectral differences between these two types of events.

4.7 MULTIPLE EXPLOSION SCENARIO

The spectral magnitude technique is especially suited for identification and discrimination of multiple explosion sequences that are designed to appear earthquake-like in terms of conventional (M_s-m_b, depth of focus, complexity, first motion) discriminants. A multiple event scenario, somewhat similar to one proposed by Kolar and Pruvost (1975), was devised by superposing eight scaled seismograms of a presumed Kazakh explosion recorded at LASA. This explosion signature is shown on the bottom-center in Fig. 4.11.

The array of explosions and their relative yields were designed to produce earthquake-like seismograms over a wide range of azimuths. The particular array configuration (spacing and firing order) is indicated in the center of Fig. 4.11. Each seismogram comprising the multiple event was delayed in time relative to the first, and scaled in amplitude. The largest explosion in the scenario is the sixth event and is scaled to give the same teleseismic ground motion as the primary signal. The amplitude scaling for all eight explosions in the scenario was 1, 3.1, 5, 10, 10, 20, 15 and 12.5.

The composite seismograms resulting from the scenario are shown in Fig. 4.11 at five different azimuths (1-5) with respect to the shot array. The first point to be noted about these composite seismograms is that with the addition of noise to the beginning of each seismogram the first motions at azimuths 1, 3 and 5 would most probably be picked as rarefactions. Secondly, the complexity of each composite signal has been greatly increased over that of the primary signal.

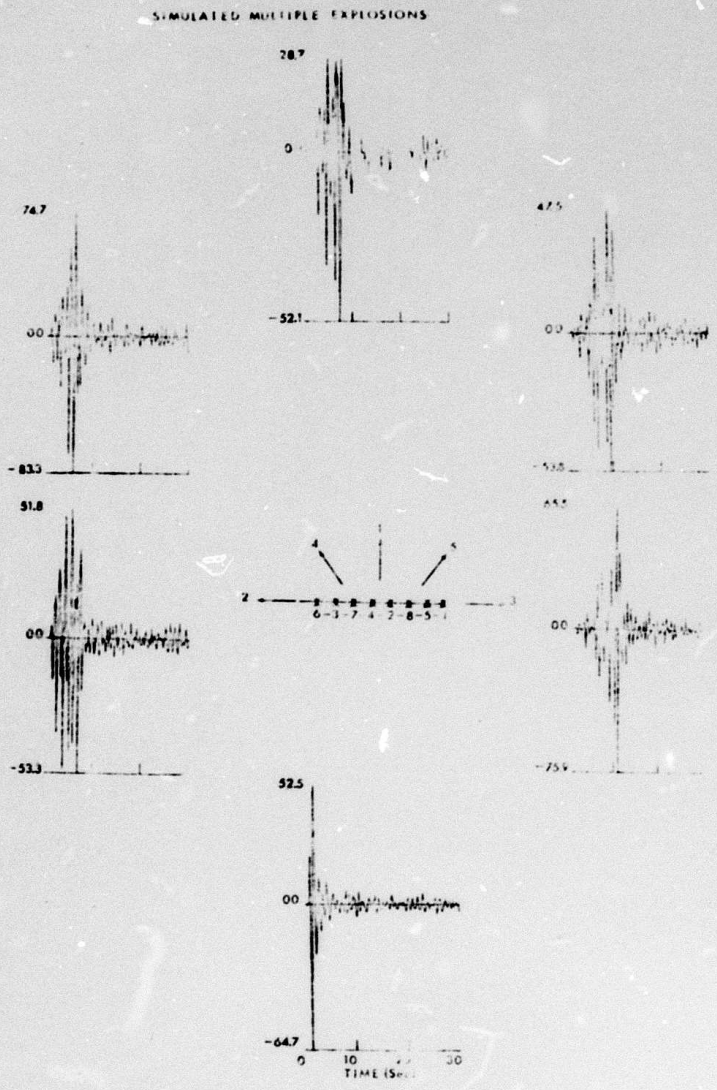


Figure 4.11. Primary explosion signature (bottom-center) used to make composite seismograms at five different azimuths from the array of eight explosions. The firing order and spacing of the explosions are indicated in the center.

Two factors work together to make the multiple event scenario appear earthquake-like on an M_s m_b basis. First an analyst making amplitude measurements to be used for m_b determinations in the conventional manner (maximum amplitude within the first 3 or 4 cycles) would undoubtedly pick amplitudes corresponding to the earlier smaller explosions in the sequence. On the other hand the M_s measurements would be mainly based on the superposed surface waves from the three large yield explosions occurring late in the sequence. The net result would be a reduced m_b and an enhanced M_s resulting in the scenario moving into the earthquake population on an M_s-m_b plot.

Application of the spectral magnitude technique, however, results in complete discrimination of the multiple explosion scenario. In Fig. 4.12 the spectral magnitude estimates, computed for the five azimuths indicated in Fig. 4.11 are indicated by the x's. A most significant result in Fig. 4.12 is that the spectral magnitude estimates of the multiple explosion sequence cluster around the estimates of the primary signal used in the construction of the scenario (the closed circle immediately to the right of x-1). This means that the VFM technique has based the magnitude estimates on the largest amplitude arrival in the wavetrain, corresponding to the largest yield explosion in the sequence. This is a very important result for yield determination of both single and multiple explosions.

4.8 SUMMARY

A variable frequency magnitude technique designed to exploit spectral differences between earthquakes and explosions was developed and applied to a large population of Eurasian events recorded at LASA and a limited array (Oyer) in Norway. The magnitude estimates are based on the output amplitudes of variable frequency narrow band phaseless filters

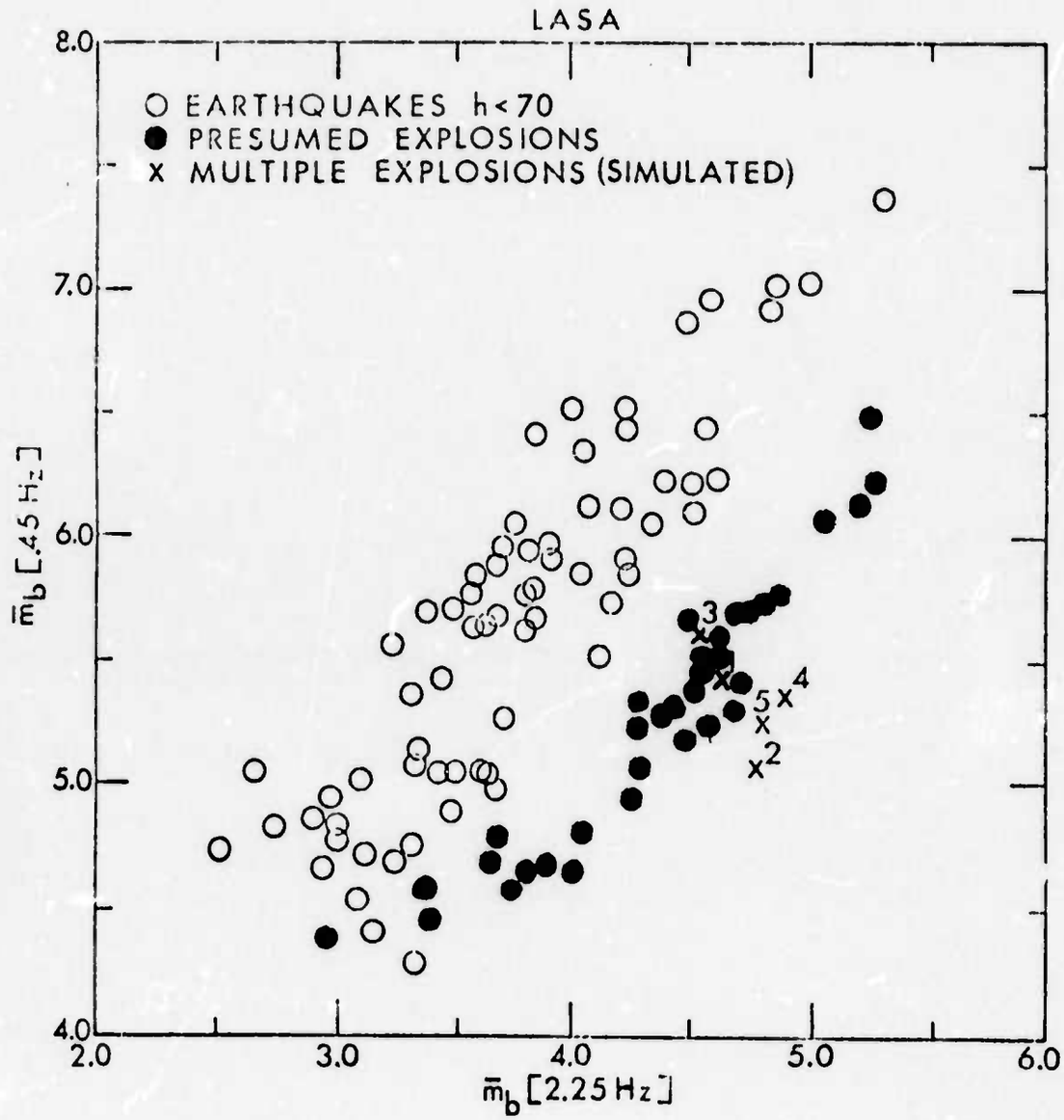


Figure 4.12. Spectral magnitudes for same event population and filter parameters as in Fig. 4.2 with estimates for multiple explosions (x's) showing complete discrimination.

applied to short period recordings of body waves. The most significant results pertaining to event identification, discrimination and yield determination obtained with this discriminant are the following:

1. Complete and positive discrimination of earthquakes and explosions down to explosion magnitudes of LASA $m_b = 4.2$.
2. Multi-azimuth discrimination of a multiple explosion scenario with the correct identification of the largest yield explosion in the scenario.
3. Simultaneous discrimination at a single recording site of events, both earthquakes and explosions, distributed over a wide geographical region.

V. MULTIPLE DISCRIMINANT TEST

5.1 INTRODUCTION

During the past 10 years or more, several different techniques for discriminating between earthquakes and underground explosions have been proposed. These techniques, which have met with varying degrees of success, depend upon differences in the time- and/or frequency-domain between earthquake and explosion signals. In this section of the report we will compare the effectiveness of the VFM discriminant to the following proposed discriminants; complexity, spectral ratio, higher moments of frequency and m_b-M_s. A most important aspect of this comparison is that all the discriminants are applied to the same data base: the large Eurasian population of events recorded at LASA.

5.2 COMPLEXITY

In the early 1960's the research group at Blacknest proposed that a measure of the complexity of the P-wave trains from earthquakes and underground explosions could possibly serve as a technique for identifying these two types of events (Thirlaway, 1963; Carpenter, 1963 and 1964). They noted that teleseismically recorded P-wave signals from underground explosions were often simple, consisting of one or two cycles of relatively large amplitude followed by a tail or coda of much lower amplitude. P-wave signals from earthquakes, however, often consisted of a series of arrivals of comparable amplitude spread over several tens of seconds. The original definition of complexity (Carpenter, 1964) involved comparison of the inverse ratio of the signal energy in the first five seconds of the P-wave train to the signal energy in the subsequent 30 seconds. This definition was applied to the cross-correlation function between two steered

beams, formed from different portions of an array of seismometers.

In the late 1960's, members of the Lincoln Laboratory research group (Kelly, 1968; Lacoss, 1969) proposed a modified method of computing signal complexity and applied it to Eurasian events recorded at LASA. In particular, Lacoss made linear complexity measurements on best LASA beams for bandpass filtered (0.6 Hz to 2.0 Hz) P-wave signals using the following definition of complexity:

$$C_L = \int_5^{35} |x(t)|dt \Big/ \int_0^5 |x(t)|dt \ , \qquad (5.1)$$

where x(t) is the time series corresponding to the best filtered beam, the time-origin is chosen at the event onset, and in practice the integrals are replaced by summations in the case of digitized data samples.

Using Eq. (5.1), values of complexity were computed for the same population of shallow earthquakes and explosions plotted in Fig. 4.2. These complexity values are plotted in Fig. 5.1 versus m_b (LASA). While many of the earthquakes separate by nearly an order of magnitude from the explosion population, there is significant overlap of the two populations over the entire magnitude range. Thus, in terms of complete separation of event populations it is quite obvious that the VFM discriminant (Fig. 4.2) is superior to complexity.

The behavior of complexity in the case of very small magnitude events is controlled by background noise. As the magnitudes, and hence the signal-to-noise ratios, of events decrease, the values of complexity for both earthquakes and explosions (Fig. 5.1) approach a value of $C_L = 6$. This is to be expected since in the limiting case of pure noise (assumed to be stationary) C_L from Eq. (5.1) becomes equal to the ratio of the number of equal time intervals; namely

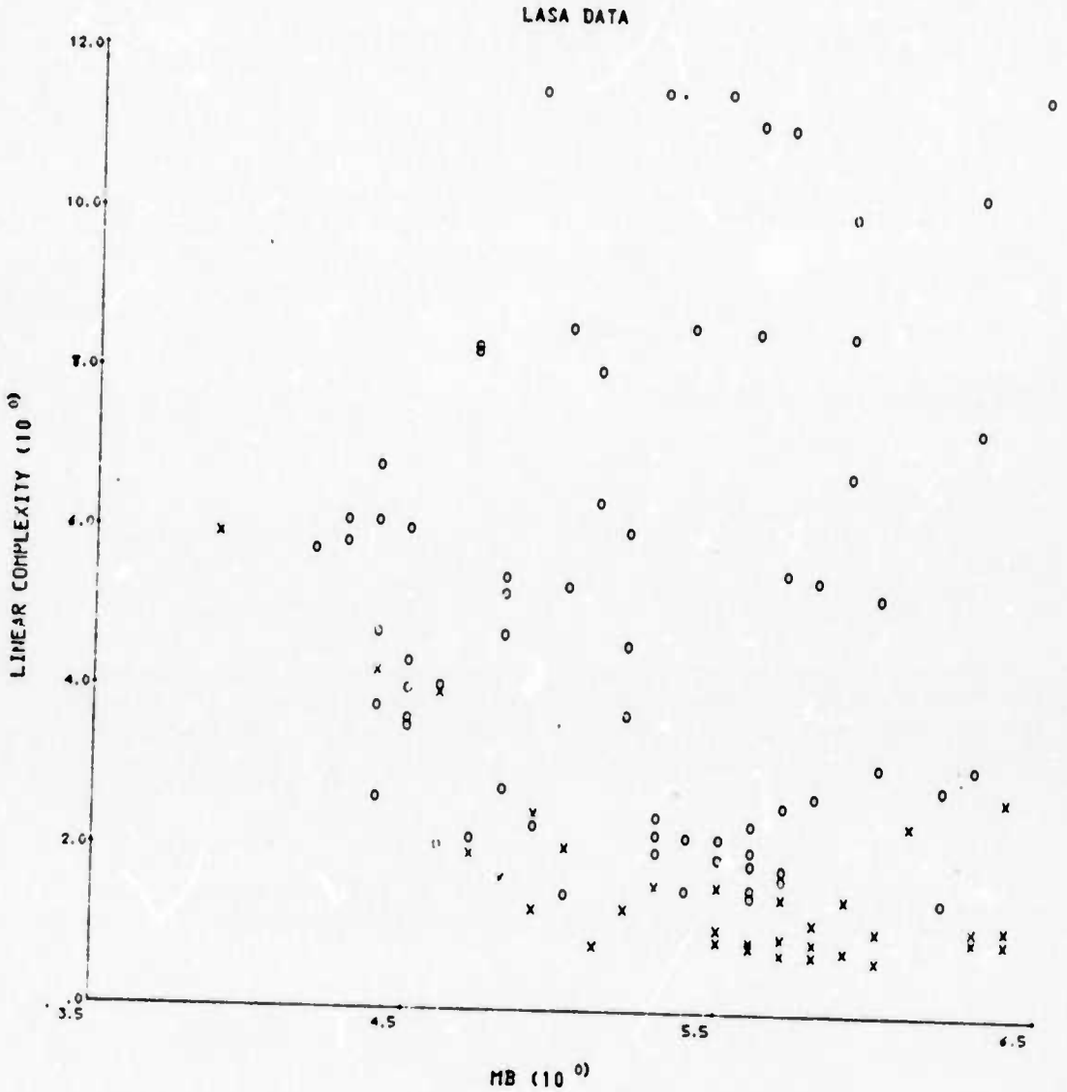


Figure 5.1. Complexity as a function of LASA m_b for all reported shallow earthquakes (O's) and presumed explosions (X's) in the data base.

6/1 for the 0 to 5 sec and 5 to 35 sec time intervals considered here.

Complexity values computed for the two large presumed explosions at Novaya Zemlya (C_L = 2.4, m_b = 6.1; C_L = 2.7, m_b = 6.4) are greater than values for explosions of comparable magnitude (Fig. 5.1) detonated in different geographical regions. The relatively complex character of P-wave trains from events at Novaya Zemlya has been studied by other investigators (Douglas, et al., 1973; Frasier and Yang, 1975). The explanation that appears most consistent with all the available data is that body waves are scattered in the source region and travel relatively high-Q paths to receivers as compared to the direct P-wave. Whether or not this explanation is correct, the fact is that the event population would have to be substantially regionalized for complexity versus m_b to be an effective discriminant.

5.3 SPECTRAL RATIO

Kelly (1968) and Lacoss (1969) evaluated a spectral ratio criteria that discriminates between earthquakes and explosions based on recordings of short period P-waves. The definition of spectral ratio employed by these investigators is:

$$R = \frac{\sum_{i=p}^{q} A(f_i)}{\sum_{j=\ell}^{m} A(f_j)} \qquad (5.2)$$

where $A(f_k)$ are the spectral estimates at frequencies f_k based on 10 to 20 seconds of data beginning with the onset of the P-wave. In practice the numerator is summed over

high frequency components and the denominator over low frequency components. Several combinations of frequency parameters (ℓ, m; p, q) and two time windows (12.8 and 6.4 secs) were tested using the LASA data base. A sampling of the results, including those combinations that yielded the best discrimination, are shown in Figs. 5.2a-c. The frequency bands for the results in Fig. 5.2a are similar to those used by Lacoss (1969), while the data in Figs. 5.2b and c shew the results of emphasizing the high frequency (> 2 Hz) portion of the event spectra.

Examination of Figs. 5a-c indicates that, as in the case of the VFM discriminant, as the separation of the high and low frequency bands increases, discrimination is enhanced. The degree of discrimination achieved in the case of Fig. 5.2c is in fact comparable to that achieved with the VFM technique (Fig. 4.2). This is not terribly surprising since the VFM discriminant can be considered as a finely tuned (frequency-wise) spectral ratio technique. The major advantage of the VFM over the spectral ratio discriminant is the fact that the VFM technique, in addition to providing for event identification, can be used for determination of explosion yields. The large amount of scatter of the explosion populations in the case of spectral ratio versus m_b (Figs. 5-2a-c) with, if anything, an inverse relationship between spectral ratio and event size, would seem to preclude the possibility of using this technique as an explosion yield indicator.

5.4 HIGHER MOMENTS OF FREQUENCY

Recently Canadian researchers (Anglin, 1971; Weichert, 1971; Manchee, 1972) proposed combinations of time and frequency domain algorithms as short period discriminants between earthquakes and underground explosions. These algorighms are

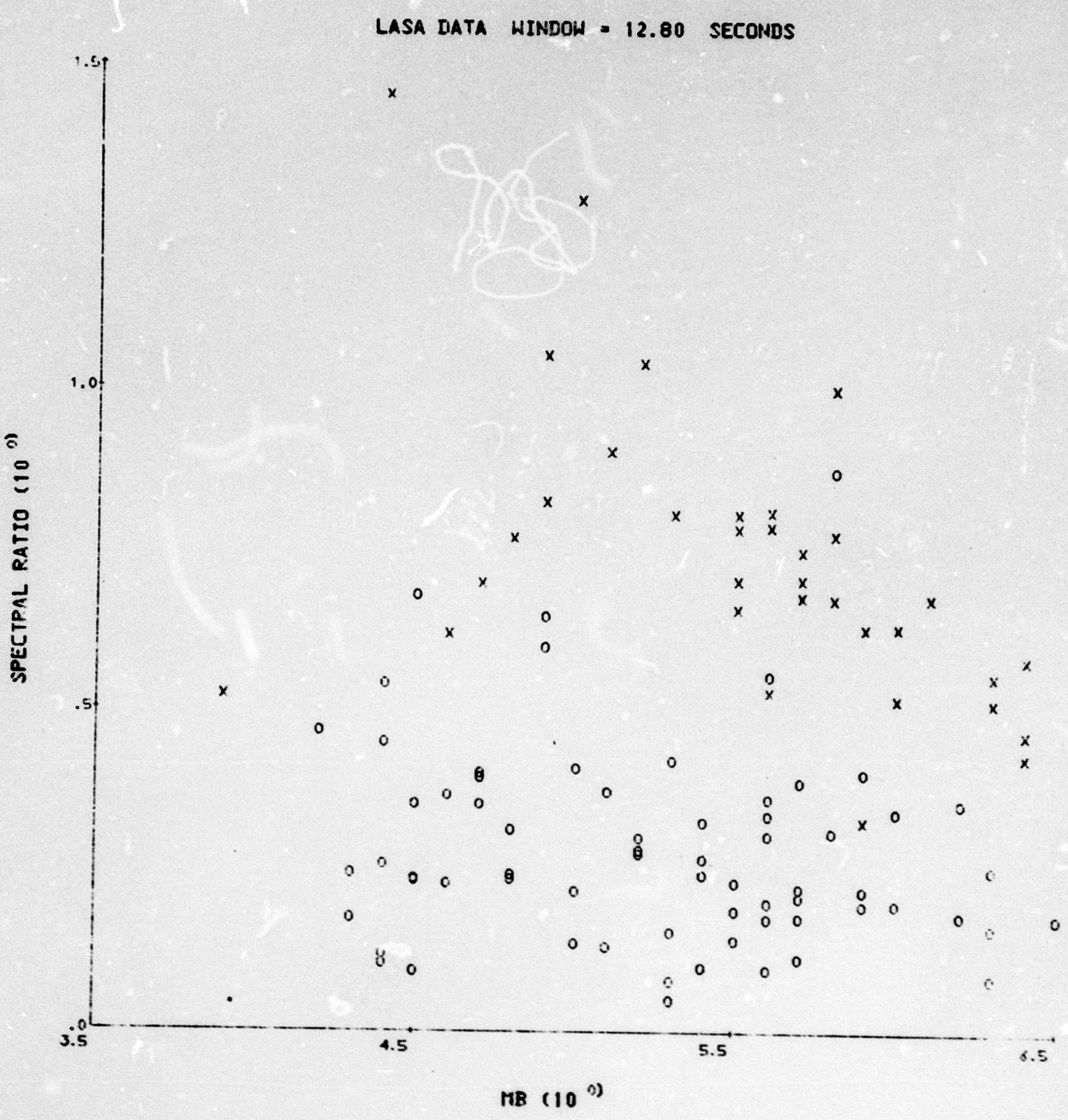


Figure 5.2a. Spectral ratio versus LASA m_b for the Eurasian data base. Shallow earthquakes are indicated by O's and presumed explosions by X's. In this case ℓ = 12 (0.47 Hz), m = 25 (0.98 Hz), p = 37 (1.45 Hz) and q = 50 (1.95 Hz).

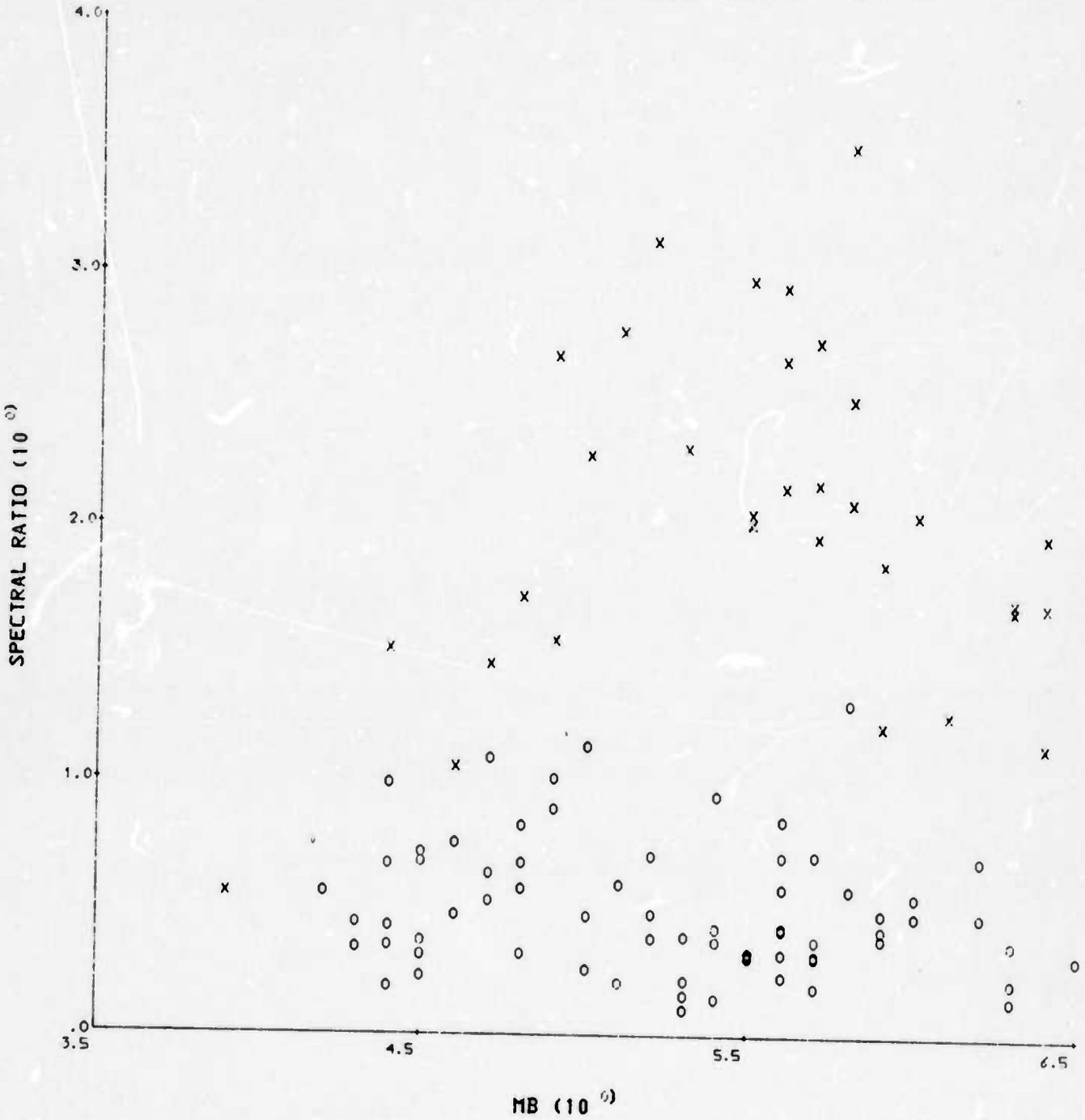


Figure 5.2b. Spectral ratio versus LASA m_b. In this test ℓ = 8 (0.31 Hz), m = 19 (0.74 Hz), p = 37 (1.45 Hz) and q = 64 (2.50 Hz).

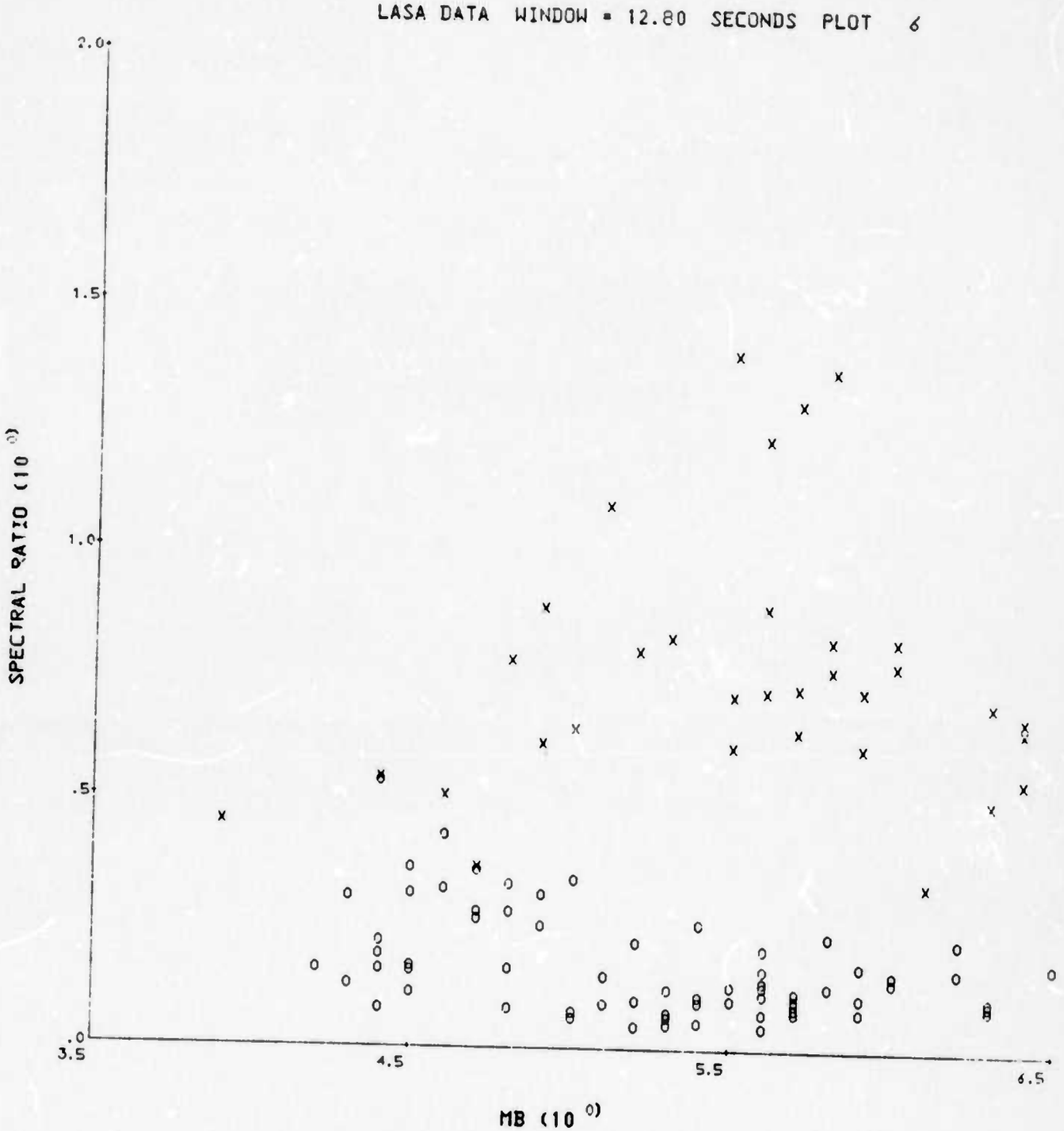


Figure 5.2c. Spectral ratio versus LASA m_b. In this test ℓ = 8 (0.31 Hz), m = 19 (0.74 Hz), p = 51 (1.99 Hz) and q = 76 (2.97 Hz).

referred to as the third moment of frequency (TMF) and modified moment of frequency (MMF). The definition of MMF given by Manchee includes TMF and is

$$MMF = J\left(\frac{\sum_{k=r}^{s}([A(f_k) - N(f_k)]*f_k^J}{\sum_{k=r}^{s}[A(f_k) - N(f_k)]}\right)^{1/2} - M\left(\frac{\sum_{k=p}^{q}([A(f_k) - N(f_k)]*[f_q - f_k + f_p]^M)}{\sum_{p}^{q}[A(f_k) - N(f_k)]}\right)^{1/2} \quad (5.3)$$

where $A(f_k)$ and $N(f_k)$ are the amplitudes of the kth spectral estimates of the signal and preceding noise sample, respectively; J, M are the orders of the moments being considered in their respective terms; r, p correspond to the lowest frequency components; and s, q to the highest frequency components. When used as a discriminant MMF, or TMF given by the first term in Eq. (5.3), is plotted against either the body wave magnitude or complexity of an event.

The rationale behind these discriminants is based on the recognized spectral differences between earthquakes and explosions. The effects of the multipliers f_k^J and $(f_q - f_k + f_p)^M$ in Eq. (5.3) are to enhance the spectral differences at high and low frequencies, respectively, between earthquakes and explosions while minimizing the central portion of the event spectra.

The TMF and MMF algorithms were coded and applied to the LASA data base. Two time windows, 6.4 seconds and

and 12.8 seconds, and various combinations of frequency parameters were tested. As explained previously no noise corrections were made in these tests. The results are shown in Figs. 5.3a and b and Figs. 5.4a and b.

TMF versus m_b and linear complexity, C_L, are plotted in Figs. 5.3a and b, respectively, for the Eurasian population of shallow earthquakes (O's) and presumed explosions (X's). The results of these two figures represent the best discrimination achieved for many different sets of parameters (r, s; Eq. (5.3)) tested.

In the case of TMF versus m_b (Fig. 5.3a) the event populations exhibit complete separation of m_b's > 4.7. The small magnitude explosions that plot within the earthquake population also failed, because of background noise, to discriminate using the VFM technique (Fig. 4.2). For TMF versus C_L (Fig. 5.3b) the two event populations nearly separate over the entire magnitude range. The degree of separation using the TMF technique, however, is not as great in either case (Figs. 5.3a and b) as the separation of the event populations realized with the VFM discriminant.

Values of MMF were computed for the Eurasian event population using Eq. (5.3) and are plotted in Figs. 5.4a and b versus m_b and linear complexity, (C_L) respectively. While there is substantial overlap of the event populations in Fig. 5.4b (MMF versus C_L), the data in Fig. 5.4a indicate that MMF versus m_b is a very effective discriminant. In fact the degree of separation of the earthquake and explosion populations in Fig. 5.4a is as good as or better than that achieved with the VFM technique.

Both of the higher moments of frequency techniques (TMF and MMF), while useful as positive discriminants, do not appear to be dependent on event size, except in an inverse manner. Thus, the combined application of the higher

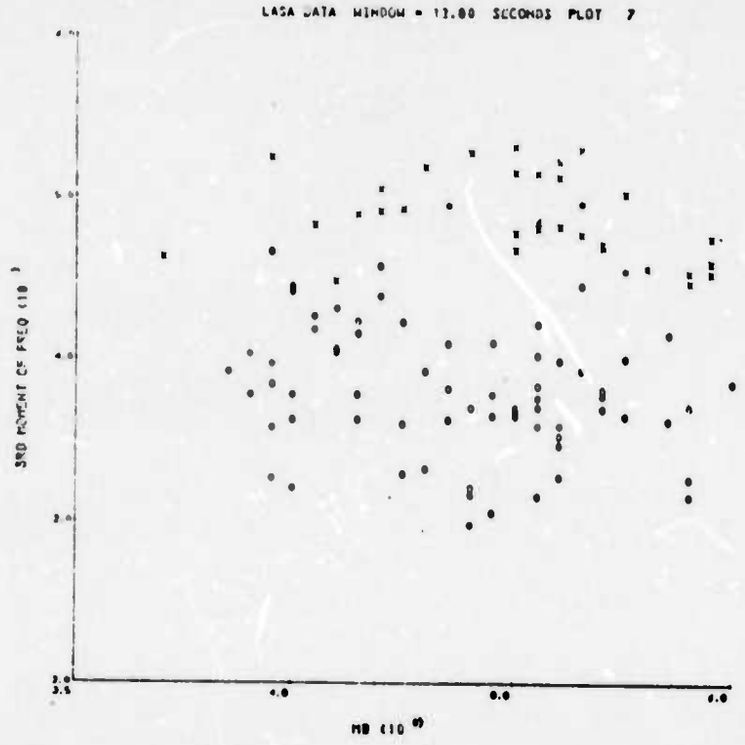


Figure 5.3a. TMF versus m_b for the Eurasian population of shallow earthquakes (O's) and presumed explosions (X's). The parameters used in this test are r = 8 (.31 Hz) and s = 64 (2.5 Hz) (see Fq. (5.3)).

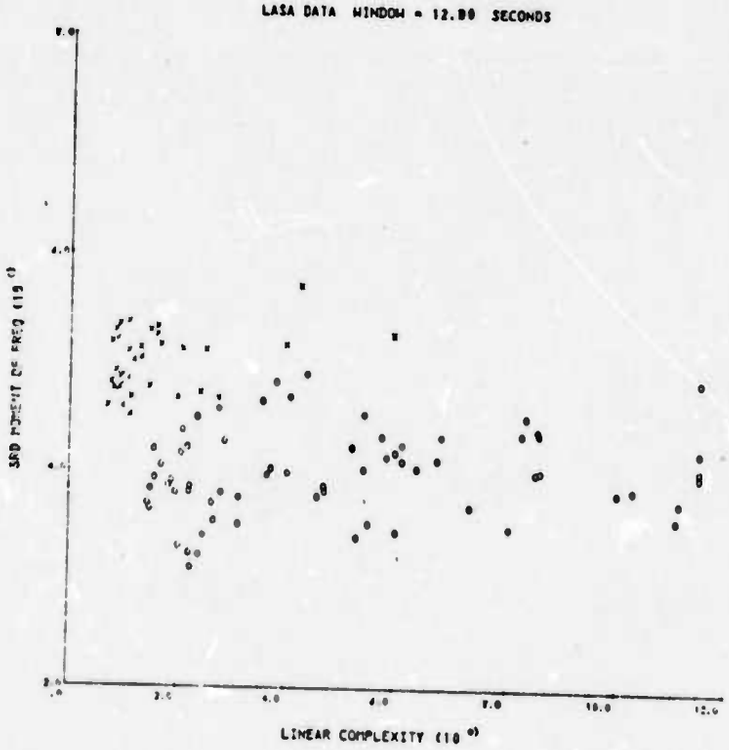


Figure 5.3b. TMF versus linear complexity. Parameters used are r = 12 (.47 Hz) and s = 64 (2.5 Hz).

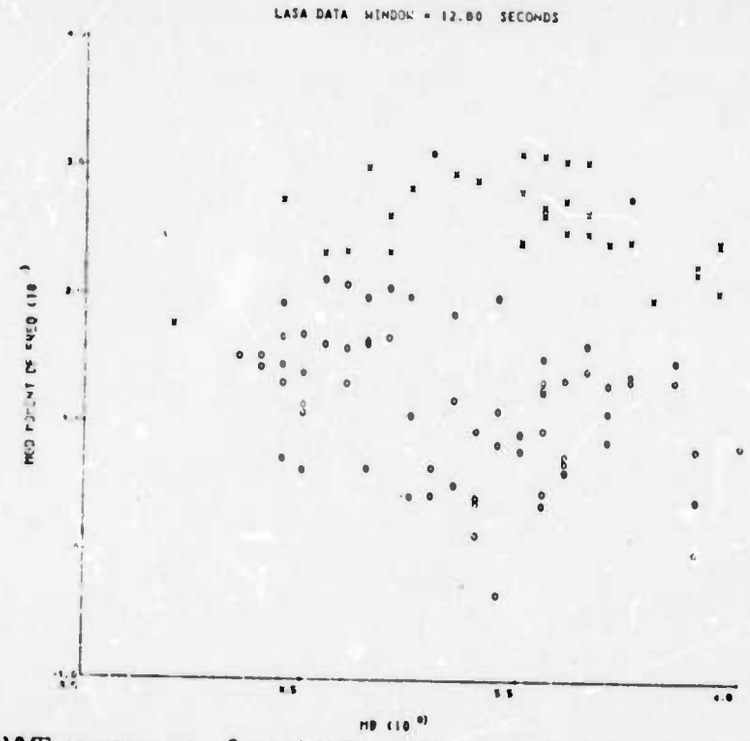


Figure 5.4a. MMF versus m_b for the Eurasian population of earthquakes (O's) and explosions (X's). The parameters used in this test are r = 12 (.47 Hz), s = 64 (2.5 Hz), p = 12 (.47 Hz) and q = 26 (1.02 Hz).

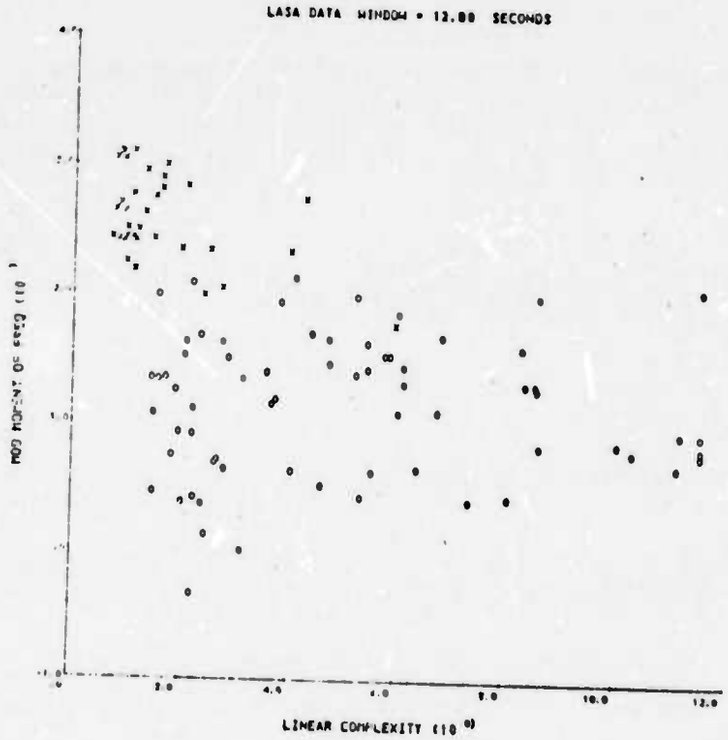


Figure 5.4b. MMF versus linear complexity for Eurasian event population.

moment discriminants and the VFM discriminant would offer a very powerful approach to the problems of event identification and explosion yield determination.

5.5 $M_s - m_b$

Lacoss (1969) applied the $M_s - m_b$ discriminant to the Eurasian population of events under consideration here. As in the case for all the short period techniques, many of the deep earthquakes were found to appear explosion-like by the $M_s - m_b$ criterion. Thus, the results shown in Fig. 5.5 are for shallow events only.

While the majority of earthquakes separate comfortably from the explosion population in Fig. 5.5, one fairly large magnitude earthquake, a reported shallow event in the Kurile Islands, lies within the explosion population. In addition, a rather large magnitude ($m_b = 5.5$) presumed explosion plots quite close to the limit of the earthquake population. More important than this overlap of populations, however, is the fact that the $M_s - m_b$ criterion is limited in its application to explosions of relatively large magnitude. In this particular case (Fig. 5.5) there are no detected surface waves from explosions of $m_b < 5.1$ and several instances of no observed surface waves from explosions with m_b's in the range 5.4 to 5.8. On this count the VFM and other short period discriminants previously described appear quite superior in that their range of applicability extends to events approximately one full magnitude unit smaller than in the case of $M_s - m_b$.

5.6 MULTIPLE EXPLOSION SCENARIO

The various short period discriminants (complexity, spectral ratio, TMF and MMF) were applied to the multiple explosion scenario previously described in Section 4.7 of this report. The results of this test are given in Table 5.1.

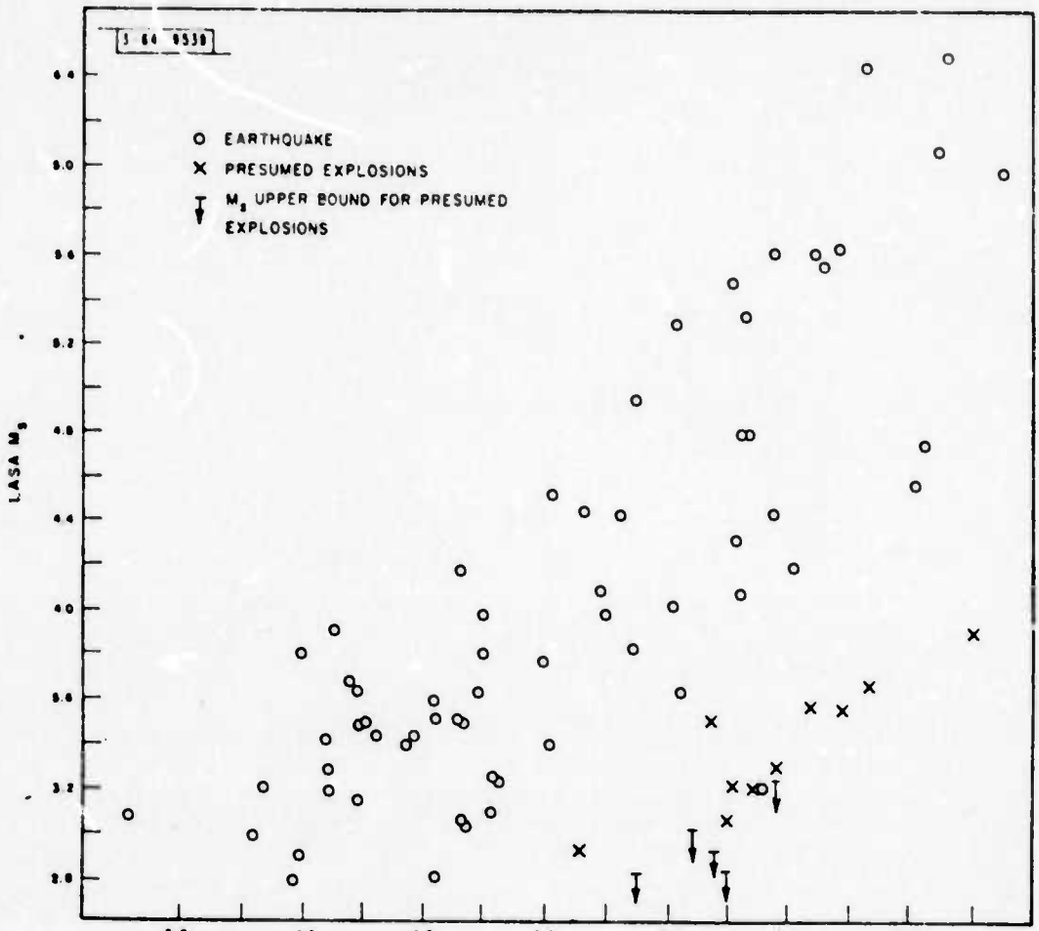


Figure 5.5. LASA M_S versus LASA m_b for events with detected surface waves (events with USCGS depth $\geq$ 100 km excluded). Arrows pointing down attached to the horizontal bars denote no Rayleigh waves detected.

TABLE 5.1

SHORT-PERIOD DISCRIMINANTS APPLIED TO ORIGINAL AND MULTIPLE EXPLOSION SCENARIO

	Linear Complexity	Spectral Ratio	TMF	MMF
Original Explosion Time Series	0.90	1.00	5.35	3.05
Simulated Multiple Explosion				
1	3.35	0.70	5.18	2.78
2	3.19	1.11	5.44	3.51
3	19.43	1.58	5.11	2.87
4	3.11	0.84	5.15	3.27
5	11.97	1.93	5.74	3.60

The parameters used in this test were the same as those used in each of the previous tests. For instance, the TMF discriminant was applied to the first 12.8 seconds of the simulated multiple time series with r = 12 (0.47 Hz) and s = 64 (2.5 Hz). The integers (1-5) in the far left-hand column refer to the different shot-array to receiver azimuths.

As explained in Section 4.7, the scenario was designed to produce teleseismic signatures that resemble those from earthquakes when examined in light of certain proposed discriminants. Comparing the multi-azimuth values of linear complexity for the simulated multiple explosion with the value for the original presumed explosion in Table 5.1, we find that the scenario has, at least in the case of this particular discriminant, produced the desired result. That is the multiple time series appears earthquake-like and, in

fact, at certain azimuths (3,5) more earthquake-like than most of the events plotted in Fig. 5.1.

The situation (Table 5.1) in the case of the other short period discriminants is quite different, however. The values of spectral ratio, TMF and MMF for the multiple explosion at all five azimuths remain within the respective explosion populations (Figs. 5.2a, 5.3a and 5.4a). Thus, while this scenario may appear earthquake-like in terms of first motion, complexity and $M_s - m_b$, the short-period discriminants examined here would correctly identify this event as an explosion.

5.7 SUMMARY

The relative effectiveness of the VFM and several other short- and long-period discriminants was compared using the same population of well-recorded Eurasian events. The most significant results obtained are the following:

1. The short-period techniques (VFM, spectral ratio, TMF and MMF) can be applied to earthquakes and explosions over a much greater magnitude range than the $M_s - m_b$ discriminant. In particular, the short-period discriminants provide positive event identification for explosions approximately 1 magnitude unit smaller than can be tested with the $M_s - m_b$ technique.
2. The combined application of the VFM and MMF discriminants should prove to be a very effective method for event discrimination and explosion yield determination.
3. Short-period discriminants based on spectral differences between earthquakes and explosions can be used to discriminate earthquakes and multiple explosions as well.

VI. DATA ACQUISITION AND EDITING

From the outset of this research program, the acquisition of data has been guided by the requirement for a comprehensive data base for several criteria including: testing and verification of our waveform modeling capabilities; the applicability of new and existing discriminants; and the specification of a matched filter for improved event detection and identification. To date we have acquired both digital and analog data for more than 400 events originating in Eurasia and North America and recorded at several different world-wide locations. The present in-house library of events consists of the following:

1. Best beam short-period (P-waves) digital recordings from LASA of 190 Eurasian events (155 earthquakes, 35 explosions).
2. Best beam short-period (P-wave) digital recordings from the original Oyer subarray in Norway of 44 Eurasian events (36 earthquakes, 8 explosions).
3. Three component short- and long-period digital recordings from numerous LRSM stations for 21 NTS explosions, the Aleutian explosion Longshot, and a presumed Eurasian explosion.
4. Copies of seismograms from the Palmer network of short-period stations located throughout Alaska and the Aleutians for more than 100 Eurasian and North American earthquakes and explosions.
5. Copies of seismograms from selected WWNSS stations for a suite of NTS explosions.
6. Copies of high-gain long-period seismograms of NTS and Eurasian explosions.

7 Digital data from the Yellowknife array in Canada for a suite of NTS explosions and earthquakes located in western North America.

While most of the above data are for events recorded at teleseismic distances, we expect to receive digital data (courtesy of Lane Johnson) for NTS explosions and nearby earthquakes recorded at Jamestown, California (JAS), as well as WWNSS seismograms for stations closer than about 20° to certain Eurasian source regions. These data will provide important checks on our modeling capabilities at regional distances.

An editing program for handling variable formatted digital data has been written. This program converts the tape data that comes into S^3 to a format that is compatible with the various on-line seismic analysis codes. Plotting routines are included in the editing program and allow us to check the quality of the digital data before processing.

VII. REFERENCES

Alexander, S. S., and J. W. Lambert (1971), "Single Station and Array Methods for Improved Surface Wave Spectral Estimates," Teledyne Geotech Report No. 264.

Anglin, F. M. (1971), "Discrimination of Earthquakes and Explosions Using Short Period Seismic Array Data," Nature, 233, 51-52.

Archambeau, C. B. (1964), "Elastodynamic Source Theory," Ph.D. Thesis, California Institute of Technology, Pasadena, California.

Archambeau, C. B. (1968), "General Theory of Elastodynamic Source Fields," Rev. of Geophys., 6, 241-288.

Archambeau, C. B., E. A. Flinn, and D. G. Lambert (1969), "Fine Structure of the Upper Mantle," J. Geophys. Res., 74, 5825-5865.

Archambeau, C. B. (1972), "The Theory of Stress Wave Radiation from Explosions in Prestressed Media," Geophys. J. Roy. Astr. Soc., 29, 329-366.

Archambeau, C. B., D. G. Harkrider, and D. V. Helmberger (1974), "Studies of Multiple Seismic Events," California Institute of Technology, Final Contract Report (Draft) prepared for U. S. Arms Control and Disarmament Agency.

Bache, T. C., J. T. Cherry, and J. M. Savino (1974), "Application of Advanced Methods for Identification and Detection of Nuclear Explosions from the Asian Continent," Systems, Science and Software Semi-Annual Contract Report, SSS-R-75-2483.

Bache, T. C., and D. G. Harkrider (1975), "The Seismic Body Waves Generated by a Point Source in a Layered Medium," (Abstract) presented at the 70th Annual Meeting of the Seismological Society of America, Los Angeles, California.

Bjork, R. L., and M. L. Gittings (1972), "Wave Generation by Shallow Underwater Explosions," DNA-2949Z, 3SR-1008.

Bracewell, R. (1965), "The Fourier Transform and Its Applications," McGraw-Hill, 267-272.

Cameron, I. G., and G. C. Scorgie (1968), "Dynamics of Intense Underground Explosions," J. Inst. Maths. Applics., 4, 194-222.

Carpenter, E. W. (1963), "Explosion Seismology," Science, 147, 363-373.

Carpenter, E. W. (1964), "Teleseismic Methods for the Detection, Identification and Location of Underground Explosions," Vesiac State-of-the-Art Report 4410-67-X, University of Michigan.

Carpenter, E. W. (1966), "A Quantitative Evaluation of Teleseismic Explosion Records," Proc. Roy. Soc., A290, 396-407.

Cherry, J. T., and F. L. Petersen (1970), "Numerical Simulation of Stress Wave Propagation from Underground Nuclear Explosions," in Engineering With Nuclear Explosives, ANS, USAEC, CONF-700101.

Cherry, J. T., C. B. Archambeau, G. A. Frazier, A. J. Good, K. G. Hamilton, and D. J. Harkrider (1973), "The Teleseismic Radiation Field from Explosions: Dependence of Seismic Amplitudes upon Properties of Materials in the Source Region," Systems, Science and Software Final Contract Report, DNA 3113Z.

Cherry, J. T., T. C. Bache, and D. F. Patch (1974a), "The Teleseismic Ground Motion Generated by a Nuclear Explosion in a Tunnel and Its Effects on the M_s/m_b Discriminant," Systems, Science and Software Final Contract Report (Draft), SSS-R-74-2124.

Cherry, J. T., T. C. Bache, and C. B. Archambeau (1974b), "A Deterministic Approach to the Prediction of Teleseismic Ground Motion from Nuclear Explosions," Systems, Science and Software Final Contract Report, DNA 2231F.

Cherry, J. T. (1974), "Near Field Small Earthquake-Computer Simulation," Systems, Science and Software Report SSS-R-75-2475.

Cherry, J. T., T. C. Bache, J. M. Savino, and C. B. Archambeau (1975), "A Deterministic Approach to the Prediction of Teleseismic Ground Motion from Nuclear Explosions," Trans. Amer. Geophys. Union, EOS (Abstract), 56, 1148.

Douglas, A., P. D. Marshall, P. G. Gibbs, J. B. Young, and C. Blamey (1973), "P Signal Complexity Re-examined," Geophys. J. R. Astr. Soc., 33, 195-221.

Evernden, J. F., and J. Filson (1971), "Regional Dependence of Surface-Wave Versus Body-Wave Magnitudes," J. Geophys. Res., 76, 3303-3308.

Ewing, W. M., W. S. Jardetsky, and F. Press (1957), Elastic Waves in Layered Media, McGraw-Hill, New York.

Frasier, C. W. (1972), "Observations of pP in the Short-Period Phases of NTS Explosions Recorded at Norway," Geophys. J. R. Astr. Soc., 31, 99-109.

Frasier, C. W., and M. Yang (1975), "Three Component Analysis of Seismic Codas from Novaya Zemlya Explosions," Trans. Amer. Geophys. Union, EOS (Abstract), 56, 394.

Fuchs, K. (1966), "The Transfer Function for P Waves for a System Consisting of a Point Source in a Layered Medium," BSSA, 56, 75-108.

Futterman, W. I. (1962), "Dispersive Body Waves," J. Geophys. Res., 67, 5279-5291.

Gupta, I. N. (1967), "Body Wave Radiation Patterns from Elementary Sources Within a Half Space," BSSA, 57, 657-674.

Harkrider, D. G. (1964), "Surface Waves in Multilayered Media. I. Rayleigh and Love Waves from Sources in a Multilayered Half-space," BSSA, 54, 627-679.

Harkrider, D. G., and C. B. Archambeau (1975), "Theoretical Rayleigh and Love Waves from an Explosion in Pre-stressed Source Regions," to be submitted for publication.

Harkrider, D. G., and T. C. Bache (1975), "A Theoretical Investigation of the Effect of Differing Near Source and Long Range Propagation Media on Surface Wave Magnitudes from Explosions," (Abstract) presented at the Annual Meeting of the Eastern Section of the Seismological Society of America.

Haskell, N. A. (1962), "Crustal Reflection of Plane P and SV Waves," J. Geophys. Res., 67, 4751-4767.

Haskell, N. A. (1967), "Analytic Approximation for the Elastic Radiation from a Contained Underground Explosion," J. Geophys. Res., 72, 2583-2587.

Helmberger, D. V. (1968), "The Crust-Mantle Transition in the Bering Sea," BSSA, 58, 179-214.

Helmberger, D. V. (1973), "On the Structure of the Low Velocity Zone," Geophys. J. R. Astr. Soc., 34, 251-263.

Herrmann, W. (1969), "Constitutive Equation for the Dynamic Compaction of Ductile Porous Materials," J. Appl. Phys., 40, 6.

Hildebrand, F. B. (1956), Introduction to Numerical Analysis, McGraw-Hill, New York.

Hill, P., and C. Pakiser (1967), "Seismic-Refraction Study of Crustal Structure Between the Nevada Test Site and Boise, Idaho," Geol. Soc. of Amer. Bull., 78, 685-704.

Hudson, J. A. (1969a), "A Quantitative Evaluation of Seismic Signals at Teleseismic Distances--I. Radiation from Point Sources," Geophys. J. R. Astr. Soc., 18, 233-249.

Hudson, J. A. (1969b), "A Quantitative Evaluation of Seismic Signals at Teleseismic Distances--II. Body and Surface Waves from an Extended Source," Geophys. J. R. Astr. Soc., 18, 353-370.

Julian, B. R., and D. L. Anderson (1968), "Travel Times, Apparent Velocities and Amplitudes of Body Waves," Bull. Seism. Soc. Amer., 58, 339-366.

Kelly, E. J. (1968), "A Study of Two Short-Period Discriminants," Lincoln Laboratory Technical Note, ESD-TR-68-16, 56 pages.

Kogeus, K. (1968), "A Synthesis of Short-Period P Wave Records from Distant Explosion Sources," Bull. Seism. Soc. Amer., 58, 663-680.

Kolar, O. C., and N. L. Pruvost (1975), "Earthquake Simulation by Nuclear Explosions," Nature, 253, 242-245.

Lacoss, R. T. (1969), "A Large Population LASA Discrimination Experiment," Lincoln Laboratory Contract Report 1969-24.

Lomnitz, C. (1957), "Linear Dissipation in Solids," J. Appl. Phys., 28, 201-205.

Manchee, E. B. (1972), "Short Period Seismic Discrimination," Nature, 239, 152-153.

Marshall, P. D. (1970), "Aspects of the Spectral Differences between Earthquakes and Underground Explosions," Geophys. J. R. Astr. Soc., 20, 397-416.

Minster, J. B. (1974), "Elastodynamics of Failure in a Continuum," Ph.D. Thesis, California Institute of Technology, Pasadena.

Morse, P. M., and H. Feshbach (1953), Methods of Theoretical Physics, McGraw-Hill, New York.

Riney, T. D., J. K. Dienes, G. A. Frazier, S. K. Garg, J. W. Kirsch, D. H. Brownell, and A. J. Good (1972), "Ground Motion Models and Computer Techniques," DNA-2915Z, 3SR-1071.

Savage, J. C., and M. E. O'Neill (1975), "The Relation Between the Lomnitz and Futterman Theories of Internal Friction," J. Geophys. Res., 80, 249-251.

Savino, J. M., and C. B. Archambeau (1974), "Discrimination of Earthquakes from Single and Multiple Explosions Using Spectrally Defined Event Magnitudes," Trans. Amer. Geophys. Union, EOS (Abstract), 56, 1148.

Springer, D. L., and W. J. Hannon (1973), "Amplitude-Yield Scaling for Underground Nuclear Explosions," Bull. Seism. Soc. Amer., 63, 477-500.

Springer, D. L. (1974), "Secondary Sources of Seismic Waves from Underground Explosions," Bull. Seism. Soc. Amer., 64, 581-594.

Strick, E. (1970), "A Predicted Pedestal Effect for Pulse Propagation in Constant-Q Solids," Geophysics, 35, 387-403.

Thirlaway, H. I. S. (1963), "Earthquake or Explosion," New Scient., 18, 311-315.

Weichert, D. H. (1971), "Short-Period Spectral Discriminant for Earthquake-Explosion Differentiation," Zeitschrift für Geophysik, 37, 147-152.

Werth, G. C., and R. F. Herbst (1963), "Comparison of Amplitudes of Seismic Waves from Nuclear Explosions in Four Mediums," J. Geophys. Res., 68, 1463-1475.

Wiggins, R. A., and D. V. Helmberger (1974), "Synthetic Seismogram Computation by Expansion in Generalized Rays," Geophys. J. R. Astr. Soc., 37, 73-90.

APPENDIX A

THE REFLECTION OF SPHERICAL WAVES AT A FREE SURFACE

It is often useful and enlightening to represent an explosion or earthquake in terms of an equivalent elastic point source. For studies of teleseismic body and surface waves, this representation is computationally convenient and nearly always a reasonable approximation of reality.

Among the most important phases in the teleseismic body wave signature of a complex event are the free surface reflected phases pP, pS, sS and sP. Using frequency independent free surface reflection coefficients, these phases may be related to the direct P and S waves emanating from the source region, thereby deducing a great deal of information about the source.

The reflection coefficients for plane waves impinging on a free surface may be found in many textbooks (e.g., Ewing, Jardetsky and Press (1957), Chapter 2). However, we have not seen in the literature a straightforward presentation of the reflection coefficients for the case of a point source.* Further, we believe there may be a certain amount of confusion on this point.

In sophisticated methods employing generalized rays (e.g., Wiggins and Helmberger (1974)), or propagator matrices (e.g., Fuchs (1966)), the sphericity of the wave front is automatically included in the computation. However, it is often desirable to treat the source region as a homogeneous half space and compute the reflected phases directly from the upgoing P and S waves generated by the source. In these

*It is true that these coefficients can be deduced, albeit with a fair amount of algebra, from results such as those of Gupta (1967).

cases the plane wave coefficients suffice for the pP and sS phases, but a sphericity correction is needed to compute pS and sP. In the following paragraphs the necessary sphericity corrections for obtaining the plane wave phases pS and sP from the point source generated spherical waves incident on a free surface will be given. While there are many ways to derive these correction factors, a method employing a saddle point approximation to an appropriate branch line integral is convenient and illuminating.

Plane Wave Reflection Coefficients

Consider a homogeneous, isotropic half space with the free surface at $z = 0$ in a cylindrical coordinate system (r,θ,z). Assuming azimuthal symmetry, the Fourier transformed displacements in the r and z directions may be written in terms of potentials as follows:

$$\bar{q}(r,z,w) = \frac{\partial\bar{\phi}}{\partial r} + \frac{\partial\bar{\psi}}{\partial r\partial z} \quad ,$$

$$\bar{w}(r,z,w) = \frac{\partial\bar{\phi}}{\partial z} + k^2\bar{\psi} \quad , \tag{A.1}$$

where $k \equiv \omega/c$, with c the usual horizontal phase velocity.

For plane waves incident at a free surface, the reflection coefficients are easily derived using these potentials. In terms of displacements, these are

$$|U_{pP}| = A|U_p| \quad ,$$

$$|U_{sS}| = A|U_s| \quad , \tag{A.2}$$

where

$$A = \frac{4r_\alpha r_\beta - (r_\beta^2 - 1)^2}{4r_\alpha r_\beta + (r_\beta^2 - 1)^2} \quad ,$$

and

$$|U_{ps}| = - \frac{r_\alpha \alpha}{\beta} B|U_p| \quad ,$$

$$U_{sP} = \frac{r_\beta \beta}{\alpha} B|U_s| \quad , \qquad \text{(A.3)}$$

where

$$B = \frac{4(r_\beta^2 - 1)}{4r_\alpha r_\beta + (r_\beta^2 - 1)^2} \quad .$$

In these equations $r_\alpha = (c^2/\alpha^2 - 1)^{1/2}$ and $r_\beta = (c^2/\beta^2 - 1)^{1/2}$ while $|U_p|$, $|U_{pP}|$, etc., are the amplitudes of the incident and reflected plane waves at the free surface.

Sphericity Corrections

Consider now a point source at a depth z = h in the half space. At teleseismic distances the waves from the source and nearby free surface may be treated as plane waves. However, the sphericity of the wave front should be taken into account when computing the waves reflected from the free surface. For the reflected phases in which the wave type remains unchanged (U_{pP} and U_{sS}), the plane wave coefficients of (A.2) are equally valid for a point source. However, for the converted phases (U_{sP} and U_{pS}) a sphericity correction is required. This correction takes the simple form $(r_\alpha/r_\beta)^{\pm 1}$. That is, for spherical waves incident on a free surface (A.3)

must be replaced by

$$|U_{pS}| = -\frac{r_{\beta}^{\alpha}}{\beta} B|U_p| \quad ,$$

$$|U_{sP}| = \frac{r_{\alpha}\beta}{\alpha} B|U_s| \quad . \tag{A.4}$$

In the following section a derivation of this correction factor for the pS phase is given.

The S Waves Due to a Center of Dilatation in a Half Space

Consider a point compressional wave source at a depth h in a homogeneous elastic half space. The distortional potential $\bar{\psi}$ for this problem has been given by a number of authors, e.g., Wiggins and Helmberger (1974). It is conveniently written

$$\bar{\psi}(r,z,w) = \int_0^{\infty} \frac{B}{k} e^{-ikr_{\alpha}h} e^{-ikr_{\beta}z} J_0(kr)\, dk \quad , \tag{A.5}$$

where B is given by (A.3).

Integrals of the form (A.5) have been extensively studied in seismology. Numerous examples appear in Ewing, Jardetsky and Press (1957). For our purposes it is simplest to evaluate (A.5) for far field body waves using the procedure followed by Fuchs (1966) in treating an integral of similar form using contour integration. Omitting the details, this procedure allows transformation of (A.5) into a branch line integral of the form

$$\bar{\psi}(r,z,w) = \int_{L_{\alpha}} \frac{B}{\zeta\sqrt{2\pi\zeta r}} e^{-i\left(\zeta r_{\beta}z + \zeta r_{\alpha}h + \zeta r - \frac{\pi}{4}\right)} d\zeta \quad , \tag{A.6}$$

where L_α is a path in the fourth quadrant of the complex ζ plane. This representation is for body waves only and is valid in the far field ($kr >> 1$).

The integral (A.6) has a saddle point and may be approximated using the method of steepest descent. The pertinent geometry is shown in Fig. A.1.

The single real saddle point of (A.6) may be written

$$\zeta_0 = \sin\theta_p \, \zeta_\alpha \quad , \tag{A.7}$$

where ζ_α is the branch point associated with r_α. Taking the path of steepest descent through the saddle point, it is found that (returning to real wave number)

$$\bar{\psi}(r,z,w) = \frac{B}{k_0 D} e^{-i(k_\alpha R_1 + k_\beta R_2)} \tag{A.8}$$

where $k_\alpha = \omega/\alpha$, $k_\beta = \omega/\beta$ and $k_0 = \sin\theta_p k_\alpha = \sin\theta_s k_\beta$. The lengths R_1, R_2 are defined in Fig. A.1. Further,

$$D^2 = \left(\frac{r_2}{\cos^2\theta_s} + \frac{r_1}{\cos^2\theta_p} \right) r \quad . \tag{A.9}$$

The meaning of (A.8) is that for a given z, h and r there is only one ray, specified by θ_p, which travels between source and receiver. The phase given in (A.8) is the <u>exact</u> phase travel time for the pS ray while the amplitude is approximate.

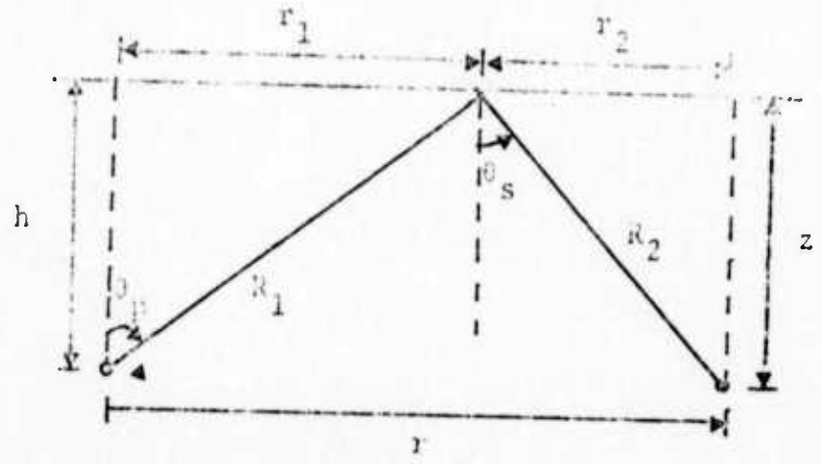


Figure A.1 Geometry for the S waves arriving at a depth z and a distance r from a source of P waves at a depth h.

Plane Wave Interpretation

The plane wave approximation is valid when the point of observation is removed a great distance from the source. For (A.8) this approximation is of interest for two limiting cases:

Case 1 $r_1 >> r_2$

Since (A.8) is valid only for $kr >> 1$, this case may be viewed as equivalent to $h >> z$; that is, a deep source as viewed near the surface. Since the total displacement is $u_{pS} = q \cos\theta_s - w \sin\theta_s$, it can be shown that

$$\bar{U}_{pS}^{(1)} \approx -k_\beta r_\alpha \frac{B}{R_1} e^{-i(k_\alpha R_1 + k_\beta R_2)} , \qquad (A.10)$$

where the superscript indicates that the displacement applies for Case 1.

Case 2 $r_2 >> r_1$

In this case

$$U_{pS}^{(2)} \approx -k_\beta r_\beta \frac{B}{R_2} e^{-i(k_\alpha R_1 + k_\beta R_2)} . \qquad (A.11)$$

The latter case is equivalent to $z >> h$ and is appropriate for teleseismic observations of nearly any earthquake or explosion source.

From (A.10) it is easily shown that the reflection coefficient at the free surface for the pS phase is identical to that given in (A.3), that is, the plane wave coefficient.

On the other hand, Case 2 gives the coefficient including the correction for the sphericity of the wave front incident on the free surface. For the pS phase this correction is r_β/r_α.

Carrying out a similar analysis for a center of rotation, it may be shown that the sphericity correction to be applied to the plane wave coefficients for the sP phase is r_α/r_β. Thus, the free surface reflection coefficients for the pS and sP phases, including the effect of sphericity of the wave front, are given by (A.4).

Concluding Remarks

It is commonly observed that plane wave approximations are valid for sources viewed at a great distance and, therefore, for teleseismic observations of almost any earthquake or explosion source. Elementary calculations of the free surface reflected phases made by applying a simple multiplicative constant to the direct source generated wave are often useful. For the phases pP and sS the plane wave reflection coefficients will suffice. However, for the converted phases pS and sP, a sphericity correction $(r_\beta/r_\alpha)^{\pm 1}$ must be included. Failure to include this factor will result in an error which is on the order of $(2)^{\pm 1}$.

APPENDIX B

THE SEISMIC BODY WAVES GENERATED BY A POINT SOURCE IN A LAYERED MEDIUM

I. INTRODUCTION

Details of the crustal structure in the vicinity of both the source and the receiver can have an important effect on the recorded body waves. In the receiver region one can use the theory of Haskell (1962) in which the emergent waves from the upper mantle are treated as plane waves incident from below on a stack of plane layers representing the crust. This procedure has been in widespread use for a number of years and is quite successful in regions where the plane. parallel layer assumption is not too far removed from reality.

Assuming a source region crustal model made up of a stack of plane elastic layers, a theory analogous to that for the receiver crust can be constructed. Due to the presence of the source in one of the layers, this theory is a good deal more complex. Fuchs (1966) developed a transfer function representing the effect of the layered crustal model on the P waves at large distances for three types of point sources: a center of dilatation, a single couple and a double couple of arbitrary orientation. Kogeus (1968) used Fuchs' theory to compute teleseismic synthetic seismograms for explosion sources. Hudson (1969a,b) extended Fuchs' results to apply to quite general sources of finite extent. However, the representation of complicated sources at arbitrary orientation in a form compatible with the layered crust theory given by Hudson appears to be a complex and difficult task. Thus, the usefulness of Hudson's theory, especially for routine numerical computations, seems to be limited by the inherent complexity of the source representation.

Archambeau (1964, 1968) has pointed out that the radiation field external to any kind of volume source can be represented in an expansion in spherical harmonics. The expansion coefficients, called multipole coefficients, then provide a unique and compact numerical representation of a source of arbitrary complexity and orientation. This representation, called an equivalent elastic source representation, provides a convenient link with powerful elastic wave propagation techniques. The way in which the equivalent elastic source may be obtained for any source for which the outgoing elastic wave can be computed is discussed in Section II.

Harkrider and Archambeau (1975) computed the surface waves excited by an equivalent elastic source in the form of Section II embedded in a stack of plane layers. The corresponding theory for far field body waves is presented here. Having the body waves exciting the plane layered crustal model, one can use generalized rays (e.g., Wiggins and Helmberger (1974)) or other means to propagate the waves through the upper mantle. Then one may apply appropriate transfer functions for the receiver crustal model and sensing instrument to compute synthetic seismograms. In short, this theory provides a merging of arbitrary nonlinear source calculations with the linear elastic wave propagation techniques developed in seismology.

It should be pointed out that the results to be presented here are completely equivalent to those of Hudson. The difference is, of course, the specification of the source in the computationally convenient multipolar coefficient form.

II. EQUIVALENT ELASTIC SOURCE REPRESENTATION

The Fourier transformed equations of motion in a homogeneous, isotropic, linearly elastic medium may be written

$$\underset{\sim}{\bar{u}} = -\left(\frac{1}{k_\alpha^2}\right)\nabla\bar{\chi}^{(4)} + \left(\frac{2}{k_\beta^2}\right)\nabla \times \underset{\sim}{\bar{\chi}} \tag{2.1}$$

where $\underset{\sim}{\bar{u}}$ is particle displacement and k_α and k_β are the compressional and shear wave numbers. The Cartesian potentials $\bar{\chi}^{(4)}$ and $\underset{\sim}{\bar{\chi}}$ are defined by

$$\begin{aligned} \bar{\chi}^{(4)} &= \nabla \cdot \underset{\sim}{\bar{u}} \\ \underset{\sim}{\bar{\chi}} &= \frac{1}{2}\nabla \times \underset{\sim}{\bar{u}} \end{aligned} \tag{2.2}$$

and may be easily shown to satisfy the wave equation

$$\nabla^2\bar{\chi}^{(j)} + k_i^2\bar{\chi}^{(j)} = 0 \ , \ j = 1, 2, 3, 4, \tag{2.3}$$

where $k_4 \equiv k_\alpha = \omega/\alpha$, $k_i \equiv k_\beta = \omega/\beta$, $i = 1,2,3$. This equation has as a solution the following expansion in spherical eigenfunctions (e.g., Morse and Feshbach (1953)),

$$\bar{\chi}^{(j)}(\underset{\sim}{R},\omega) = \sum_{\ell=0}^{\infty} h_\ell^{(2)}(k_\alpha R) \sum_{m=0}^{\ell} \left[A_{\ell m}^{(j)}(\omega) \cos m\phi + B_{\ell m}^{(j)}(\omega) \sin m\phi\right] P_\ell^m(\cos\theta) \tag{2.4}$$

where the $h_\ell^{(2)}$ are spherical Hankel functions of the second kind and the P_ℓ^m are associated Legendre functions. The vector $\underset{\sim}{R}$ has as components the spherical coordinates R,θ,ϕ.

Equations (2.4) together with (2.1) provide an equivalent elastic source representation of the outgoing elastic

waves. The values of the multipole coefficients $A_{\ell m}^{(j)}(\omega)$, $B_{\ell m}^{(j)}(\omega)$, $j = 1,2,3,4$, prescribe the displacement field at all points in the homogeneous elastic medium where (2.1) applies.

The point source representation, Eq. (2.4), provides a generalization of the commonly used center of dilatation ($\ell = 0$), couple ($\ell = 1$) and double couple ($\ell = 2$) point sources, as well as more complex sources. For example, for a horizontal double couple source of unit amplitude, the non-zero coefficients in (2.4) are

$$-A_{21}^{(1)} = B_{21}^{(2)} = A_{22}^{(3)} = (\beta^2/\alpha^2)\, B_{22}^{(4)} \ .$$

Given the displacement, $\bar{u}_i$, or, alternatively, the potentials $\bar{\chi}^{(j)}$, one may determine the multipole coefficients using (2.4). For example, using the orthogonality of the spherical eigenfunctions, one may derive

$$\begin{Bmatrix} A_{\ell m}^{(j)}(\omega) \\ B_{\ell m}^{(j)}(\omega) \end{Bmatrix} = \frac{C_{\ell m}}{h_\ell^{(2)}(k_\alpha \hat{R})} \int_0^{2\pi} \int_0^{\pi} \bar{\chi}^{(j)}(\hat{R},\omega)\, P_\ell^m(\cos\theta) \begin{Bmatrix} \cos m\phi \\ \sin m\phi \end{Bmatrix} \sin\theta d\theta d\phi \tag{2.5}$$

where

$$C_{\ell m} = \frac{(2\ell+1)(\ell-m)!}{2\pi(\ell+m)} \ , \ m \neq 0 \ ,$$

$$C_{\ell 0} = (2\ell+1)/4\pi \ .$$

That is, given the displacements, $\bar{u}(\hat{R},\omega)$ on a sphere of radius $\hat{R}$, one can use (2.2), (2.5) and (2.4) to compute the displacements at any point in the elastic regime. This procedure was first suggested for geophysical applications by Archambeau (1968).

Using the equivalent elastic source representation, highly nonlinear finite difference calculations of the near

source earthquake or explosion displacement fields may be coupled to the elastic field where efficient elastic wave propagation techniques can be applied. Carrying the nonlinear computation out to a radius at which the material response is in the elastic regime, Eq. (2.5) may be applied to compute the multipole coefficients and, thereby, the equivalent elastic source.

For a spherically symmetric explosion, the explosion induced elastic field is often represented by the reduced displacement potential, $\psi(\tau)$, defined by

$$u_r(r,t) = \frac{\Psi(\tau)}{R^2} + \frac{1}{R_\alpha}\frac{d\Psi(\tau)}{d\tau} \quad , \tag{2.6}$$

where $\tau = t - R/\alpha$, is the retarded time. Note that $\Psi(\tau)$ is independent of R.

Applying the Fourier transform, (2.6) becomes

$$\bar{u}_r(R,\omega) = \frac{(1 + ik_\alpha r)}{R^2} e^{-ik_\alpha R} \bar{\Psi}(\omega) \quad . \tag{2.7}$$

Then, carrying out the algebra (observing that the $\bar{\underset{\sim}{u}}$ of (2.2) is the Cartesian displacement vector), it may be shown that the multipole coefficients reduce to a single nonzero term, the monopole:

$$A_{00}^{(4)}(\omega) = -ik_p^3\bar{\Psi}(\omega) \quad . \tag{2.8}$$

For more complex sources, additional nonzero coefficients are present. For example, in the case of an explosion in an axisymmetric (about the z axis) cavity the coefficients $A_{\ell_0}^{(4)}$, $B_{\ell_1}^{(1)}$, $A_{\ell_1}^{(2)}$, $\ell = 2,4,5, \ldots$, are also nonzero (Cherry, et al., 1974). Also, Archambeau (1972) has given a theory for tectonic stress release due to underground explosions which leads to nonzero quadrupole coefficients $A_{2m}^{(j)}$, $B_{2m}^{(j)}$, $m = 0,1,2$.

To this point the discussion has been independent of the orientation of the source with reference to a free surface, which must be included to study the source as a generator of body and surface waves. Minster (1974) has derived a general transformation by which the multipole coefficients in a standard coordinate system (e.g., fixed with respect to the free surface) may be obtained from any rotated coordinate system. Therefore, the multipole coefficients may be computed in a convenient source related system and then rotated to a fixed geographical system.

III. AN ELASTODYNAMIC SOURCE IN A PLANE LAYERED HALF SPACE

Harkrider and Archambeau (1975) have developed the theory for computing surface waves for an equivalent elastic point source, given by Eq. (2.4), embedded in a stack of homogeneous, isotropic elastic plane layers. This required the formulation of the displacements in terms of certain integrals over wave number. The surface waves are then given by the residue contribution to these integrals. The body waves exiting the plane layered model are given by the branch line contributions to the same integrals. The essential steps for deriving the k integrals in a form suitable for computation of body waves are outlined below. For the most part the notation is that of Harkrider (1964) and Harkrider and Archambeau (1975).

Consider a semi-infinite elastic medium made up of n parallel, homogeneous, isotropic elastic layers. Number the layers from 1 at the free surface to n for the underlying half space. Place the origin of a cylindrical coordinate system (r,ϕ,z) at the free surface and denote the layer interfaces by z_i, $i = 1,2, \ldots, n-1$. This geometry is depicted in Fig. 1. Let $(\bar{q}_i, \bar{v}_i, \bar{w}_i)$ be the components of the Fourier transformed displacements in the (r,ϕ,z) directions in the ith layer. Then, following Harkrider (1964), the potentials $\bar{\Phi}_i, \bar{\Psi}_i, \bar{\Omega}_i$ are defined by

$$\bar{q}_i(r,\phi,z) = \frac{\partial \bar{\Phi}_i}{\partial r} + \frac{\partial^2 \bar{\Psi}_i}{\partial r \partial z} + \frac{1}{r}\frac{\partial \bar{\Omega}_i}{\partial \phi} \quad ,$$

$$\bar{v}_i(r,\phi,z) = \frac{1}{r}\frac{\partial \bar{\Phi}_i}{\partial \phi} + \frac{1}{r}\frac{\partial^2 \bar{\Psi}_i}{\partial z \partial \phi} - \frac{\partial \bar{\Omega}_i}{\partial r} \quad , \tag{3.1}$$

$$\bar{w}_i(r,\phi,z) = \frac{\partial \bar{\Phi}_i}{\partial z} + \frac{\partial^2 \bar{\Psi}_i}{\partial z^2} + k^2 \beta_i^2 \bar{\Psi}_i, \quad i = 1, 2, \ldots, n.$$

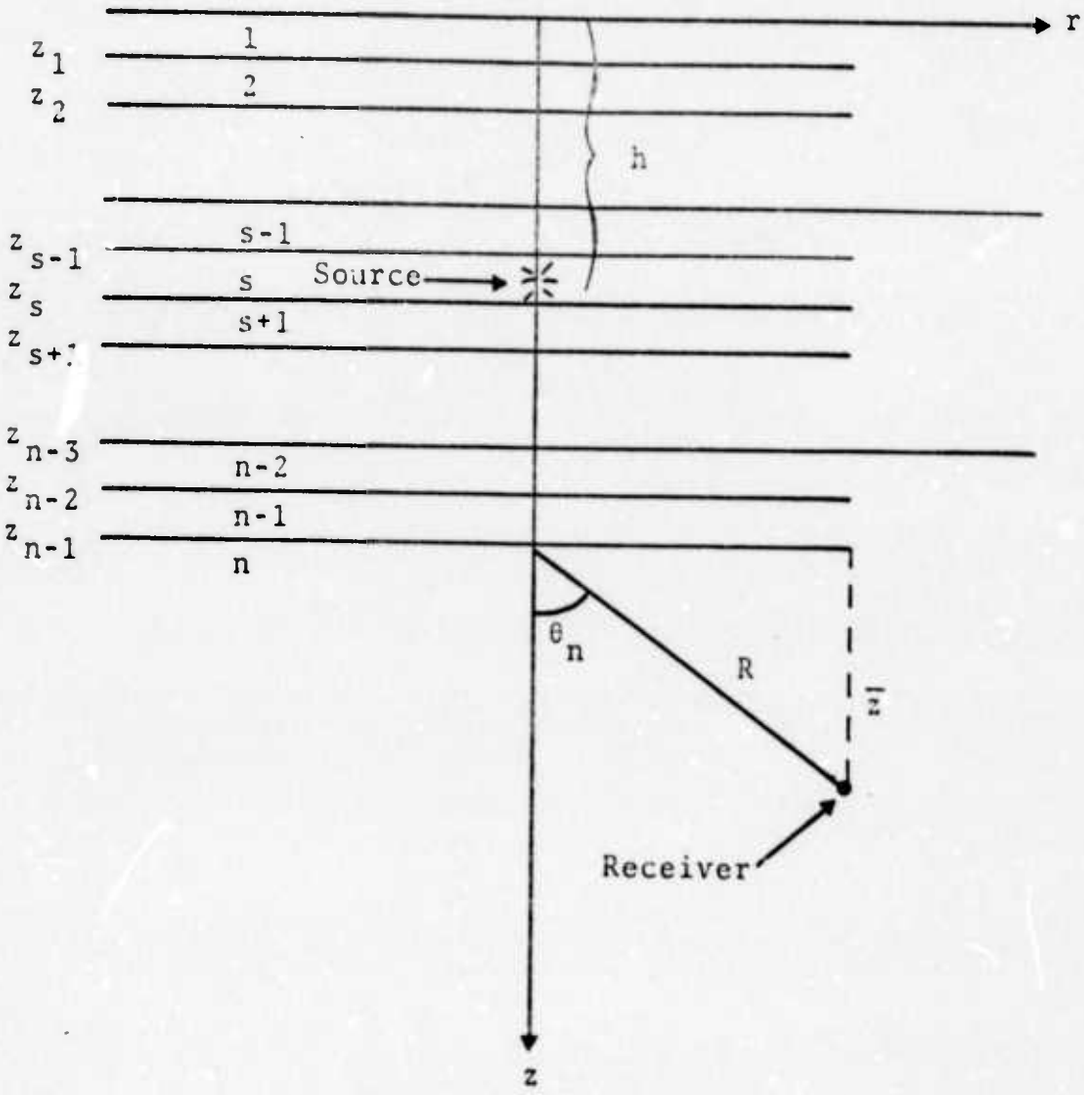


Figure 1. The geometry and coordinate system for a point source at a depth h in a stack of n-1 plane layers underlain by a half space.

We will subsequently be interested in an equivalent elastic point source at a depth $z = h$. Let the source layer be denoted by a subscript s; that is, $z_s < h < z_{s-1}$. It is necessary to express the cylindrical potentials $(\bar{\Phi}_s, \bar{\psi}_s, \bar{\Omega}_s)$ in the source layer in terms of the spherical potentials $(\chi_s^{(\alpha)})$ from Eq. (2.4). The equivalence is given by Harkrider and Archambeau (1975) and is as follows:

$$\bar{\Phi}_s = \sum_{m=0}^{\ell} \int_0^{\infty} \left\{ \bar{A}_m \cos m\phi + \bar{B}_m \sin m\phi \right\} \frac{e^{-ikr_\alpha |z-h|}}{r_\alpha} J_m(kr)\,dk ,$$

$$\bar{\psi}_s = \sum_{m=0}^{\ell} \int_0^{\infty} \left\{ \bar{E}_m \cos m\phi + \bar{F}_m \sin m\phi \right\} \frac{e^{-ikr_\beta |z-h|}}{r_\beta} J_m(kr)\,dk , \tag{3.2}$$

$$\bar{\Omega}_s = \sum_{m=0}^{\ell} \int_0^{\infty} \left\{ \bar{C}_m^{(3)} \cos m\phi + \bar{D}_m^{(3)} \sin m\phi \right\} \frac{e^{-ikr_\beta |z-h|}}{r_\beta} \frac{J_m(kr)}{k^2}\,dk ,$$

where

$$\bar{A}_m = -\frac{1}{k_\alpha^3} \sum_{\ell=m}^{\infty} (i)^{m-n} [\mathrm{sgn}(h-z)]^{m+\ell} A_{\ell m}^{(4)} P_\ell^m \left(\frac{kr_\alpha}{k_\alpha} \right) ,$$

$$\bar{B}_m = -\frac{1}{k_\alpha^3} \sum_{\ell=m}^{\infty} (i)^{m-n} [\mathrm{sgn}(h-z)]^{m+\ell} B_{\ell m}^{(4)} P_\ell^m \left(\frac{kr_\alpha}{k_\alpha} \right) , \tag{3.3}$$

$$\bar{C}_m^{(j)} = \frac{2}{k_\beta^3} \sum_{\ell=m}^{\infty} (i)^{m-n} [\mathrm{sgn}(h-z)]^{m+\ell} A_{\ell m}^{(j)} P_\ell^m \left(\frac{kr_\beta}{k_\beta} \right) ,$$

$$\bar{D}_m^{(j)} = \frac{2}{k_\beta^3} \sum_{\ell=m}^{\infty} (i)^{m-n} [\mathrm{sgn}(h-z)]^{m+\ell} B_{\ell m}^{(j)} P_\ell^m \left(\frac{kr_\beta}{k_\beta} \right) ,$$

where $j = 1,2,3$ in the definitions of $\overline{C}_m^{(j)}$, $\overline{D}_m^{(j)}$, and

$$k = w/c, \quad k_\gamma = w/\gamma ,$$

$$r_\gamma = (c^2/\gamma^2 - 1)^{\frac{1}{2}} , \quad \gamma = \alpha \text{ or } \beta , \tag{3.4}$$

c = horizontal phase velocity.

The coefficients $\overline{E}_m$, $\overline{F}_m$ in the expression for $\overline{\psi}_s$ are defined from the $\overline{C}_m^{(j)}$, $\overline{D}_m^{(j)}$ as follows:

$$\begin{aligned} 2k\overline{E}_0 &= \overline{C}_1^{(2)} - \overline{D}_1^{(1)} , \quad \overline{F}_0 = 0 \\ 2k\overline{E}_1 &= \overline{C}_2^{(2)} - \overline{D}_2^{(1)} - 2\overline{C}_0^{(2)} , \\ 2k\overline{F}_1 &= \overline{C}_2^{(1)} + \overline{D}_2^{(2)} + 2\overline{C}_0^{(1)} , \end{aligned} \tag{3.5}$$

and, taking $\overline{C}_m^{(i)} = D_m^{(j)} = 0$ for $m > \ell$,

$$\begin{aligned} 2k\overline{E}_m &= \overline{C}_{m+1}^{(2)} - \overline{C}_{m-1}^{(2)} - \overline{D}_{m+1}^{(1)} - \overline{D}_{m-1}^{(1)} , \\ 2k\overline{F}_m &= \overline{C}_{m+1}^{(1)} + \overline{C}_{m-1}^{(1)} + \overline{D}_{m+1}^{(2)} - \overline{D}_{m-1}^{(2)} , \quad 2 \le m \le \ell . \end{aligned}$$

Since the location of material boundaries depends only on z, the dependence on r and ϕ will be everywhere the same as in the source layer. Therefore, separate the potentials in the layers as follows:

$$\begin{Bmatrix} \overline{\Phi}_i(r,\phi,z) \\ \overline{\psi}_i(r,\phi,z) \\ \overline{\Omega}_i(r,\phi,z) \end{Bmatrix} = \sum_{m=0}^{\ell} \int_0^\infty \begin{Bmatrix} \phi_i^{(m)}(\phi,z) \\ \psi_i^{(m)}(\phi,z) \\ \Omega_i^{(m)}(\phi,z) \end{Bmatrix} J_m(kr)dk , \tag{3.6}$$

$i = 1, 2, \ldots, n.$

The potentials $\phi_i^{(m)}$, $\psi_i^{(m)}$, $\Omega_i^{(m)}$ satisfy wave equations for which the general solutions may be written:

$$\phi_i^{(m)}(\phi,z) = \tilde{\Delta}_i^{(m)} e^{-ikr\alpha_i z} + \tilde{\Delta}_i^{(m)'} e^{ikr\alpha_i z} ,$$

$$\psi_i^{(m)}(\phi,z) = \tilde{\omega}_i^{(m)} e^{-ikr\beta_i z} + \tilde{\omega}_i^{(m)'} e^{ikr\beta_i z} , \qquad (3.7)$$

$$\Omega_i^{(m)}(\phi,z) = \tilde{\varepsilon}_i^{(m)} e^{-ikr\beta_i z} + \tilde{\varepsilon}_i^{(m)'} e^{ikr\beta_i z} ,$$

in Eq. (3.7) and subsequent equations subscripts i, $i = 1,2, \ldots, n$, denote quantities in the ith layer.

Then, define

$$\hat{\Delta}_i^{(m)} = -k^2\left(\frac{c}{\alpha_i}\right)^2 e^{-kr\alpha_i z_{i-1}} \tilde{\Delta}_i^{(m)} ,$$

$$\hat{\omega}_i^{(m)} = \frac{ik^3}{\gamma_i} e^{-ikr\beta_i z_{i-1}} \tilde{\omega}_i^{(m)} , \qquad (3.8)$$

$$\hat{\varepsilon}_i^{(m)} = k\, e^{-ikr\beta_i z_{i-1}} \tilde{\varepsilon}^{(m)} .$$

We will subsequently be interested in the values of the potential in the half space ($i = n$). Applying the radiation condition at infinity, (3.7) and (3.8) give

$$\phi_n^{(m)}(\phi,z) = -\frac{1}{k_{\alpha_n}^2} e^{-ikr_{\alpha_n}\bar{z}} \hat{\Delta}_n^{(m)} ,$$

$$\psi_n^{(m)}(\phi,z) = -\frac{i\gamma_n}{k^3} e^{-ikr_{\beta_n}\bar{z}} \hat{\omega}_n^{(m)} , \qquad (3.9)$$

$$\Omega_n^{(m)}(\phi,z) = \frac{1}{k} e^{-ikr_{\beta_n}\bar{z}} \hat{\varepsilon}_n^{(m)} ,$$

where

$$\bar{z} = z - z_{n-1} ,$$

$$\gamma_i = 2\beta_i^2/c^2 . \qquad (3.10)$$

Now, combining Eqs. (3.6) and (3.9), we have

$$\bar{\Phi}_n(r,\phi,z) = \sum_{m=0}^{\ell} \int_0^{\infty} \left(-\frac{1}{k_{\alpha_n}^2}\right) \hat{\Delta}_n^{(m)} e^{-ikr_{\alpha_n}\bar{z}} J_m(kr)dk ,$$

$$\bar{\Psi}_n(r,\phi,z) = \sum_{m=0}^{\ell} \int_0^{\infty} -\frac{i}{k}\left(\frac{2}{k_\beta^2}\right) \hat{\omega}_n^{(m)} e^{-ikr_{\beta_n}\bar{z}} J_m(kr)dk, \qquad (3.11)$$

$$\bar{\Omega}_n(r,\phi,z) = \sum_{m=0}^{\ell} \int_0^{\infty} \frac{1}{k} \hat{\varepsilon}_n^{(m)} e^{-ikr_{\beta_n}\bar{z}} J_m(kr)dk .$$

In Eqs. (3.11) we now have the cylindrical potentials $\bar{\Phi}_n$, $\bar{\Psi}_n$, $\bar{\Omega}_n$, in the nth layer (half space) in terms of a sum of integrals of the Sommerfeld type. The coefficients $\hat{\Delta}_n^{(m)}$, $\hat{\omega}_n^{(m)}$, $\hat{\varepsilon}_n^{(m)}$ depend on azimuth, ϕ, as well as wave number, k, and include the modification of the source generated pulse by the material discontinuities in the layered half space. Following Harkrider (1964, Eqs. (62)

and (122)), these coefficients are solutions of the matrix equation.

$$\begin{bmatrix} \hat{\Delta}_n^{(m)} \\ \hat{\Delta}_n^{(m)} \\ \hat{\omega}_n^{(m)} \\ \hat{\omega}_n^{(m)} \end{bmatrix} = J^R \left\{ \begin{bmatrix} \dot{u}_{R_1}(0)/c \\ \dot{w}_{R_1}(0)/c \\ 0 \\ 0 \end{bmatrix} + A_{R_{S1}}^{-1} \begin{bmatrix} \delta U_m \\ \delta W_m \\ \delta Z_m \\ \delta X_m \end{bmatrix} \right\} ,$$

$$\begin{bmatrix} \hat{\varepsilon}_n^{(m)} \\ \hat{\varepsilon}_n^{(m)} \end{bmatrix} = J^L \left\{ \begin{bmatrix} \dot{v}_{L_1}(0)/c \\ 0 \end{bmatrix} + A_{L_{S1}}^{-1} \begin{bmatrix} \delta V_m \\ \delta Y_m \end{bmatrix} \right\} , \qquad (3.12)$$

where the J^R and J^L are given by Eqs. (61) and (124) of Harkrider (1964). The matrix $A_{R_{S1}}$ is defined by Harkrider and is the layer product matrix which gives the displacement-stress vector for P - SV motion at the source depth in terms of the displacement-stress vector at the surface. Similarly, $A_{L_{S1}}$ is the transfer matrix for the displacement-stress vector associated with SH motion.

The source terms in (3.12) are given by Harkrider and Archambeau (1975) as follows:

$$\delta U_m = \delta\left(\frac{\dot{u}_s}{c}\right)^c_m \cos m\phi + \delta\left(\frac{\dot{u}_s}{c}\right)^s_m \sin m\phi \quad ,$$

$$\delta W_m = \delta\left(\frac{\dot{w}_s}{c}\right)^c_m \cos m\phi + \delta\left(\frac{\dot{w}_s}{c}\right)^s_m \sin m\phi \quad ,$$

$$\delta Z_m = \delta\sigma^c_m \cos m\phi + \delta\sigma^s_m \sin m\phi \quad ,$$

$$\delta X_m = \delta\tau^c_{Rm} \cos m\phi + \delta\tau^s_{Rm} \sin m\phi \quad , \qquad (3.13)$$

$$\delta V_m = \delta\left(\frac{\dot{v}_s}{c}\right)^c_m \cos m\phi + \delta\left(\frac{\dot{v}_s}{c}\right)^s_m \sin m\phi \quad ,$$

$$\delta Y_m = \delta\tau^c_{Lm} \cos m\phi + \delta\tau^s_{Lm} \sin m\phi \quad ,$$

where

$$\delta\left(\frac{\dot{u}_s}{c}\right)^c_m = 2k^2\left[\frac{\overline{A}^o_m}{r_\alpha} - ik\,\overline{E}^e_m\right] \quad ,$$

$$\delta\left(\frac{\dot{u}_s}{c}\right)^s_m = 2k^2\left[\frac{\overline{B}^o_m}{r_\alpha} - ik\,\overline{F}^e_m\right] \quad ,$$

$$\delta\left(\frac{\dot{w}_s}{c}\right)^c_m = 2k^2\left[\overline{A}^e_m + ik\,\frac{\overline{E}^o_m}{r_\beta}\right] \quad ,$$

$$\delta\left(\frac{\dot{w}_s}{c}\right)^s_m = 2k^2\left[\overline{B}^e_m + ik\,\frac{\overline{F}^o_m}{r_\beta}\right] \quad ,$$

$$\delta\sigma^c_m = 2\rho c^2k^2\left[(\gamma-1)\,\frac{\overline{A}^o_m}{r_\alpha} - ik\gamma\,\overline{E}^e_m\right] \quad ,$$

$$\delta\sigma^s_m = 2\rho c^2k^2\left[(\gamma-1)\,\frac{\overline{B}^o_m}{r_\alpha} - ik\gamma\,\overline{F}^e_m\right] \quad ,$$

$$\delta\tau^{c}_{Rm} = 2\rho c^2 k^2 \left[-\gamma \bar{A}^{e}_{m} - ik(\gamma-1) \frac{\bar{F}^{e}_{m}}{r_\beta} \right] ,$$

$$\delta\tau^{s}_{Rm} = 2\rho c^2 k^2 \left[-\gamma \bar{B}^{e}_{m} - ik(\gamma-1) \frac{\bar{F}^{o}_{m}}{r_\beta} \right]$$

$$\delta\left(\frac{\dot{v}_s}{c}\right)^{c}_{m} = i2k_\beta^2 \frac{\bar{C}^{(3)o}_{m}}{r_\beta} ,$$

$$\delta\left(\frac{\dot{v}_s}{c}\right)^{s}_{m} = i2k_\beta^2 \frac{\bar{D}^{(3)o}_{m}}{r_\beta} ,$$

$$\delta\tau^{c}_{Lm} = - i2k_\beta^2 \mu \, \bar{C}^{(3)e}_{m} ,$$

$$\delta\tau^{s}_{Lm} = - i2k_\beta^2 \mu \, \bar{D}^{(3)e}_{m} . \qquad (3.14)$$

The quantities r_α, r_β, ρ, μ, γ, k_β refer to the layer in which the source occurs, with ρ and μ being the density and shear modulus. The coefficients $\bar{A}_m$, $\bar{B}_m$, etc. are given by (3.3) with the following modification. The series are separated into two parts;

$$\bar{A}_m = \bar{A}^{e}_{m} + \bar{A}^{o}_{m} , \qquad (3.15)$$

with the e superscript denoting a series made up of terms with $m + \ell$ even and the o superscript denoting a similar series from terms with $m + \ell$ odd.

Equations (3.12) may be viewed as a set of simultaneous linear algebraic equations and solved for $\hat{\Delta}^{(m)}_{n}$, $\hat{\omega}^{(m)}_{n}$, $\hat{\varepsilon}^{(m)}_{n}$ in terms of known quantities. The result is:

$$
\begin{aligned}
2\hat{\Delta}_{..}^{(m)} &= \left\{ R_1 \left(J_{11}^R + J_{21}^R \right) - R_2 \left(J_{12}^R + J_{22}^R \right) + J_{13}^R + J_{23}^R \right\} Y_m \\
&\quad + \left\{ R_3 \left(J_{11}^R + J_{21}^R \right) - R_4 \left(J_{12}^R + J_{22}^R \right) + J_{14}^R + J_{24}^R \right\} Z_m \quad , \\
2\hat{\omega}_n^{(m)} &= \left\{ R_1 \left(J_{31}^R + J_{41}^R \right) - R_2 \left(J_{32}^R + J_{42}^R \right) + J_{33}^R + J_{43}^R \right\} Y_m \\
&\quad + \left\{ R_3 \left(J_{31}^R + J_{41}^R \right) - R_4 \left(J_{32}^R + J_{42}^R \right) + J_{34}^R + J_{44}^R \right\} Z_m \quad , \\
\hat{\epsilon}_n^{(m)} &= L_1 X_m \quad ,
\end{aligned}
\tag{3.16}
$$

where

$$
\begin{aligned}
F_R R_1 &= \left(J_{13}^R - J_{23}^R \right) \left(J_{32}^R - J_{42}^R \right) - \left(J_{12}^R - J_{22}^R \right) \left(J_{33}^R - J_{43}^R \right) \quad , \\
F_R R_2 &= \left(J_{13}^R - J_{23}^R \right) \left(J_{31}^R - J_{41}^R \right) - \left(J_{11}^R - J_{21}^R \right) \left(J_{33}^R - J_{43}^R \right) \quad , \\
F_R R_3 &= \left(J_{14}^R - J_{24}^R \right) \left(J_{32}^R - J_{42}^R \right) - \left(J_{12}^R - J_{22}^R \right) \left(J_{34}^R - J_{44}^R \right) \quad , \\
F_R R_4 &= \left(J_{14}^R - J_{24}^R \right) \left(J_{31}^R - J_{41}^R \right) - \left(J_{11}^R - J_{21}^R \right) \left(J_{34}^R - J_{44}^R \right) \quad , \\
F_R &= \left(J_{12}^R - J_{22}^R \right) \left(J_{31}^R - J_{41}^R \right) - \left(J_{11}^R - J_{21}^R \right) \left(J_{32}^R - J_{42}^R \right) \quad , \\
L_1 &= \left(J_{11}^L J_{22}^L - J_{12}^L J_{21}^L \right) \Big/ \left(J_{11}^L - J_{21}^L \right) \quad ,
\end{aligned}
$$

and

$$
\begin{aligned}
Y_m &= \left(A_{R_{S1}} \right)_{42} \delta U_m - \left(A_{R_{S1}} \right)_{32} \delta W_m + \left(A_{R_{S1}} \right)_{22} \delta Z_m - \left(A_{R_{S1}} \right)_{12} \delta X_m \quad , \\
Z_m &= -\left(A_{R_{S1}} \right)_{41} \delta U_m + \left(A_{R_{S1}} \right)_{31} \delta W_m - \left(A_{R_{S1}} \right)_{21} \delta Z_m + \left(A_{R_{S1}} \right)_{11} \delta X_m \quad , \\
X_m &= - \left(A_{L_{S1}} \right)_{21} \delta V_m + \left(A_{L_{S1}} \right)_{11} \delta Y_m \quad .
\end{aligned}
\tag{3.18}
$$

Equations (3.16) gives us $\hat{\Delta}_n^{(m)}$, $\hat{\omega}_n^{(m)}$, $\hat{\varepsilon}_n^{(m)}$ in terms of the known multipolar coefficients defining the source and the layer matrices of the layered half space. Then (3.11), together with (3.1), give closed form solutions for the displacements in the nth layer or half space. It remains to evaluate the integrals in (3.11) to extract the solution for the steeply emergent body waves which are of interest here. This evaluation is the subject of the following section.

IV. COMPUTATION OF BODY WAVES

To compute the displacement potentials in the half space, (3.11), it is necessary to evaluate integrals of the form

$$I_m = \int_0^\infty f_m(k,\omega)\, e^{-ikr_\gamma \bar{z}}\, J_m(kr)\, dk \,, \qquad (4.1)$$

$\gamma = \alpha_n$ or β_n , $m = 0, 1, 2, \ldots$.

For $m = 0$ the dilatational potential, ϕ_n, was evaluated at large distances from the source by Fuchs (1966) using saddle point methods. Hudson (1969a,b) encountered integrals very similar to those in (3.11) when solving for the body waves due to a point source in a layered media. As pointed out in the Introduction, Hudson's solution is completely equivalent to that obtained here, with the difference being in the specification of the source.

Hudson solved for the far field body wave contribution to integrals of the form of (4.1) using contour integration in the complex plane and approximating the branch line contribution using the saddle point method. The details of this integration may be found in the works of Fuchs and Hudson and will not be reproduced here. It will suffice to give the results which are

$$I_m = i^{m+1}\, f(k,\omega)\, r_\gamma \frac{e^{-ik_\gamma R}}{R} \qquad (4.2)$$

where $R^2 = r^2 + \bar{z}^2$. The geometry is shown in Fig. 1. The saddle point approximation is valid as long as $R >> r$; that is, as long as the receiver is sufficiently far from the base of the stack of plane layers. Alternatively, since

$r/R = \sin\theta_n$, this approximation is valid for steeply incident body waves.

With the solution (4.2), we may now write the far field body wave contribution to the potentials (3.11):

$$\bar{\Phi}_n(r,\phi,z) = \sum_{m=0}^{\ell} \left(-\frac{1}{k_{\alpha_n}^2}\right) i^{m+1} r_{\alpha_n} \hat{\Delta}_n^{(m)} \frac{e^{-ik_{\alpha_n}R}}{R},$$

$$\bar{\Psi}_n(r,\phi,z) = \sum_{m=0}^{\ell} \left(\frac{2}{k_{\beta_n}^2}\right) \frac{i^m}{k} r_{\beta_n} \hat{\omega}_n^{(m)} \frac{e^{-ik_{\beta_n}R}}{R}, \qquad (4.3)$$

$$\bar{\Omega}_n(r,\phi,z) = \sum_{m=0}^{\ell} \frac{i^{m+1}}{k} r_{\beta_n} \hat{\varepsilon}_n^{(m)} \frac{e^{-ik_{\beta_n}R}}{R}.$$

The displacements in the half space are given in the cylindrical coordinate system by applying (3.1) to (4.3). It is more convenient to deal with the displacement field polarized into its P, SV and SH components. In the far field, these are given by:

$$\bar{U}_P = \sin\theta_n \frac{\partial\bar{\Phi}_n}{\partial r} + \cos\theta_n \frac{\partial\bar{\phi}_n}{\partial z},$$

$$\bar{U}_{SV} = \cos\theta_n \frac{\partial^2\bar{\Psi}_n}{\partial r\partial z} - \sin\theta_n k^2\bar{\Psi}_n, \qquad (4.4)$$

$$\bar{U}_{SH} = -\frac{\partial\bar{\Omega}_n}{\partial r}.$$

Then carrying out the indicated differentiations and retaining only terms of $O(R^{-1})$, the displacements are:

$$\bar{U}_P = \sum_{m=0}^{\ell} \left(-\frac{1}{k_{\alpha_n}} \right) i^m r_{\alpha_n} \hat{\Delta}_n^{(m)} \frac{e^{-ik_{\alpha_n} R}}{R} ,$$

$$\bar{U}_{SV} = \sum_{m=0}^{\ell} \left(\frac{2}{k_{\beta_n}} \right) i^{m-1} r_{\beta_n} \hat{\omega}_n^{(m)} \frac{e^{-ik_{\beta_n} R}}{R} , \qquad (4.5)$$

$$\bar{U}_{SH} = \sum_{m=0}^{\ell} i^m r_{\beta_n} \hat{\varepsilon}_n^{(m)} \frac{e^{-ik_{\beta_n} R}}{R} .$$

These are the far field body waves propagating into the half space at a specified horizontal phase velocity c. Equations (4.5), together with (3.16), provide a straightforward computational algorithm for computing these displacements. An outline of the steps required to compute the displacements in (4.5) provides a useful summary of the theory that has been developed.

Assume that an equivalent elastic source in terms of multipole coefficients (2.4) is available, or has been computed via (2.5). We are interested in the P and S waves propagating into the half space at a takeoff angle θ_n, in which case a different horizontal wave speed is required for the P and S wave computations. Alternatively, we are interested in the half space displacements corresponding to a fixed phase velocity c, in which case the takeoff angle is different for P and S waves.

Having the multipole coefficients, the phase velocity c and the azimuth of interest ϕ, the following steps are carried out for each frequency, ω.

1. Compute the source layer potentials $\overline{\phi}_s$, $\overline{\psi}_s$, $\overline{\Omega}_s$ from (3.2-3.5).
2. Compute the displacement-stress discontinuity quantities δU_m, δW_m, etc., from (3.13-3.14) for each m.
3. Compute the layer product matrices $A_{R_{S1}}$, $A_{L_{S1}}$, J^R, J^L. The latter two matrices are independent of the source, while the first two depend only on source depth.
4. Compute the source terms Y_m, Z_m, X_m from (3.18).
5. Compute $\hat{\Delta}_n^{(m)}$, $\hat{\omega}_n^m$, $\hat{\varepsilon}_n^{(m)}$ from (3.16).
6. Compute the displacements at a selected R from (4.5).

APPENDIX C

A COMPARISON OF THE SEISMIC BODY WAVES GENERATED BY A POINT COMPRESSIONAL WAVE SOURCE AND A CONCENTRATED FORCE AT THE FREE SURFACE

While most investigators studying the teleseismic signature of underground nuclear explosions have been primarily concerned with the most common example, fully contained blasts, another class of explosion, the cratering shot, is becoming of increasing interest. Before embarking on more complex and sophisticated investigations of the properties of the teleseismic signal generated by cratering shots, useful guidance can be obtained by comparing cratering and contained explosions using very simple models. In particular, elastic half space solutions are often quite helpful in understanding the gross features of the elastic waves generated by seismic sources.

Two elementary point source representations; (1) A point compressional wave source at shallow depth, and (2) A concentrated force on the free surface, will be studied and compared. The first is useful for representing a confined explosion while the second provides a simple representation of an explosion on the surface. The latter, in turn, is expected to give some indication of the features which make cratering and contained explosions different.

The elastic waves in a half space from the two sources will be given in elementary form and compared. Most of these results follow directly from material presented in Ewing, Jardetsky and Press (1957), Chapter 2. The important results will then be cast in terms of the familiar reduced displacement potential to facilitate comparison. Note that <u>all</u> secular quantities are given in the Fourier transform domain. For convenience, the bar generally used to indicate Fourier transformation is omitted.

Consider a cylindrical coordinate system (r,θ,z). For the half space problems let the origin be at the surface with z positive downward. The sources to be considered will be azimuthally independent. Let q and w be the displacements in the r and z directions and define dilatational and rotational potentials Φ and ψ such that

$$q(r,z) = \frac{\partial \Phi}{\partial r} + \frac{\partial^2 \psi}{\partial r \partial z} \quad ,$$

$$w(r,z) = \frac{\partial \Phi}{\partial z} + \frac{\partial^2 \psi}{\partial z^2} + k_\beta^2 \psi \quad . \tag{C.1}$$

Let $R^2 = z^2 + r^2$. The P wave displacement along R is then

$$U_p = q_p \sin\theta + w_p \cos\theta = \frac{\partial \Phi}{\partial R} \quad . \tag{C.2}$$

We shall subsequently be concerned with the reduced displacement potential, Ψ, defined by

$$U_p = - \frac{\partial}{\partial R} \left(\frac{\Psi}{R} e^{-ik_\alpha R} \right) \quad . \tag{C.3}$$

Therefore,

$$\Phi = - \Psi \frac{e^{-ik_\alpha R}}{R} \quad . \tag{C.4}$$

Point Compressional Wave Source in a Half Space

Consider a point source of compressional waves in an unlimited solid. The potentials may then be written

$$\Phi_{cw} = A_0 \frac{e^{-ik_\alpha R}}{R} \quad , \quad \psi_{cw} = 0 \quad . \tag{C.5}$$

Let such a source be embedded at depth h in a half space. The dilatational potential is then

$$\Phi_{cw} = -iA_0 \int_0^\infty \left\{ e^{-ikr_\alpha(z-h)} - P\, e^{-ikr_\alpha(z+h)} \right\} \frac{J_0(kr)}{r_\alpha}\, dk \,, \tag{C.6}$$

where

$$P \equiv \frac{(r_\beta^2 - 1)^2 - 4\, r_\alpha r_\beta}{(r_\beta^2 - 1)^2 + 4\, r_\alpha r_\beta} \,, \tag{C.7}$$

$$r_\alpha = \left(\frac{c^2}{\alpha^2} - 1\right)^{1/2} \,, \quad r_\beta = \left(\frac{c^2}{\beta^2} - 1\right)^{1/2} \,,$$

$$\sin\theta = \alpha/c \,,$$

and c is horizontal phase velocity while θ may be identified as the takeoff angle for waves emitted by the source.

The integral (C.6) may be evaluated by contour integration. The poles of the integral give the surface waves while body waves are obtained by evaluating the branch line contribution. Restricting attention to the far field ($kr \gg 1$), the method of steepest descent may be applied. In this case the result is

$$\Phi_{cw} = A_0 \cos\theta \left\{ \frac{e^{ikr_\alpha h}}{z - h} - P\, \frac{e^{-ikr_\alpha h}}{z + h} \right\} e^{-ik(r_\alpha z + r)} \,. \tag{C.8}$$

Consider the case $z \gg h$ which is more or less implied by our far field assumption. Then

$$\Phi_{cw} = A_0 \left\{ e^{ikr_\alpha h} - P\, e^{-ikr_\alpha h} \right\} \frac{e^{-ik_\alpha R}}{R} \,. \tag{C.9}$$

As $h \to 0$ the coefficient in parentheses approaches

$$1 - P = \frac{8\, r_\alpha r_\beta}{(r_\beta^2 - 1)^2 + 4\, r_\alpha r_\beta} \quad . \tag{C.10}$$

A Concentrated Force Acting on the Free Surface of an Elastic Half Space

Let us impose a vertical concentrated force on the free surface in the following way. Let the stresses at the free surface be given by

$$\begin{aligned} [\tau_{zz}]_{z=0} &= -\frac{L}{2\pi} \int_0^\infty J_0(kr)\, k\, dk \ , \\ [\tau_{zr}]_{z=0} &= 0 \ . \end{aligned} \tag{C.11}$$

With this boundary condition the dilatational potential can be shown to be

$$\Phi_{PF} = -\frac{L}{2\pi\mu} \int_0^\infty \frac{(2k^2 - k_\beta^2)}{F(k)}\, e^{-ikr_\alpha z}\, J_0(kr)\, k\, dk \tag{C.12}$$

where the Rayleigh function

$$F(k) \equiv k^4[(r_\beta^2 - 1)^2 + 4\, r_\alpha r_\beta] \ , \tag{C.13}$$

and μ is the shear modulus.

Once again, contour integration may be applied to obtain the dilatational potential for <u>far</u> field P waves:

$$\Phi_{PF} = \frac{iL}{2\pi\mu k}\, r_\alpha Q\, \frac{e^{-ik_\alpha R}}{R} \ , \tag{C.14}$$

where

$$Q = \frac{(r_\beta^2 - 1)}{(r_\beta^2 - 1)^2 + 4\, r_\alpha r_\beta} \quad . \tag{C.15}$$

Relation Between a Compressional Wave Source and a Point Force

It is immediately apparent that a compressional wave source at vanishingly small depth is a distinctly different source type than a point force acting downward on the free surface. In the first case a stress free boundary is assumed, while in the second a stress is imposed on the free surface. For the case of a whole space the differential relation between the two is given below.

In an unlimited solid the dilatational potential for a vertical point force may be written

$$\Phi_{PF} = - \frac{L}{4\pi\omega^2\rho} \frac{\partial}{\partial z} \frac{e^{-ik_\alpha R}}{R} \quad , \tag{C.16}$$

where ρ is density.

Comparing to (C.5), this implies that

$$\Phi_{PF} = - \frac{L}{4\pi\omega^2\rho A_0} \frac{\partial \Phi_{cw}}{\partial z} \tag{C.17}$$

That is, the dilatational potential for a concentrated force is proportional to the space derivative of that for the point source. This result may be generalized by taking the component of $\nabla\Phi_{cw}$ in the direction of the concentrated force. In fact, Eq. (C.17) may be written

$$\nabla^2\Phi_{PF} = \frac{L}{4\pi\rho\alpha^2 A_0} \underset{\sim}{n} \cdot \nabla\Phi_{cw} \quad , \tag{C.18}$$

where $\underset{\sim}{n}$ is a unit vector in the concentrated force direction.

Application to an Explosion Given by a Reduced Displacement Potential (RDP)

Comparing Eqs. (C.4) and (C.5), the compressional wave source amplitude A_0 is related to the RDP by

$$A_0 = -\Psi \, . \tag{C.19}$$

Therefore, from (C.2) and (C.9), the far field displacement for a shallow source may be written

$$U_{cw} = ik_\alpha \Psi \left\{ e^{ikr_\alpha h} - P e^{-ikr_\alpha h} \right\} \frac{e^{-ik_\alpha R}}{R} \tag{C.20}$$

Now consider a point force at the surface. In order to write the point force amplitude L in terms of a contained explosion quantity like the RDP, one must make assumptions about the coupling of the explosion into the ground. That is, one must specify the free surface boundary condition (C.11) in terms of explosion quantities.

It is reasonable for our purposes to assume that the stresses on the free surface are

$$\begin{aligned} \left[\tau_{zz}\right]_{z=0} &= -\eta P, \\ \left[\tau_{zr}\right]_{z=0} &= 0, \end{aligned} \tag{C.21}$$

where η is a constant ($< 1.$) and P is the pressure generated by a contained explosion with RDP Ψ. That is,

$$\left[\tau_{zz}\right]_{z=0} = \eta k_\alpha^2 K \Psi \frac{e^{-ik_\alpha R}}{R} \, , \tag{C.22}$$

where K is the bulk modulus.

From (C.11),

$$\left[\tau_{zz}\right]_{z=0} = -\frac{L}{2\pi}\int_0^\infty J_0(kr)\, k\, dk,$$

$$= \frac{L}{2\pi}\frac{\partial}{\partial z}\frac{e^{-ik_\alpha R}}{R}\bigg|_{z=0}, \qquad (C.23)$$

$$= -i\frac{Lk}{2\pi} r_\alpha \frac{e^{-ik_\alpha R}}{R}\bigg|_{z=0}.$$

Then

$$L = \frac{2\pi i k_\alpha}{\cos\theta}\eta K \Psi \qquad (C.24)$$

Using (C.24) in (C.14) and applying (C.2), the far field displacement is then

$$U_{PF} = \frac{ik_\alpha}{\mu \sin^2\theta}\eta K Q \Psi \frac{e^{-ik_\alpha R}}{R}. \qquad (C.25)$$

Comparison of Displacement for the Two Source Types

Now compare the displacement radiation patterns for the point force and the compressional wave source buried at vanishingly small depth. From (C.20) the far field displacement for a compressional wave source with $h \to 0$ may be written

$$U_{cw} = ik_\alpha A_{cw} \Psi \frac{e^{-ik_\alpha R}}{R}. \qquad (C.26)$$

where $A_{cw} = 1 - P$ and is given by (C.10). The corresponding displacement for the displacement due to a point force at the free surface is given by (C.25). This may be written

$$U_{PF} = ik_\alpha A_{PF} \Psi \frac{e^{-ik_\alpha R}}{R} \tag{C.27}$$

where

$$A_{PF} = \frac{\eta K Q}{\mu \sin^2\theta} \tag{C.28}$$

For the case of $\alpha^2 = 3\beta^2$, (28) reduces to

$$A_{PF} = \frac{5}{3} \frac{\eta Q}{\sin^2\theta} \tag{C.29}$$

Comparing (26) and (27), we see that the displacements take the same form for both sources, differing only by the take-off angle dependent factors ηA_{PF} and A_{cw}. These factors are tabulated below and are plotted in Fig. C.1.

θ	A_{cw}	A_{PF}/η
0	0	0.556
10	0.046	0.554
20	0.178	0.549
30	0.374	0.542
40	0.602	0.536
50	0.825	0.536
60	1.000	0.556
70	1.072	0.627
80	0.921	0.848
90	0	1.667

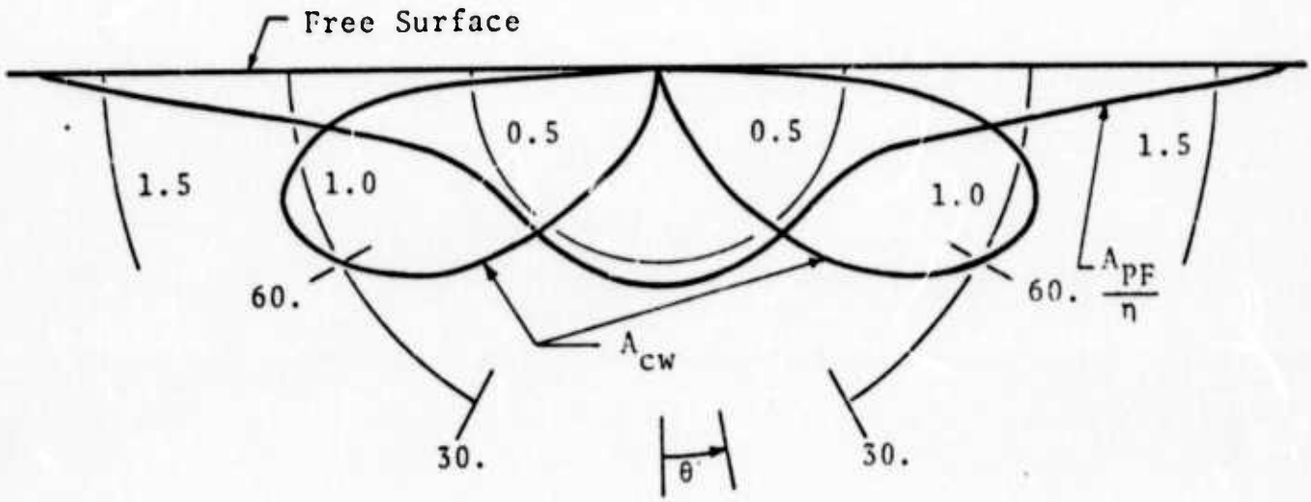


Figure C.1. The takeoff angle (θ) dependent factors in the far field displacement due to a compressional wave source at vanishingly small burial depth (A_{CW}) and a concentrated force applied at the free surface (A_{PF}/η). The material properties are such that $\alpha^2 = 3\beta^2$.

Summary

As is seen in Fig. C.1, the seismic waves directed downward (of interest for teleseismic monitoring) are distinctly different for a compressional wave source at vanishingly small depth and a concentrated force applied to the surface. These two radiation patterns are at least roughly representative of those to be expected from fully contained and cratering shots. In reality there is, of course, a continuous limit between the two as one decreases the depth of burial of a fully contained explosion. However, elastically there is no such continuous limit due to the different free surface boundary conditions for the two cases.

APPENDIX D

THEORETICAL AMPLITUDE SCALING FOR RAYLEIGH WAVES GENERATED BY UNDERGROUND NUCLEAR EXPLOSIONS

I. INTRODUCTION

An understanding of the gross scaling properties of the various kinds of waves generated by seismic events provides a useful frame of reference for understanding the actual data. As has been pointed out by Bache, et al. (1974), the surface wave theory developed by Harkrider (1964) predicts that surface wave magnitude should scale with the product of the source material shear modulus, μ, and the static value of the reduced displacement potential, Ψ_∞. That is,

$$M_s \approx \log [\mu \Psi_\infty] , \tag{1.1}$$

where M_s is a consistently measured Rayleigh wave magnitude. The appearance of this scaling law in the data is, of course, complicated by travel path and depth of burial effects, as well as by the difference between the actual explosion source and the pure center of dilatation model - r which the scaling law is derived. Still, our understanding of the spherically symmetric explosion contribution to the Rayleigh wave is quite helpful in separating out the contribution of these other effects.

The scaling law (1.1) is not widely known among those interested in nuclear explosion seismology and, indeed, there seems to be a certain amount of confusion on this point. For this reason a detailed derivation of the law is given below. We begin with a discussion of the elastic half space solutions cited by others (e.g., Marshall (1970)), to provide a scaling law for surface waves. After noting the logical inconsistency of this kind of analysis, we proceed to give a modified half

space solution which provides an elementary verification of the scaling law (1.1). Finally, the appearance of the same scaling law for an explosion in a layered half space is briefly discussed.

Before proceeding with the detailed analysis, a brief discussion of the physical basis underlying this scaling law is in order. In terms of the reduced displacement potential, the radial stress may be written

$$\tau_{RR} = -\left[4\mu \frac{\Psi}{R^3} + \frac{4\mu}{\alpha} \frac{\dot{\Psi}}{R^2} + \rho \frac{\ddot{\Psi}}{R}\right] , \tag{1.2}$$

where α is the P wave velocity, ρ is density, R is the distance to the point of observation and the dot indicates differentiation with respect to the reduced time, $t - R/\alpha$. Then at late time,

$$\tau_{RR} \approx -\frac{4\mu}{R^3} \Psi_\infty \ . \tag{1.3}$$

In the same fashion it can be shown that the long time limiting value of the hoop stress is

$$\tau_{\theta\theta} \approx \frac{2\mu}{R^3} \Psi_\infty \ . \tag{1.4}$$

Therefore, we see that the stress in the cavity vicinity scales the same way as the teleseismic Rayleigh wave. It can be said that it is this quantity that couples directly into the Rayleigh wave.

II. ELASTIC HALF SPACE SOLUTION

Consider a spherically symmetric explosion in a homogeneous, isotropic medium. The radial displacement, $U_R(R,t)$, may be written in terms of the reduced displacement potential $\Psi(t-R/\alpha)$ as follows:

$$U_R(R,t) = -\frac{\partial}{\partial R}\left[\frac{\Psi(t-R/\alpha)}{R}\right] \tag{2.1}$$

where R is the radial distance from the source, t is the time and α is compressional wave velocity. Equation (2.1) is equivalent to the assumption that a radial stress $\tau_{RR} = -P(t)$ is applied to the surface of a spherical cavity of some radius a.

Taking Fourier transforms, (2.1) may be written

$$\bar{U}_R = -\frac{\partial}{\partial R}\left[\bar{\Psi}(\omega)\,\frac{e^{-ik_\alpha R}}{R}\right] , \tag{2.2}$$

where $k_\alpha = \omega/\alpha$, the compressional wave number.

For a source of this form at a depth h in an elastic half space, the surface displacements are given by Ewing, Jardetsky and Press (1957), Eq. (2.86). The vertical component, $\bar{\omega}_0$ is

$$\bar{\omega}_0(r,\omega) = 2\bar{\Psi}(\omega)\int_0^\infty k_\beta^2 k\,\frac{(2k^2-k_\beta^2)}{F(k)}\,e^{-\nu_\alpha h}\,J_0(kr)\,dk , \tag{2.3}$$

where the Rayleigh function

$$F(k) = (2k^2-k_\beta^2)^2 - 4k^2\nu_\alpha\nu_\beta ,$$

with

$$\nu_\gamma = k^2 - k_\gamma^2 \quad , \quad \gamma = \alpha \text{ or } \beta \quad ,$$

and $k_\beta = \omega/\beta$, the shear wave number.

The Rayleigh wave contribution to the integral (2.3) is easily found by evaluating the residues at the poles of the Rayleigh function. At large epicentral distances, the Rayleigh waves are:

$$\bar{\omega}_0 = -4i(2\pi)^{\frac{1}{2}}\bar{\Psi}(\omega)\,\frac{k_r^{\frac{1}{2}}k_\beta^2(2k_r^2-k_\beta^2)}{r^{\frac{1}{2}}F'(k_r)}\exp\left[-i(\nu'_\alpha h+k_r R-\pi/4)\right] \quad ,$$

$$F'(k_r) = \frac{dF(kr)}{dk} \quad , \tag{2.4}$$

where $k_r = \omega/c_r$ is the Rayleigh wave number with c_r the velocity of Rayleigh waves. Also, $\nu'_\alpha = k_r^2 - k_\alpha^2$. There appear to be errors in the analogous expression of Marshall (1970) accounting for differences between the two. These differences do not, however, affect the scaling properties.

The surface wave magnitude M_s is measured from long period surface waves. Therefore, a scaling law is deduced from the low frequency behavior of (2.4). Now, we note that

$$\lim_{\omega\to 0} i\omega\bar{\Psi}(\omega) = \lim_{t\to\infty}\Psi(t) = \Psi_\infty \quad . \tag{2.5}$$

Cherry, et al., (1973, 1974) have shown that $i\omega\bar{\Psi}(\omega)$ is constant over a considerable frequency range and certainly for those frequencies of interest for teleseismic surface waves. Therefore, for low frequencies

$$\bar{\omega}_0 = -4(2\pi)^{\frac{1}{2}}\psi_\infty \frac{k_r^{\frac{1}{2}} k_\beta (2k_r^2 - k_\beta^2)}{\beta r^{\frac{1}{2}} F'(k_r)} \exp\left[-i(\nu'_\alpha h + k_r r - \pi/4)\right] \quad . \qquad (2.6)$$

If the simplifying assumption $\lambda = \mu$ is made, the amplitude of the teleseismic Rayleigh wave is

$$|\bar{\omega}_0| \approx 2.85 \frac{\omega^{\frac{1}{2}}}{r^{\frac{1}{2}}} \frac{\psi_\infty}{\beta^{3/2}} \quad . \qquad (2.7)$$

This dependence on $\psi_\infty/\beta^{3/2}$ is essentially the same as that deduced by Marshall (1970). It is equivalent to the scaling law

$$M_S \approx \log \frac{\psi_\infty}{\beta^{3/2}} \quad , \qquad (2.8)$$

which is rather different from (1.1).

The difficulty with the scaling law (2.8) is that the analysis on which it is based is not relevant to the problem at hand. The objective is to determine the scaling of Rayleigh waves with the source properties, deleting travel path effects. In the foregoing, changes in the source and travel path properties are linked and the practical meaning of (2.8) is obscure. In the following section a modified half space solution in which this difficulty is surmounted will be given.

III. THE RAYLEIGH WAVES FROM AN EXPLOSION IN ONE MATERIAL EMBEDDED IN A HALF SPACE OF A SECOND MATERIAL

We are interested in the effect of changing source region properties on the Rayleigh waves in a half space for which the material properties are held constant. A simple model providing interesting results is that of a spherical inclusion embedded in a whole space of the half space material (Harkrider and Bache (1975)). The source region geometry is illustrated in Fig. 1. The P waves emanating from the spherical inclusion of radius R_s will then be treated as the source for the half space problem, with the source region assumed to be transparent.

Referring to Fig. 1, we begin by computing the P waves in material 2 due to the imposition of a pressure pulse on the spherical cavity of radius R_0. For the spherically symmetric source in a whole space the displacement (U_R) and radial stress (τ_{RR}) written in potential form are:

$$\bar{U}_{R_i} = \frac{\partial \bar{\Phi}_i}{\partial R} ,$$

$$\bar{\tau}_{RR_i} = (\lambda_i + 2\mu_i) \frac{\partial^2 \bar{\Phi}_i}{\partial R^2} + \frac{2\lambda_i}{R} \frac{\partial \bar{\Phi}_i}{\partial R} , \tag{3.1}$$

where the subscript i = 1, 2, indicates the material and λ, μ are the Lamé constants. The potentials satisfy wave equations and have the general solution form

$$\bar{\Phi}_1 = A_1 \frac{e^{-ik_{\alpha_1} R}}{R} + B_1 \frac{e^{ik_{\alpha_1} R}}{R} ,$$

$$\bar{\Phi}_2 = A_2 \frac{e^{-ik_{\alpha_2} R}}{R} . \tag{3.2}$$

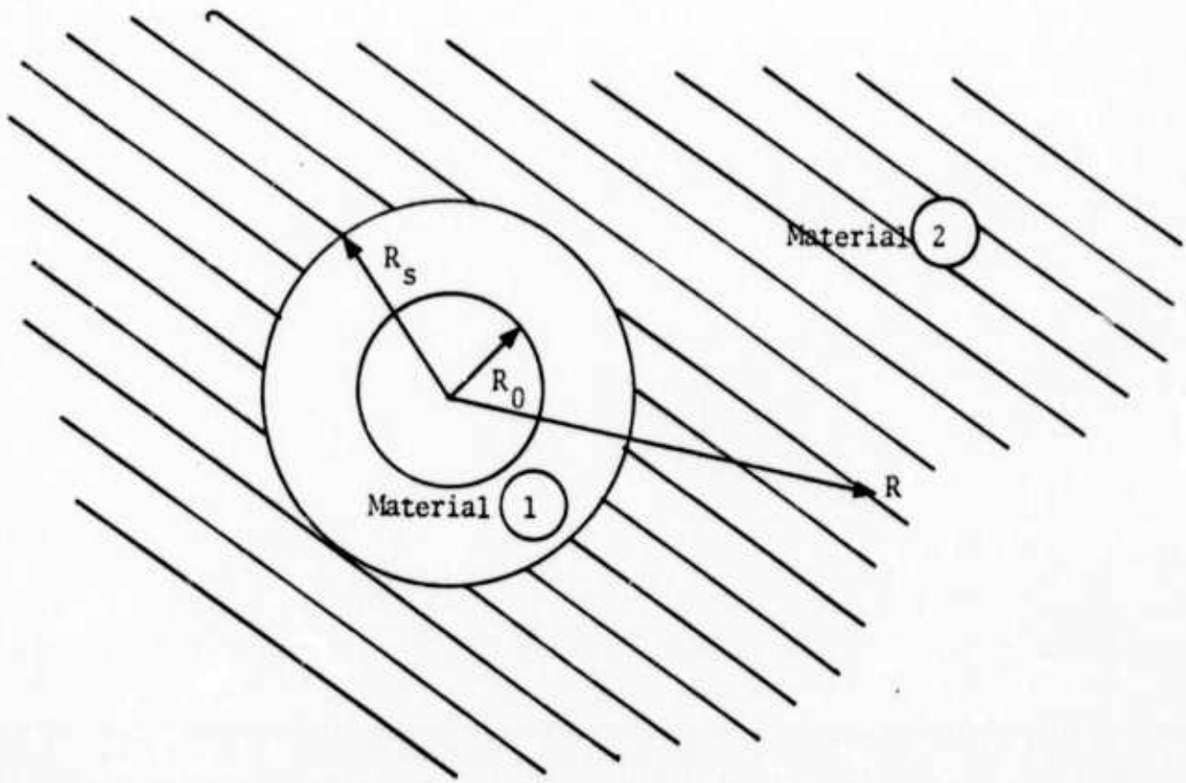


Figure 1. Geometry for an explosion in a spherical cavity of radius R_0 embedded in a spherical inclusion of radius R_s. The inclusion is made up of material 1 and is embedded in a whole space of material 2.

The appropriate boundary conditions are continuity of stress and displacement at the material discontinuity and the imposition of a spectral pressure on the wall of the cavity. That is,

$$\bar{\tau}_{RR_1}(R_0) = -\bar{P}(\omega) \quad ,$$

$$\bar{U}_{R_1}(R_s) = \bar{U}_{R_2}(R_s) \quad , \tag{3.3}$$

$$\bar{\tau}_{RR_1}(R_s) = \bar{\tau}_{RR_2}(R_s) \quad .$$

Using (3.1) and (3.2), the boundary conditions give three equations in the three unknown coefficients A_1, B_1, A_2. Since we are interested in the P waves emanating from the source region in material 2, A_2 is of primary interest. Solving (3.1) - (3.3) this is

$$A_2 = -\frac{\bar{P}(\omega)R_0^3}{\mu_2 E_1(R_0)} \left\{ \frac{P\, e^{-iF_1(R_s)} - H\, e^{iF_1(R_s)}}{P\, e^{-iF_1(R_0)} - H\, e^{iF_1(R_0)}} \right\} \frac{E_1(R_s)}{E_2(R_s)}\, e^{iF_2(R_s)} \tag{3.4}$$

where

$$H = \frac{D_1(R_s)}{D_2(R_s)}\, e^{i[G_2(R_s)-G_1(R_s)]} - \frac{\mu_1}{\mu_2}\frac{E_1(R_s)}{E_2(R_s)}\, e^{i[F_2(R_s)-F_1(R_s)]} \quad ,$$

$$P = \frac{D_1(R_s)}{D_2(R_s)}\, e^{i[G_2(R_s)+G_1(R_s)]} - \frac{\mu_1}{\mu_2}\frac{E_1(R_s)}{E_2(R_s)}\, e^{i[F_2(R_s)+F_1(R_s)]} \quad ,$$

$$D_i(R) = \left(1 + k_{\alpha_i}^2 R^2\right)^{\frac{1}{2}} \quad ,$$

$$E_i(R) = \left[\left(4 - k_{\beta_i}^2 R^2\right)^2 + 16\, k_{\alpha_i}^2 R^2\right]^{\frac{1}{2}} ,$$

$$F_i(R) = k_{\alpha_i} R - \xi_i(R) ,$$

$$G_i(R) = k_{\alpha_i} R - \eta_i(R) ,$$

$$\xi_i(R) = \tan^{-1}\left[\frac{4k_{\alpha_i} R}{4 - k_{\beta_i} R^2}\right] , \quad \eta_i(R) = \tan^{-1}\left(k_{\alpha_i} R\right), \quad i = 1,2.$$

Comparing (3.1) to (2.2), the reduced displacement potential is related to the potential Φ by

$$\overline{\Phi}_1(\omega) = -\overline{\Psi}_1(\omega)\, \frac{e^{-ik_\alpha R}}{R} . \tag{3.5}$$

It is easily verified that the pressure pulse boundary condition of (3.3) is equivalent to a reduced displacement potential in the source material which is

$$\overline{\Psi}_1(\omega) = \frac{\overline{P}(\omega)\, R_0^3}{\mu_1 E_1(R_0)}\, e^{-i\left[\xi_1(R_0) - k_{\alpha_1} R_0\right]} \tag{3.6}$$

Using (3.6), we may write

$$\overline{\Phi}_2 = A_2 \frac{e^{-ik_{\alpha_2} R}}{R} , \tag{3.7}$$

with

$$A_2 = -\frac{\mu_1 E_1(R_s)}{\mu_2 E_2(R_s)} \bar{\Psi}_1(\omega) \left\{ \frac{P e^{-iF_1(R_s)} - H e^{iF_1(R_s)}}{P e^{-iF_1(R_0)} - H e^{iF_1(R_0)}} \right\} e^{i[F_2(R_s)+\xi_1(R_0)]} .$$

Using the source specified by (3.7) as the transparent source in a half space, the vertical surface displacement is given by

$$\bar{\omega}_0(r,\omega) = -2A_2 \int_0^\infty k_{\beta_2}^2 \frac{k\left(2k^2-k_{\beta_2}^2\right)}{F_2(k)} e^{-\nu_{\alpha_2} h} J_0(kr)\, dk . \quad (3.8)$$

where r is epicentral distance in a cylindrical coordinate system.

Comparing (3.8) to the analogous expression (2.3) for a homogeneous half space, we see that (3.8) may be viewed as the vertical surface displacement due to a source specified by a modified reduced displacement potential, $\bar{\Psi}_2(\omega)$, written in terms of $\bar{\Psi}_1(\omega)$ and a source transmission coefficient, $T(\omega)$. That is, set

$$A_2(\omega) = -\bar{\Psi}_2(\omega)$$

with

$$\bar{\Psi}_2(\omega) = T(\omega)\, \bar{\Psi}_1(\omega) \quad , \quad (3.9)$$

and

$$T(\omega) = \frac{\mu_1 E_1(R_s)}{\mu_2 E_2(R_s)} \left\{ \frac{P e^{-iF_1(R_s)} - H e^{iF_1(R_s)}}{P e^{-iF_1(R_0)} - H e^{iF_1(R_0)}} \right\} e^{i[F_2(R_s)+\xi_1(R_0)]}$$

The Rayleigh wave contribution to the far field vertical surface displacement is now given by (2.4) with Ψ_2 replacing Ψ.

The low frequency behavior of the Rayleigh wave vertical surface displacement is needed to determine the dependence of M_s on the source parameters. It can be shown that

$$\lim_{\omega \to 0} |T(\omega)| = \frac{\mu_1}{\mu_2} \left\{ \frac{Q\left(1 - \frac{\mu_1}{\mu_2}\right) + \left(1 + Q\frac{\mu_1}{\mu_2}\right)}{Q\left(1 - \frac{\mu_1}{\mu_2}\right)\left(\frac{R_0}{R_s}\right)^3 + \left(1 + Q\frac{\mu_1}{\mu_2}\right)} \right\} \tag{3.10}$$

where the notation

$$Q = \frac{3\alpha_1^2}{4\beta_1^2} - 1$$

has been introduced. If the simplifying assumption $\alpha_1^2 = 3\beta_1^2$ is made, (3.10) reduces to

$$\lim_{\omega \to 0} |T(\omega)| = \frac{\mu_1}{\mu_2} \left\{ \frac{9}{5\left(\frac{R_0}{R_s}\right)^3 \left(1 - \frac{\mu_1}{\mu_2}\right) + 4 + \frac{5\mu_1}{\mu_2}} \right\}$$

$$= \frac{\mu_1}{\mu_2} \hat{T} \quad . \tag{3.11}$$

Then, combining (3.11) with (3.9) and taking the appropriate long period limits (see (2.5)), the amplitude of the teleseismic Rayleigh wave (analogous to (2.7) for the homogeneous half space) takes the form:

$$|\bar{\omega}_0| \approx 2.85 \frac{\omega^{\frac{1}{2}}}{r^{\frac{1}{2}}\beta_2^{3/2}\mu_2} \mu_1 \hat{T} \Psi_\infty \quad , \tag{3.12}$$

where Ψ_∞ is taken to be the static value of the explosion reduced displacement potential, $\bar{\Psi}_1(\omega)$.

Therefore, the dependence of M_S on the source parameters for this simplified model is

$$M_S \approx \log [\mu_1 \hat{T} \Psi_\infty] \quad . \tag{3.13}$$

This is identical to the scaling law (1.1), which was our objective, with the exception of the factor $\hat{T}$.

Let us now take a closer look at what will be termed the Ψ_∞ transfer function, $\hat{T}$. Consider the static problem of applying a constant pressure in the cavity of radius R_0 in Fig. 1. This problem can be solved by taking the strain potential of (3.1) and assuming solutions in the two materials of the form:

$$\phi_1 = \frac{A_1}{R} + B_1 R^2 \quad ,$$

$$\phi_2 = \frac{A_2}{R} \quad . \tag{3.14}$$

Applying a pressure of $-P$ at $R = R_0$ and requiring continuity of radial stress and displacement at $R = R_S$, one can solve for the constant coefficients. It is easily shown that

$$A_2 = -\frac{\mu_1}{\mu_2} \left\{ \frac{Q\left(1 - \frac{\mu_1}{\mu_2}\right) + \left(1 + Q\frac{\mu_1}{\mu_2}\right)}{Q\left(1 - \frac{\mu_1}{\mu_2}\right)\left(\frac{R_0}{R_S}\right)^3 + \left(1 + Q\frac{\mu_1}{\mu_2}\right)} \right\} \Psi_\infty \quad , \tag{3.15}$$

where

$$\Psi_\infty = - \frac{P R_0^3}{4\mu_1} \quad .$$

This result is identical to the low frequency limiting case for the dynamic problem given in (3.9) and (3.10).

Note that in material 1 the radial stress is given by

$$\tau_{RR_1}(R) = 4\mu_1 \left(\frac{A_1}{R^3} + 2QB_1 \right) \tag{3.16}$$

with the uniform stress term being required to maintain welded contact at the material interface. It is this term which is responsible for the presence of the non-unity factor $\hat{T}$ in (3.12) or (3.13).

From the examination of the static solution it appears that $\hat{T} \neq 1$ is, at least in part, a result of the idealized geometry that has been chosen. The meaning of this term for the physical problem of interest can be better understood by examining its value for typical problem parameters.

Consider first the case $R_0/R_S \approx 1$. Then $\hat{T} \approx 1$ and (3.13) is identical to (1.1). On the other hand, when $R_0/R_S \approx 0$,

$$\hat{T} = - \frac{9}{4 + \frac{5\mu_1}{\mu_2}} \quad . \tag{3.17}$$

Values of $\hat{T}$ for these two limiting cases and two intermediate examples are plotted versus μ_1/μ_2 in Fig. 2.

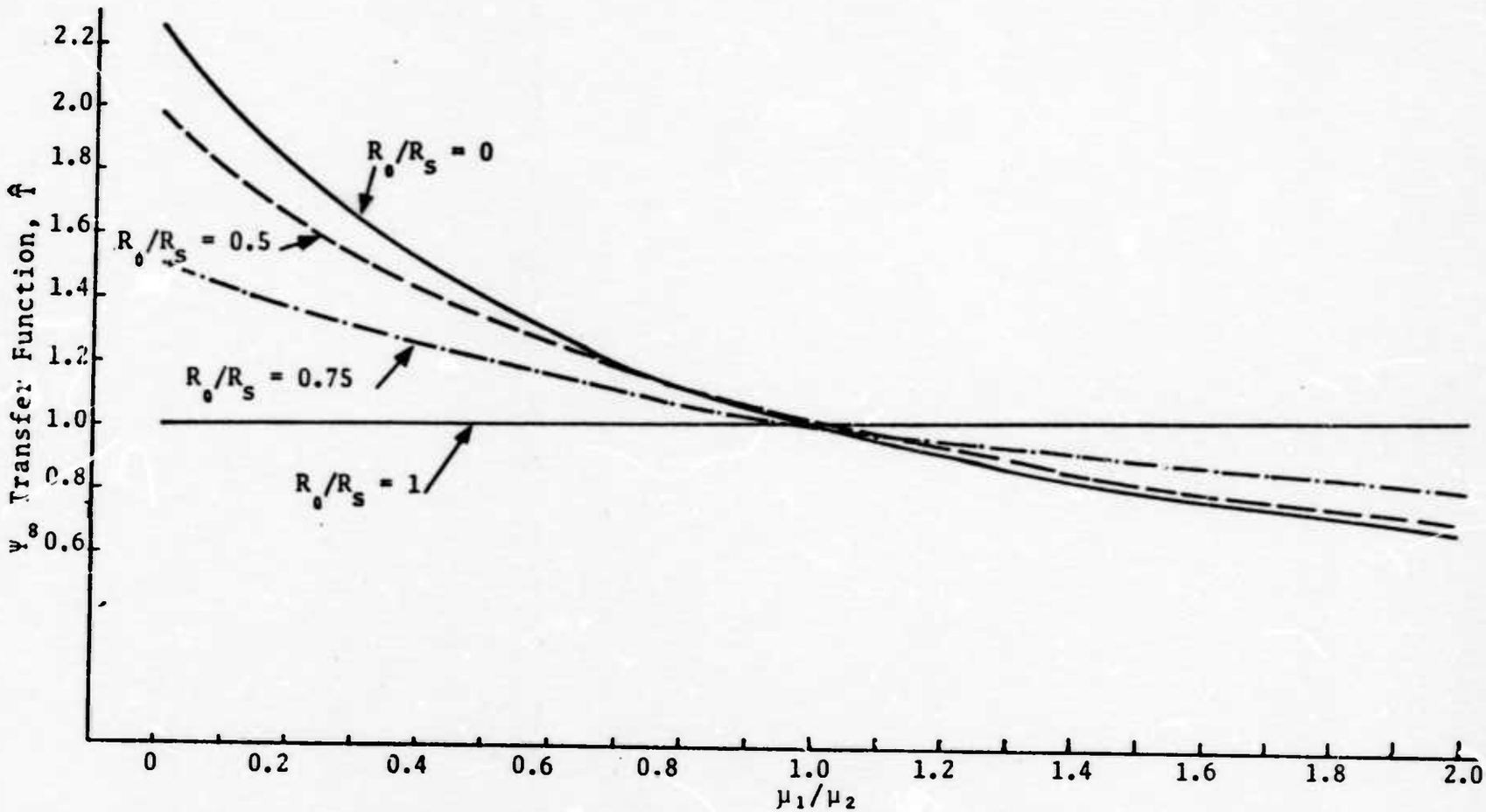


Figure 2. The Ψ_∞ transfer function, $\hat{T}$, plotted versus μ_1/μ_2 for four values of R_0/R_S. The source material is assumed to be a Poisson solid ($\alpha_1^2/\beta_1^2 = 3$).

In relating the simplified model studied here to the more general problem of interest, we first note that μ_1 represents the elastic properties of the explosion source region while μ_2 represents the "average" elastic properties of the source-receiver travel path for long period Rayleigh waves. The latter quantity is relatively constant over the earth's surface and should be approximately that for crustal granite, i.e., $\mu_2 \approx 400\text{-}500$ kbar. Nuclear explosions have been detonated in a variety of materials ranging from soft alluviums to hard granites. The range of μ_1/μ_2 values of practical interest are therefore from something less than 0.1 to nearly 1.0. It should also be noted that a Poisson's ratio of 0.25 has been assumed for the source material for Fig. 2. For many earth materials Poisson's ratio is somewhat lower; for example, a value of 0.20 is more appropriate for NTS tuff. Assuming this value, the curves of Fig. 2 are closer to unity. For example, $\hat{T} = 2.0$ for $R_0/R_s = \mu_1/\mu_2 = 0$, and the other values scale down proportionally.

In any case, for realistic explosion events it is very difficult to justify choices of the material and geometric constants for our simplified model which give values of $\hat{T}$ much different than unity. With this heuristic argument we conclude that the appropriate Rayleigh wave scaling is

$$M_s \approx \log [\mu_1 \Psi_\infty] \quad . \tag{3.18}$$

IV. THE RAYLEIGH WAVES FROM AN EXPLOSION IN A LAYERED HALF SPACE

Harkrider (1964) has given an expression for the Rayleigh waves from an explosion at depth in a layered half space. The explosion source was modeled as a pressure applied to the walls of a spherical cavity of radius R_0 just as in Section III above. That is, the source potential is given by (3.6).

The appropriate expression for the Fourier time transformed Rayleigh wave surface displacements due to the presence of this source in a layer denoted with subscript s is given by Harkrider (1964), Eq. (85). In our notation this is

$$\bar{w}_0 = 4\pi i \mu_s \Psi(\omega)\, k_r\, K_s\, \underset{\sim}{A}_R\, H_0^{(2)}(k_r r) \qquad (4.1)$$

where $\underset{\sim}{A}_R$ is the amplitude response of the layered medium and depends only on the layered earth model for the propagation path. The remaining undefined quantity, K_S, is the Rayleigh wave excitation factor which depends weakly on the source properties in the following sense. The explosion may be viewed as a discontinuity in displacements and stresses at the source depth. The factor K_S is related to this discontinuity and is therefore dependent on the properties of the source layer.

The Eq. (4.1) is only rigorously valid when the material in the layered earth model at the source depth and the material immediately around the explosion source are the same. This is a consequence of the form of the term K_S. Therefore, a direct derivation of the dependence of (4.1) on the source parameters encounters the same difficulty as the half space analysis of Section II; that is, one is forced to

change the properties of the propagation path along with the source material. There are several ways to circumvent this difficulty: (1) Replace the material at the source depth in the layered earth model with a thin layer of the local source material; (2) Use the simplified source region modeling of Section III to carry the explosion generated wave into the average crustal model for the travel path; (3) Ignore the inconsistency and change only $\mu_s \Psi(\omega)$ in (4.1) from event to event. All three of these methods lead to the same conclusion; the scaling of Rayleigh wave amplitude with $\mu_s \Psi_\infty$. A brief discussion of this result is given below.

For the long periods of interest for M_s, the amplitude response, $\underset{\sim}{A}_R$, and the Rayleigh wave excitation factor, K_S, are essentially unaffected by the presence of a thin layer of contrasting material at shallow depths. This is physically reasonable and has been verified computationally. Then (4.1) is equivalent to the scaling law (1.1).

In Section III an equivalent explosion source was developed for the case of an explosion in a spherical region of one material embedded in a second material. This equivalent source can be used in the half space solution. The resulting Rayleigh waves are given by (4.1) multiplied by the source transfer function $T(\omega)$ of (3.9). The scaling law is then given by (3.13). Just as in Section III it can be argued that $\hat{T} \approx 1$ for physically realistic problems and, once again, the scaling law (4.1) results.

The simplest procedure when dealing with the Rayleigh waves from explosions in different source materials but for which the average properties of the travel path remain constant is to ignore the inconsistency in the theory. The result is essentially the same as for the more elaborate procedures outlined above; scaling of M_s with $\log [\mu_s \Psi_\infty]$.

APPENDIX E

NARROW BAND FREQUENCY DISCRIMINANT CODES

MAGIC

MAGIC (MAGnitude Indication Code) is flowcharted in Fig. E.1.

MAGIC obtains its instructions from cards, and then prints out information to identify the particular run being performed. The code next proceeds to tape or drum, in order to input the event time series upon which the analysis is to be carried out. This time series is usually a single event; the code does, however, have the capability of summing several time series in order to artificially produce a multiple event signal.

If more than one event has been specified, MAGIC will add the individual time series, each with a different time lag and scale factor,

$$X(t) = \sum_i A_i X_i(t + \tau_i) ,$$

in order to produce a multiple event record, which is used in the rest of the program. This system allows considerable flexibility in the construction of synthetic multiple events. If, on the other hand, only one individual event is specified, then MAGIC will operate on this time series alone. Where a "multiple event" is specified in the flow chart, it should be kept in mind that this could also be one individual event, in which case the first loop shown would be inactive.

The single or multiple-event time series is then narrow-band filtered. In MAGIC, this can be accomplished in one of two ways.

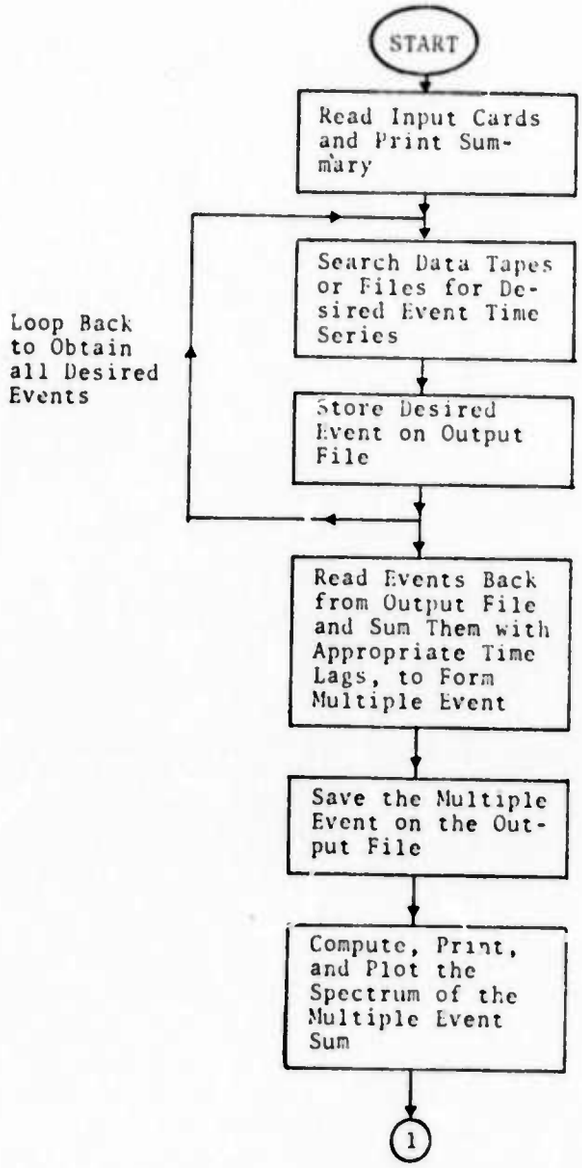


Figure E.1. MAGIC86 Flowchart.

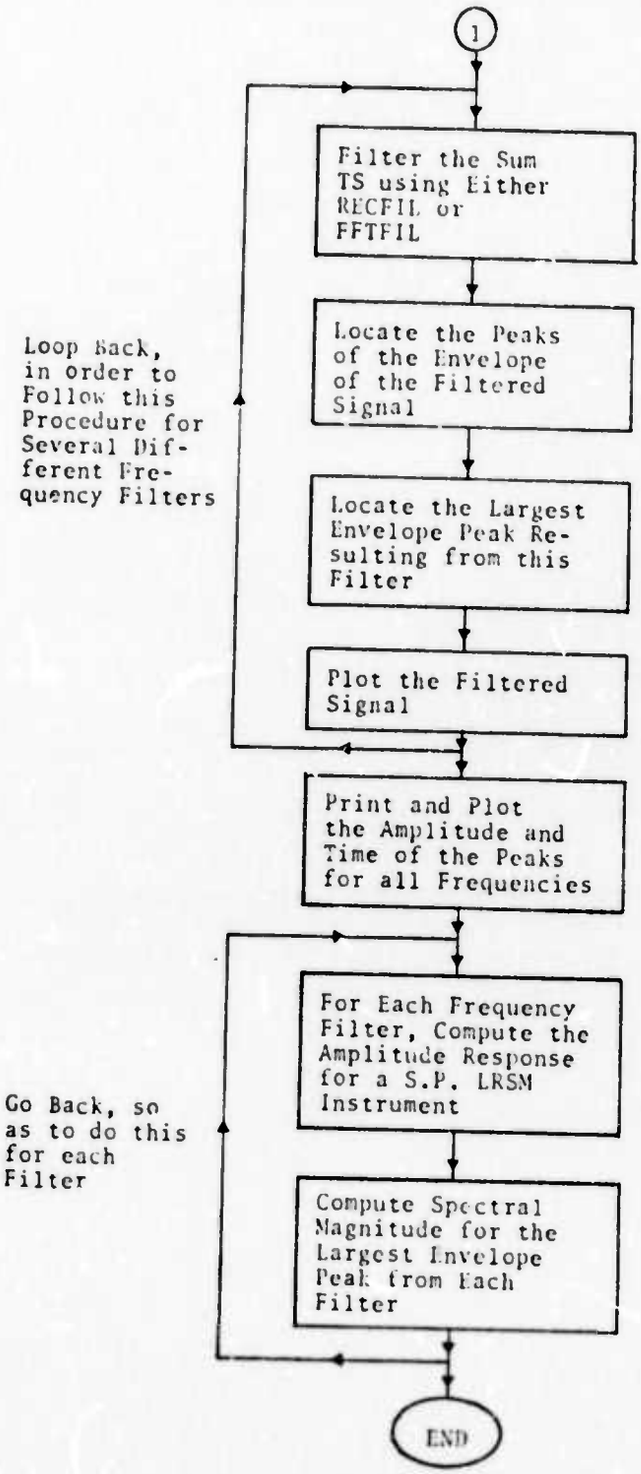


Figure E.1. MAGIC86 Flowchart (continued).

The first filter method is a recursive method, implemented in subroutine RECFIL. In this procedure, the time series is filtered by a four-term recursion relation which approximates the filter

$$F(\omega) = \left\{1 + \frac{Q(\bar{\omega}^2 - \omega^2)}{i\omega\bar{\omega}}\right\}^{-1},$$

in both the forward and backward time sense, and the two results are summed, in order to produce the effect of a phaseless filter. This filter is centered at frequency $\bar{\omega}$, and has a quality factor of Q.

Another filter method consists of performing a Fast Fourier Transform (FFT), multiplying the event in the frequency domain by a transfer function representing the same filter, and then inverse transforming to obtain the filtered signal.

Regardless of which filtering method is used, the result will appear as a sinusoidal carrier wave centered at $\bar{\omega}$, with an envelope containing information about the event time series.

MAGIC then calls a subroutine, PARAMA which, following a very complicated procedure, locates the peaks of the envelope. The peak of peaks at the envelope corresponding to this particular $\bar{\omega}$ is also located.

The program performs this filtering and maxima-selecting procedure for each of up to 20 filters, and stores the results.

MAGIC next cycles through the filter frequencies $\bar{\omega}$ again, and computes a spectral magnitude for each. The spectral magnitude is calculated as

$$M = \log_{10}(A_g) + B(\Delta)$$

for body waves, and

$$M = \log_{10}(A_g) + 1.656 \log_{10}(\Delta) + 1.689$$

for surface waves, where

Δ = event to detector distances in degrees,

$B(\Delta)$ = distance correction function from a table,

$A_g = Y_{MAX}\ \bar{\omega}/2\pi A_{inst}$,

Y_{MAX} = maximum of envelope for filter frequency $\bar{\omega}$,

A_{inst} = amplitude response of short-period LRSM seismometer at frequency $\bar{\omega}$.

MARS

As a result of experience with MAGIC, a more rapid and sophisticated method of processing data was devised, and this formed the theoretical basis for the program MARS (Multiple Arrival Recognition System). This code is in the process of development, and those features which are currently operational are flowcharted in Fig. E.2.

MARS begins by reading instructions from cards, and then reading a single time series from drum or tape file. No multiple event summation is currently implemented in this program.

A FFT is performed on the time series, and the spectrum is displayed. The transform is preserved throughout the program, so that only one forward transform need be done during the run.

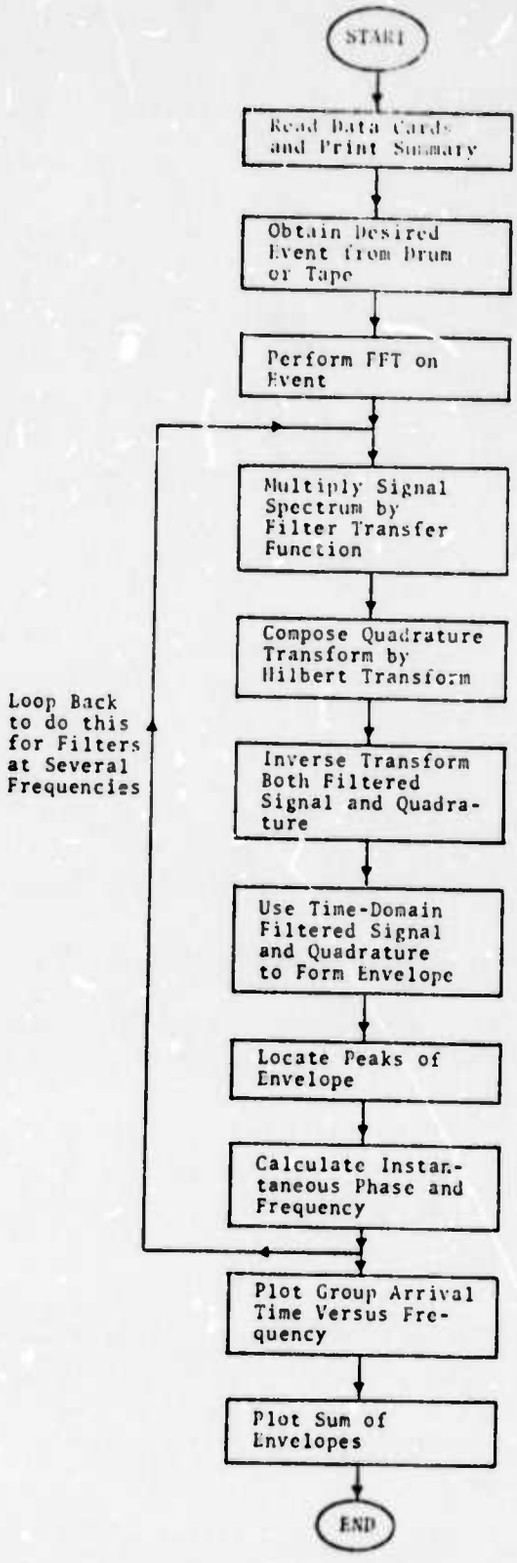


Figure E.2. MARS19 Flowchart.

MARS constructs the envelope of a narrow-band filtered signal by means of the Hilbert transform method (Bracewell, 1965). The Fourier transform of the input signal is multiplied by the transfer function of a filter, to give the Fourier transform of the filtered signal. This, in turn, is multiplied by $-i\ \mathrm{sgn}(\omega)$ to produce the quadrature transform. Both the filtered-signal transform and the quadrature transform are then inverse FFTed.

The filtered time series and the quadrature signal, now both in the time domain, are then regarded as the real and imaginary parts at a complex analytical signal; the modulus of the analytical signal is the envelope of the filtered signal. An instantaneous phase can also be calculated for the analytical signal, and differentiation yields an instantaneous frequency.

After these calculations, the envelope peaks can be located with relative ease. Each of these peaks represents the arrival of a wave group having the same center frequency as the filter. All of this can then be repeated for filters of different center frequencies. After doing this for a number of frequencies, the group arrival time versus filter frequency can be plotted, in order to obtain a display of the arrival at dispersed and undispersed wave modes.

The envelopes produced by the different filters can be added together in order to observe the arrival of various wave groups. If the envelopes are simply stacked, this will tend to emphasize the arrival of undispersed groups. On the other hand, if the envelopes being added are lagged relative to one another in the proper manner, then dispersed wave forms will manifest themselves.

Since MARS does all filtering in the frequency domain, this method grants much greater flexibility in the choice of filter shapes than was the case in MAGIC. Experimentation

with MARS has shown that the filter shape is very important; this point can best be illustrated with pictures.

Figure E.3 shows an input time series, LASA Event 1507, which was obtained from ACDA. This signal was passed through a square filter, centered at f_c = 0.5 Hz, with quality factor Q = 10. (All of the filters to be described are shown in Fig. E.4.) The sharp sides of the filter are reflected in the result, Fig. E.5, where a pervasive 0.05 Hz ringing is evident, which makes it difficult to locate the arrival with any certainty.

When the filter employed by MAGIC is used, the result is as shown in Fig. E.6. This is a much more reasonable result, the envelope appearing only when the signal does, and with roughly the same shape. This envelope has a problem, however, one which can barely be seen in the plot: there are actually 74 maxima in this curve. The source of this problem is not hard to find; considered in the frequency domain, this filter never actually goes to zero, no matter how far away from the center frequency one looks at it. The Event 1507 spectrum peaks at 1 Hz, where the amplitude is approximately 6 times greater than it is at the filter frequency of 0.5 Hz. The filter does not completely block this strong component, which is able to leak through and contaminate the envelope, with the result described. The lesson from this is that the filter must have a complete cutoff at some point in frequency.

When a semicircularly-shaped filter is used, the result is as shown in Fig. E.7. This looks quite a bit like the square filter, and is unacceptable for the same reasons.

A triangular filter brings about the result shown in Fig. E.8, a distinct improvement over the other envelopes.

The best results, however, come from a cusp-shaped filter, the envelope from which is displayed in Fig. E.9.

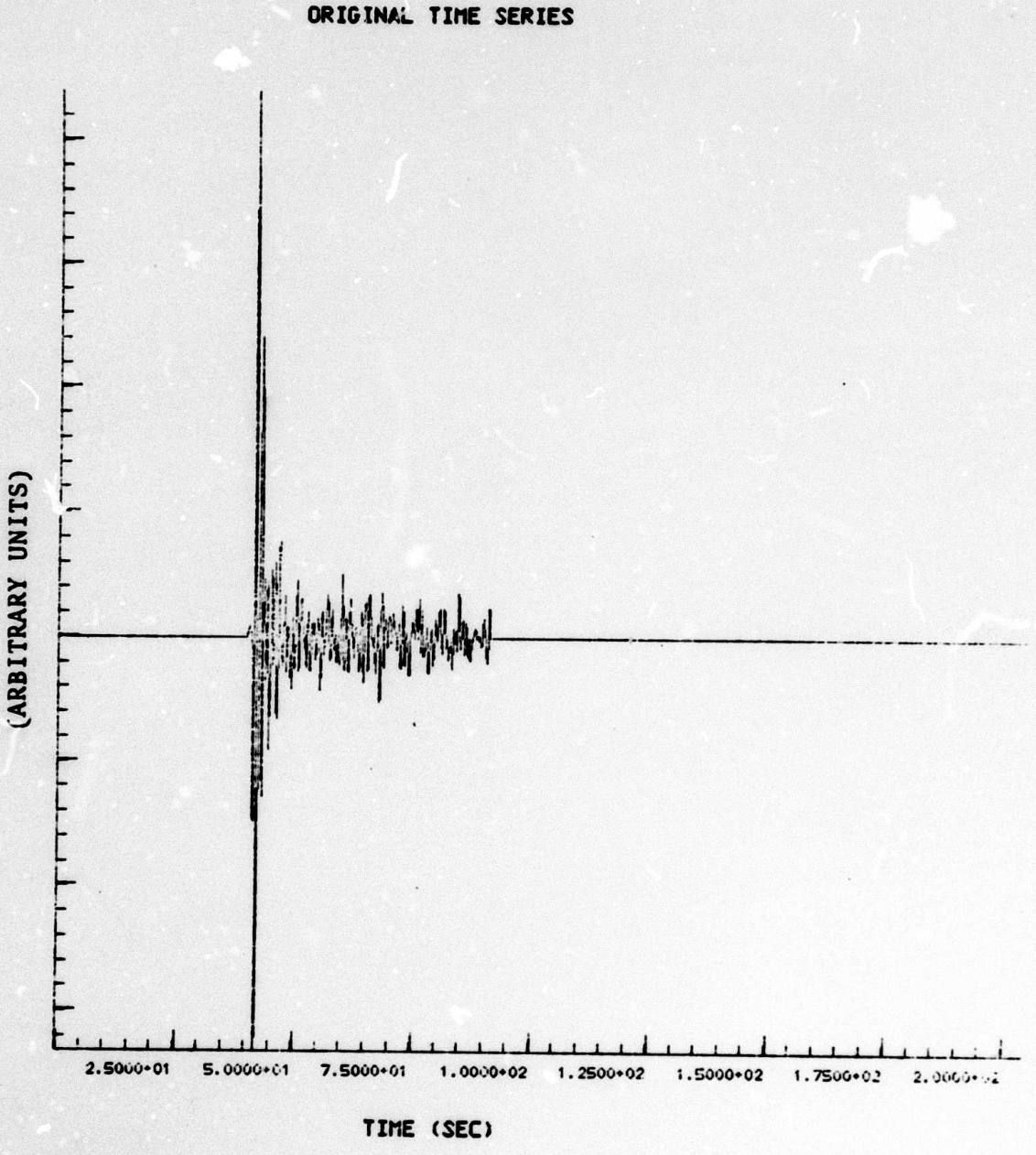


Figure E.3. LASA Event 1507, unfiltered. Amplitude (arbitrary units) (take at y-axis numbers).

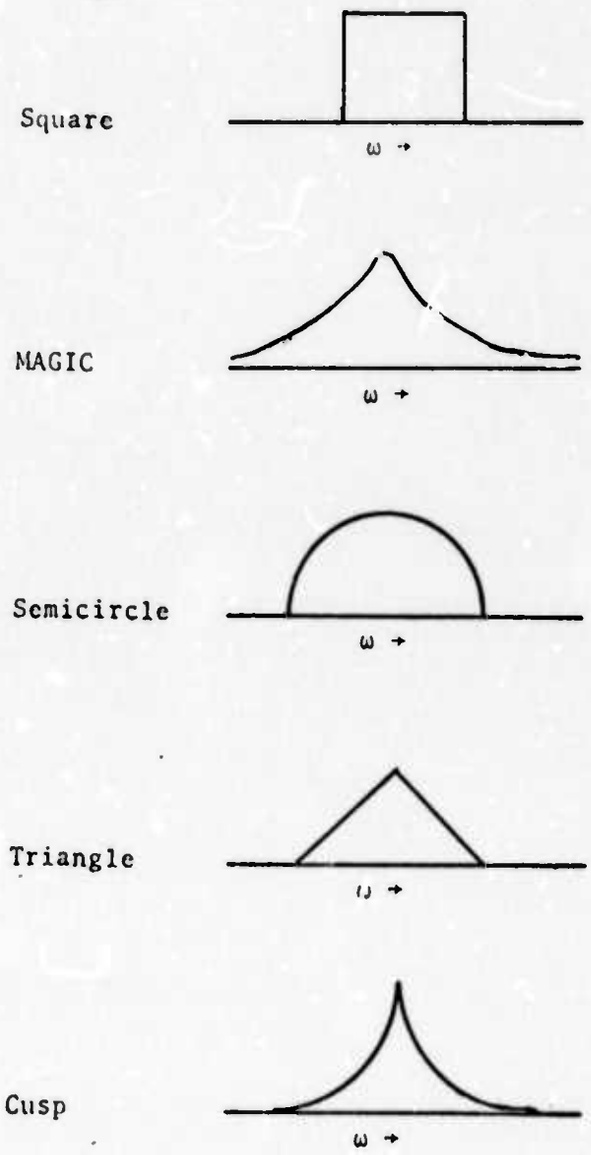


Figure E.4. Filter shapes.

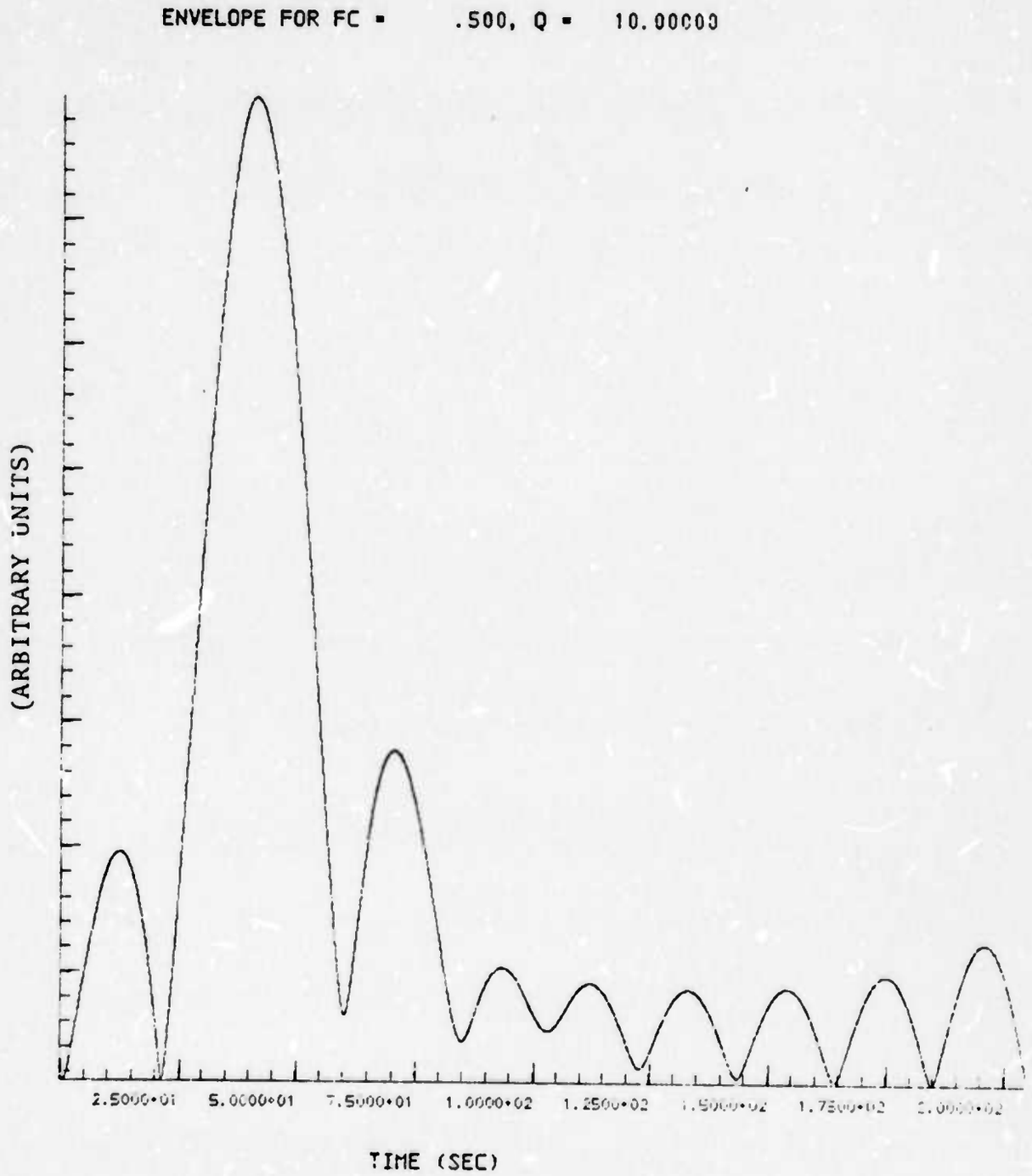


Figure E.5. LASA Event 1507, after passing through square filter of f_c = 0.5 Hz, Q = 10.

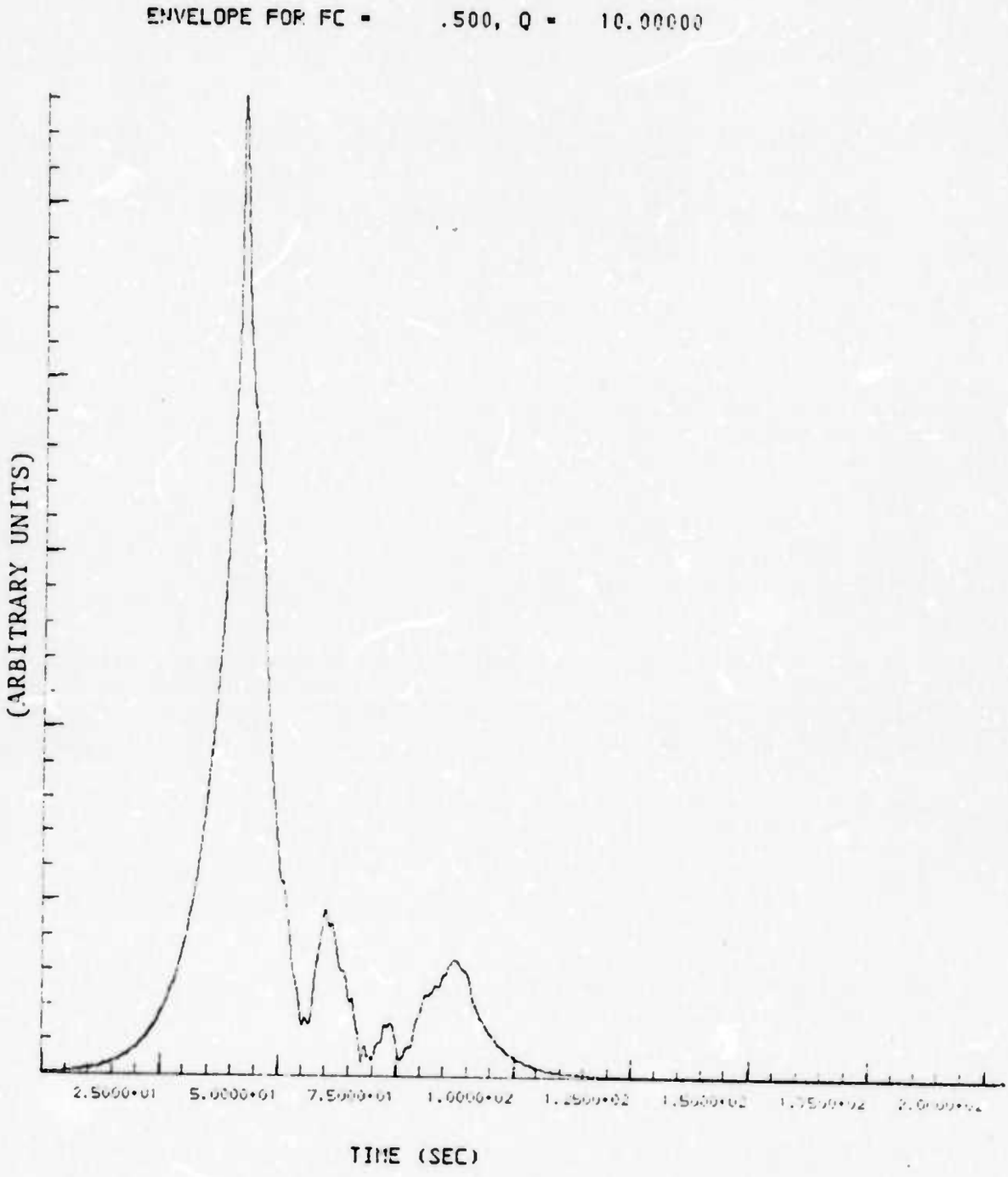


Figure E.6. LASA Event 1507, after passing through MAGIC filter of f_c = 0.5 Hz, Q = 10.

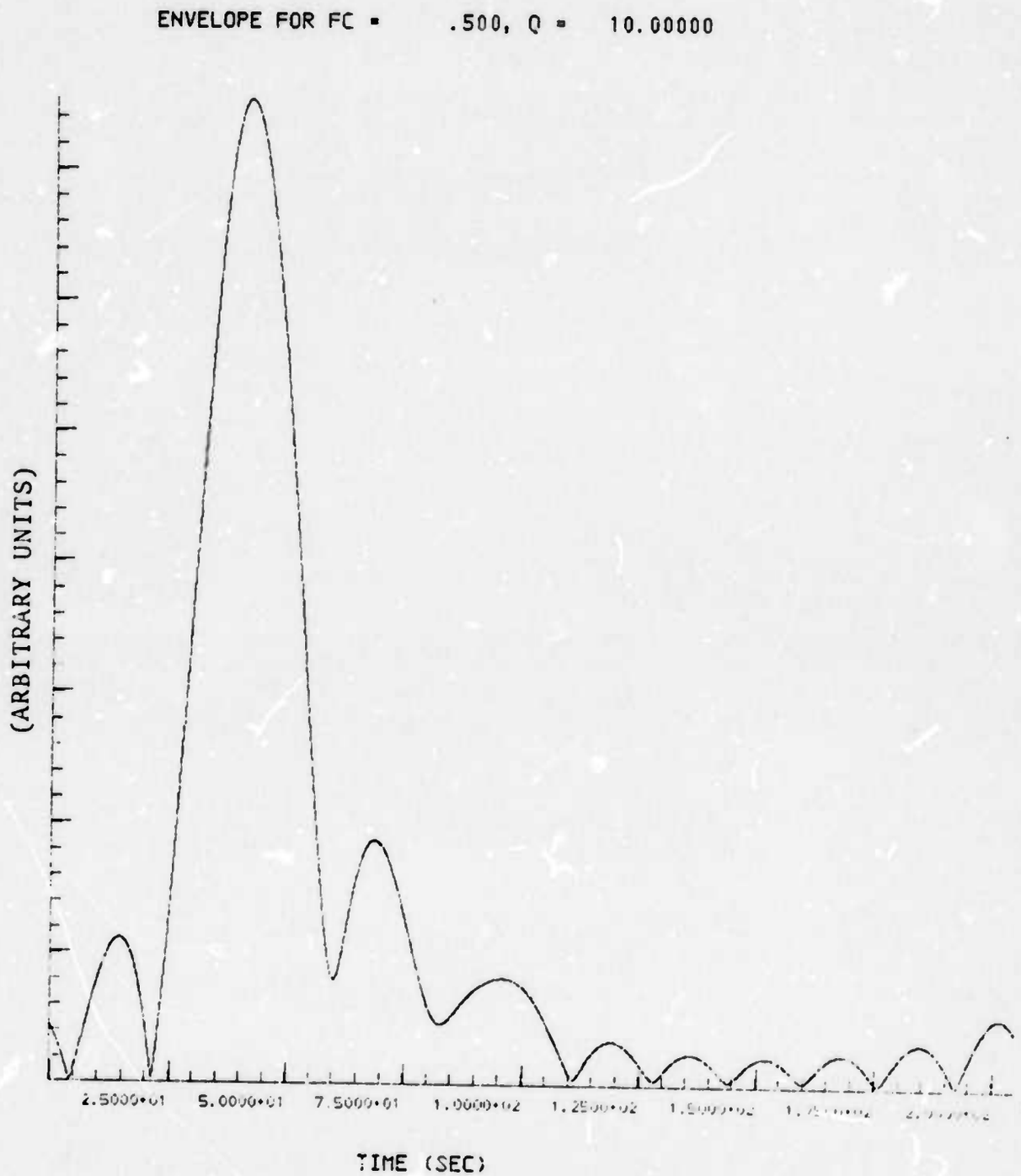


Figure E.7. LASA Event 1507, after passing through semi-circular filter of f_c = 0.5 Hz, Q = 10.

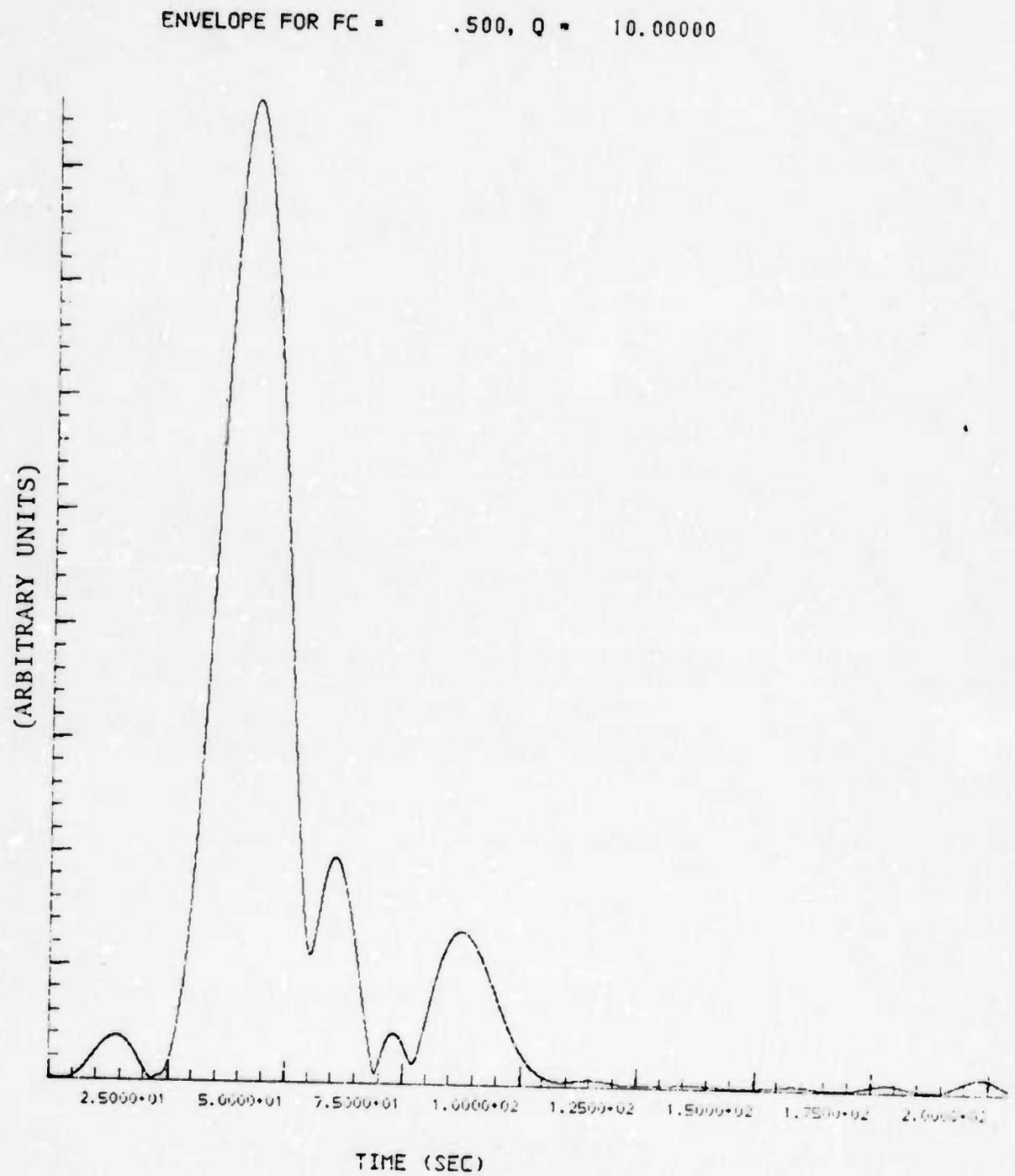


Figure E.8. LASA Event 1507, after passing through triangular filter of f_c = 0.5 Hz, Q = 10.

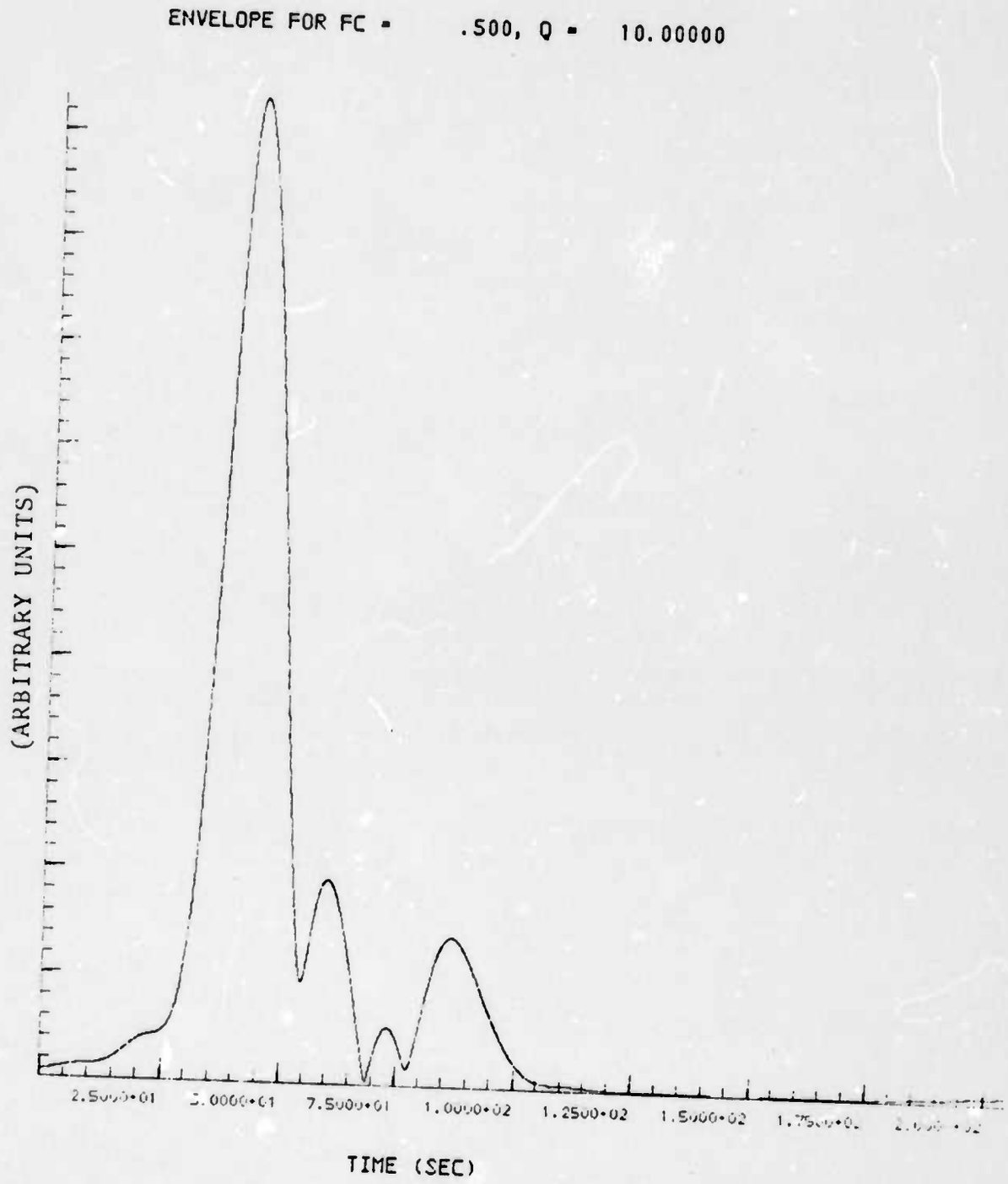


Figure E.9. LASA Event 1507, after passing through cusp-shaped filter of f_c = 0.5 Hz, Q = 10.

This case possesses the optimum features of (a) low amplitude in the absence of signal, and (b) immunity to noise outside the passband, leading to a smooth envelope, with a small number of easily locatable maxima. Of all the filters explored to date (there are a number which have not been shown here), the cusp filter appears to be the best.

APPENDIX F

MATCHED FILTERING

The COLLAPSE code, written by D. B. Rabenstine and J. W. Lambert of Teledyne Geotech SDL, was obtained and made operational on the S^3 Univac 1108. The program is flowcharted in Fig. F.1.

In the process of adapting this code for the S^3 computer, major restructuring of the main program was performed, along with numerous minor adjustments; these alterations do not affect the logical system described in Fig. F.1, but do considerably speed up the execution of the program, shorten the overall length of Fortran coding, and provide a small amount of storage optimization. Further improvement can be expected to include a probable speed-up of the Fourier transform operation, which forms the backbone of the program.

COL30, the latest version of COLLAPSE, is capable of drawing plots both on the line printer and on S^3's Gould 5000 plotter.

Since the COLLAPSE code, and the matched filtering operation which it performs, have been described in detail elsewhere (Alexander, et al., 1971), the remainder of this discussion will be concerned only with a demonstration of the program's ability.

Figure F.2a shows Event 6545, a presumed explosion in eastern Kazakhstan, as recorded at the Oyer subarray in Norway. A two second time window, commencing with the start of the P-wave signal at approximately t = 20 seconds, was extracted and used as a filter. Figure F.2b is for Event 6550, also a presumed Kazakhstan explosion, which is submerged in strong microseismic noise; the explosion itself is indicated by an arrow.

Reproduced from best available copy.

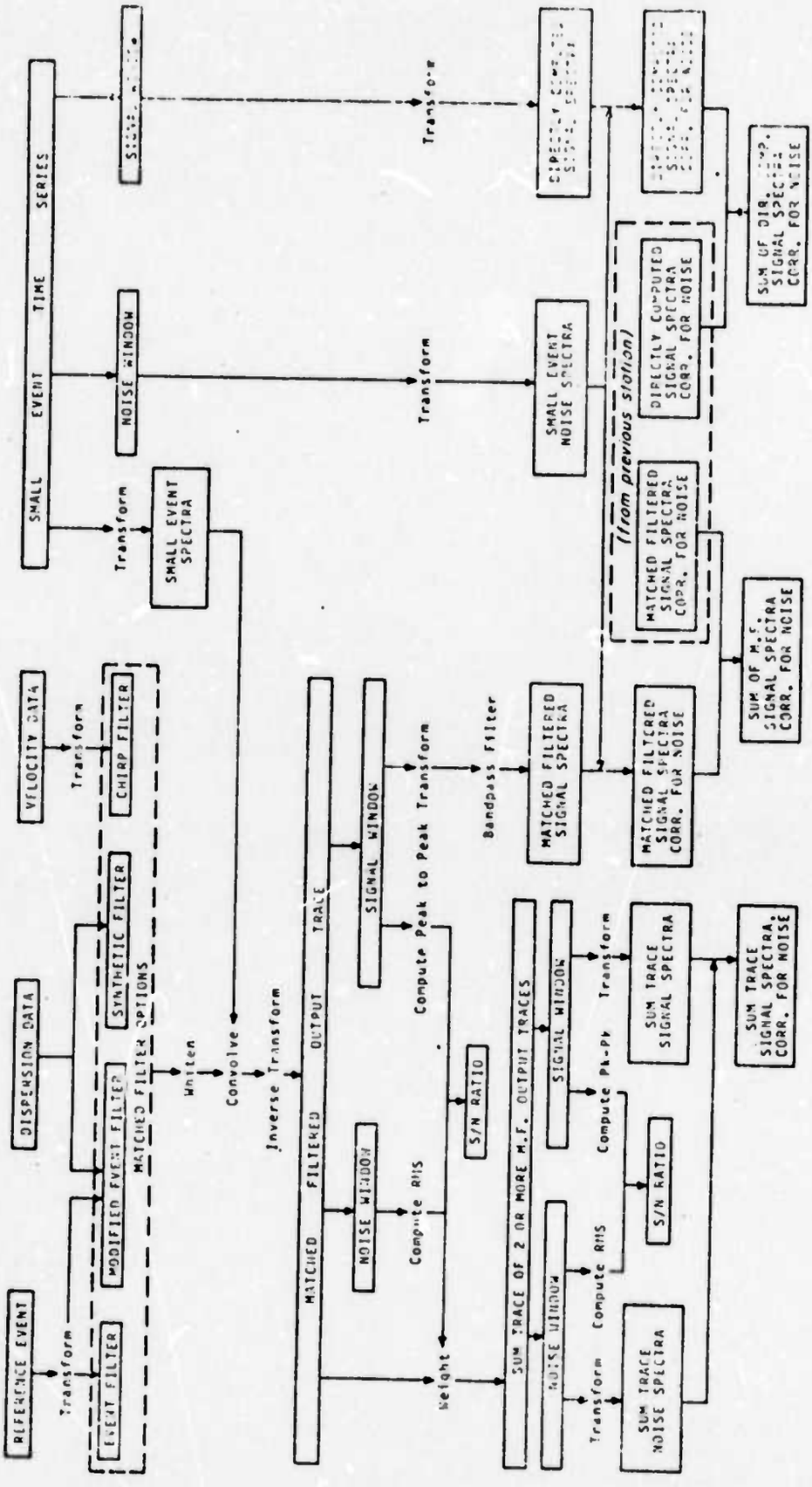


Figure F.1. COLLAPSE Code Flow Chart.

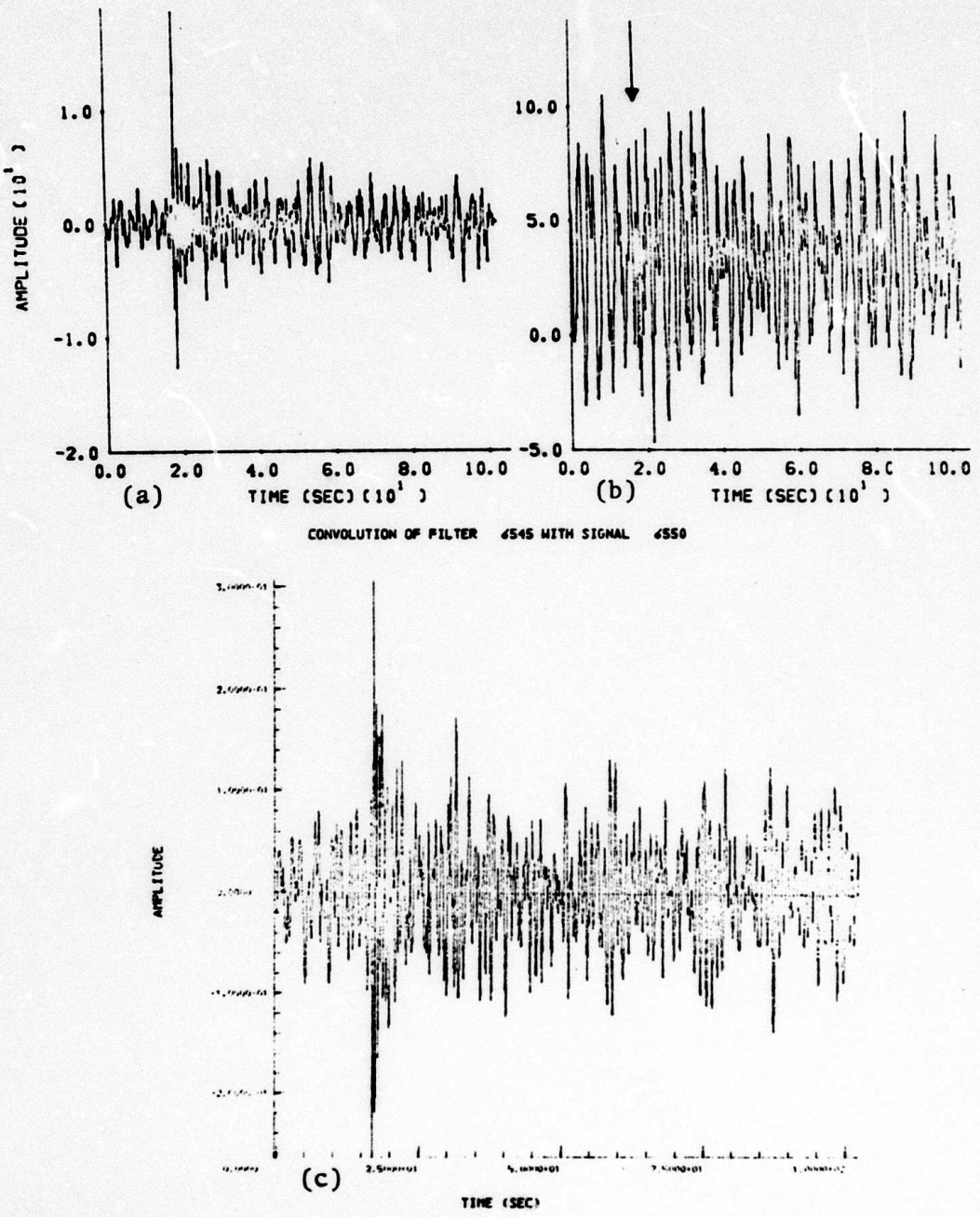


Figure F.2. Matched filter test for two presumed Russian explosions. A portion of the event in (a) was used as a filter for the event in (b), resulting in the response shown in (c).

When the matched filtering operation is performed, the result (Fig. F.2c) shows a very clear and significant response to the hidden event, at approximately t = 17 seconds.

Figure F.3a is the time series of an Asian earthquake, Event 6224. When this is used as a filter for Event 6550 (Fig. F.3b), the result (Fig. F.3c) indicates no significant response.

This demonstrates the ability of the matched filtering operation to discriminate between different classes of events. The principal question which remains concerning matched filtering consists of estimating the confidence level (or false alarm probability) associated with a given level of response.

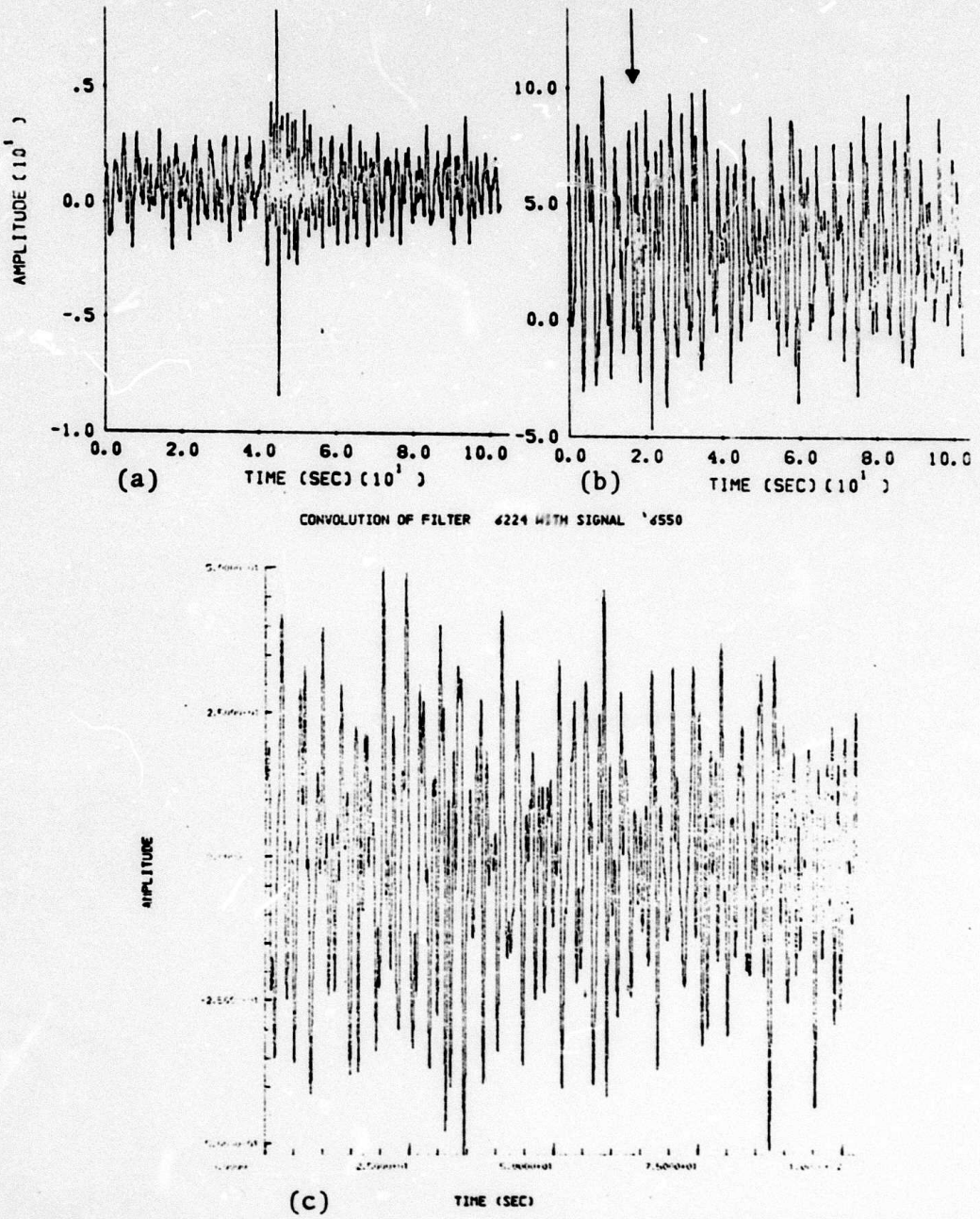


Figure F.3. Matched filter test for an apparent Russian explosion (b), filtered by an Asian earthquake (a), yielding the result shown in (c).

APPENDIX G

THE EQUIVALENT ELASTIC SOURCE DETERMINATION FOR NONLINEAR, FINITE DIFFERENCE EARTHQUAKE AND EXPLOSION SOURCE CALCULATIONS

G.1 INTRODUCTION

Powerful nonlinear finite difference computational techniques can be applied to obtain a realistic deterministic representation of an earthquake or explosion source of seismic energy. In order to link these nonlinear numerical calculations with efficient elastic wave propagation techniques, it is necessary to represent the source in terms of an equivalent elastic source. Such a representation in terms of an expansion in spherical harmonics was first suggested for geophysical applications by Archambeau (1964, 1968). For any arbitrary nonlinear source calculation, this equivalent elastic source representation can be derived, if the source calculation can be carried into the small displacement, elastic regime.

The linkage between nonlinear numerical explosion calculations and elastic wave propagation techniques via an equivalent elastic source has been routinely accomplished at S^3 for spherically symmetric explosions (e.g., Cherry, et al., (1973, 1974b)). A much more complex source configuration, an explosion in an axisymmetric tunnel, has also been treated (Cherry, et al., (1974a)) with the equivalent elastic source determined from the output of a 2-D axisymmetric Lagrangian finite difference code which had previously been linked to an Eulerian hydrodynamic calculation of the explosion. Recently, a 3-D deterministic simulation of a stick-slip earthquake faulting has been incorporated into a Lagrangian finite difference code (Cherry (1974)). In order to obtain an equivalent elastic source for this model, it was necessary to construct a code of complete generality, that is, with no

special symmetries built in. This code is the subject of this appendix.

We have developed a series of general purpose computer programs that determine the equivalent elastic source (EES) representation for any arbitrary nonlinear numerical source. The MULTEES (MULTipole Coefficients for an Equivalent Elastic Source) series of programs calculates the multipole coefficients for any general numerical (earthquake or explosion) source for which the calculation has been carried into the small displacement elastic region. MULTEES has been designed to process the output generated by either two or three dimensional source codes. Thus, the same programs can be applied to underground explosions and earthquakes. Furthermore, the numerical source codes linking to MULTEES can be configured for any arbitrary source. No special symmetries are demanded.

The primary mathematical, numerical analysis, and computational techniques underlying MULTEES will be described in the following sections along with a narrative outline of how MULTEES operates.

G.2 MULTIPOLE COEFFICIENTS IN TERMS OF POTENTIALS

The representation of a spatially limited source in terms of a multipole expansion in spherical harmonics has been discussed in a number of previous S^3 reports (e.g., Cherry, et al. (1974a), Bache, et al. (1974)). However, in order to introduce the definitions and notation required for describing MULTEES, the derivation of the expansion (multipole) coefficients in terms of potentials will be reviewed here.

The equation of motion in a homogeneous, isotropic, linearly elastic medium may be expressed as

$$\frac{\partial^2 \underset{\sim}{u}}{\partial t^2} = v_p^2 \nabla(\nabla \cdot \underset{\sim}{u}) - v_s^2 \nabla \times (\nabla \times \underset{\sim}{u}) , \qquad (G.1)$$

where $\underset{\sim}{u}(\underset{\sim}{r},t)$ is the particle displacement, while v_p and v_s are the compressional and shear wave velocities. Define the scalar and vector potentials by

$$\chi_4 = \nabla \cdot \underset{\sim}{u} ,$$

$$\underset{\sim}{\chi} = \frac{1}{2} \nabla \times \underset{\sim}{u} . \qquad (G.2)$$

By introducing these potentials, the equation of motion reduces to

$$\frac{\partial^2 \underset{\sim}{u}}{\partial t^2} = v_p^2 \nabla \chi_4 - 2 v_s^2 \nabla \times \underset{\sim}{\chi} . \qquad (G.3)$$

Taking first the divergence, then the curl of Eq. (G.3), the scalar and vector potentials may be shown to satisfy the wave equation for an elastic medium,

$$\left(\nabla^2 - \frac{1}{v_\alpha^2} \frac{\partial^2}{\partial t^2} \right) \chi_\alpha (\underset{\sim}{r},t) = 0 , \qquad (G.4)$$

where $\alpha = 1,2,3,4$ with $v_j = v_s$ for $j = 1,2,3$ and $v_4 = v_p$.

To derive solutions to Eq. (G.4), introduce the Fourier transform of the potentials defined as

$$\tilde{\chi}_\alpha(r,\omega) = \int_{-\infty}^{\infty} \chi_\alpha(\underset{\sim}{r},t)\ e^{-i\omega t}\ dt\ ; \tag{G.5}$$

conversely, by means of the Fourier integral theorem, χ can be expressed in terms of $\tilde{\chi}$ as

$$\chi_\alpha(\underset{\sim}{r},t) = \frac{1}{2\pi} \int_{-\infty}^{\infty} \tilde{\chi}_\alpha(r,\omega)\ e^{i\omega t}\ d\omega\ . \tag{G.6}$$

For convenience herein, let $F(f)$ represent the Fourier transform of the function f; that is,

$$F[f(t)] \equiv \tilde{f}(\omega) = \int_{-\infty}^{\infty} f(t)\ e^{-i\omega t}\ dt\ . \tag{G.7}$$

Thus, Eq. (G.4) reduces to the wave equation for the Fourier transform, namely,

$$\left(\nabla^2 + k_\alpha^2\right) \tilde{\chi}_\alpha(\underset{\sim}{r},\omega) = 0\ , \tag{G.8}$$

where the wave number $k_\alpha \equiv \omega/v_\alpha$. By this means, the wave equation for elastic body waves (G.4) has been reduced to the standard Helmholtz equation (G.8), which is separable in spherical coordinates. The "outgoing wave" solution for $\tilde{\chi}_\alpha$ can therefore be expanded in terms of spherical eigensolutions of Eq. (G.8):

$$\tilde{\chi}_\alpha(r,\theta,\phi,\omega) = \sum_{\ell=0}^{\infty} \sum_{m=0}^{\ell} \sum_{s=0}^{1} h_\ell^{(2)}(k_\alpha r)\, \tilde{A}_{\ell ms}^{(\alpha)}(\omega)\, Y_{\ell ms}(\theta,\phi) \qquad (G.9)$$

where $\tilde{A}_{\ell ms}^{(\alpha)}$ are multipole coefficients, $h_\ell^{(2)}$ are spherical Hankel functions of the second kind, and $Y_{\ell ms}$ are (unnormalized) spherical harmonics (Morse and Feshbach (1953)). In terms of the notation used in earlier S^3 reports, e.g., Cherry, et al. (1974a), $\tilde{A}_{\ell m_0}^{(\alpha)} \equiv \tilde{A}_{\ell m}^{(\alpha)}$ and $\tilde{A}_{\ell m_1}^{(\alpha)} \quad \tilde{B}_{\ell m}^{(\alpha)}$. For these discussions the following definitions will suffice:

$$h_\ell^{(2)}(k_\alpha r) = j_\ell(k_\alpha r) - i y_\ell(k_\alpha r)\ , \qquad (G.10)$$

$$Y_{\ell ms}(\theta,\phi) = \left\{ \begin{matrix} P_\ell^m(\cos\theta)\, \cos m\phi, & s = 0 \\ P_\ell^m(\cos\theta)\, \sin m\phi, & s = 1 \end{matrix} \right\}\ , \qquad (G.11)$$

where j_ℓ and y_ℓ are spherical Bessel functions of the first and second kind, respectively, and $P_\ell^m(\cos\theta)$ are associated Legendre functions. The orthogonality of the (unnormalized) spherical harmonics is expressed by

$$\int_0^{2\pi}\int_0^{\pi} Y_{\ell' m' s'}(\theta,\phi)\, Y_{\ell ms}(\theta,\phi)\, \sin\theta\, d\theta\, d\phi$$

$$= N_{\ell m}^2\, \delta_{\ell' \ell}\, \delta_{m' m}\, \delta_{s' s} \quad (m \neq 0)$$

$$= N_{\ell 0}^2\, \delta_{\ell' \ell}\, \delta_{m' 0}\, \delta_{s' 0}\, \delta_{s 0} \quad (m = 0) \qquad (G.12)$$

where the normalization factor $N_{\ell m}$ is

$$N_{\ell m}^2 = \frac{(4\pi/\varepsilon_m)(\ell+m)!}{(2\ell+1)(\ell-m)!} \qquad (G.13)$$

with $\varepsilon_0 = 1$ and $\varepsilon_m = 2$, $m \neq 0$.

$$\tilde{\chi}_\alpha(r,\theta,\phi,\omega) = \sum_{\ell=0}^{\infty} \sum_{m=0}^{\ell} \sum_{s=0}^{1} h_\ell^{(2)}(k_\alpha r)\, \tilde{A}_{\ell ms}^{(\alpha)}(\omega)\, Y_{\ell ms}(\theta,\phi) \qquad (G.9)$$

where $\tilde{A}_{\ell ms}^{(\alpha)}$ are multipole coefficients, $h_\ell^{(2)}$ are spherical Hankel functions of the second kind, and $Y_{\ell ms}$ are (unnormalized) spherical harmonics (Morse and Feshbach (1953)). In terms of the notation used in earlier S^3 reports, e.g., Cherry, et al. (1974a), $\tilde{A}_{\ell m_0}^{(\alpha)} \equiv \tilde{A}_{\ell m}^{(\alpha)}$ and $\tilde{A}_{\ell m_1}^{(\alpha)} \equiv \tilde{B}_{\ell m}^{(\alpha)}$. For these discussions the following definitions will suffice:

$$h_\ell^{(2)}(k_\alpha r) = j_\ell(k_\alpha r) - i y_\ell(k_\alpha r)\ , \qquad (G.10)$$

$$Y_{\ell ms}(\theta,\phi) = \left\{ \begin{matrix} P_\ell^m(\cos\theta)\, \cos m\phi, & s = 0 \\ P_\ell^m(\cos\theta)\, \sin m\phi, & s = 1 \end{matrix} \right\}\ , \qquad (G.11)$$

where j_ℓ and y_ℓ are spherical Bessel functions of the first and second kind, respectively, and $P_\ell^m(\cos\theta)$ are associated Legendre functions. The orthogonality of the (unnormalized) spherical harmonics is expressed by

$$\int_0^{2\pi}\int_0^{\pi} Y_{\ell' m' s'}(\theta,\phi)\, Y_{\ell ms}(\theta,\phi)\, \sin\theta\, d\theta\, d\phi$$

$$= N_{\ell m}^2\, \delta_{\ell' \ell}\, \delta_{m' m}\, \delta_{s' s} \quad (m \neq 0)$$

$$= N_{\ell_0}^2\, \delta_{\ell' \ell}\, \delta_{m' 0}\, \delta_{s' 0}\, \delta_{s 0} \quad (m = 0) \qquad (G.12)$$

where the normalization factor $N_{\ell m}$ is

$$N_{\ell m}^2 = \frac{(4\pi/\varepsilon_m)(\ell+m)!}{(2\ell+1)(\ell-m)!} \qquad (G.13)$$

with $\varepsilon_0 = 1$ and $\varepsilon_m = 2$, $m \neq 0$.

Application of the orthogonality of the spherical harmonics to Eq. (G.9) yields the following expression for the multipole coefficients:

$$\tilde{A}^{(\alpha)}_{\ell ms}(\omega) = \frac{1}{N^2_{\ell m}} \frac{1}{h^{(2)}_\ell (k_\alpha R)} \int_0^{2\pi} \int_0^{\pi} \tilde{\chi}_\alpha (R,\theta,\phi,\omega) \times Y_{\ell ms}(\theta,\phi) \sin\theta \, d\theta \, d\phi \, . \tag{G.14}$$

Substituting Eq. (G.5) for $\tilde{\chi}$ in the above expression shows that

$$\tilde{A}^{(\alpha)}_{\ell ms}(\omega) = \frac{1}{h^{(2)}_\ell (k_\alpha R)} F\left[A^{(\alpha)}_{\ell ms}(R,t)\right] = \frac{1}{h^{(2)}_\ell (k_\alpha R)} \int_{-\infty}^{\infty} A^{(\alpha)}_{\ell ms}(R,t) \, e^{-i\omega t} \, dt \, , \tag{G.15}$$

where

$$A^{(\alpha)}_{\ell ms}(R,t) \equiv \frac{1}{N^2_{\ell m}} \int_0^{2\pi} \int_0^{\pi} \chi_\alpha (R,\theta,\phi,t) \, Y_{\ell ms}(\theta,\phi) \times \sin\theta \, d\theta \, d\phi \, . \tag{G.16}$$

The quantities $A^{(\alpha)}_{\ell ms}(R,t)$ defined by Eq. (G.16) are referred to as the multipole coefficients in the time domain. An interpretation of $A^{(\alpha)}_{\ell ms}$ can be derived in the following manner. Starting with the expression for χ_α given by Eq. (G.6), replace $\tilde{\chi}_\alpha$ by its multipole expansion Eq. (G.9). Then substitute (G.15) for $\tilde{A}^{(\alpha)}_{\ell ms}$. Applying the Fourier integral theorem then yields in the time domain,

$$\chi_\alpha(\underset{\sim}{r},t) = \sum_{\ell=0}^{\infty} \sum_{m=0}^{\ell} \sum_{s=0}^{1} A^{(\alpha)}_{\ell ms}(r,t)\, Y_{\ell ms}(\theta,\phi) \ , \qquad (G.17)$$

which is analogous to the multipole expansion of $\tilde{\chi}_\alpha(\underset{\sim}{r},\omega)$ given in (G.9).

G.3 THE NUMERICAL CALCULATION OF THE MULTIPOLE COEFFICIENTS (MULTEES)

The numerical calculation of the multipole coefficients for the equivalent elastic source centers on the following set of integrals:

$$\tilde{A}^{(\alpha)}_{\ell ms}(\omega) = \frac{1}{h^{(2)}_\ell(k_\alpha R)} \int_{-\infty}^{\infty} \left\{ \frac{1}{N^2_{\ell m}} \int_0^{2\pi} \int_0^{\pi} \chi_\alpha(R,\theta,\phi,t)\, Y_{\ell ms}(\theta,\phi) \sin\theta \, d\theta \, d\phi \right\} \times e^{-i\omega t} \, dt \ . \qquad (G.18)$$

The form of these integrals shows that the equivalent elastic source representation for any arbitrary nonlinear earthquake or explosion source can be derived, if the numerical calculation can be carried to some radius R in the elastic region.

In MULTEES, the integral (G.18) is carried out in two steps:

1. Double numerical integration on the surface of a sphere of radius R for each time at which the potentials are sampled. This spatial or area integration yields the multipole coefficients in the time domain, $A^{(\alpha)}_{\ell ms}(R,t)$, as given by Eq. (G.16).
2. Integration over time to obtain the coefficients $\tilde{A}^{(\alpha)}_{\ell ms}(\omega)$.

The second (single or 1-D) integration poses no special computational problem and is carried out using fast Fourier transform techniques.

Computational step (1), the calculation of the multipole coefficients in the time domain defined by Eq. (G.16), requires the evaluation of a set of double integrals over the surface of a sphere of radius R. These double integrals are of the general form

$$A(R) = \int_0^{2\pi} \int_0^{\pi} F(R,\theta,\phi) \sin\theta \, d\theta \, d\phi \, , \qquad \text{(G.19)}$$

where $F(R,\theta,\phi) = \frac{1}{N^2_{\ell m}} \chi_\alpha(R,\theta,\phi,t) \, Y_{\ell ms}(\theta,\phi)$. While the $Y_{\ell ms}(\theta,\phi)/N^2_{\ell m}$ are well behaved functions, the $\chi_\alpha(R,\theta,\phi)$ are to be obtained from discreetly sampled values on a finite difference grid. In general, these values will be available at a limited number of non-uniformly spaced points in the neighborhood of the spherical surface of radius R. The program MULTEES evaluates the integral (G.19) by first performing a spatial interpolation to obtain an evenly spaced discreet representation of $F(R,\theta,\phi)$ on the spherical surface, then performing a numerical double integration. Before describing the computational techniques, it is necessary to discuss briefly the form of the finite difference code output expected by MULTEES.

G.4 MULTEES INPUT

MULTEES is designed to operate with any numerical source code employing a two- or three-dimensional rectangular grid system. For compatibility with codes employing spherical or cylindrical coordinate systems, only minor modifications are required. In fact, the majority of the special techniques formulated in developing MULTEES were required for compatibility with rectangular grid systems.

Inasmuch as the multipole coefficients are defined in terms of potentials, it is necessary that the source calculation generate either values of χ_α directly or related variables from which χ_α can be derived. The potentials were defined in terms of the divergence and curl of the displacement field by (G.2). In its current form, MULTEES accepts the divergence (χ_4) and 0.5 times the curl ($\underset{\sim}{\chi}$) as generated output from the source calculation at specific points of interest in the elastic region.

The determination of these selected points of interest will be described below, but it is first necessary to discuss another point that should be addressed in order to ensure the valid linking of MULTEES to a source calculation. The discussions below will be carried out with general reference to three spatial dimensions, since the primary objective in developing MULTEES was to make available a general purpose code for computing multipole coefficients for any 3-D numerical source.

In a finite difference code, saved and computed values are computed either at node points or at zone centers. The potentials are zone-centered quantities and therefore are available at the centers of the rectangular prisms or cells formed by the grid system. This fact is important, first for determining the points at which the potentials are to be saved by the source calculation; and, secondly, in

communicating to the source code the identification of the stations at which these variables are to be monitored.

In order to maintain the proper spatial definition of source variables, such as displacements, velocities and potentials, the rectangular grid or "source coordinate system" on which MULTEES is based must be identical with that used by the numerical source code. This is accomplished in MULTEES by applying the same algorithm to generate the rectangular grid system that was used in the source code iteself. The grid system, which need not be evenly spaced, is defined by three one-dimensional real arrays: CSX(NX), CSY(NY), and CSZ(NZ). A grid point is specified by a set of three integer indexes (I,J,K) where the X, Y, and Z coordinates of the point are defined by CSX(I), CSY(J), and CSZ(K), respectively. In order to apply the general algorithm referred to above, the following five input specifications must be given for all three coordinates:

CSX(1) = location of the first point along the X-axis;

NX = total number of grid points on the X-axis;

DELX = the original or constant interval spacing between grid points on the X-axis;

SCALEX = a scale factor that is multiplied by the previous interval spacing in order to introduce "stretching" of successive grid points on the X-axis; for example, if SCALEX = 1.10, and DELX = 1.0, the spacing between successive grid points would be 1.000, 1.100, 1.210, 1.331, 1.464, etc.;

NSCALEX = the grid point index that identifies the start of "stretching" of the grid points on the X-axis.

One of the primary functions of MULTEES is to specify in advance the set of stations to be monitored during the numerical source calculation. A "monitoring" or "save" station is identified by a set of three indexes (I,J,K) that define the point in the rectangular grid at which the X-, Y-, and Z-components of the displacement field and velocity are to be saved. In addition to the displacement and velocity components at the save station grid point, the source calculation will also sample the four potentials χ_α ($\alpha = 1,2,3,4$) defined at the centers of the eight cells surrounding the point (I,J,K). Following the labeling convention that any given cell is identified by the three indexes of the grid point with the three highest integer values, the station (I,J,K) will sample χ_α's at the centers of the following eight cells:

1. I+1, J+1, K+1
2. I, J+1, K+1
3. I, J, K+1
4. I+1, J, K+1
5. I+1, J+1, K
6. I, J+1, K
7. I, J, K
8. I+1, J, K .

In short, the key information that MULTEES provides to the source code is a list of monitoring stations. The corresponding output that the source code then generates for MULTEES during each time cycle is the set of saved variables for each monitoring station. There are a total of 38 saved variables for each station per time cycle generated by the source calculation, namely,

1. X-, Y-, and Z-components of the displacement field (u, v, and w);
2. X-, Y-, and Z-components of the velocity ($\dot{u}$, $\dot{v}$, and $\dot{w}$);
3. χ_α (α = 1,2,3,4) at the center of the 8 surrounding cells in the sequence defined by the convention given above.

In addition, the cycle number and total elapsed time are also saved with the above variables for each time cycle the source calculation is run.

G.5 DOUBLE NUMERICAL INTEGRATION METHOD

By a double application of the familiar one-dimensional integration formula, known as Simpson's rule, the integral

$$\int_{XA}^{XB}\int_{YA}^{YB} F(X,Y)\, dX\, dY \qquad (G.20)$$

may be approximated by

$$(hk/9)\,[(F_{11} + F_{13} + F_{31} + F_{33}) + 4(F_{12} + F_{21} + F_{23} + F_{32}) + 16\,F_{22}]\,, \qquad (G.21)$$

where

$$X(I) = XA + (I-1)h$$

$$Y(J) = YA + (J-1)k$$

$$F_{IJ} \equiv F(X(I), Y(J))\,.$$

The numerical integration of the double integral Eq. (G.20) has thus been reduced to a simple two-way integration over a rectangle using only two evenly-spaced intervals in both X and Y.

By applying the formula given in Eq. (G.21) to sub-rectangles, and adding the results, the two-dimensional generalization of the parabolic rule can be derived in the form, as given in Hildebrand (1956)

$$\int_{XA}^{XB}\int_{YA}^{YB} F(X,Y)\,dX\,dY$$

$$= (HX \cdot HY/9)\,[(F_{11} + 4F_{21} + 2F_{31} + \ldots + F_{n_1})$$

$$+ 4(F_{12} + 4F_{22} + 2F_{31} + \ldots + F_{n_2})$$

$$+ 2(F_{13} + 4F_{23} + 2F_{33} + \ldots + F_{n_3})$$

$$+ \ldots + (F_{1m} + 4F_{2m} + 2F_{3m} + \ldots + F_{nm})] + E\,, \qquad (G.22)$$

where

$$E = -\frac{HX \cdot HY}{90}\left[n(HX)^4 \frac{\partial^4 F(\bar{\xi}_1, \bar{\eta}_1)}{\partial X^4} + m(HY)^4 \frac{\partial^4 F(\bar{\xi}_2, \bar{\eta}_2)}{\partial Y^4}\right]$$

$HX = (XB-XA)/(NX-1)$

$HY = (YB-YA)/(NY-1)$

$F_{IJ} \equiv F(I,J) = F(X(I),Y(J))$

NX $\equiv$ n = number of points in the one-dimensional X integration

NY $\equiv$ m = number of points in the one-dimensional Y integration

XB, XA = upper and lower limits of integration for the X variable

YB, YA = upper and lower limits of integration for the Y variable

ξ_1, ξ_2 lie in the interval (XA,XB), and

η_1, η_2 lie in the interval (YA,YB).

Both NX and NY are odd integers, not necessarily equal, corresponding to a division of the rectangle XA-XB-YB-YA into an even number of subrectangles. A major consequence of using evenly spaced intervals (HX and HY) in the double integration formula is the reduction of the error term to the analytic expression given above. A corresponding formula can be derived for non-equal spacing, but the error will not be so readily known.

In order to perform the numerical evaluation of the required double integrals defined in Eq. (G.16), MULTEES applies the formula Eq. (G.22) to approximate these integrals by multiple sums of the following form:

$$\int_{XA}^{XB}\int_{YA}^{YB} F(X,Y)\,dX\,dY \simeq$$

$$(HX \cdot HY/9)\left\{F(1,1) + F(1,NY) + F(NX,1) + F(NX,NY)\right.$$

$$+ 4 \sum_{\substack{I=2 \\ (\text{even})}}^{NX-1} [F(I,1) + F(I,NY)]$$

$$+ 4 \sum_{\substack{J=2 \\ (\text{even})}}^{NY-1} [F(1,J) + F(NX,J)]$$

$$+ 4 \sum_{\substack{J=3 \\ (\text{odd})}}^{NY-2} \sum_{\substack{I=3 \\ (\text{odd})}}^{NX-2} F(I,J)$$

$$+ 2 \sum_{\substack{J=3 \\ (\text{odd})}}^{NY-2} [F(1,J) + F(NX,J)]$$

$$+ 2 \sum_{\substack{I=3 \\ (\text{odd})}}^{NX-2} [F(I,1) + F(I,NY)]$$

$$+ 8 \sum_{\substack{J=2 \\ (\text{even})}}^{NY-1} \sum_{\substack{I=3 \\ (\text{odd})}}^{NX-2} F(I,J)$$

$$+ 8 \sum_{\substack{J=3 \\ (\text{odd})}}^{NY-2} \sum_{\substack{I=2 \\ (\text{even})}}^{NX-1} F(I,J)$$

$$+ 16 \sum_{\substack{J=2 \\ (\text{even})}}^{NY-1} \sum_{\substack{I=2 \\ (\text{even})}}^{NX-1} F(I,J) \Bigg\} \qquad \text{(G.23)}$$

F(I,J) is not an analytic function but represents values of the integrand at the point (I,J) that must be available in tabular form.

Before this double numerical integration formula can be applied, the "integration points" (I,J) on the surface of the sphere of radius R must first be determined. MULTEES offers the user the option of specifying both the integration limits and the number of integration points to be used by means of the input variables:

N1, N2 = number of points in the one-dimensional θ and ϕ integrations, respectively.

θ_1, θ_2, ϕ_1, ϕ_2 = lower and upper limits in the θ and ϕ integrations, respectively.

MULTEES calculates the interval spacings and the integration points (in radians) by means of the definitions given above for HX, HY, X(I), and Y(J). The integration points for the θ and ϕ integrations are stored in the one-dimensional real arrays

THETA(N1) and PHI(N2),

so that the integration point (I,J) is given by

THETA(I), PHI(J).

The total number of integration points is the simple product of N1 and N2. Both N1 and N2 must be odd integers, though not necessarily equal. To assist the user in selecting values for N1 and N2, MULTEES also calculates the number of points (odd integer) in both the θ and ϕ integrations corresponding to an angular interval having an arc length approximately equal to the linear spacing between successive grid points in the rectangular grid system. In other words, the largest odd integer is computed corresponding to

$$R \cdot (\theta_2 - \theta_1)/DEL ,$$

where R is the radius of the sphere, θ_2 and θ_1 are the upper and lower limits of the integration over θ, and DEL is an average linear spacing between grid points used in the source calculation.

In order to apply MULTEES in a two-dimensional case, one of the input variables, for example, N2, must be set equal to 1. The effect of setting N2 = 1 is to reduce the double (area) integration over a spherical surface to a one-dimensional or single integration along an arc on the sphere.

The double integration routine in MULTEES is designed to handle automatically such an event and to produce the correct numerical value of the corresponding single integral. The only adjustment that is made by MULTEES when N2 = 1, is the removal from Eq. (G.23) of the factor 2 H2/3, where H2 is the interval spacing for the ¢ integration. In other words, when N2 = 1 the double integration routine yields (2/3)H2 times the result of applying the one-dimensional parabolic rule for the θ integration.

MULTEES is designed to perform the required double numerical integrations on the sphere between any arbitrary set of angular limits $\theta_1 - \theta_2$ and $\phi_1 - \phi_2$, as specified by the user. The purpose for offering this flexibility is to allow the user to set up the operation of MULTEES in the most efficient configuration that is suitable for the conditions pertinent to the problem at hand. If the source displacement field possesses certain symmetry properties, one or both of the one-dimensional angular integrations can be reduced to a shorter interval. In such cases, the source calculation itself would be restricted to a fraction of full space, perhaps only a hemisphere or a single octant of a sphere. In the latter case, the limits on both θ and φ might therefore be reduced correspondingly to 0.0 and π/2. While the default values in MULTEES are 0 to π for θ and 0 to 2π for φ, the system offers the user convenient options corresponding to other frequently requested configurations.

G.6 THREE-DIMENSIONAL SPATIAL INTERPOLATION METHOD

In order to derive values of the integrand in Eq. (G.18) at the prescribed integration points on the surface of the sphere, given a set of values in the neighborhood of the sphere, a three-dimensional interpolation method is applied. If the values of a function $f(X_p,Y_p,Z_p)$ are available at the eight nodes defining a rectangular prism, then the value of $f(X,Y,Z)$ at any spatial point within the prism can be derived according to the following interpolation formula (see Zienkiewicz, Finite Element Methods in Engineering Science, p. 121),

$$f(\xi,\eta,\zeta) = \sum_{p=1}^{8} f(\xi_p,\eta_p,\zeta_p)S(p) \ , \qquad (G.24)$$

where the shape functions for a "linear" element (8 nodes) rectangular prism are given as

$$S(p) = (1/8)(1 + \xi\xi_p)(1 + \eta\eta_p)(1 + \zeta\zeta_p) \ . \qquad (G.25)$$

The set (ξ,η,ζ) specify a point in a normalized coordinate system for the rectangular prism, defined by the following eight nodes:

Node	ξ_p	η_p	ζ_p
1	1	1	1
2	-1	1	1
3	-1	-1	1
4	1	-1	1
5	1	1	-1
6	-1	1	-1
7	-1	-1	-1
8	1	-1	-1

(G.26)

For each integration point (X,Y,Z), a transformation must first be made to the normalized coordinate system (ξ,η,ζ) according to the following prescription:

$$\xi = \frac{2(X - X_0)}{X_1 - X_2}$$

$$\eta = \frac{2(Y - Y_0)}{(Y_1 - Y_4)}$$

$$\zeta = \frac{2(Z - Z_0)}{Z_1 - Z_5} \quad , \qquad \text{(G.27)}$$

where the origin of the rectangular prism is given by

$$X_0 = X_1 - (X_1 - X_2)/2$$

$$Y_0 = Y_1 - (Y_1 - Y_4)/2$$

$$Z_0 = Z_1 - (Z_1 - Z_5)/2 \qquad \text{(G.28)}$$

and the subscripts specify the nodes of the prism (P = 1,2, ... 8). In other words, the first node of the prism is given by (X_1,Y_1,Z_1) in rectangular coordinates and by (1,1,1) in the normalized coordinate system having an origin at (X_0,Y_0,Z_0).

To illustrate how the interpolation formula is applied in MULTEES, the required computational operations performed during pre-processing will be outlined below. Since the source calculation is performed in a rectnagular grid, each integration point (I,J) defined by THETA(I) and PHI(J) must first be transformed to rectangular coordinates (X,Y,Z). From the coordinates of the grid system defined by CSX(NX), CSY(NY), CSZ(NZ), MULTEES then determines the 8 grid points and corresponding grid indexes that define the cell in which the integration point (X,Y,Z) is located. As discussed above,

however, this cell is not the correct prism to be used when interpolating the potentials. Since the curl and divergence of the displacement field, and hence the potentials themselves, are available in the source calculation only at the centers of the rectangular cells, MULTEES must next determine in which eighth subcell the point (X,Y,Z) is located. Each of the eight subcell regions will be associated with a different rectangular prism, in which the eight nodes are centers of the rectangular grid cells. A 2-D illustration of the method under discussion is presented in Fig. G.1. In this example, MULTEES determines that the point P(X,Y) is located within cell (3,3), that is, the rectangular cell bounded by the grid points (3,3), (2,3), (2,2), and (3,2). MULTEES then determines that P is located in the "upper-right" subcell region of cell (3,3) and therefore must be in the rectangular prism formed by the centers of the four cells (4,4), (3,4), (3,3) and (4,3), where a cell (center) is identified by its "upper-righthand" grid point.

Once MULTEES has determined the rectangular prism formed by the eight cell centers surrounding the point (X,Y,Z), the rectangular coordinates of these center nodes are computed and saved along with the cell indexes identifying each of the eight nodes. In this manner the monitoring station for the integration point (X,Y,Z) is determined. The station is defined by the three indexes corresponding to the grid point at the "origin" or "center" of the eight cells required for application of the 3-D interpolation formula. The indexes of the monitoring station are identical to the cell indexes corresponding to the seventh node, following the labeling convention described above. For the 2-D example, illustrated in Fig. G.1, the monitoring station for the point "P" is (3,3). Notice that the (3,3) grid point is at the "center" of the four cells whose centers are the nodes of the prism in which P is located.

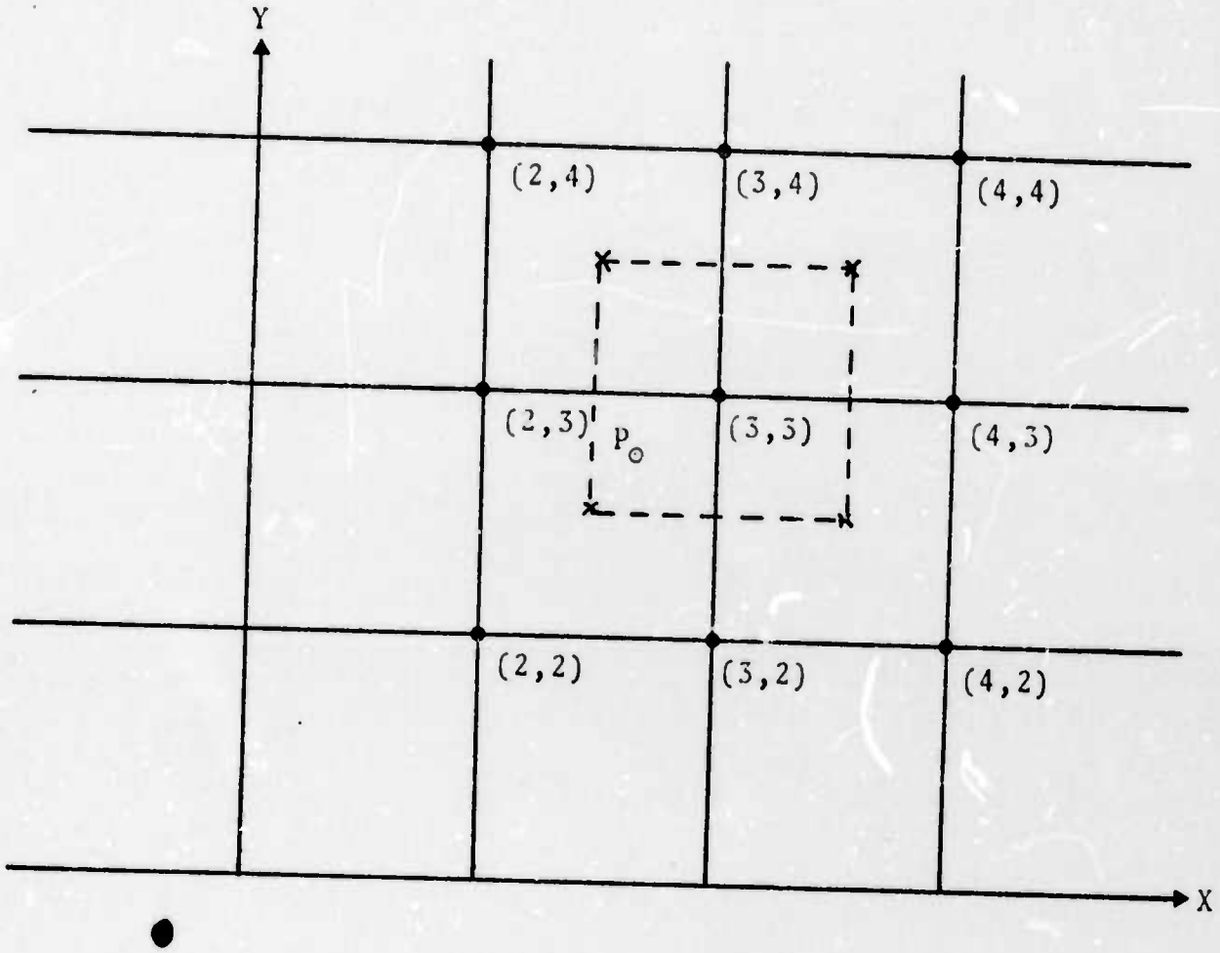


Figure G.1. Illustration in 2-D of cell identification for application of 3-D interpolation formula.

The next operation performed by MULTEES is the calculation of the eight shape functions corresponding to the center nodes. The origin of the normalized coordinate system is given by Eq. (G.28). The coordinate transformation for the point (X,Y,Z) is made according to Eq. (G.27). Then the shape functions S(p) defined in Eq. (G.25) are computed using these coordinates (ξ,η,ζ) for the integration point and the definition of the eight nodes in the normalized coordinate system given in Eq. (G.26).

The series of pre-processing operations described above must be performed for each integration point (I,J). In order to calculate the appropriate shape functions, a different normalized coordinate system is computed for each point, unless possibly more than one point is located within the same prism. The primary output generated by these pre-processing operations is a set of eight shape functions and a set of three indexes that identifies the monitoring station corresponding to each integration point. The acutal application of the 3-D interpolation formula given by Eq. (G.24) is performed by a subsequent program in MULTEES during processing of the output generated by the source calculation at the prescribed monitoring stations. For each station, the source code must save values of the four potentials at the centers of each of the eight cells surrounding the station.

G.7 SELECTION OF MONITORING STATIONS

Once the monitoring station corresponding to each integration point has been determined as described above, three further pre-processing operations must be performed by MULTEES to insure efficient linking with the source code. First, the set of monitoring stations are sorted by MULTEES in such a manner that the stations will be arranged according to the requirements of the specific source code to which it will be linked. This step is necessary because each source code operating with a rectangular grid system proceeds in a prescribed rectilinear sequence. The monitoring stations, on the other hand, have been determined according to the angular requirements of a spherical integration. By means of this sorting operation MULTEES can arrange the stations to suit the rectangular sequence followed by the source code.

After sorting, MULTEES then eliminates all duplications among the set of monitoring stations. Depending on the angular interval between successive integration points and the linear dimensions of the rectangular cells, several integration points, especially those corresponding to small values of θ, may be located within the same prism and therefore be associated with the same monitoring station. While the shape functions for such points will be different, only a single set of values for the potentials at the eight cell centers surrounding the monitoring station need be saved. It is this sorted set of unique monitoring stations that is generated by MULTEES and passed to the source code. In this way, the source code is informed of precisely which cells are to be monitored for further processing by MULTEES.

As the third step in the selection of a set of monitoring stations, a correspondence table must be produced linking each integration point (I,J) to a sequence

number for the sorted stations. When the potentials are passed to MULTEES for further processing, it must be possible to determine which station, identified by its sequence number, corresponds to any given integration point. The one-to-one correspondence initially holding between a point (I,J) and a set of three indexes (IX,IY,IZ) identifying a station must be preserved even after the stations are sorted and the duplications are eliminated. This association is preserved by means of a correspondence table that is generated and saved by MULTEES during the first stage or preprocessing operation.

G.8 PRELIMINARY VALIDATION OF THE MULTEES PROGRAMS

Preliminary validation of the MULTEES program series was achieved by means of a comparison with the multipole coefficients in the time domain calculated previously for an underground explosion in an axisymmetric cavity and reported by Cherry, et al. (1974). This control calculation was performed using a two-dimensional Lagrangian finite difference source code. The divergence and curl of the displacement field required for the equivalent elastic source determination were monitored at twenty evenly spaced points on an arc subtending 90 degrees at a radius of 140.68 meters.

Two approaches were followed for testing purposes. In the first test series, by applying the symmetry properties for an axisymmetric source field, a set of three-dimensional potentials $\chi_\alpha(R,\theta,\phi)$ defined at evenly spaced points on the surface of a sphere of radius 140.68 meters were generated for each time cycle at which the divergence and curl were available at the 20 points on the arc. The general purpose MULTEES program was then used to compute the series of multipole coefficients. Excellent agreement with the earlier results of better than 1 percent was observed.

In a second test series, the limited set of values of χ_u available at 20 points on the arc corresponding to a range in θ of 0° to 90°, that is, output from a two-dimensional source calculation, were processed directly by MULTEES under the 2-D mode of operation. In this case, again excellent agreement was found with the results calculated previously.

The routines for applying the 3-D interpolation method were tested separately in a number of ways. In one approach, a set of analytic functions were used in the place of values of the potentials at the eight nodes surrounding each integration point. The interpolated value at each point was then compared to the exact value given directly by the analytic function. In this manner, the accuracy of the interpolation method was determined as a function of the position of the integration point on the surface of the sphere and the dimensions of the rectangular grid system chosen for the source calculation.